2019

Development of Ligand-Directed Drug-Loaded Liposomes to Target Heterogeneous Tumour Cell Populations in Metastatic Breast Cancer

Lisa Belfiore

UNIVERSITY
OF WOLLONGONG
AUSTRALIA

Development of Ligand-Directed Drug-Loaded Liposomes to Target Heterogeneous Tumour Cell Populations in Metastatic Breast Cancer

A thesis submitted in fulfilment of the requirements for the award of the degree

Doctor of Philosophy

from

University of Wollongong

by

Lisa Belfiore

School of Chemistry and Molecular Bioscience
Faculty of Science, Medicine and Health

June 2019

This research has been conducted with the support of an Australian Government Research Training Program Scholarship.

Declaration

I declare that this thesis, submitted in fulfilment of the requirements for the award of the degree of Doctor of Philosophy from the University of Wollongong is wholly my own work unless otherwise referenced or acknowledged. This document has not been submitted for qualifications at any other academic institution.

Lisa Belfiore
June 2019

Abstract

The tendency for breast cancer cells in the primary tumour to spread to other parts of the body and form new tumours in vital organs, termed metastasis, is the main cause of breast cancer-related mortality. Therapies that target highly metastatic cells have proved successful in the clinic, but the development of therapeutic resistance to these targeted therapies significantly limits clinical efficacy. Therefore, new anticancer therapies that target invasive tumour cells while minimising systemic toxicity are required. The urokinase plasminogen activator receptor (uPAR) is recognised as a biomarker for metastasis in breast cancer. Targeting uPAR in breast cancer can be achieved by attaching plasminogen activator inhibitor-2 (PAI-2) to the surface of drug-loaded liposomes in order to facilitate liposome uptake into uPAR-positive cells. This thesis aimed to develop and evaluate novel uPAR-targeted liposomes containing a potent anti-mitotic cytotoxin, *N*-alkylisatin (*N*-AI), for the treatment of metastatic breast cancer.

Novel *N*-AI-loaded PAI-2-functionalised (*N*-AI PAI-2) liposomes were prepared and characterised for the first time using optimisations to previously reported methods. *N*-AI PAI-2 liposomes were 141.1 ± 5.0 nm in diameter, were monodisperse (polydispersity index of 0.086 ± 0.030), had a zeta potential of –4.66 ± 0.52 mV and contained *N*-AI at a concentration of 2.2 mM, equating to 43.1% drug loading (% w/w). PAI-2 conjugation to the surface of *N*-AI-loaded liposomes was confirmed using size-exclusion chromatography and Western blotting. A PAI-2 inhibitory activity assay confirmed that PAI-2 attached to the surface of liposomes remained active against urokinase plasminogen activator after conjugation, making *N*-AI PAI-2 liposomes suitable for further *in vitro* and *in vivo* evaluation against breast cancer cells.

In vitro, cellular uptake of fluorescently labelled PAI-2 liposomes into MDA-MB-231 breast cancer cells (uPAR-positive) was increased ($P < 0.01$) relative to MCF-7 breast cancer cells (uPAR-negative) as measured by flow cytometry. Confocal microscopy confirmed uptake of PAI-2 liposomes and localisation within lysosomes. *N*-AI PAI-2 liposomes showed a potent cytotoxic effect against MCF-7 and MDA-MB-231 cells grown in 2D after 72 h (IC_{50} values of 31.84 ± 8.20 µM and 5.40 ± 1.14 µM, respectively) and in 3D as multicellular tumour spheroids after 96 h (IC_{50} values of 40.2 ± 4.0 µM and

60.4 ± 7.1 μM, respectively). *In vivo*, *N*-AI PAI-2 liposomes had a plasma half-life of 5.82 h and showed an increased accumulation at the primary tumour site in an orthotopic MDA-MB-231 BALB/c-Fox1nu/Ausb xenograft mouse model relative to non-functionalised liposomes at the 10 min, 3 h and 6 h post-injection time points ($P < 0.001$). However, *N*-AI PAI-2 liposomes did not have a significant effect on primary tumour growth or metastatic burden in the lungs and liver relative to non-functionalised *N*-AI-loaded liposomes or empty control liposomes in the two breast tumour mouse models used.

Finally, quantification of PAI-2 attached to the surface of liposomes was achieved using single-molecule fluorescence microscopy. Liposome and protein signals showed a high degree of colocalisation, indicating that proteins were bound to intact liposomes. The average number of attached PAI-2 molecules per liposome was determined to be 11 ± 4. Imaging of dual-functionalised liposomes revealed stoichiometries of the two attached proteins in accordance with the molar ratios of protein added during preparation. For dual-ligand liposomes, the post-insertion method generated liposomes with a more equal ratio of the two ligands than the conventional method (2.1 ± 2.5 and 17 ± 18, respectively). This work demonstrated, for the first time, the practical utility of single-molecule fluorescence microscopy to quantify the density and stoichiometry of ligands attached to the surface of liposomes.

Together, the findings in this thesis support the rationale for targeting uPAR-positive breast cancer cells using *N*-AI-loaded PAI-2-functionalised liposomes. The results provide a basis for the further development of dual-ligand liposomes that can target heterogeneous tumour cells within the HER2-positive and triple-negative breast cancer subtypes in which uPAR has been shown to play a key role in driving metastasis. The development of novel liposomal drug carriers that can target uPAR to deliver cytotoxic drugs to heterogeneous populations of breast cancer cells is a promising therapeutic strategy to improve the treatment of metastatic breast cancer. This thesis will guide future work exploring targeting of the urokinase plasminogen activator system as a strategy to overcome breast cancer metastasis.

Acknowledgements

Firstly, I would like to acknowledge my primary supervisor, Kara Vine-Perrow, for her consistent encouragement and support throughout the completion of my research. Kara, you made my PhD experience a truly pleasant one. I appreciate how you always made time for me – whether it was brainstorming, troubleshooting experiments or proofreading manuscripts, I always felt supported by you. It was clear that you were invested in my success as a PhD student and you made me feel like I could handle anything. I couldn't have asked for a better supervisor and mentor over these past four years – thank you so much! Thank you also to my co-supervisor Marie Ranson and associate supervisor Darren Saunders for your guidance and unique perspectives which greatly strengthened my research.

Thank you to the current and past members of the Perrow and Ranson research groups at IHMRI for all your help and advice with experiments, especially Samantha Wade, Liyu Chen, Clare Watson, Benjamin Buckley and Elahe Minaei. Thank you to Nathanial Harris and Jordan Cater for assisting with PAI-2 expression and purification. Thank you to Lisanne Spenkelink and Antoine van Oijen for your meaningful collaboration with the single-molecule fluorescence microscopy experiments. Thank you to Lesley Castillo, Adelaide Young, Andrew Law and Samantha Oakes at the Garvan Institute of Medical Research for your assistance with the research I conducted as a visiting student.

Thank you to the Illawarra Police Charity Ball Committee and UOW for providing me with a Cancer Research Top-Up Scholarship in honour of Illawarra police chaplain Jayne Wilson. Thank you to the Faculty of Science, Medicine and Health at UOW for providing me with a Higher Degree Research Student Travel Grant to present my research in Rome, Italy. Thank you to Global Challenges at UOW for awarding me with a PhD Student Travel Scholarship to present my research in Boston, USA.

Finally, thank you to those closest to me for your encouragement and support throughout this journey. In particular, I want to thank my amazing sister. Samantha, thank you for everything that you've helped me with over the past four years, including proofreading this thesis!

Contents

Figures

Tables

Abbreviations

µCi	microcurie
µg	microgram
µL	microlitre
µm	micrometre
µM	micromolar
2D	two-dimensional
3D	three-dimensional
^{3}H-CHE	tritiated cholesteryl hexadecyl ether
ABC	accelerated blood clearance
APH	acid phosphatase
BBB	blood-brain barrier
BCA	bicinchoninic acid
BEB	brain-endothelial barrier
BSA	bovine serum albumin
CO	conventional (method)
cryo-TEM	cryogenic-transmission electron microscopy
Da	dalton
DLS	dynamic light scattering
DOL	degree of labelling
DPPC	dipalmitoylphosphatidylcholine
DSPE	1,2-distearoyl-sn-glycero-3-phosphoethanolamine
ECM	extracellular matrix
EDTA	ethylenediaminetetraacetic acid
EGFR	epidermal growth factor receptor
EMA	European Medicines Agency
EMCCD	electron-multiplying charge-coupled device
EMP	empty (liposome)
EPR	enhanced permeability and retention
ER	estrogen receptor
ESI-MS	electrospray ionisation mass spectrometry
FBS	fetal bovine serum

FDA	Food and Drug Administration
FITC	fluorescein isothiocyanate
FSC	forward scatter
g	gram
h	hour
HER2	human epidermal growth factor receptor 2
HPLC	high-performance liquid chromatography
IC_{50}	half maximal inhibitory concentration
ID	injected dose
kDa	kilodalton
L	litre
M	molar
mal-PEG_{2000}-DSPE	1,2-distearoyl-*sn*-glycero-3-phosphoethanolamine-N-[maleimide(polyethylene glycol)-2000]
MFI	mean fluorescence intensity
mg	milligram
min	minute
mL	millilitre
mM	millimolar
mol	mole
mPEG_{2000}-DSPE	1,2-distearoyl-*sn*-glycero-3-phosphoethanolamine-N-[(polyethylene glycol)-2000]
MPS	mononuclear phagocyte system
MTS	3-(4,5-dimethylthiazol-2-yl)-5-(3-carboxymethoxyphenyl)-2-(4-sulfophenyl)-2H-tetrazolium
mV	millivolt
MW	molecular weight
N-AI	5,7-dibromo-*N*-(*p*-hydroxymethylbenzyl)isatin (*N*-alkylisatin)
NF	non-functionalised (liposome)
ng	nanogram
nm	nanometre
NTA	nanoparticle tracking analysis
OD	optical density

PAI-1	plasminogen activator inhibitor-1
PAI-2	plasminogen activator inhibitor-2
PBS	phosphate-buffered saline
PC	L-α-phosphatidylcholine
PDI	polydispersity index
PEG	polyethylene glycol
P-gp	P-glycoprotein
PI	post-insertion (method)
PR	progesterone receptor
PVDF	polyvinylidene fluoride
R123	rhodamine 123
R18	octadecyl rhodamine B chloride
RME	receptor-mediated endocytosis
RT	room temperature
s.d.	standard deviation
s.e.m.	standard error of the mean
SDS-PAGE	sodium dodecyl sulfate polyacrylamide gel electrophoresis
SEC	size-exclusion chromatography
SSC	side scatter
TBS	tris-buffered saline
TBST	tris-buffered saline with Tween-20
TIRF	total internal reflection fluorescence
TNBC	triple-negative breast cancer
TZ	trastuzumab (Herceptin®)
uPA	urokinase plasminogen activator
uPAR	urokinase plasminogen activator receptor
uPAS	urokinase plasminogen activator system
VEGF	vascular endothelial growth factor
x g	relative centrifugal force

Publications

1. **Belfiore, L**, Saunders, DN, Ranson, M & Vine, KL 2019, '*N*-alkylisatin-loaded liposomes targeting the urokinase plasminogen activator system in breast cancer', manuscript in preparation for submission to *Nanomedicine: Nanotechnology, Biology, and Medicine*.

2. **Belfiore, L**, Spenkelink, LM, Ranson, M, van Oijen, AM & Vine, KL 2018, 'Quantification of ligand density and stoichiometry on the surface of liposomes using single-molecule fluorescence imaging', *Journal of Controlled Release*, vol. 278, pp. 80-86.

3. **Belfiore, L**, Saunders, DN, Ranson, M, Thurecht, K, Storm, G & Vine, KL 2018, 'Towards clinical translation of ligand-functionalized liposomes in targeted cancer therapy: challenges and opportunities', *Journal of Controlled Release*, vol. 277, pp. 1-13.

4. Vine, KL, **Belfiore, L**, Jones, L, Locke, JM, Wade, S, Minaei, E & Ranson, M 2016, 'N-alkylated isatins evade P-gp mediated efflux and retain potency in MDR cancer cell lines', *Heliyon*, vol. 2, e00060.

Conference Presentations

1. **Belfiore, L**, Spenkelink, LM, Ranson, M, van Oijen, AM & Vine, KL 2018, 'Quantification of ligand stoichiometries in nanoparticle drug delivery systems using single-molecule fluorescence imaging', Poster Presentation, 1st Controlled Release Society Asia Meeting, Singapore

2. **Belfiore, L**, Spenkelink, LM, Ranson, M, van Oijen, AM & Vine, KL 2018, 'Quantification of ligand stoichiometries in nanoparticle drug delivery systems using single-molecule fluorescence imaging', Oral Presentation, International Conference on Nanoscience and Nanotechnology, Wollongong, Australia
    - Student Presenter Bursary, Australian Nanotechnology Network

3. **Belfiore, L**, Johnstone, C, Anderson, RL, Saunders, DN, Ranson, M & Vine, KL 2018, 'Development of targeted drug-loaded liposomes to treat uPA/uPAR+ HER2+ metastatic breast cancer', Poster Presentation, International Conference on Nanoscience and Nanotechnology, Wollongong, Australia

4. **Belfiore, L**, Spenkelink, LM, Ranson, M, van Oijen, AM & Vine, KL 2017, 'Characterisation of targeted liposomes using single-molecule fluorescence microscopy', Oral Presentation, School of Biology Postgraduate Conference, Kioloa, Australia

5. **Belfiore, L**, Spenkelink, LM, Ranson, M, van Oijen, AM & Vine, KL 2017, 'Quantification of dual-ligand attachment to the surface of liposomes using single-molecule fluorescence microscopy', Poster Presentation, 11th Drug Delivery Australia Conference, Wollongong, Australia

6. **Belfiore, L**, Saunders, DN, Ranson, M & Vine, KL 2017, 'Development of dual-targeted drug-loaded liposomes for metastatic breast cancer treatment', Oral Presentation, 11th Drug Delivery Australia Conference, Wollongong, Australia
    - Best Oral Presentation $1000 Travel Award, ATA Scientific

7. **Belfiore, L**, Spenkelink, LM, Ranson, M, van Oijen, AM & Vine, KL 2017, 'Quantification of dual-ligand attachment to the surface of liposomes using single-molecule fluorescence microscopy', Poster Presentation, 44th Annual Controlled Release Society Meeting & Exposition, Boston, USA

8. **Belfiore, L**, Saunders, DN, Ranson, M & Vine, KL 2016, 'Development of targeted drug-loaded liposomes to treat metastatic breast cancer', Oral Presentation, 1st Annual Western Australia Symposium of Nanobiotechnology, Perth, Australia
    - Best Student Presentation Prize, University of Western Australia

9. **Belfiore, L**, Spenkelink, LM, Ranson, M, van Oijen, AM & Vine, KL 2016, 'Development of targeted drug-loaded liposomes to treat breast cancer', Oral Presentation, School of Biology Postgraduate Conference, Kioloa, Australia
    - Highly Commended Oral Presentation Prize, School of Biology

10. **Belfiore, L**, Saunders, DN, Ranson, M & Vine, KL 2016, 'Development of drug-loaded liposomes targeting the urokinase plasminogen activator system to treat metastatic breast cancer', Oral Presentation, 24th Annual Thompson Prize Talks, Wollongong, Australia
    - Thompson Prize Finalist, Sydney Protein Group

11. **Belfiore, L**, Saunders, DN, Ranson, M & Vine, KL 2016, 'Development of dual-targeted drug-loaded liposomes to treat uPAR/HER2-positive metastatic breast cancer', Oral Presentation, 5th Sydney Cancer Conference, Sydney, Australia

12. **Belfiore, L**, Johnstone, C, Anderson, RL, Saunders, DN, Ranson, M & Vine, KL 2016, 'Development of novel dual-targeted drug-loaded liposomes for the treatment of uPAR+/HER2+ metastatic breast cancer', Oral Presentation, 7th International Nanomedicine Conference, Coogee, Australia
    - Student Conference Travel Bursary, Australian Nanotechnology Network

13. **Belfiore, L**, Johnstone, C, Anderson, RL, Saunders, DN, Ranson, M & Vine, KL 2016, 'Development of targeted drug-loaded liposomes to treat uPA/uPAR+ HER2+ metastatic breast cancer', Poster Presentation, Australian Society for Medical Research NSW State Scientific Meeting, Sydney, Australia
    - Registration Sponsorship, Illawarra Health and Medical Research Institute

14. **Belfiore, L**, Johnstone, C, Anderson, RL, Saunders, DN, Ranson, M & Vine, KL 2016, 'Development of dual-targeted drug-loaded liposomes to treat metastatic breast cancer', Oral Presentation, Australia–New Zealand Chapter of the Controlled Release Society Student Workshop, Melbourne, Australia
    - Young Scientist $2000 Travel Award, ATA Scientific

15. **Belfiore, L**, Johnstone, C, Anderson, RL, Saunders, DN, Ranson, M & Vine, KL 2015, 'Development of targeted drug-loaded liposomes to treat metastatic breast cancer', Oral Presentation, School of Biology Postgraduate Conference, Kioloa, Australia
    - Best Initial Seminar Presentation Prize, School of Biology

16. **Belfiore, L**, Johnstone, C, Anderson, RL, Saunders, DN, Ranson, M & Vine, KL 2015, 'Development of targeted drug-loaded liposomes to treat uPA/uPAR+ HER2+ metastatic breast cancer', Poster Presentation, 15th International Workshop of Molecular and Cellular Biology of Plasminogen Activation, Rome, Italy
    - International Conference Fellowship Award, National Institutes of Health

17. **Belfiore, L**, Johnstone, C, Anderson, RL, Saunders, DN, Ranson, M & Vine, KL 2015, 'Development of drug-loaded liposomes to treat uPA/uPAR+ HER2+ metastatic breast cancer', Oral Presentation, 15th International Workshop of Molecular and Cellular Biology of Plasminogen Activation, Rome, Italy
    - Outstanding Graduate Student Oral Presentation Prize, University of Notre Dame

Chapter 1:

Literature Review

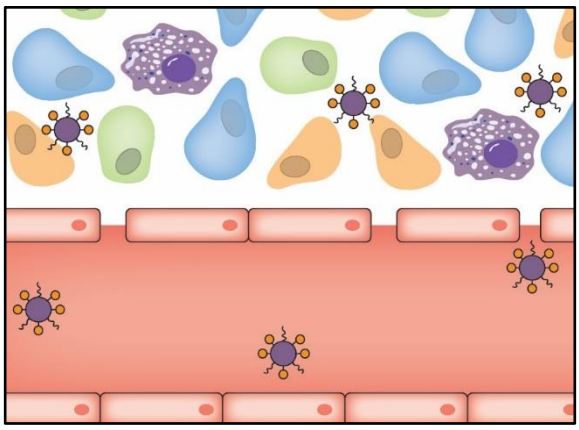

Liposome targeting of tumour cells

Portions of this chapter have been published in the following work:

Belfiore, L, Saunders, DN, Ranson, M, Thurecht, KJ, Storm, G & Vine, KL 2018, 'Towards clinical translation of dual-ligand liposomes in cancer therapy: Challenges and opportunities', *Journal of Controlled Release*, vol. 277, pp. 1-13.

Author contributions: LB wrote the manuscript; DNS, MR, KJT, GS and KLV edited the manuscript for submission.

1.1 Introduction

The development of therapeutic resistance to targeted anticancer therapies remains a significant clinical problem in the treatment of breast cancer, with intratumoural heterogeneity playing a key role. In this context, improving the therapeutic outcome through simultaneous targeting of multiple tumour cell subtypes within a heterogeneous breast tumour is a promising approach. Liposomes have emerged as useful drug carriers that can reduce systemic toxicity and increase drug delivery to the tumour site. While clinically used liposomal drug formulations show marked therapeutic advantages over free drug formulations, ligand-functionalised liposomes that can target multiple tumour cell subtypes may further improve therapeutic efficacy by facilitating drug delivery to a broader population of tumour cells making up the heterogeneous tumour tissue. Ligand-directed liposomes enable the active targeting of cell receptors via surface-attached ligands that direct drug uptake into tumour cells or tumour-associated stromal cells and therefore can increase the selectivity of drug delivery. This literature review will discuss the utility of recent ligand-directed liposome approaches, with a focus on dual-ligand liposomes for targeting intratumoural heterogeneity, for the treatment of solid tumours.

1.2 Breast cancer growth and metastasis

Breast cancer is the most common invasive cancer in women worldwide, accounting for approximately one quarter of all cancer cases in women, and remains a leading cause of cancer-related morbidity and mortality (Jemal et al. 2011). While overall survival rates have improved steadily over the last several decades, breast cancer still accounts for almost half a million deaths each year (Ward et al. 2015). Breast cancer is a particularly deadly disease due to the tendency for cancer cells of the primary tumour to spread to other parts of the body and form new tumours in vital organs – most commonly the bones, liver, lungs and brain (Lee 1983). This process, termed metastasis, is the leading cause of breast cancer-related mortality, with more than 90% of patient deaths resulting from metastatic disease (Dolznig et al. 2011). Despite a growing understanding of the molecular biology of breast cancer metastasis and several key advancements in treatment options, there is currently no cure for metastatic breast cancer (Sledge 2016).

Metastasis occurs when tumour cells break away from the primary tumour and form new tumours at distant sites (Fig. 1.1). The primary tumour microenvironment is a complex heterogeneous structure, consisting of an extracellular matrix (ECM), blood vasculature and a collection of cell types that support tumour cell growth, including endothelial cells, fibroblasts and immune cells (Thoma et al. 2014). Through the activation or inactivation of particular genes, tumour cells acquire the ability to proliferate indefinitely and utilise key cellular systems to facilitate their tumourigenic properties (Hanahan & Weinberg 2011; Klein 2008). One of the key processes facilitating metastasis is the degradation of the ECM, the physical barrier separating distinct tissue types in the body. Proteolytic enzymes expressed by tumour cells and tumour-associated cells (Section 1.5) degrade structural proteins of the ECM and create a passageway that allows the movement of tumour cells out of the area (Krueger et al. 2005). Angiogenesis, the process by which the tumour creates its own vasculature to obtain vital nutrients and remove waste products, facilitates the escape of tumour cells into the bloodstream and lymphatic system (Weidner et al. 1991). This process, termed intravasation, enables tumour cells to travel to distant sites in the body and form new secondary metastatic tumours.

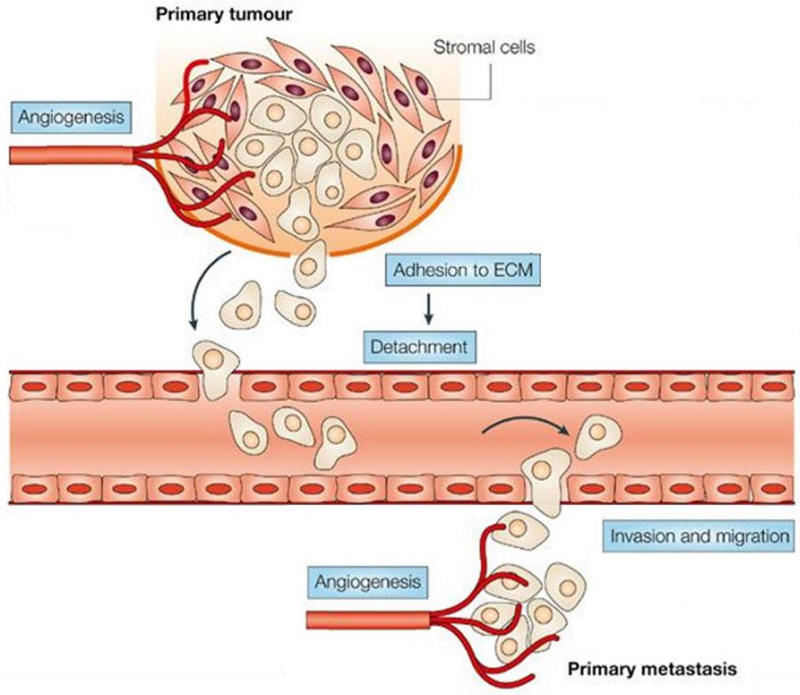

Figure 1.1: Tumour cell invasion and metastasis in breast cancer. Cells of the primary tumour produce proteolytic enzymes that degrade components of the extracellular matrix (ECM), allowing tumour cells to escape from the area and enter the bloodstream or lymphatic system. Tumour cells can then travel to other sites in the body and form secondary tumours. Figure adapted from Liu et al. (2005).

1.3 Molecular classification of breast cancer

The identification of tumour biomarkers and the associated molecular classification of breast cancer is highly useful for determining the most appropriate treatment course and evaluating prognosis. Many important biomarkers and cellular pathways involved in tumour progression and metastasis have been identified and assist in the prediction of patient responses to hormone-, chemo-, immuno- and molecular-targeted therapies, the determination of mechanisms of therapeutic resistance, and the prediction of disease progression and likelihood of relapse (Bailey et al. 2016; Schnitt 2010). Overexpression of specific cell surface receptors by tumour cells may be exploited to directly target tumour cells using antibodies or smaller molecules, or to enable targeted delivery of cytotoxic compounds to tumour cells. Such targeted approaches enable more specific anti-tumour effects, potentially resulting in enhanced tumour cell kill and/or a reduction in off-target effects.

Several important biomarkers involved in breast cancer progression and metastasis have been identified, including the estrogen receptor (ER), progesterone receptor (PR) and human epidermal growth factor receptor 2 (HER2) (Schnitt 2010). These biomarkers can be used to classify breast cancer into broad molecular subtypes (Table 1.1) (Howlader et al. 2014), which assist in the prediction of patient responses to chemotherapy treatments, the determination of mechanisms of resistance to treatments, the prediction of disease course and likelihood of relapse, and provide a possible target for anticancer therapies (Dos Anjos Pultz et al. 2014). The following sections will focus on the HER2-enriched subtype and the triple-negative breast cancer (TNBC) subtype. For further information regarding the hormone receptor-positive breast cancer subtypes, see previously published reviews on these topics (Abraham & Staffurth 2016; Basile et al. 2017; De Marchi et al. 2016).

Table 1.1: Breast cancer molecular subtypes. Breast cancer can be broadly divided into four main subtypes: Luminal A, Luminal B, HER2-enriched and triple-negative. ER, estrogen receptor; PR, progesterone receptor; HER2, human epidermal growth factor receptor 2.

Clinical Features	Luminal A	Luminal B	HER2-enriched	Triple-negative
ER expression	+	+	–	–
PR expression	+	+	–	–
HER2 expression	–	+ or –	+	–
Incidence (%)	~30-70	~10-20	~5-15	~15-20
Targeted therapies	Endocrine	Endocrine	Anti-HER2	None
Rate of metastasis	Low	Low	High	High
Prognosis	Good	Good	Poor	Poor

1.3.1 Triple-negative breast cancer

The TNBC subtype is characterised by a lack of expression of ER and PR, and a lack of overexpression and/or amplification of HER2 (Gluz et al. 2009). As this subtype lacks these three main breast cancer molecular biomarkers, there are no targeted therapy options for TNBC, and the use of conventional chemotherapies remains the standard of care (Waks & Winer 2019). In addition, TNBC is a markedly heterogeneous subtype at both the clinical and molecular scale, which can make treatment difficult. The prognosis of TNBC is generally poor, with high rates of disease recurrence and relapse (Liedtke & Kiesel 2012). The progression-free survival and overall survival rates of TNBC patients are significantly shorter than those of non-TNBC patients (Keam et al. 2007) (Fig. 1.2).

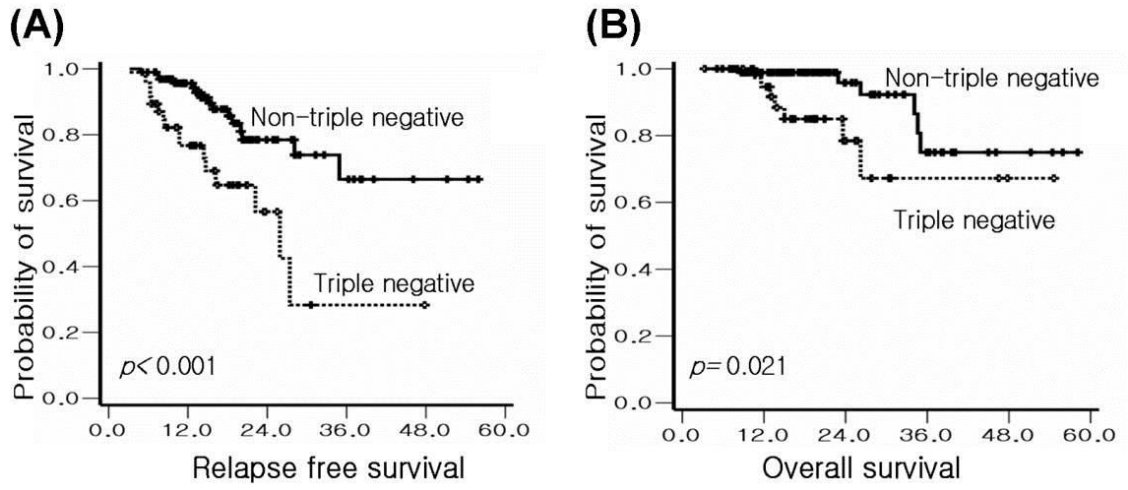

Figure 1.2: Probability of survival in triple-negative breast cancer. Kaplan-Meier analyses of (**A**) relapse-free survival and (**B**) overall survival according to triple-negative and non-triple-negative breast cancer. Figure from Keam et al. (2007).

In order to develop novel and effective targeted treatment options for TNBC, the discovery and validation of genetic targets relevant to the TNBC subtype remains an active area of research (Denkert et al. 2017). Research has focused on identifying prognostic and predictive markers for this subtype, such as overexpression of the *TP53* gene, mutations in *BRCA1/2* and dysregulation of the PI3K/AKT/mTOR pathway (Sporikova et al. 2018), and several clinical trials are in progress for novel molecular therapies and immunotherapies (Vikas et al. 2018). Therefore, the continued validation of further novel molecular targets for TNBC, and breast cancer more broadly, is an important area of research (Dos Anjos Pultz et al. 2014).

1.3.2 HER2-positive breast cancer

HER2 (also known as Erb-B2 receptor tyrosine kinase 2 (ERBB2)) belongs to the transmembrane epidermal growth factor receptor subfamily of tyrosine kinases involved in the initiation of signal transduction pathways that regulate cell growth and differentiation (Yarden 2001). Amplification and overexpression of *HER2* (chromosome position 17q12) occurs in 15–25% of breast cancers and results in uncontrolled tumour cell proliferation (Slamon et al. 1987). The HER2-positive breast cancer subtype is associated with an aggressive disease course, increased resistance to chemotherapy, increased likelihood of metastasis and recurrence, and is indicative of an overall poor patient prognosis (Schnitt 2010). For this reason, HER2 has been identified as an important biomarker for breast cancer, as well as for several other cancer types where HER2 may be overexpressed, including ovarian, uterine and pancreatic cancers (Asuthkar et al. 2013).

Several HER2-targeted therapies have been developed to treat HER2-positive breast cancer. Trastuzumab (TZ; trade name Herceptin®) is a humanised monoclonal antibody that specifically binds to the extracellular domain of HER2 to prevent tumour cell proliferation (Cho et al. 2003). TZ was approved for clinical use in the treatment of breast cancer by the US Food and Drug Administration (FDA) in 1998 (Shak et al. 1998). The administration of TZ in combination with chemotherapy results in a 5-month median increase in survival but with a small increased risk of severe cardiotoxicity due to the mechanism of action of doxorubicin (Rossi et al. 2016). Other HER2-targeted therapies have been developed to decrease toxicity and improve efficacy, including pertuzumab,

another humanised monoclonal antibody that binds to the HER2 extracellular domain, and lapatinib, a small-molecule tyrosine kinase inhibitor that targets HER2 kinase activity (Higa & Abraham 2007). Current clinical trials are testing the use of a combination of these HER2-targeted therapies in an effort to improve overall clinical efficacy and reduce the incidence of therapeutic resistance (Ahn & Vogel 2012), which is now recognised as a significant clinical problem despite TZ therapy still being the standard of care for HER2-positive breast cancer.

Resistance to targeted therapies can develop via a number of mechanisms and may be intrinsic to the patient or acquired over time with the progression of treatment. Intrinsic resistance can arise from a lack of expression of a drug target, a mutated drug target or via target-independent signalling mechanisms (Masoud & Pages 2017). For example, some patients are intrinsically resistant to HER2-targeted therapies because of the ability of HER2 to form heterodimers with other human epidermal growth factor receptors, allowing differential intracellular signalling (Croucher et al. 2016). Intrinsic resistance to TZ affects a significant proportion of patients, with only 30% of HER2-positive breast tumours responding initially to TZ therapy (Ludyga et al. 2013). In contrast, acquired (also known as pleiotropic or evasive) resistance can develop in patients that were once responsive to treatment and can arise from de novo mutations or from clonal selection of intrinsically resistant clones (Wood 2015). The development of acquired resistance renders HER2-targeted therapies ineffective, and subsequent cancer recurrence often results in death from metastatic disease (Menyhart et al. 2015). Of the tumours that initially respond, acquired resistance to TZ therapy develops in approximately 70% of patients within the first year of treatment (Nahta & Esteva 2006). Several mechanisms of acquired TZ resistance have been hypothesised, including the expression of truncated forms of HER2 that prevent binding of TZ (Scaltriti et al. 2007), the activation of alternative signalling pathways (Ludyga et al. 2013) and the clonal selection and expansion of HER2-negative tumour cells as a result of the intratumoural heterogeneity of breast cancer (Gerlinger et al. 2012).

1.4 Tumour heterogeneity and therapeutic resistance

The genomic, functional and spatiotemporal heterogeneity that is characteristic of many solid tumours plays a key role in the development of resistance to targeted therapies (Fig.

1.3) (Alizadeh et al. 2015; Venkatesan & Swanton 2016). Mechanisms of acquired resistance to molecular-targeted therapies have been extensively reviewed elsewhere (Holohan et al. 2013; Lackner et al. 2012). The intratumoural heterogeneity of tumours provides a template for the clonal selection and expansion of target-negative tumour cells (Eirew et al. 2015) and is a known mechanism of acquired resistance to targeted therapies (Gerlinger et al. 2012; Sebolt-Leopold & English 2006). Individual tumours are comprised of a mixture of both target-positive and target-negative tumour cells (Solomayer et al. 2006). The administration of a targeted therapy inevitably places a selection pressure on a genetically and functionally heterogeneous population of tumour cells, resulting in the selection of tumour cells that are no longer responsive to the targeted therapy (Gillies et al. 2012). With time and the continuation of therapy, the target-negative tumour cell population is able to expand so that the tumour becomes predominately target-negative, at which point the patient no longer shows a response to the original targeted therapy (Zardavas et al. 2015). In this way, the intratumoural heterogeneity of cancer can reduce the potential efficacy of targeted therapies and thus contributes to cancer recurrence and metastasis (Hayes 2016).

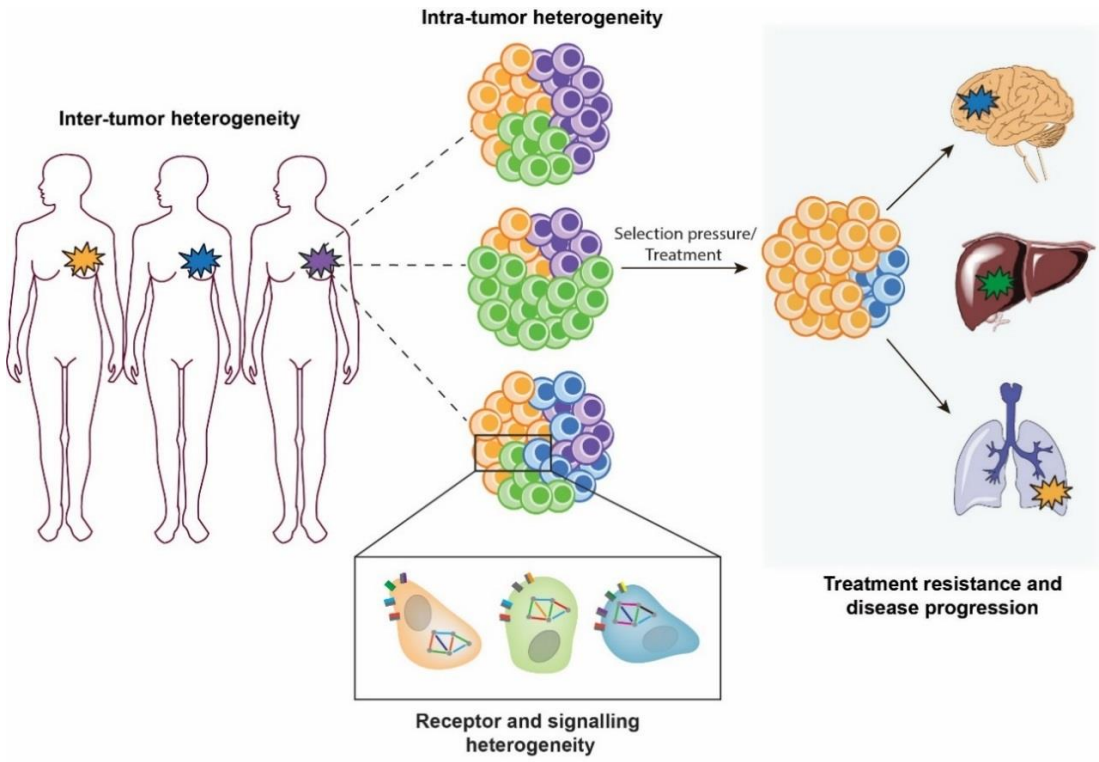

Figure 1.3: Schematic representation of tumour heterogeneity. Tumour heterogeneity includes intertumoural and intratumoural (biomarker) heterogeneity, receptor heterogeneity and signalling heterogeneity. Figure from Belfiore et al. (2018a).

The intratumoural heterogeneity of breast cancer suggests that a multiple biomarker targeting strategy may be of benefit in order to target a broader range of tumour cell subtypes (Doolittle et al. 2015). This concept has been demonstrated by dual knockdown of HER2 and the commonly co-overexpressed protein tyrosine kinase 6, which showed a reduction of breast cancer cell migration, invasion and proliferation *in vitro* and a reduction of tumour growth *in vivo* (Ludyga et al. 2013). As the binding of TZ to HER2 results in the internalisation of the complex through receptor-mediated endocytosis (RME), TZ may be used as a targeting ligand to deliver cytotoxin to HER2-positive tumour cells. Phase II clinical trials using a TZ-drug conjugate demonstrated selective targeting and enhanced efficacy of this approach in HER2-positive breast cancer patients (Burris et al. 2011). Simultaneous targeting of another breast cancer biomarker in addition to HER2 in a cytotoxin-delivery approach may provide a means to overcome therapeutic resistance and improve the efficacy of HER2-targeted therapies. Several potential biomarkers of cancer progression have been identified (Weigelt et al. 2005) to help guide decisions on adjuvant systemic therapy for women with early-stage invasive breast cancer (Harris et al. 2007). Additionally, recent evidence has shown that other cell types that support tumour cell growth and play key roles in facilitating metastasis, including endothelial cells, fibroblasts and immune cells, may also be potential targets for novel multi-targeted therapies (Thoma et al. 2014). For example, the superior efficacy of independently targeting both tumour and immune cells in various cancer types has been demonstrated previously (Bracci et al. 2014; Emens & Middleton 2015).

As previously mentioned, several receptor-targeted molecular therapies have been developed to treat cancer, including a range of monoclonal antibodies and antibody fragments that derive an anti-tumour effect through binding to cell surface receptors in order to inhibit tumour cell proliferation (Nahta & Esteva 2006) and/or to induce a cytotoxic immune response (Verschraegen 2012). Another tumour cell targeting approach involves the use of monoclonal antibodies, proteins or other ligands to facilitate targeted cell uptake of specific molecules to achieve an anti-tumour effect. For example, if the binding of a ligand to its target receptor results in the RME of the ligand-receptor complex, the targeting ligand – which may be a currently used targeted molecular therapy – can be used for the intracellular delivery of covalently attached cytotoxins or other molecules to tumour cells that express the ligand receptor (Perez et al. 2014; Sievers &

Senter 2013). This tumour targeting approach may help to circumvent intrinsic resistance driven by alternative signalling mechanisms (Menyhart et al. 2015). While the plasma half-life of most targeted molecular therapies tends to be relatively short, the association of these molecules with larger nanostructures, such as lipid-based nanoparticles or liposomes, can significantly extend the plasma circulation time of the targeted therapy and increase the therapeutic payload delivered to the tumour site (Vine et al. 2014). Such receptor-targeted nanoparticulate therapies may incorporate currently used targeting molecules, such as antibodies, onto the surface of the nanoparticle to be used as targeting ligands. These targeting ligands can direct the nanoparticle to receptor-positive tumour cells and facilitate cellular uptake of the nanoparticle, achieving intracellular delivery of the nanoparticle cargo for an anti-tumour effect (Section 1.6).

1.5 Urokinase plasminogen activator system

The urokinase plasminogen activator system (uPAS) has a demonstrated role in tumour cell invasion and metastasis (Fig. 1.4). In this system, the urokinase plasminogen activator (uPA), a serine protease, becomes active upon binding to its cell membrane-bound receptor, the urokinase plasminogen activator receptor (uPAR) (Didiasova et al. 2014). Active uPAR-bound uPA (uPA/uPAR) converts plasminogen, an inactive zymogen, to plasmin at the cell surface. Plasmin is a broad spectrum serine protease that degrades a range of extracellular proteins to facilitate remodelling of the ECM (Dass et al. 2008). The endogenous plasminogen activator inhibitors 1 and 2 (PAI-1 and PAI-2) specifically bind to the active site of uPAR-bound uPA and inhibit the uPA-mediated conversion of plasminogen to plasmin (Fig. 1.4). PAI-1, the main physiological inhibitor of uPA, has additional cell signalling roles that facilitate tumour cell invasion (Croucher et al. 2008; Dass et al. 2008), and overexpression of PAI-1 in cancer is correlated with a poor patient prognosis (Cochran et al. 2011; Croucher et al. 2008). In contrast, overexpression of PAI-2 in cancer is correlated with a good patient prognosis and prolonged survival (Croucher et al. 2008). Under normal physiological conditions, the uPA-mediated remodelling of the ECM is essential to promote immune cell migration, wound healing and other important extracellular processes (Gonias & Hu 2015). However, under pathological conditions such as cancer, the degradation of extracellular physiological barriers enables tumour cells to migrate out of the region, promoting the invasion of tumour cells into surrounding tissues and facilitating metastasis (O'Halloran et al. 2013).

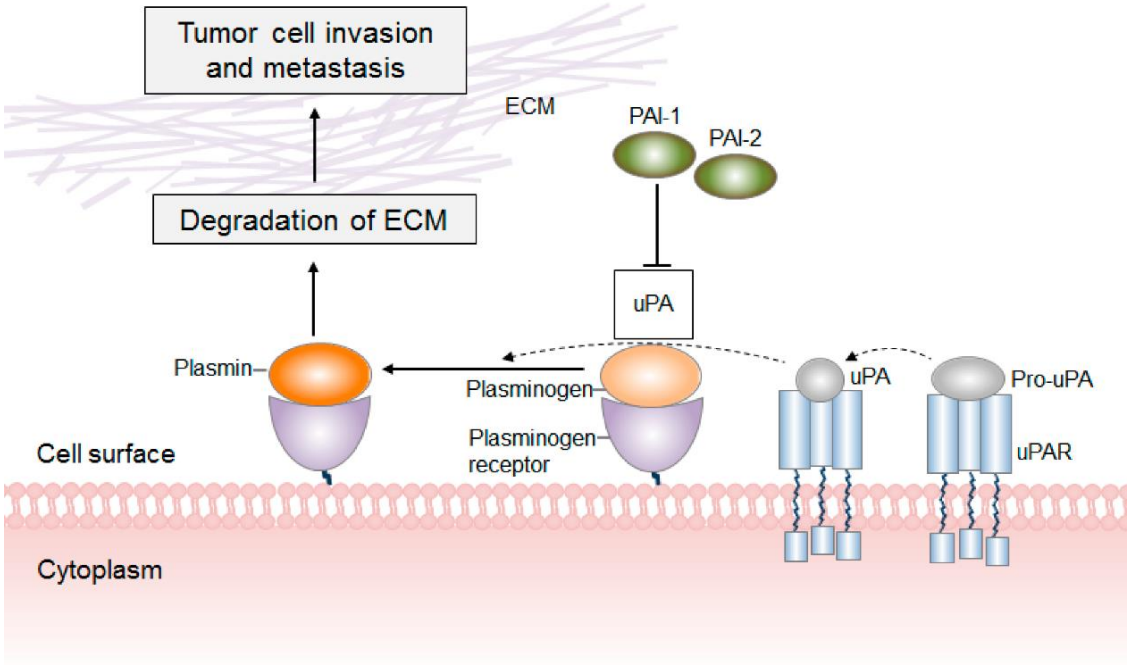

Figure 1.4: Urokinase plasminogen activator system. The urokinase plasminogen activator (uPA) becomes active upon binding to its receptor, the urokinase plasminogen activator receptor (uPAR). Active uPA converts plasminogen to plasmin, a broad-spectrum serine protease that degrades the extracellular matrix (ECM) to promote tumour cell invasion and metastasis. Plasminogen activator inhibitor-1 and inhibitor-2 (PAI-1 and PAI-2) can bind to uPAR-bound uPA to prevent the uPA-mediated conversion of plasminogen to plasmin and subsequent downstream effects promoting metastasis. Figure adapted from Didiasova et al. (2004).

Numerous studies and clinical evidence have indicated a key role for uPAS in breast cancer metastasis (Giannopoulou et al. 2007). Amplification and overexpression of uPA and uPAR are recognised biomarkers of metastasis and are indicative of an overall poor patient prognosis for several cancer types (Dass et al. 2008; Duffy et al. 2014). In breast cancer, progression-free survival is inversely correlated with uPA and uPAR expression (Duffy et al. 2014; Harris et al. 2007). Patients with high uPA mRNA levels are more likely to suffer from metastatic disease (Urban et al. 2006), and overexpression of uPAR by tumour cells and/or stromal cells is associated with poor prognosis for metastatic breast cancer (Bianchi et al. 1994). In TNBC, uPAR has been shown to increase the malignant potential (Huber et al. 2016) and has been identified as a potential novel target for treatment of this breast cancer subtype (Al-Mahmood et al. 2018; Aubele et al. 2015). Tumour hypoxia has been shown to induce uPAR overexpression, and uPAR overexpression can confer tumour cell resistance to chemotherapy (Gonias & Hu 2015). In addition, uPAR overexpression can promote tumour cell migration through signal

transduction (Carriero & Stoppelli 2011). Intracellular uPAR-dependent signalling can promote epithelial-mesenchymal transition, causing changes to tumour cell morphology and inducing stem cell-like properties that facilitate a metastatic tumour cell phenotype (Indira Chandran et al. 2015).

Within the HER2-positive breast cancer subtype, recent evidence suggests a cooperative effect of uPA/uPAR and HER2 on disease progression. In patients with metastatic HER2-positive breast cancer, amplification of both HER2 and uPAR often occurs in the same tumour cells (Pierga et al. 2005), and the overexpression of uPAR in breast cancer cells within the HER2-positive subtype facilitates tumour cell invasion and a metastatic phenotype (Berg et al. 2012; Meng et al. 2006). In HER2-normal and HER2-amplified subsets of breast cancer patients, uPAR overexpression significantly reduced the probability of metastasis-free survival, more significantly so in the short-term for HER2 amplified breast cancer (Indira Chandran et al. 2015). The presence of HER2-positive/uPAR-negative and HER2-negative/uPAR-positive cells due to the intratumoural heterogeneity of *in vivo* tumours suggests that targeting both HER2 and uPAR may be an effective way to target multiple clonal populations of tumour cells and improve the efficacy of drug-based treatments for metastatic HER2-positive breast cancer (Sugiyama et al. 2013). *In vitro* studies using RNA interference showed that downregulation of both HER2 and uPAR in breast cancer cells was synergistic in supressing tumour cell growth and inducing tumour cell death, and was more effective than downregulating either receptor alone (Li et al. 2010). Given the role of uPAS in the promotion of metastasis, targeting uPA/uPAR may be a promising therapeutic strategy for metastatic breast cancer (Matthews 2011; Mazar et al. 2011). The protective effect of PAI-2 in breast cancer progression indicates that the use of PAI-2 in uPA-targeted therapies for cancer may be a promising novel strategy for targeting uPAR in breast cancer.

1.5.1 Plasminogen activator inhibitor-2

PAI-2, also known as SerpinB2, is a serine protease inhibitor that exists as a 43 kDa intracellular form and a 60 kDa extracellular glycosylated form (Fig. 1.5). While PAI-2 is expressed by most cell types, expression is upregulated in pregnancy, in the immune response and in tumour cells (Croucher et al. 2008). As the binding of extracellular PAI-

2 to uPAR-bound uPA results in the RME of the PAI-2/uPA/uPAR complex, PAI-2 can be used as a targeting ligand for the intracellular delivery of covalently attached cytotoxin to uPAR-positive tumour cells (Cochran et al. 2011). Previous work has shown PAI-2 to be non-toxic, stable and selective for uPA inhibition. It has been shown that the CD-loop (a 33 amino acid loop situated between α-helices C and D of the protein) of PAI-2 is not relevant in cell targeting of uPA/uPAR. Recombinant ΔCD-loop PAI-2 retains its inhibitory activity against uPA, and is also easier to express and purify (Cochran et al. 2009). ΔCD-loop PAI-2 has four cysteine residues (C5, C145, C161 and C405) that are not involved in the inhibitory function of PAI-2 (Wilczynska et al. 2003) and can therefore be used as sites of conjugation to other molecules for targeting and delivery to uPA/uPAR-positive cells.

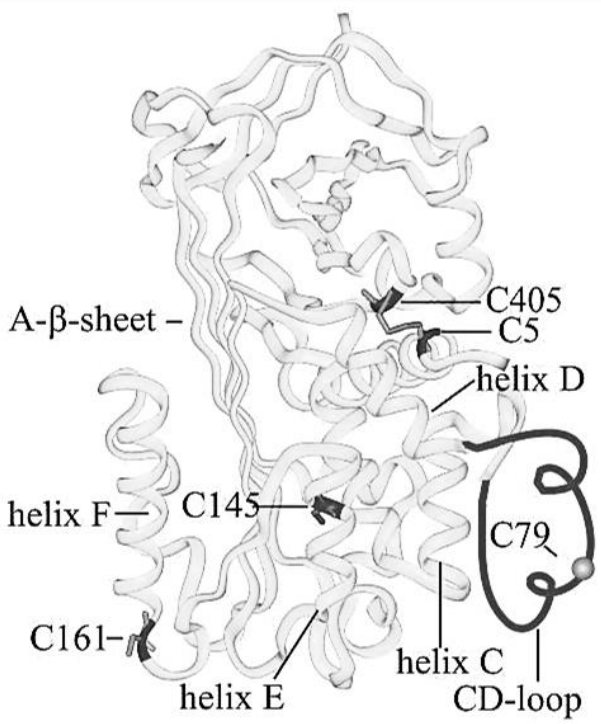

Figure 1.5: Plasminogen activator inhibitor-2. Plasminogen activator inhibitor-2 (PAI-2) is a serine protease inhibitor that exists as a 43 kDa intracellular form and a 60 kDa extracellular glycosylated form. As the binding of extracellular PAI-2 to urokinase plasminogen activator receptor (uPAR)-bound urokinase plasminogen activator (uPA) results in the receptor-mediated endocytosis of the PAI-2/uPA/uPAR complex, PAI-2 can be used as a targeting ligand via conjugation of molecules to cysteine residues C5, C145, C161 or C405. Figure adapted from Wilczynska et al. (2003).

ΔCD-loop PAI-2 has been previously used to target uPA/uPAR for drug delivery applications. PAI-2 has been successfully conjugated to the alpha-emitting radioisotope

Bi213 (Stutchbury et al. 2007) and to an *N*-alkylisatin (*N*-AI)-based cytotoxin (Section 1.6.1), a potent microtubule destabilising agent (Vine et al. 2007) that can evade P-glycoprotein (P-gp)-mediated efflux in multi-drug resistant cancer cell lines (Vine et al. 2016). The PAI-2-*N*-AI conjugate showed selective targeting to and cytotoxicity against uPA/uPAR-positive breast cancer cells *in vitro* and effective inhibition of primary tumour regrowth in an *in vivo* model of breast cancer metastasis at 1/20th of the concentration of free *N*-AI (Vine et al. 2012). The attachment of PAI-2 to larger molecules, such as polyethylene glycol (PEG), can significantly extend the plasma half-life of PAI-2 and increase tumour retention *in vivo* (Vine et al. 2014). The use of a PEG-coated drug delivery carrier, such as a lipid-based nanoparticle, may further increase the *in vivo* circulation time of PAI-2 bound to the nanoparticle surface to enhance targeting of uPAR-positive tumour cells in drug delivery applications.

1.6 Liposomes for tumour targeting and drug delivery

Liposomes have emerged as a useful delivery system for the transport of drugs and other molecules to solid tumours (Allen & Cullis 2013). Liposomes are spherical lipid-based vesicles, typically 100-200 nm in diameter, comprised of associating phospholipids that form a lipid bilayer surrounding an aqueous core (Pattni et al. 2015) (Fig. 1.6). This unique structure allows for the encapsulation of hydrophobic or hydrophilic drugs, or other small molecules, in the lipid bilayer or aqueous core, respectively (Gubernator 2011). Encapsulated drugs can then be delivered to target cells for intracellular drug release and anti-tumour effect. The circulation time of liposome particles is largely dependent on their lipid composition, size, surface charge, morphology and other physicochemical characteristics. The dominant mechanism by which liposomes are typically cleared from the bloodstream is based on interactions with the phagocytic cells of the mononuclear phagocyte system (MPS). The inclusion of hydrophilic polymers, most commonly PEG, at the outer surface of the liposome can increase the *in vivo* circulation time by reducing recognition and clearance by the MPS (Uster et al. 1996). For this reason, PEGylated liposomes have long been considered a clinically useful nanoparticle for drug delivery applications.

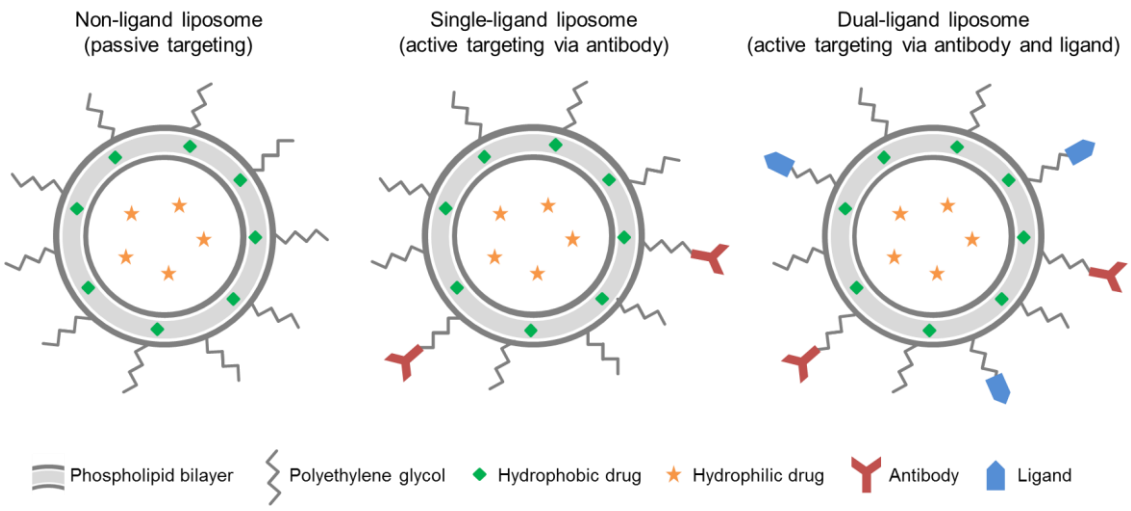

Figure 1.6: General structure of liposomes. Drug-loaded liposomes may be non-ligand (passively targeted), single-ligand or dual-ligand (actively targeted). Phospholipids associate to form a hydrophobic lipid bilayer surrounding a hydrophilic aqueous core. Drugs may be encapsulated in the liposome bilayer or core, depending on solubility. Polyethylene glycol (PEG) is incorporated into the bilayer to neutralise surface charge and decrease the rate of clearance from the bloodstream. Targeting ligands may be covalently attached to the terminal ends of PEG chains to enable selective binding of the liposome to cell surface receptors for targeted drug delivery.

Liposome-based drug formulations can offer several distinct advantages over free drug formulations in addition to an increased *in vivo* circulation time, including improved stability and solubilisation of the encapsulated drug, reduction in systemic toxicity of the drug and increased drug delivery to the tumour site (Estanqueiro et al. 2014). The superior activity of drug-loaded liposomes relies on a multi-step process involving both passive and active targeting mechanisms. Passive targeting is primarily mediated by the enhanced permeability and retention (EPR) effect (Fig. 1.7), defined as the extravasation and retention of particles less than 380-780 nm in size into the tumour interstitial space due to highly porous tumour vasculature and poor lymphatic drainage from the tumour site (Gerlowski & Jain 1986; Matsumura & Maeda 1986). The encapsulated drug can be released from liposomes in the tumour interstitium and can then be taken up by the tumour cells, or liposomes containing the drug can be internalised by the tumour cells or other tumour-associated cells (Barenholz 2012). Therefore, in theory, passive targeting enables targeting to tumours via the EPR effect. In addition, liposome formulations reduce exposure of normal tissues to the drug as liposomes cannot pass through intact continuous endothelium (except for the liver and spleen, which have a different anatomy of vasculature) and so do not localise there, minimising associated off-target effects while

simultaneously providing a mechanism for enhanced accumulation in the tumour site (Abdalla et al. 2018).

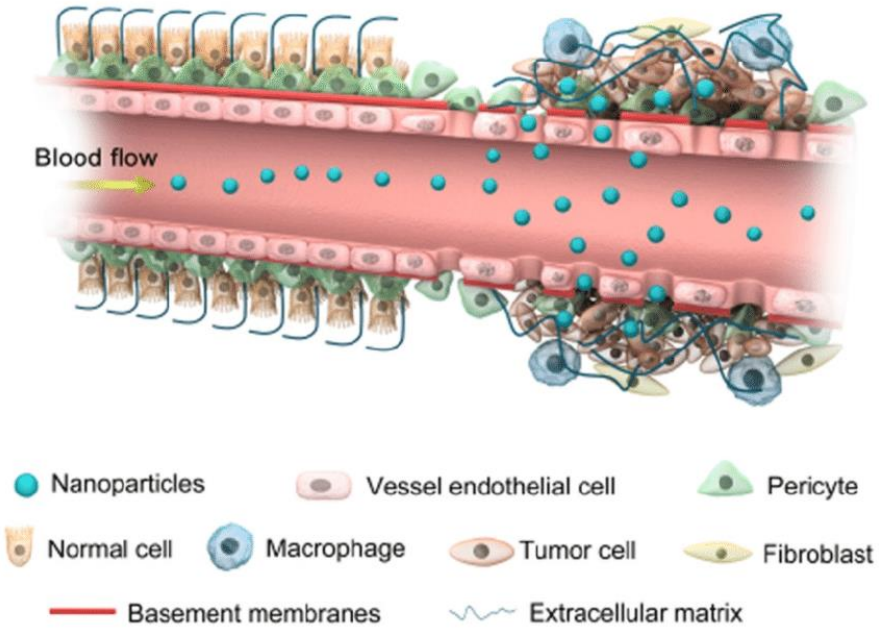

Figure 1.7: The enhanced permeability and retention effect. The extravasation and retention of nanoparticles into the tumour interstitial space occurs due to highly porous tumour vasculature and poor lymphatic drainage from the tumour site. Figure from Abdalla et al. (2018).

1.6.1 *N*-alkylisatins

N-alkylisatins are a class of molecules derived from isatin (1*H*-indole-2,3-dione) with a broad range of cytotoxic and anticancer properties (Matesic et al. 2008). The *N*-alkyl-5,7-dibromoisatins, including 7-dibromo-N-(p-hydroxymethylbenzyl)isatin (*N*-AI) (Fig. 1.8), are microtubule-destabilising cytotoxins with a potent anti-tumour cell effect against cancer cell lines *in vitro* (Vine et al. 2007), and an anti-tumour growth effect *in vivo* (Vine et al. 2012). The potency of these compounds against tumour cells is comparable to clinically used drugs such as doxorubicin and paclitaxel, but unlike many clinically used drugs, the *N*-alkylisatins are not substrates for P-gp-mediated efflux, meaning that this class of compounds has potential application in the treatment of multi-drug resistant cancers (Vine et al. 2016).

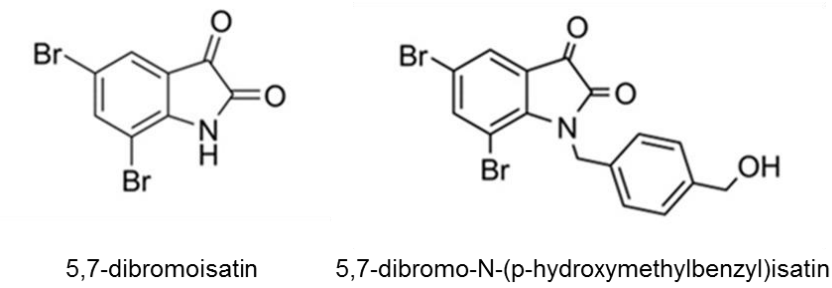

5,7-dibromoisatin 5,7-dibromo-N-(p-hydroxymethylbenzyl)isatin

Figure 1.8: Chemical structure of *N*-alkylisatin. 5,7-dibromoisatin and the *N*-alkylisatin derivative 5,7-dibromo-N-(p-hydroxymethylbenzyl)isatin.

N-AI has been previously conjugated to PAI-2 in order to target uPA/uPAR-positive tumour cells for targeted drug delivery. The *N*-AI-PAI-2 conjugate, which had an average of 1-2 cytotoxin molecules per PAI-2 molecule, demonstrated a selective increased cytotoxic effect against uPA/uPAR-positive tumour cells *in vitro*, and was efficacious *in vivo* in reducing primary tumour growth in mice (Vine et al. 2012). Given the potency and previous validation of *N*-AI as a cytotoxin for use in anticancer applications, *N*-AI is a promising candidate for further development in drug delivery research. As a hydrophobic molecule, *N*-AI has a low aqueous solubility that limits the amount of drug that can be administered intravenously (Grimaldi et al. 2016). However, *N*-AI is amenable to encapsulation within liposomes in order to improve solubility and physicochemical stability. While liposomal formulations of *N*-AI have not been previously reported in the literature, the loading of similar hydrophobic anticancer drugs, such as paclitaxel and colchicine, into the liposome bilayer has been achieved (Koudelka & Turánek 2012; Kulkarni et al. 1997).

1.6.2 Ligand-directed liposomes for active tumour cell targeting

In addition to their versatile drug encapsulation capabilities, liposomes permit the active targeting of specific cell types via the conjugation of ligands, such as monoclonal antibodies, antibody fragments, proteins, peptides, carbohydrates, glycoproteins, aptamers and small molecules, to the liposome surface for drug delivery to cells expressing the target surface receptor(s) of interest (Messerschmidt et al. 2008). Active targeting using liposomes is achieved via conjugation of one or more ligands to the liposome surface to form liposomes that bind to a target receptor expressed on the tumour

cell surface. Following liposome extravasation into the tumour interstitial space, subsequent ligand-directed surface binding and internalisation (usually via RME) promotes liposome and drug entry into specific cell types. As actively targeted liposome formulations combine both passive and active drug delivery mechanisms, ligand-directed liposomes should show superior drug delivery compared to non-ligand liposomes, depending on the tumour type (Wilhelm et al. 2016).

Currently, all clinically approved liposome drug formulations are non-ligand directed, with efficacies relying solely on passive targeting to achieve tumour accumulation. Despite extensive research into nanomedicine-based therapeutics, and the preclinical development of dozens of liposome drug formulations spanning several decades, less than a dozen liposomal drug formulations have been approved by the FDA for clinical use to date (Bobo et al. 2016; Shi et al. 2017). Of these FDA-approved liposomes, only several distinct formulations have been approved for the treatment of cancer, including Kaposi's sarcoma, acute lymphoblastic leukaemia, pancreatic cancer, ovarian cancer, multiple myeloma and metastatic breast cancer (Table 1.2). Evidently, there is a bottleneck in the translation of liposomes from preclinical development through to clinical utility, with many preclinical formulations never proceeding to clinical trials and only a small percentage of those that do eventually making it onto the market. This bottleneck is even more profound for the development of ligand-directed liposomes, where there are currently no clinically approved formulations available (van der Meel et al. 2013).

Active targeting strategies using ligand-directed liposomes have been explored extensively in the preclinical setting, showing improved efficacy over non-ligand liposomes in *in vitro* and *in vivo* models. For example, *in vitro* testing of doxorubicin-loaded liposomes (analogous to Doxil®) that were surface-functionalised with an anti-HER2 monoclonal antibody fragment demonstrated effective binding to breast cancer cells expressing HER2 and a 700-fold increase in drug uptake compared to non-ligand directed liposomes *in vivo* (Park et al. 2001). MM-302, a HER2-targeted liposomal formulation of doxorubicin, showed efficacy in xenograft models of breast cancer and proceeded through to clinical trials (Espelin et al. 2016). A phase II/III clinical trial of TZ therapy in combination with either MM-302 or chemotherapy of physician's choice was recently terminated as the TZ/MM-302 treatment did not show improved efficacy over

the current standard of care for HER2-positive breast cancer (Miller et al. 2016). This may be due to the current lack of understanding around how actively targeted liposomes behave in immune-competent animals (i.e. humans). While the development of actively targeted liposomes to improve the efficacy of their passively targeted predecessors has been explored preclinically, there has been limited progression of such formulations through to clinical trials (Table 1.2) (van der Meel et al. 2013). Given the long history of ligand-directed liposome development and the significant investment of research into this area, it is important to explore the reasons why there has been limited translation of actively targeted liposomes in the field of cancer therapy. Following an overview of previous research in the field, we will highlight and discuss some of the likely reasons for this bottleneck in clinical progression.

1.6.3 Dual-ligand liposomes for dual-targeting of tumour cells

Liposomes have been used for tumour targeting for several decades, and while no single-ligand or dual-ligand liposomes have yet been clinically adopted, actively targeted liposome formulations have been reported extensively in the literature. The utilisation of a dual-targeted approach has a range of reported purposes: most commonly, for overcoming intratumoural heterogeneity by targeting multiple tumour cell subtypes and targeting tumour-associated cells; for targeting tumour vasculature as a means to halt tumour growth; and for facilitating nanoparticle delivery across biological barriers, such as the blood-brain barrier (BBB), for drug delivery to the brain.

Given the demonstrated performance of non-ligand liposomes in drug delivery and the large number of studies describing the design of ligand-bearing liposomes to target tumour-associated receptors, the development of liposomes that can target more than one tumour cell subtype in a heterogeneous tumour may help to overcome therapeutic limitations of current therapies (Fig. 1.9). Previous *in vitro* and *in vivo* studies have demonstrated that ligand-directed liposomes targeting two different cell surface receptors can increase the total amount of liposomes binding to the cancer cells within a tumour as the liposomes are able to bind to any target cell expressing either receptor, which increases the breadth of targeting.

Table 1.2: Passively and actively targeted liposomes. Non-ligand and ligand-directed liposomes in clinical use, clinical trial and preclinical development for cancer treatment. EMA, European Medicines Agency; FDA, Food and Drug Administration. The ClinicalTrials.gov identifier is listed as the reference for liposomes in clinical trials.

Name	Cargo	Targeting ligand(s)	Indication	Status	Reference
Doxil®/Caelyx™ (Janssen)	Doxorubicin	-	Kaposi's sarcoma	FDA (1995)	(James 1995)
Doxil®/Caelyx™ (Janssen)	Doxorubicin		Ovarian cancer	FDA (2005)	(Kelland 2005)
Doxil®/Caelyx™ (Janssen)	Doxorubicin		Multiple myeloma	FDA (2008)	(Ning et al. 2007)
Doxil®/Caelyx™ (Janssen)	Doxorubicin		Metastatic breast cancer	FDA (2012)	(Lopes et al. 2013)
DaunoXome® (Galen)	Daunorubicin	-	Kaposi's sarcoma	FDA (1996)	(Money-Kyrle et al. 1993)
Myocet® (Elan Pharmaceuticals)	Doxorubicin	-	Metastatic breast cancer	EMA (2000)	(Batist et al. 2002)
Marqibo® (Onco TCS)	Vincristine	-	Acute lymphoblastic leukaemia	FDA (2012)	(Silverman & Deitcher 2013)
Onivyde® (Merrimack)	Irinotecan	-	Metastatic pancreatic cancer	FDA (2015)	(Ur Rehman et al. 2016)
Vyxeos™ (Jazz Pharmaceuticals)	Daunorubicin	-	Acute myeloid leukaemia	FDA (2017)	NCT02533115
LEP-ETU	Paclitaxel	-	Lung squamous cell carcinoma	Phase IV	NCT02996214
EndoTAG-1	Paclitaxel	-	Breast cancer	Phase III	NCT03002103
EndoTAG-1			Pancreatic cancer	Phase III	NCT03126435
Liposomal cytarabine	Cytarabine	-	Breast cancer	Phase III	NCT01645839
ThermoDox	Doxorubicin	-	Hepatocellular carcinoma	Phase III	NCT02112656
ThermoDox	Doxorubicin		Breast cancer	Phase II	NCT02850419
Liposomal Grb-2	Grb2 nucleotide	-	Acute myeloid leukaemia	Phase II	NCT02781883
Vincristine sulfate liposome	Vincristine	-	Acute myeloid leukaemia	Phase II	NCT02337478
Mitoxantrone hydrochloride liposome	Mitoxantrone	-	Metastatic breast cancer	Phase II	NCT02596373
SPI-077	Cisplatin	-	Advanced solid tumours	Phase I/II	NCT01861496
LiPlaCis	Cisplatin	-	Advanced solid tumours	Phase I/II	NCT01861496
Liposomal dexamethasone	Dexamethasone	-	Multiple myeloma	Phase I/II	NCT03033316
MM-398	Irinotecan	-	Recurrent solid tumours	Phase I	NCT02013336
Anti-EGFR immunoliposome	Doxorubicin	Cetuximab Fab fragment	Breast cancer	Phase II	NCT02833766
Anti-CD19/CD20 liposomes	Doxorubicin	Anti-CD19 and anti-CD20 monoclonal antibodies	B cell lymphoma	Preclinical	(Laginha et al. 2005)
T7/TAT-LP-PTX	Paclitaxel	Ligand peptide and cationic cell penetrating peptide	Lung cancer	Preclinical	(Wang et al. 2015)
P-selectin/avβ3 integrin liposome	Fluorescent marker	Peptides targeting P-selectin and avβ3 integrin	Metastatic breast cancer	Preclinical	(Doolittle et al. 2015)
Integrin avβ3 peptide/[D]-H6L9 liposome	Paclitaxel	Integrin avβ3 peptide and [D]-H6L9 peptide	Colon cancer	Preclinical	(Zhang et al. 2016)
RGD/TF-LP	Paclitaxel	Cyclic arginine-glycine-aspartic acid and transferrin	Brain glioma	Preclinical	(Qin et al. 2014)

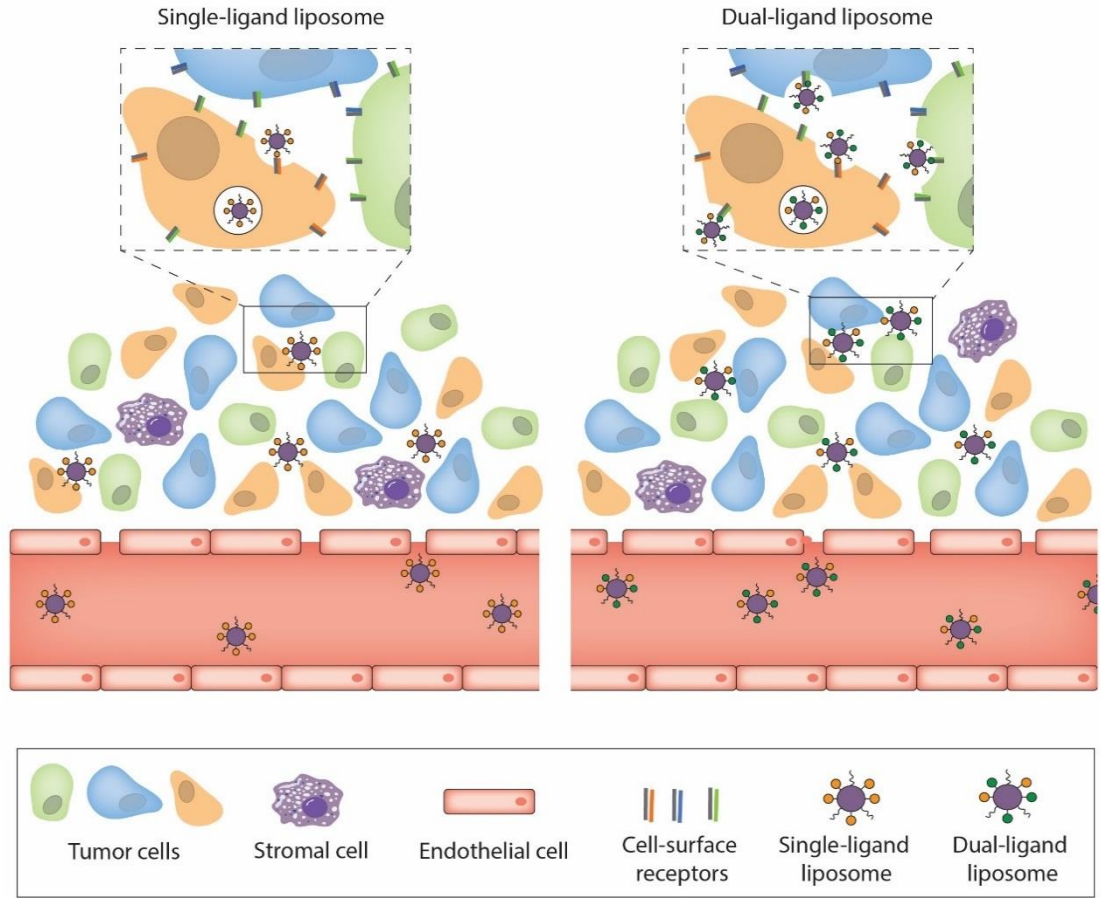

Figure 1.9: Targeting multiple tumour cell subtypes using ligand-directed liposomes. Dual-ligand-directed liposomes may help overcome therapeutic limitations caused by intratumoural heterogeneity of cancer. Liposomes bearing two disparate ligands enable liposome uptake via receptor-mediated endocytosis by tumour cells bearing either (or both) target receptors, thus increasing the range of tumour cell targeting. Single-ligand liposomes only enable targeting of the tumour cells bearing the single target receptor. Given the intratumoural heterogeneity of cancer, some tumour cells will not be targeted by the single-ligand liposome, and instead that tumour cell population may be able to expand. Ligand-directed liposomes may also be designed to target stromal cells for an intended anti-tumour effect. Figure from Belfiore et al. (2018a).

Several preclinical studies have successfully modified liposomes with two surface-bound moieties to create dual-ligand-directed, drug-loaded liposomes that show specific binding to receptor-bearing tumour cells and a resultant higher tumour cell uptake and kill than non-targeted or single-ligand liposomes (Lukyanov et al. 2004). For example, the cellular uptake and cytotoxicity of dual-ligand liposomes targeting lymphoma biomarkers CD19 and CD20, or an equal combination of the two single-ligand liposomes at equal antibody amounts, were greater than for either single-ligand liposome alone (Sapra & Allen 2004). Similarly, a pH-sensitive doxorubicin-loaded liposome formulated to promote intracellular drug release was surface-functionalised with folic acid and AS1411 aptamer

(targeting the folate receptor and nucleolin, respectively), and showed increased cancer targeting and efficacy relative to single-ligand and non-ligand liposomes (Lale et al. 2014). Dual-ligand liposomes showed enhanced cellular uptake, higher intracellular delivery of doxorubicin and greater apoptosis in human breast and pancreatic cancer cell lines than single-ligand liposomes, and had no adverse doxorubicin-related effects on a non-cancerous human cell line. Using a murine model of human B-cell lymphoma, drug-loaded liposomes functionalised with antibodies targeting CD19 or CD20 showed an improved outcome compared to non-ligand liposomes, with a trend of increased therapeutic efficacy for a combination of the two compared to each alone (Sapra & Allen 2004).

Liposomes containing paclitaxel and bearing both a cell ligand peptide and cell penetrating peptide to target lung cancer showed greater liposome internalisation in lung cancer cells, greater accumulation of paclitaxel in tumour spheroids, and significantly greater inhibition of tumour growth in a mouse model of lung cancer than single-ligand and non-ligand liposomes (Wang et al. 2015). Dual-ligand paclitaxel-loaded liposomes containing the integrin avβ3 peptide and an anti-microbial peptide showed increased cellular toxicity and improved tumour growth inhibition in a colon carcinoma mouse model relative to single-targeted liposomes (Zhang et al. 2016). This improved delivery effect of dual-ligand over single-ligand targeting was also demonstrated using a nanostructured lipid carrier containing plasmid DNA that was surface-functionalised with both transferrin and hyaluronic acid, which showed increased transfection efficiency over single-ligand or non-ligand carriers in a mouse model of lung cancer (Zhang et al. 2017). While the ligand density and stoichiometry were not quantified in any examples, ligand-directed liposomes targeting two different cell surface receptors may be able to increase the total amount of liposome binding to the tumour cell surface within a heterogeneous tumour as the liposome is able to bind to any target cell expressing either receptor (Fig. 1.9). This is likely to increase the breadth of cellular targeting beyond a single receptor or cell type, subsequently enhancing drug uptake, dose and hence the anti-tumour effect (Laginha et al. 2005). Furthermore, dual-ligand liposomes could act to unify the pharmacokinetic and biodistribution properties of different ligand-functionalised liposomes for precise delivery to target cells, rather than using two individual ligand-functionalised liposomes with disparate targeting moieties and pharmacological profiles.

In the context of glioma treatment, ligand-directed liposomal drug formulations may enhance drug transport across the BBB for drug delivery to the brain (Gulati & Wallace 2012). Dual-ligand liposomes containing daunorubicin and surface-functionalised with both transferrin and p-aminophenyl-α-D-manno-pyranoside showed increased transport across the BBB, increased cellular uptake and increased survival compared to treatment with free daunorubicin in a rat model of brain glioma (Ying et al. 2010). Another study using doxorubicin-loaded liposomes surface-functionalised with both transferrin and one of two different cell-penetrating peptides showed improved delivery of doxorubicin across the brain-endothelial barrier (BEB) compared to single-ligand and non-ligand liposomes *in vitro*, and efficient translocation across the BEB in an *in vitro* brain tumour model (Sharma et al. 2014). Similarly, docetaxel-loaded nanoparticles that were surface-functionalised with IL-13 and RGD peptide to target both tumour cells and neovasculature showed greater uptake in a glioma cell line than single-ligand and non-ligand nanoparticles, and the dual-ligand nanoparticle induced higher apoptosis of cells in the glioma site *in vivo*, indicating an improvement in cell uptake and anti-tumour effect by dual-targeting (Gao, H. et al. 2014). This was further supported by experiments using dual-ligand liposomes bearing both an aptamer and a peptide moiety to target glioma and the BBB in an *in vitro* glioma model designed to recapitulate the tumour microenvironment (Gao, Huile et al. 2014). Collectively, the aforementioned studies demonstrate the potential utility of dual-ligand-directed liposomal drug formulations for cancer therapy, with an increased degree of liposome uptake acting to improve the anti-tumour effect.

1.6.4 Dual-ligand liposomes for targeting the tumour microenvironment

The tumour microenvironment, which consists of fibroblasts, immune cells, vasculature, and ECM components such as collagen and fibrin, is increasingly being found to play a key role in tumour progression, metastasis and response to therapy. Treatment strategies that target aspects of the tumour microenvironment, such as anti-angiogenic and immunostimulatory therapies, show promising preclinical and clinical results; however, factors such as lack of drug penetration into the tumour, non-specific drug delivery, rapid clearance from serum, or toxic side effects contribute to the failure of many conventional therapies to completely eliminate the tumour. Dual-ligand liposomes offer a potential solution to some of the aforementioned problems, as many recent studies have shown

encouraging results using nanomedicines to target the tumour vasculature, the ECM and cancer-associated immune cells (Siegler et al. 2016).

For example, Doolittle et al. (2015) described the creation of dual-ligand liposomes targeting two different angiogenesis-specific receptors overexpressed at different stages of metastatic disease. Given that tumours display a dynamic, heterogeneous microenvironment that undergoes spatiotemporal changes in the expression of cell-surface biomarkers during disease progression, the authors reasoned that targeting P-selectin and αvβ3 integrin would target the liposome towards blood vessels associated with metastases at different stages of disease progression. Here, a metastatic site transitions, after initial adhesion of circulating tumour cells onto the endothelium, from P-selectin-dependent cell rolling on the endothelium to firm attachment that is αvβ3 integrin-mediated (McCarty et al. 2000). In a resectable mouse model of metastatic TNBC, their dual-ligand strategy achieved complementary targeting of different tumour sites that was missed using two independent single-ligand liposomes. This was attributed to poor colocalisation of both single-ligand liposomes at metastatic sites at the same point in time (Doolittle et al. 2015). This approach was similarly demonstrated by Kluza et al. in the context of magnetic resonance imaging of angiogenesis (Kluza et al. 2010).

Spatiotemporal changes in the expression of cell-surface molecular markers are also observed in cancer stem cells (CSCs), a small population of cells within a tumour with the ability to undergo both self-renewal and differentiation. These cells are now recognised for their role in driving the initiation, invasion, metastasis, resistance and recurrence of a tumour, and the development of targeted nanotherapies that disrupt the maintenance and survival of CSCs are the subject of intense research (Chen et al. 2013). For example, a multi-functional nanoparticle conjugated to a ligand targeting a specific CSC marker and a chemosensitiser (such as an ABC transporter inhibitor) to overcome drug resistance has been proposed (Chen et al. 2013). Altogether, these studies further support the potential advantage of a multiple receptor-targeting strategy using dual-ligand liposomes to better target the spatiotemporal changes in receptor expression that occur during metastatic disease progression. Additional examples of potential target combinations for the design of dual-ligand liposomes are listed in Table 1.3.

Table 1.3: Dual receptor targeting using liposomes. Potential target receptors for the design of dual-ligand liposomes with the ability to concomitantly target the tumour and its dynamic microenvironment.

Cancer	Biomarker 1	Cell population targeted	Biomarker 2	Cell population targeted
Breast	HER2 ER EGFR	Tumour (Ross et al. 2009) Tumour (Ariazi et al. 2006) Tumour (Diéras et al. 2003)	ALDH-1 CTLA-4 uPAR	CSC (Pan et al. 2015) CSC (Velasco-Velazquez et al. 2011) Activated fibroblasts and tumour-associated macrophages (Grondahl-Hansen et al. 1995), invasive tumour cells (LeBeau et al. 2013) and CSC (Jo et al. 2010)
Pancreatic	EGFR uPAR CD109	Tumour (Troiani et al. 2012) Tumour (Nielsen et al. 2005) Tumour (Haun et al. 2014)	CD133 CD44 CD24	CSC (Hermann et al. 2007) CSC (Li et al. 2015) CSC (Sagiv et al. 2008)
Melanoma	AXL receptor tyrosine kinase	Tumour (Boshuizen et al. 2018)	$CD20^{+}$ VEGFR	Tumour-associated B cells (in cutaneous melanoma) (Garg et al. 2016) Endothelial cells (Mehnert et al. 2007)
Prostate	PSMA	Tumour and new blood vessels (Ghosh & Heston 2004)	CD44/CD133	CSC (Collins et al. 2005)
Colorectal	uPAR	Tumour and tumour-infiltrating macrophages (Pyke et al. 1994)	VEGFR EpCAM	Endothelial cells (Shaheen et al. 1999) CSC (Dalerba et al. 2007)

HER2, human epidermal growth factor receptor 2; ER, estrogen receptor; EGFR, epidermal growth factor receptor; ALDH-1, aldehyde dehydrogenase 1; CTLA-4, cytotoxic T-lymphocyte-associated protein 4; uPAR, urokinase plasminogen activator receptor; CSC, cancer stem cell; CD, cluster of differentiation; VEGFR, vascular endothelial growth factor receptor; PSMA, prostate-specific membrane antigen; EpCAM, epithelial cell adhesion molecule.

1.7 Thesis rationale

Despite a growing understanding of the molecular biology of breast cancer metastasis, there is currently no cure for metastatic breast cancer. The HER2-positive and TNBC subtypes have high rates of metastasis and disease recurrence, and a generally poor prognosis, and therefore effective therapies are urgently required. HER2-positive breast cancer is characterised by high levels of intratumoural heterogeneity, which makes resistance to targeted therapies a common problem affecting the success of treatment. In contrast, TNBC is characterised by a lack of validated biomarkers and therefore limited effective treatment options for this breast cancer subtype. Targeting uPAS in metastatic cancer is a promising approach, given the role of this system in breast cancer progression and the cooperative effect of uPA and HER2 in the HER2-positive breast cancer subtype.

This thesis tested the hypothesis that targeting uPAS using drug-loaded liposomes is an advantageous way to enable targeting and delivery of potent anticancer drugs to tumour cells via uPAR-directed ligands at the liposome surface. Therefore, the rationale of this thesis was the development and evaluation of drug-loaded liposomes targeting uPAS as a novel way of treating breast cancer, and for the future development of dual-targeted (uPA/HER2) liposomes for targeting heterogeneous tumour cell populations to overcome therapeutic resistance of HER2-positive breast cancer treatment.

1.8 Aims

The overall aim of this thesis was to create and characterise novel *N*-AI-loaded liposomes surface-functionalised with PAI-2 as a ligand for targeting uPAR, and to evaluate the targeting ability and anti-tumour efficacy of these liposomes using various *in vitro* and *in vivo* models of uPAR-positive breast cancer. Therefore, the specific aims of this thesis were to:

1. Prepare and characterise, for the first time, *N*-AI-loaded PAI-2-functionalised (*N*-AI PAI-2) liposomes by optimising previously reported methods (Chapter 2);
2. Determine the cellular uptake, cellular localisation and receptor-dependent cytotoxicity of *N*-AI PAI-2 liposomes using monolayer cell culture and multicellular tumour spheroid models of breast cancer (Chapter 3);
3. Evaluate the biodistribution, pharmacokinetic profile and anti-tumour efficacy of *N*-AI PAI-2 liposomes in human xenograft mouse models of primary and metastatic breast cancer (Chapter 4); and
4. Develop a single-molecule fluorescence microscopy technique to determine the density and stoichiometry of protein ligands attached to the surface of functionalised liposomes to support the future development of uPAR and HER2 dual-ligand liposomes (Chapter 5).

Chapter 2:

Preparation and Characterisation of *N*-alkylisatin-Loaded Liposomes Targeting the Urokinase Plasminogen Activator System

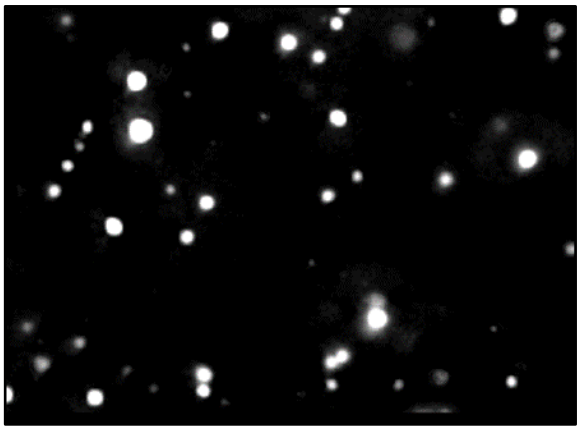

Nanoparticle tracking analysis of liposomes

Portions of this chapter have been included in the following work for publication:

Belfiore, L, Saunders, DN, Ranson, M & Vine, KL 2019, '*N*-alkylisatin-loaded liposomes targeting the urokinase plasminogen activator system in breast cancer', manuscript in preparation.

Author contributions: LB, DNS, MR and KLV designed the experiments; LB and KLV performed the experiments and analysed the data; LB wrote the manuscript; DNS, MR and KLV edited the manuscript for submission.

2.1 Introduction

The first clinically approved liposome formulation, Doxil®, has been in use for over 20 years and is still regarded as an effective and safe treatment for several cancer types. However, the liposome field has not evolved into translating effective actively targeted liposomes as all current clinically used liposomes are passively targeted (Chapter 1, Section 1.6). In the context of cancer therapy, the utility of liposome technologies is promising as ligand-directed liposomes have the potential to further increase the selectivity of therapy, improving efficacy and reducing the potential for harmful side effects. Therefore, the development of novel drug-loaded liposomes with surface-bound targeting ligands for active tumour targeting is warranted. Central to the successful evaluation of novel actively targeted liposomes is the use of high-throughput and scalable methods to produce and characterise them prior to *in vitro* and *in vivo* testing. This chapter explored and developed these methods to produce and characterise novel actively targeted liposomes for tumour cell targeting.

2.1.1 Preparation of drug-loaded liposomes

Liposomes have emerged as a useful delivery system for the transport of drugs and other molecules to solid tumours (Allen & Cullis 2013). Liposomes are spherical lipid-based vesicles, typically 100-200 nm in diameter, comprised of associating phospholipids that form a lipid bilayer surrounding an aqueous core (Pattni et al. 2015). This unique structure allows for the encapsulation of hydrophobic or hydrophilic drugs, or other small molecules, in the lipid bilayer or aqueous core, respectively (Gubernator 2011). Drug-loaded liposomes can be produced using a range of methods, including the thin film hydration method, the solvent injection method, and more recently, automated production using microfluidic devices (Pattni et al. 2015). The thin film hydration method involves dissolving liposome constituents and a hydrophobic drug in organic solvent, which is then evaporated to form a dry lipid thin film that is reconstituted in aqueous solution and extruded to create unilamellar liposomes with the encapsulated hydrophobic drug within the liposome bilayer (Fig. 2.1). For hydrophilic drug encapsulation, alternative methods, such as the ammonium sulfate active loading method, can be used for the encapsulation of hydrophilic drugs in the liposome core (Zhigaltsev et al. 2010).

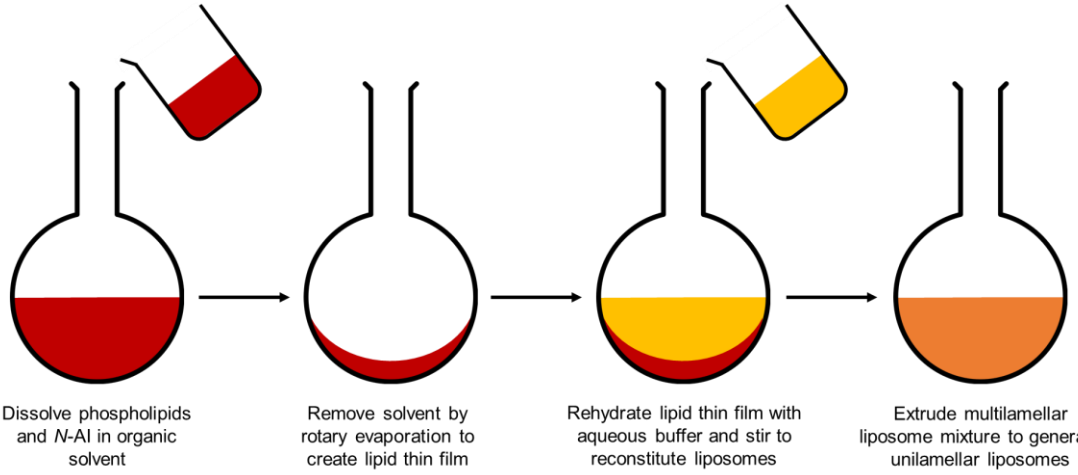

Figure 2.1: Preparation of drug-loaded liposomes using thin film hydration. Phospholipids and the anti-mitotic drug (*N*-AI) are dissolved in an organic solvent, which is then removed by rotary evaporation. The resultant thin film is hydrated with an aqueous buffer and stirring results in the formation of drug-loaded liposomes. Serial extrusion of the heterogeneous multilamellar liposome mixture through a 100 nm pore filter produces a homogenous solution of unilamellar liposomes approximately 100 nm in diameter.

2.1.2 Preparation of actively targeted liposomes

Actively targeted liposomes can be prepared by utilising simple coupling chemistry methods to covalently attach ligands to the liposome surface, typically via polyethylene glycol (PEG) chains present on the surface of the liposome (Cheng & Allen 2010). For example, free sulfhydryl groups of a protein ligand can covalently attach to maleimide-functionalised PEG phospholipids, which places the targeting ligand at the terminal end of the PEG chain at the liposome surface, allowing uninhibited access of the liposome-bound ligand to its target receptor on the cell surface (Allen et al. 1995). This coupling technique is used in two different methods of targeted liposome preparation (Fig. 2.2). The conventional (CO) method uses maleimide-functionalised PEG phospholipid groups in the initial liposome formulation, and subsequent thiolation of the ligand and incubation with preformed liposomes permits covalent attachment of the ligand to the terminal ends of the liposome PEG chains (Allen et al. 1995). Alternatively, the post-insertion (PI) method first utilises small micelles composed of maleimide-functionalised PEG phospholipids to covalently bind to the thiolated ligand before the micelles are incubated with preformed liposomes at a high temperature to facilitate insertion of the PEG phospholipid-bound targeting ligands into the outer leaflet of the liposomes (Moreira et al. 2002). The PI method forms stable liposomes with negligible drug leakage during the

post-insertion step, and similar *in vitro* cytotoxicity and *in vivo* therapeutic efficacy to liposomes prepared using the CO method (Iden & Allen 2001). The PI method also offers a practical approach to creating liposomes that bear two or more different targeting ligands to further enhance the targeting selectivity of the liposome. Dual-ligand or multi-ligand liposomes can be created by incubating liposomes with differently functionalised micelles at varying concentrations to control ligand stoichiometry (Saul et al. 2006).

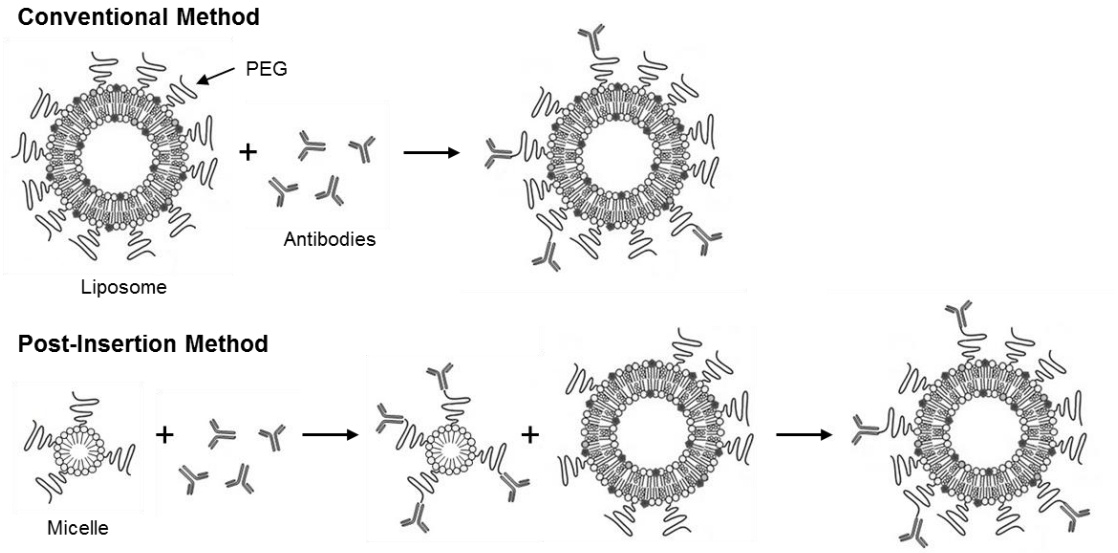

Figure 2.2: Conventional and post-insertion methods for ligand conjugation. The conventional method involves incubation of preformed liposomes with thiolated ligands, which attach covalently to the liposome surface via terminal maleimide-functionalised polyethylene glycol (PEG) groups. The post-insertion method involves attaching thiolated ligands to maleimide-functionalised PEG phospholipid micelles, which are then incubated with preformed liposomes at 60°C to facilitate the transfer of micelle phospholipids with covalently attached proteins into the outer leaflet of the liposome bilayer.

2.1.3 Characterisation of targeted liposomes

It is well understood that the biophysical characteristics of targeted liposomes influence their stability, *in vivo* circulation time, clearance properties, tumour uptake and therapeutic efficacy. Therefore, various methods for liposome characterisation have been reported (Honary & Zahir 2013). Commonly measured characteristics include liposome size and polydispersity by dynamic and static light scattering, surface charge by measuring zeta potential, degree of drug encapsulation by spectrophotometry or high-performance liquid chromatography (HPLC), and morphology and physical state by cryogenic-transmission electron microscopy (cryo-TEM) or atomic force microscopy

(Kang et al. 2015). While the methods for characterisation of passively targeted liposomes are relatively well developed, characterisation methods for more complex liposomes, particularly ligand-directed liposomes, are lacking, and this may be a potential barrier to the feasible and practical development of actively targeted liposomes for clinical utility (Saul et al. 2006). Therefore, the validation of methods to comprehensively characterise actively targeted liposomes is an important aspect of actively targeted liposome production and evaluation.

2.1.4 Experimental rationale

Previous research has shown that plasminogen activator inhibitor-2 (PAI-2) can be used to target urokinase plasminogen activator/urokinase plasminogen activator receptor (uPA/uPAR)-positive breast cancer cells *in vitro* and *in vivo*. PAI-2 has been conjugated to the potent anti-tumour cytotoxin and anti-mitotic agent *N*-alkylisatin (*N*-AI) (Chapter 1, Section 1.6.1). The *N*-AI-PAI-2 conjugate, which had an average of 1-2 *N*-AI molecules per PAI-2 molecule, showed targeting of and a selective cytotoxic effect against uPA/uPAR-positive cells *in vitro*, and anti-tumour growth effects *in vivo* (Vine et al. 2012). In order to increase the *in vivo* circulation time and payload of *N*-AI to the tumour site for increased anti-tumour effect, *N*-AI can be encapsulated in the bilayer of PEGylated liposomes for drug delivery, and PAI-2 can be attached to the liposome surface in order to actively target and deliver *N*-AI to uPAR-positive tumour cells. As *N*-AI-encapsulated liposomes have not been reported previously, there is a need to utilise and build upon previous liposome preparation methods to formulate and characterise novel *N*-AI-loaded PAI-2-functionalised liposomes before proceeding to *in vitro* and *in vivo* evaluation.

2.1.5 Aims

The overall aim of this chapter was to prepare and characterise novel *N*-AI-loaded PAI-2-functionalised (*N*-AI PAI-2) liposomes. Specifically, the aims of this chapter were to:

1. Prepare *N*-AI PAI-2 liposomes using modifications to previously published methods for forming ligand-directed, drug-loaded liposomes; and
2. Determine the biophysical characteristics of *N*-AI PAI-2 liposomes, including liposome size, particle concentration, surface charge, drug encapsulation

efficiency, PAI-2 ligand attachment to the liposome surface and the ability of PAI-2 liposomes to inhibit uPA activity.

2.2 Methods

2.2.1 Liposome preparation

Liposomes were prepared using the thin film hydration method, as described previously (Ishida et al. 1999). Liposomes were composed of 20 mM soy PC (L-α-phosphatidylcholine) and 0.6 mM $mPEG_{2000}$-DSPE (1,2-distearoyl-sn-glycero-3-phosphoethanolamine-N-[(polyethylene glycol)-2000]) (Avanti Polar Lipids, AL, USA), with the addition of either 5 mM cholesterol (Sigma-Aldrich, MO, USA) to form empty liposomes, or 5 mM 5,7-dibromo-*N*-(*p*-hydroxymethylbenzyl)isatin (*N*-AI) (prepared in-house (Vine et al. 2016)) to form *N*-AI-loaded liposomes. Reagents were weighed out into a round-bottom flask and dissolved in a 2:1 (v/v) mixture of chloroform/methanol (Sigma-Aldrich, MO, USA). Organic solvents were removed by rotary evaporation and subsequent freeze drying to form a lipid film. Dried liposome films were rehydrated in deoxygenated 25 mM HEPES buffer (115 mM NaCl, 20 mM HEPES, 2.4 mM K_2PO_4, 1.2 mM $CaCl_2$, 1.2 mM $MgCl_2$; pH 7.4) at a phospholipid concentration of 20 mM by shaking for 1 h at room temperature (RT) with intermittent sonication. Once reconstituted, liposomes were passed through a 0.22 µm polyvinylidene fluoride (PVDF) membrane (Merck Millipore, Germany) and then serially extruded 11 times through a 0.1 µm PVDF membrane using a syringe-driven extruding apparatus (Avanti Polar Lipids, AL, USA) at RT.

2.2.2 PAI-2 conjugation to liposomes

Liposomes were surface-functionalised with PAI-2 using either the conventional (CO) method or post-insertion (PI) method (Allen et al. 2002). Human recombinant PAI-2, ΔCD-loop, prepared as described previously (Cochran et al. 2009), has free cysteine residues for conjugation to terminal maleimide groups of maleimide-functionalised PEG (Oswald et al. 2016). For the CO method, preformed liposomes were incubated with PAI-2 at a molar ratio of 3333:1 liposome phospholipid:protein for 2 h at RT. For the PI method, micelles composed of 0.8 mM mal-PEG_{2000}-DSPE (1,2-distearoyl-sn-glycero-3-phosphoethanolamine-N-[maleimide(polyethylene glycol)-2000]) and 0.2 mM

mPEG$_{2000}$-DSPE were prepared as per previously reported methods (Moreira et al. 2002), and PAI-2 was added to the micelles at a molar ratio of 10:1 (mal-PEG$_{2000}$-DSPE:protein) to form PAI-2-functionalised micelles. PAI-2-functionalised micelles were added to preformed liposomes and heated to 60°C for 1 h to facilitate the post-insertion of micelle lipids into the outer leaflet of the liposomes. Following the liposome functionalisation steps, unbound PAI-2 was removed from liposomes by either size-exclusion chromatography (SEC) using Sepharose CL-4B (Sigma-Aldrich, MO, USA) according to the manufacturer's protocol, or repeated centrifugation at 20,000 x g for 1.5 h at 4°C.

2.2.3 Liposome characterisation

2.2.3.1 Dynamic light scattering

Liposome size distribution, peak intensity and polydispersity index (PDI), as well as stability over time using repeated measurements, were determined by dynamic light scattering (DLS) using a Zetasizer APS instrument (Malvern Instruments, UK). Liposome samples (60-100 µL) in phosphate-buffered saline (PBS) or HEPES were added to 96-well plates and analysed at 25°C using the manufacturer's measurement protocol for liposomes (13 reads per sample, triplicate measurements). Data were presented as the intensity distribution for liposomes and the number distribution for micelles in order to enable visualisation of small particles. Zeta potential (surface charge) of liposomes was determined by DLS using a Zetasizer Nano ZS instrument (Malvern Instruments, UK) (10-100 reads per sample, triplicate measurements).

2.2.3.2 Nanoparticle tracking analysis

Liposome size distribution and particle concentration were determined using a NanoSight LM 10 instrument (Malvern Instruments, UK) according to the manufacturer's protocol. Liposomes were diluted to a concentration of between 1×10^8 and 25×10^8 particles/mL in PBS to ensure an optimal concentration for accurate analysis of samples (NanoSight Ltd, UK). Imaging of 20-100 particles per field of view was performed using an optical microscope fitted with a charge-coupled device camera at 25°C. Particle movement was recorded at 20 frames per second for 60 seconds. Average particle size and concentration were calculated using Nanoparticle Tracking Analysis (NTA) software (version 2.3, NanoSight Ltd, UK) from triplicate measurements.

2.2.3.3 Phospholipid assay

Liposome phospholipid concentration was determined using a commercial phospholipid kit (Sigma-Aldrich, MO, USA), as per the manufacturer's instructions. Briefly, phosphatidylcholine standards were prepared 0-20 µM, 20 µL of each standard was added to a 96-well plate in duplicate, as well as 20 µL of each liposome sample (at various dilutions). 80 µL of reaction mix containing assay buffer, enzyme mix, phospholipase D enzyme and dye reagent, was added to each well and incubated at RT for 30 min. Absorbance was measured at 570 nm using a Spectramax spectrophotometer (Molecular Devices, CA, USA). The absorbance values of the phospholipid standards were used to create a standard curve and unknown sample concentrations were determined by interpolation.

2.2.3.4 N-AI encapsulation in liposomes

Drug encapsulation efficiency was determined by high-performance liquid chromatography (HPLC). *N*-AI-loaded liposomes were mixed with water/acetonitrile (60:40 v/v) and centrifuged. The *N*-AI concentration was determined using an Atlantis T3 reverse-phase C18 analytical column (Waters, UK) and a Waters HPLC machine (Waters, MA, USA). Analysis was performed using an injected volume of 10 µL with a gradient elution and monitored with a photodiode array at 435 nm. Concentration was determined by interpolating from a standard curve after analysis of standards and samples using Empower Pro V2 software (Waters, UK).

2.2.3.5 Lowry assay

Protein concentration of PAI-2 and PAI-2-functionalised liposomes was determined using the DC Protein Assay kit (Bio-Rad Laboratories, CA, USA) according to the manufacturer's protocol. Bovine serum albumin (BSA) was used as a standard (0-2 mg/mL) and 5 µL of standard or sample was added to a 96-well plate. Bio-Rad reagent A (25 µL) and reagent B (200 µL) were added to each well, the plate incubated at RT for 10 min, and the absorbance measured using a Spectramax spectrophotometer (Molecular Devices, CA, USA) at 750 nm. The absorbance values of the BSA were used to create a standard curve and unknown sample concentrations were determined by interpolation.

2.2.3.6 BCA assay

The Bicinchoninic Acid (BCA) assay is one of the most sensitive colourimetric protein assays and can detect protein at concentrations as low as 5 μg/mL (Walker 1996). Due to phospholipid interference in the Lowry analysis of liposome samples, protein concentration of PAI-2-functionalised liposomes was additionally determined using the BCA assay according to previously published methods. Solution A, consisting of 20 g/L sodium carbonate, 9.5 g/L sodium bicarbonate and 1.6 g/L sodium tartrate, was brought to pH 11.25 with the addition of 1 M sodium hydroxide. Immediately prior to use, 0.5 g BCA powder (Sigma-Aldrich, MO, USA) was dissolved in 50 mL of solution A. Solution A was combined with solution B, which was made up of 4% (w/v) copper sulfate in water, in a ratio of 50:1 to produce BCA working reagent (solution C). BSA protein standards, ranging in concentration from 0-1 mg/mL, were prepared in PBS, and 10 μL of each protein standard was added to a 96-well plate in triplicate. Various dilutions of samples in PBS were prepared and 10 μL of each solution was added to the plate in triplicate. 80 μL of solution C was added to each well and the plate incubated at 60°C for 15 min. The absorbance of the solutions within the wells was determined using a FLUOstar OPTIMA plate reader (BMG Labtech, Germany) at a wavelength of 544 nm. The absorbance of the BSA was used to create a standard curve and unknown sample concentrations were determined by interpolation.

2.2.3.7 SDS-PAGE

For sodium dodecyl sulfate-polyacrylamide gel electrophoresis (SDS-PAGE) analysis, loading buffer (containing 50% (v/v) glycerol, 2% or 6% (w/v) sodium dodecyl sulfate and 0.02% (v/v) bromophenol blue in distilled water) was added to samples. For reducing conditions, 5 μL of β-mercaptoethanol (Sigma-Aldrich, MO, USA) was added to samples. Samples were denatured by heating to 100°C for 5 min and were then loaded into a 10% gel to run by SDS-PAGE at 100 V for 2 h.

2.2.3.8 Western blotting

Western blotting was used to detect and quantify PAI-2 conjugated to liposomes. Proteins in SDS-PAGE gels were transferred to PVDF membranes using Bio-Rad transfer equipment (Bio-Rad Laboratories, CA, USA) at 100 V for 1.5 h. Membranes were rinsed in TBST (1X TBS buffer with 0.05% v/v Tween-20) and blocked using 10% skim milk

in TBST for 1 h at RT. After rinsing membranes twice with TBST, membranes were incubated with primary antibody (anti-SerpinB2; Abcam, Cambridge, UK) at 1:2000 dilution in 2% skim milk/TBST at 4°C overnight. Membranes were washed with TBST four times (10 min each wash) and then incubated with secondary antibody (anti-rabbit-HRP; Abcam, Cambridge, UK) at 1:5000 dilution in 2% skim milk/TBST for 2 h at RT. Membranes were then washed in TBST three times for 5 min and then in TBS (no Tween-20) three times for 5 min. Membranes were developed using ECL peroxidase reaction (Pierce PicoWest ECL reagent; Thermo Fisher Scientific, MA, USA), according to the manufacturer's instructions. Membranes were visualised using x-ray film after developing and fixing (Bio-Rad Laboratories, CA, USA) or using a Gel Logic 2200 Digital Imager (Carestream Molecular Imaging, CT, USA). Band intensities were quantified using ImageJ (National Institutes of Health, MD, USA).

2.2.3.9 Flow cytometric analysis of liposomes

Flow cytometry was used to further assess liposome size and quantify the efficiency of micelle insertion into preformed liposomes. Fluorescent liposomes were prepared by loading with rhodamine-123 (R123) (Sigma-Aldrich, MO, USA) or by post-inserting micelles that were prepared in the absence or presence of varying percentages of FITC-DSPE-PEG (Avanti Polar Lipids, AL, USA). Events (50,000) were collected using an LSR II flow cytometer (BD Biosciences, NJ, USA; excitation 488 nm, emission collected with a 515/20 band-pass filter). Data were analysed using FlowJo software version 10 (FlowJo LLC, OR, USA).

2.2.3.10 Fluorogenic uPA activity assay

To determine whether PAI-2 conjugated to the surface of liposomes retained inhibitory activity against uPA, the activity of PAI-2-functionalised liposomes was quantified using a fluorogenic uPA activity assay, as described previously (Cochran et al. 2009). Briefly, liposomes were diluted in 100 μL reaction buffer (20 mM HEPES, pH 7.6, 100 mM NaCl, 0.5 mM EDTA, 0.01% (v/v) Tween 20) containing 0.25 mM uPA fluorogenic substrate (Z-Gly-Gly-Arg-AMC; Merck Millipore, MA, USA). After a brief pre-incubation at 37 ºC, high molecular weight urokinase plasminogen activator (HMW-uPA) (final concentration 0.675 nM) was added to start the reaction and fluorescence emission was

measured at 37 ºC using a microplate reader (POLARstar Omega; BMG Labtech, Germany). All assays were performed in triplicate and values corrected by subtracting the background well values (reaction buffer and substrate only).

2.2.4 Data analysis

All data analysis, including the generation of graphs and statistical tests, was performed using GraphPad Prism version 7 for Windows (GraphPad Software, CA, USA), unless stated otherwise. Data are presented as the mean ± standard deviation (s.d.) or standard error of the mean (s.e.m.) as stated. Pairwise comparisons were made using Student's t-test and multiple comparisons were made using one-way ANOVA with Tukey's post-test.

2.3 Results

2.3.1 Preparation of empty and *N*-AI-loaded liposomes

Modifications to previously reported methods (Allen et al. 1995) were used to prepare and characterise soy PC PEGylated liposomes containing the potent microtubule-destabilising cytotoxin *N*-alkylisatin (*N*-AI). Empty and *N*-AI-loaded liposomes were prepared by the thin film hydration method and were analysed by dynamic light scattering (DLS) (Table. 2.1). Empty (EMP) liposomes were 137.6 ± 5.6 nm in diameter, while *N*-AI-loaded liposomes were 139.9 ± 3.9 nm in diameter. The polydispersity index (PDI) for both liposomes was < 0.1 for both samples, indicating monodispersity. Both liposomes had a peak intensity of 100%, further indicating the liposome populations were monodisperse and the absence of aggregation or large particle populations in the samples. EMP and *N*-AI liposomes exhibited an equivalent zeta potential (small negative surface charge) and equivalent phospholipid concentrations.

Table 2.1: Characterisation of empty and *N*-AI PEGylated liposomes. Empty (EMP) liposomes and *N*-AI-loaded liposomes were prepared by the thin film hydration method and analysed by dynamic light scattering. Values are means ± s.d. (n = 3).

Liposome	Diameter (nm)	Polydispersity index	Intensity (%)	Zeta potential (mV)	Phospholipid (mM)
EMP	137.6 ± 5.6	0.067 ± 0.035	100	–3.63 ± 0.80	16.44
N-AI	139.9 ± 3.9	0.093 ± 0.023	100	–3.64 ± 0.59	16.45

The size and morphology of *N*-AI liposomes were further confirmed by cryogenic transmission electron microscopy (cryo-TEM), performed by Delfine Cheng at the Sydney Microscopy & Microanalysis Facility of the University of Sydney. Cryo-TEM indicated that the *N*-AI liposomes had an average diameter of 138.7 ± 18.4 nm (Fig. 2.3). Cryo-TEM additionally revealed *N*-AI liposomes to be spherical, monodisperse and unilamellar. The *N*-AI loaded in the liposome bilayer showed no evidence of crystallisation. The concentration of *N*-AI encapsulated in the liposomes could not be determined by spectrophotometry and interpolation from a standard curve as the liposome phospholipid interfered with the peak absorbance of *N*-AI at 310 nm and 435 nm (Appendix A). Therefore, the concentration of *N*-AI loaded into liposomes was determined by high performance liquid chromatography (HPLC), which revealed an *N*-AI concentration of 2.2 mM, equating to 43.1% drug loading (% w/w) based on the starting amount of *N*-AI used in the liposome preparation (Appendix B).

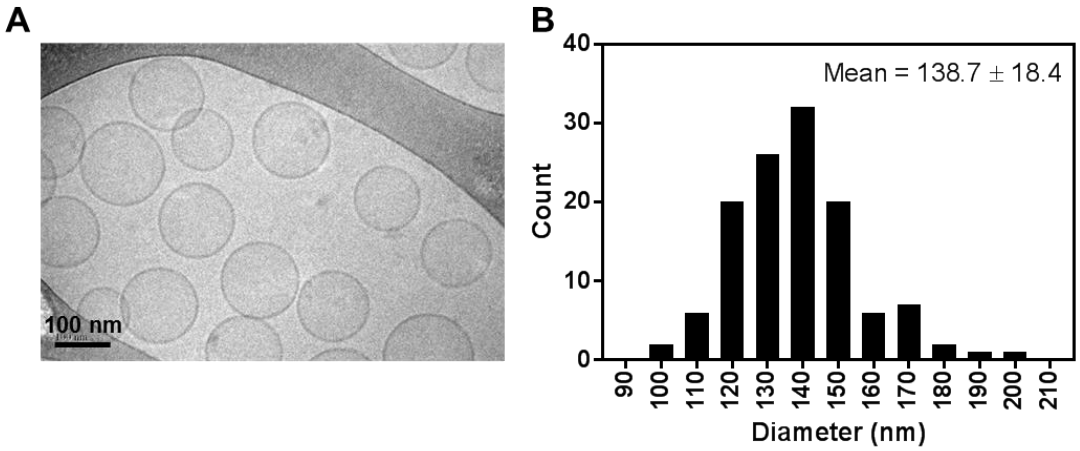

Figure 2.3: Cryo-TEM of *N*-AI-loaded liposomes. *N*-alkylisatin (*N*-AI)-loaded liposomes were prepared using the thin film hydration method, and cryogenic transmission electron microscopy (cryo-TEM) was performed to visualise liposome size and morphology. (**A**) Representative image of *N*-AI-loaded liposomes. (**B**) Determination of average liposome diameter from cryo-TEM image analysis.

2.3.2 Preparation of recombinant human PAI-2

Recombinant human PAI-2 for covalent attachment to the liposome surface was prepared using established protocols (Cochran et al. 2009). SDS-PAGE analysis showed that the PAI-2 produced was pure, with a single band corresponding to the size of PAI-2 of approximately 45 kDa (Fig. 2.4A). Prior to conjugating PAI-2 to liposomes, a fluorogenic uPA activity assay was used to confirm that the recombinant PAI-2 was active. PAI-2

activity was indicated by the complete inhibition of uPA at a 2-fold molar excess of PAI-2:uPA compared to the positive control (no PAI-2) (Fig. 2.4B).

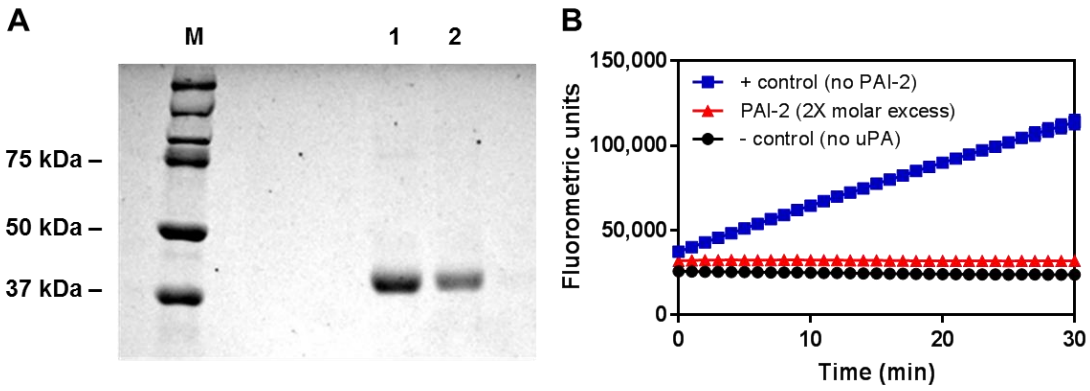

Figure 2.4: Production of recombinant human PAI-2. (**A**) SDS-PAGE analysis of purified plasminogen activator inhibitor-2 (PAI-2) fractions (1, 2); M = marker. (**B**) Urokinase activity assay to confirm inhibitory activity of purified PAI-2 over 30 min. + = positive control, - = negative control.

2.3.3 Conjugation of PAI-2 to liposomes using the conventional method

To attach PAI-2 to the surface of liposomes using the conventional method, recombinant human PAI-2 was incubated with preformed liposomes for 2 h at RT, and unconjugated PAI-2 was removed using size-exclusion chromatography (SEC) (Fig. 2.5). Analysis of fractions by spectrophotometry at 280 nm to detect protein revealed the presence of two peaks, indicating that unconjugated PAI-2 had separated from PAI-2 that had covalently attached to liposomes.

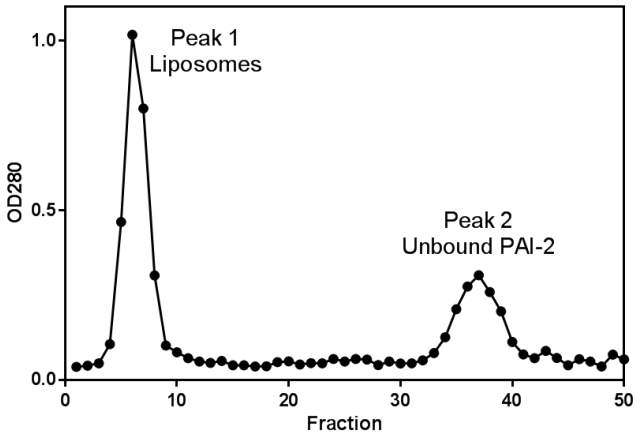

Figure 2.5: Size-exclusion chromatogram of liposomes after PAI-2 conjugation. After conjugation, free plasminogen activator inhibitor-2 (PAI-2) was removed from PAI-2 liposomes using size-exclusion chromatography. The absorbance of the fractions at 280 nm was used to detect PAI-2.

Following SEC, the fractions corresponding to the liposome peak were pooled and the sample was analysed by DLS. DLS revealed that the average diameter of the *N*-AI-loaded PAI-2-functionalised (*N*-AI PAI-2) liposomes was 141.1 ± 5.0 nm, while that of the empty PAI-2-functionalised (EMP PAI-2) liposomes was 139.7 ± 4.9 nm (Table 2.2). The diameter and the PDI of both samples remained similar to the measurements before the PAI-2 conjugation step (Table 2.1). The peak intensity of both liposome preparations was 100%, indicating that the final liposome formulations were monodisperse. The zeta potential of the PAI-2-functionalised liposomes became more negative (Table 2.2), shifting slightly for both empty and *N*-AI-loaded liposomes. The phospholipid concentration of both EMP PAI-2 and *N*-AI PAI-2 liposomes was equivalent at 16.67 mM and 16.62 mM, respectively.

Table 2.2: Characterisation of liposomes prepared by the conventional method. Empty plasminogen activator inhibitor-2 (PAI-2)-functionalised liposomes (EMP PAI-2) and *N*-alkylisatin (*N*-AI)-loaded PAI-2-functionalised liposomes (*N*-AI PAI-2) were prepared by the conventional method and analysed by dynamic light scattering. Values are means ± s.d. (n = 3).

Liposome	Diameter (nm)	Polydispersity index	Intensity (%)	Zeta potential (mV)	Phospholipid (mM)
EMP PAI-2	139.7 ± 4.9	0.109 ± 0.017	100	–4.05 ± 0.53	16.67
N-AI PAI-2	141.1 ± 5.0	0.086 ± 0.030	100	–4.66 ± 0.52	16.62

2.3.4 Quantification of PAI-2 bound to liposomes by protein assays

The quantification of PAI-2 attached to liposomes was attempted using two common laboratory assays: the BCA assay and the Lowry assay. Empty non-functionalised and empty PAI-2-functionalised liposomes at an equivalent phospholipid concentration were analysed to determine protein concentration according to the manufacturer's protocols for the assays. The protein concentration resulting from interpolation of a standard curve (using bovine serum albumin) revealed the protein concentration of both liposome preparations to be just over 1 mg/mL in both assays, with protein concentration between the non-functionalised and PAI-2-functionalised liposomes not significantly different in both assays (Fig. 2.6). This indicated a high degree of interference in the assay from the liposome phospholipid. Therefore, the PAI-2 concentration of liposome samples could not be determined using biochemical protein assays.

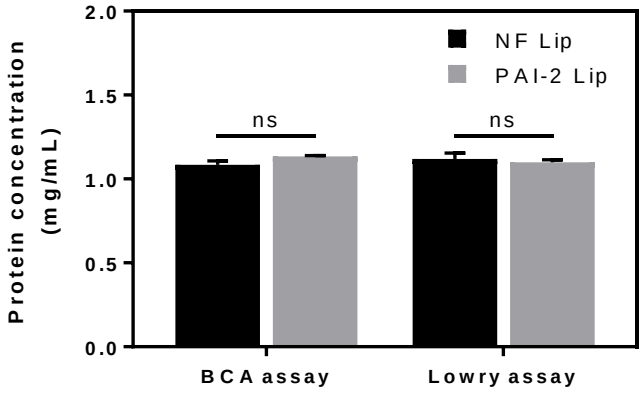

Figure 2.6: Phospholipid interference in protein assays. Non-functionalised (NF) and plasminogen activator inhibitor-2 (PAI-2) liposomes were analysed via the BCA assay and Lowry assay, and protein concentration was determined by interpolation from a bovine serum albumin standard curve. ns = not significant. Data are the mean ± s.d. (n = 3).

2.3.5 Detection of liposome-bound PAI-2 by Western blotting

As PAI-2 could not be detected or quantified using commercial biochemical protein assays, Western blotting was used to confirm successful conjugation of PAI-2 to liposomes and to attempt to quantify protein amount post-conjugation. Following SEC to remove free PAI-2 from PAI-2 liposomes, fractions corresponding to the PAI-2 liposome (peak 1) and free PAI-2 (peak 2), as well as a sample of unpurified PAI-2 liposomes, were analysed via Western blotting (Fig. 2.7). Covalent conjugation of PAI-2 to liposome phospholipid (PEG-DSPE; molecular weight ~2940 kDa) to form PAI-2-PEG-DSPE was confirmed by a lag in gel migration of PAI-2 in the peak 1 fraction (Fig. 2.7, sample #1) relative to the peak 2 fraction (Fig. 2.7, sample #2), which corresponded with the 45 kDa molecular weight of free PAI-2. The absence of a band corresponding to free PAI-2 in peak 1 indicated that removal of unbound PAI-2 was successful. The bands revealed in the unpurified PAI-2 liposome sample (Fig. 2.7, sample #3) appeared as a combination of the two former, further indicating separation via size-exclusion was successful. It was observed that liposome-bound PAI-2 migrates differently through a gel compared to pure PAI-2, causing a smearing effect and multiple PAI-2 bands, limiting the accuracy of densitometry for quantification of liposome-bound protein using a PAI-2 standard curve. Estimates using densitometry indicated that the ratio of mean grey value between the PAI-2 bands in peaks 1 and 2 was 53:47 (Appendix C). This ratio was roughly reflected in the OD280 peak height of the size-exclusion chromatogram (56:44). The amount of protein

in sample 2 (unconjugated PAI-2) was determined to be 37 ng (via BCA assay), which indicated that the amount of PAI-2 associated with the liposome fraction in sample 1 was approximately 42 ng, based on the densitometry ratio between the two samples.

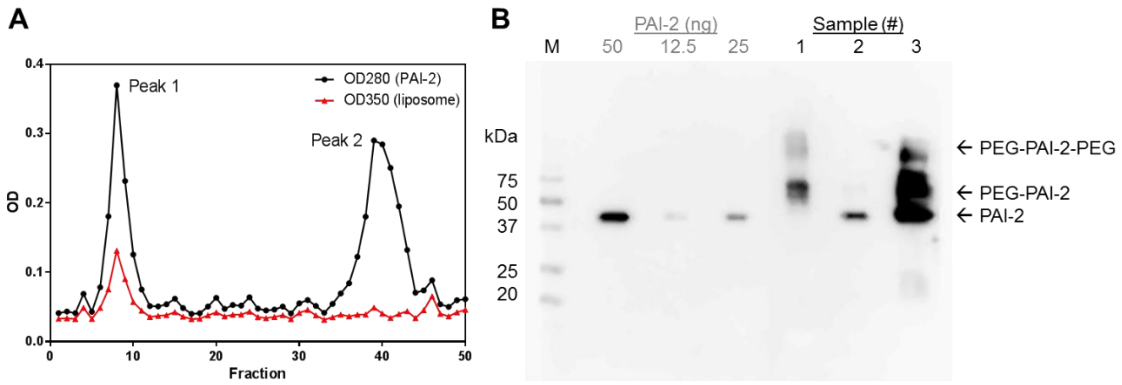

Figure 2.7: Western blot analysis of PAI-2 liposomes. (**A**) Size-exclusion chromatograph of PAI-2 liposome fractions after, including PAI-2 liposomes (peak 1) and unbound PAI-2 (peak 2). (**B**) Western blot detection of PAI-2 in size-exclusion fractions (1, 2), unpurified liposomes (3), and purified PAI-2 (50, 25 and 12.5 ng). OD = optical density, M = marker, PEG = polyethylene glycol. Data are representative from two experimental repeats.

2.3.6 Fluorogenic urokinase plasminogen activator inhibition assay

To confirm that the PAI-2 attached to the surface of liposomes was still able to inhibit uPA activity, a fluorogenic uPA activity assay was performed (Cochran et al. 2009). Empty (EMP) liposomes were used instead of *N*-AI-loaded liposomes as *N*-AI is slightly fluorescent and may interfere with the assay (Chapter 3, Section 3.3.2). Liposome phospholipid had a positive interfering effect in fluorescence measurements, with both EMP and EMP PAI-2 liposomes showing a shift above baseline at the start of measurements. The rate of fluorescence (RFLU) was 4026.9 ± 206.2 FLU/min for EMP liposomes and 43.5 ± 24.9 FLU/min for EMP PAI-2 liposomes, and the mean fluorescence intensity of the EMP liposomes was 3.7-fold higher than the EMP PAI-2 liposomes at the 30 min time point (Fig. 2.8). The 92.6-fold reduction in RFLU for EMP PAI-2 liposomes relative to EMP liposomes indicates that the former inhibits uPA activity whereas the latter does not, demonstrating that PAI-2 is present and active in the PAI-2 liposome sample.

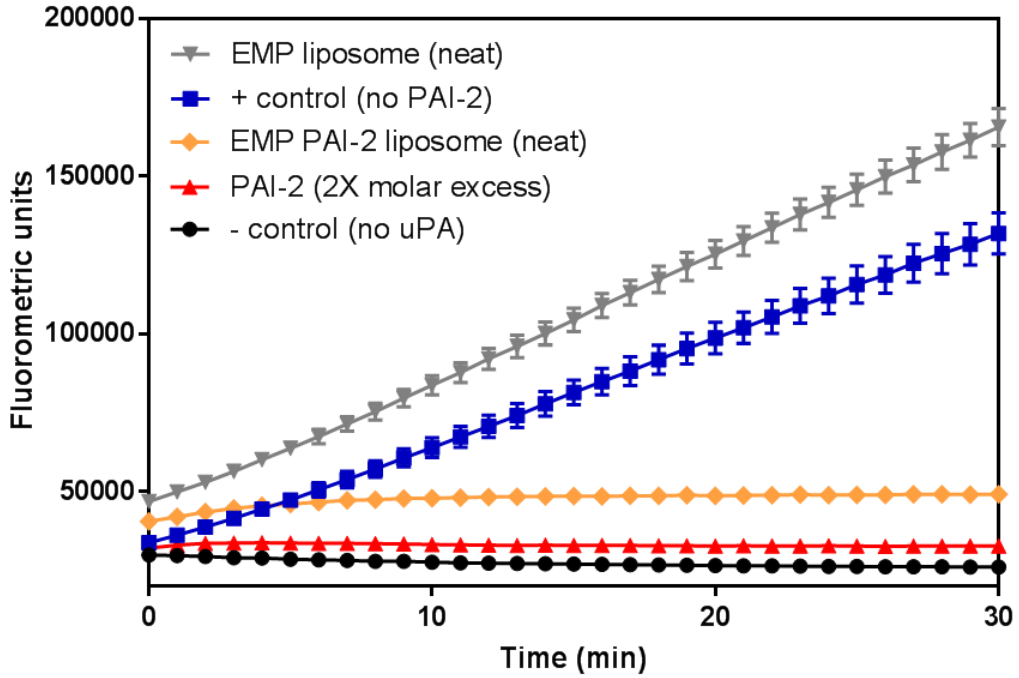

Figure 2.8: Fluorogenic uPA activity assay of PAI-2 liposomes. Liposomes were prepared and added to assay to see if PAI-2 bound to the surface of liposomes would still be active in inhibiting uPA over a period of 30 minutes at 37°C as compared to unconjugated PAI-2. Values are means ± s.d. (n = 3).

2.3.7 Centrifugation of liposomes to remove unbound PAI-2

SEC is the most commonly used method to remove free protein from liposomes following conjugation. Although standard in the field, research has noted that liposome loss using SEC may be a concern as liposomes may non-specifically adsorb to the resin (Ruysschaert et al. 2005). Further, this method causes dilution of the sample, takes time if performed by gravity, and only allows for analysis of one sample at a time. There are reports in the literature of using high-speed centrifugation to spin and pellet liposomes, primarily for the purpose of removing unencapsulated soluble drug (Zhigaltsev et al. 2010). As small soluble protein ligands, such as 45 kDa PAI-2, do not pellet out of solution under high-speed centrifugation, it was posited that unbound PAI-2 could be removed from liposomes by high-speed centrifugation, which would increase the efficiency of liposome production and potentially increase liposome recovery.

Firstly, to determine how liposomes pellet under different centrifugal forces, EMP liposomes were spun at 20,000 x g for 0-4 h, with phospholipid in the pellet measured by spectrophotometry at 350 nm. The results showed a time-dependent increase in OD350

signal in the liposome pellet and a corresponding decrease in OD350 signal in the supernatant (Fig. 2.9). Liposome size remained constant in the pellet, deviating little from the starting diameter of 145 nm. However, size decreased linearly with time up to the 2 h time point as larger particles settled to form the pellet first, leaving smaller particles behind in the supernatant and leading to a smaller average diameter. All samples displayed 100% peak intensity, as determined by DLS.

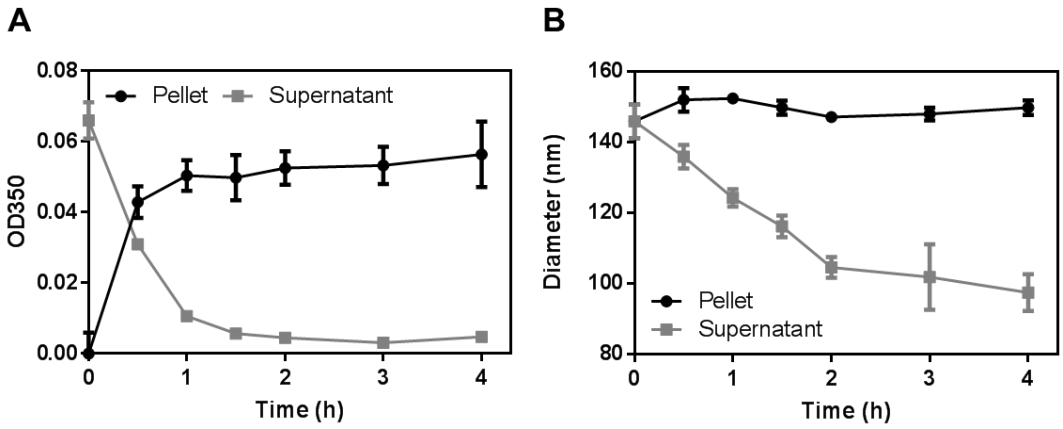

Figure 2.9: Centrifugation of liposomes over time. (**A**) Liposomes were centrifuged at 20,000 x g for up to 4 h and OD350 measured of pellet and supernatant to locate which fraction the phospholipid (liposome) resided. (**B**) Liposome samples taken at different time points from either the supernatant or pellet were analysed by dynamic light scattering to determine changes in average liposome diameter with high-speed centrifugation. Data are the mean ± s.e.m. (n = 3).

To examine the effect of centrifugation on empty PAI-2-functionalised liposomes, liposomes were centrifuged for 4 h and then analysed by nanoparticle tracking analysis (NTA) to determine average particle diameter and concentration relative to non-centrifuged liposomes (Table 2.3). The centrifuged liposomes showed a small but not significant ($P > 0.05$) increase in average diameter from 148.0 ± 4.2 nm to 153.9 ± 5.9 nm and a significant ($P < 0.01$) 22.9% reduction in particle concentration relative to non-centrifuged liposomes. NTA images revealed the distributions and monodispersity of the centrifuged and non-centrifuged liposomes to be similar (Fig. 2.10).

Table 2.3: Effect of centrifugation on liposome diameter and particle concentration. Liposomes were centrifuged at 20,000 x g at 4°C for 4 h and analysed by nanoparticle tracking analysis. Data are the mean ± s.d. (n = 3).

Liposome	Diameter (nm)	Concentration (particles/mL)
Non-centrifuged PAI-2 liposomes	148.0 ± 4.2	$2.40 \times 10^{13} \pm 4.24 \times 10^{11}$
Centrifuged PAI-2 liposomes	153.9 ± 5.9	$1.85 \times 10^{13} \pm 1.36 \times 10^{12}$

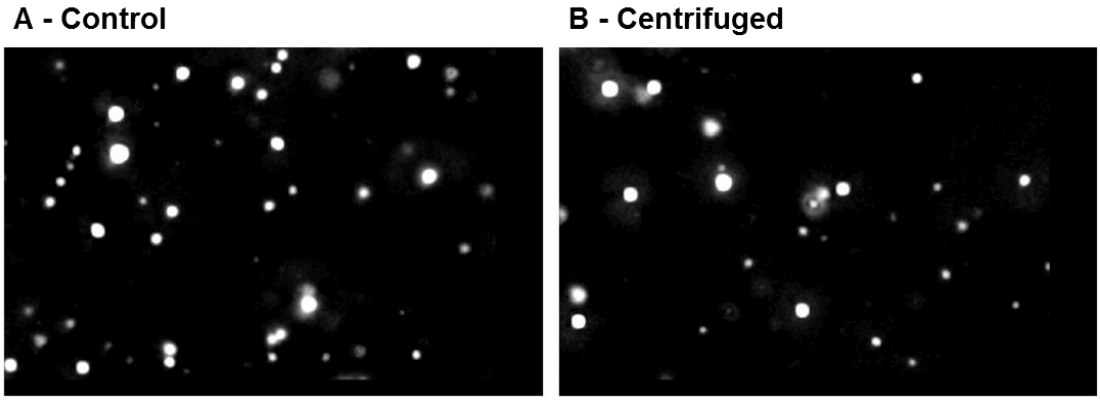

Figure 2.10: Nanoparticle tracking analysis of liposomes after centrifugation. Liposomes were centrifuged at 20,000 x g for a total of 4 h. (**A**) Control (non-centrifuged) and (**B**) centrifuged liposomes were analysed using nanoparticle tracking analysis (NTA) to determine particle size and concentration. Images are representative frames from 60 second analysis via NTA. Images are representative from triplicate measurements.

2.3.8 Conjugation of PAI-2 to liposomes using the post-insertion method

The post-insertion method of liposome functionalisation requires the formation of functionalised micelles that are then inserted into preformed liposomes (Fig. 2.2). Micelles were prepared using PEG_{2000}-DSPE and analysed by DLS. Prior to 0.22 µm filtration, the average diameter of the micelles was approximately 300 nm, and this was reduced following filtration to remove large aggregates, where the average diameter was 14.1 nm (Table 2.4). Size distributions of the filtered micelles showed the presence of larger peaks in the intensity distribution but a single peak in the volume and number distributions, indicating the presence of small micelles as the predominant population with some larger aggregates (Fig. 2.11). To form PAI-2-functionalised micelles, PAI-2 was added to PEG_{2000}-DSPE micelles containing 20% maleimide-functionalised PEG_{2000}-DSPE to enable attachment of PAI-2 via cysteine residues to the terminal end of PEG. DLS analysis of PAI-2 micelles showed that the average diameter was 15.9 nm. Micelles

before and after PAI-2 conjugation showed similar PDI values of 0.165 and 0.178, respectively (Fig. 2.11).

Table 2.4: Characterisation of PEG2000-DSPE micelles. Micelles were prepared by thin film hydration, filtered using a 0.22 µm membrane and analysed by dynamic light scattering. Values are means ± s.d. (n = 3). NF = non-functionalised.

Micelle	Diameter (nm)	Polydispersity index
NF micelle	14.1 ± 0.526	0.165 ± 0.014
PAI-2 micelle	15.9 ± 0.273	0.178 ± 0.031

PAI-2 micelles were then added to preformed *N*-AI-loaded liposomes to create PAI-2-functionalised liposomes. Following the post-insertion step, liposomes were purified by SEC as for conventional liposomes. DLS revealed 100% peak intensity across all distributions, indicating no remaining micelles were present in the liposome sample (Fig. 2.12).

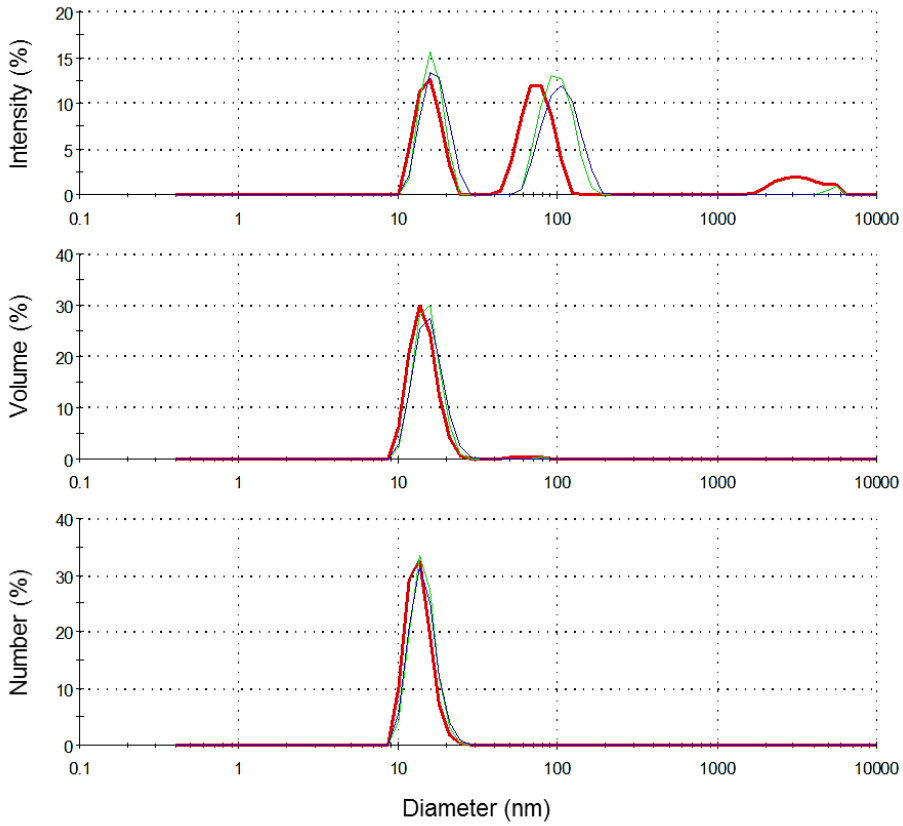

Figure 2.11: Dynamic light scattering analysis of PEG2000-DSPE micelles. Micelles were prepared by thin film hydration, filtered using a 0.22 µm membrane and analysed by dynamic light scattering to determine average liposome diameter. Traces are replicate measurements (n = 3).

There was a noticeable and significant ($P < 0.01$) increase in average liposome diameter from 141.2 ± 4.7 nm to 154.1 ± 1.3 nm following *N*-AI-loaded liposome incubation with PAI-2 micelles (the post-insertion step) (Fig. 2.13). A small increase in diameter was observed for *N*-AI liposomes that were incubated with maleimide-PEG micelles alone (145.0 ± 1.7 nm) or with a mixture of micelles that contained non-maleimide-functionalised PEG and PAI-2 (145.4 ± 4.7 nm), but this was not significantly different to the liposome diameter prior to the post-insertion step.

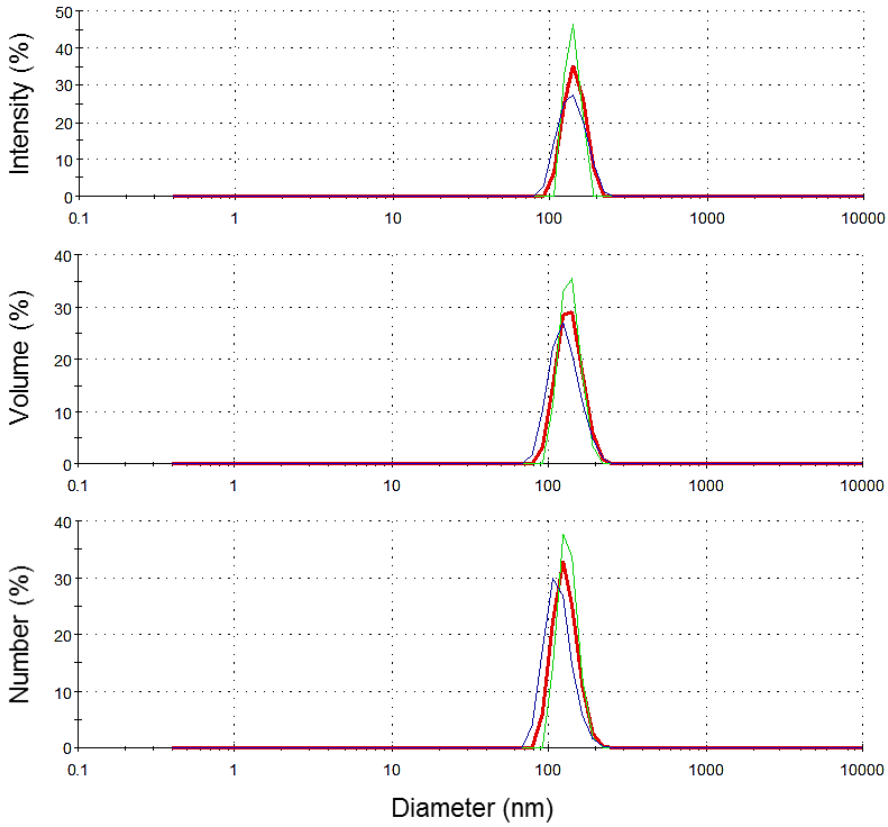

Figure 2.12: Dynamic light scattering analysis of post-insertion liposomes. Liposomes were prepared using the post-insertion method and analysed by dynamic light scattering. Traces are replicate measurements (n = 3).

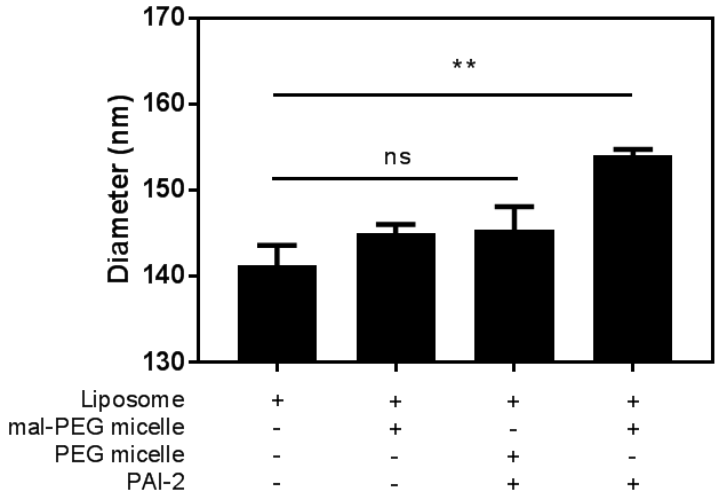

Figure 2.13: *N*-AI PAI-2 liposomes prepared by the post-insertion method. Liposomes were functionalised with PAI-2 via the post-insertion method using micelles. Dynamic light scattering was used to determine average liposome diameter. Values are the mean ± s.d. (n = 3). ns = not significant; ** = $P < 0.01$.

2.3.9 Flow cytometric analysis of micelle post-insertion into liposomes

To further confirm the insertion of micelle phospholipids into the liposome bilayer using the post-insertion method, the transfer of fluorescent micelles into liposomes was detected using flow cytometry (Mack et al. 2012). Firstly, to determine whether liposomes could be detected using the flow cytometer and to optimise settings, empty liposomes and fluorescent rhodamine-123 (R123)-loaded liposomes were prepared and analysed by DLS (Table 2.5) before being run on the flow cytometer to detect fluorescence of the particles (Fig. 2.14). R123-loaded liposomes were slightly larger than empty liposomes, but both had low polydispersity and 100% peak intensity of the particle population. Flow cytometry revealed the liposome populations of both samples, with similar forward and side scatter profiles. The R123 liposome population (MFI = 43.8 ± 0.5) showed a peak shift and 20.7-fold increase in MFI relative to that of empty liposomes (MFI = 2.1 ± 1.3), indicating that the fluorescence of R123 liposomes could be detected by flow cytometry. Analysis of PBS only showed a minimal presence of small particles at the detection settings used to analyse the liposomes.

Table 2.5: Characterisation of R123-loaded liposomes. Empty liposomes and liposomes containing rhodamine-123 (R123) were prepared by the thin film hydration method and analysed by dynamic light scattering. Values are means ± s.d. (n = 3).

Liposome	Diameter (nm)	Polydispersity index	Intensity (%)
Empty	135.3 ± 6.0	0.080 ± 0.038	100
R123-loaded	148.1 ± 3.6	0.066 ± 0.010	100

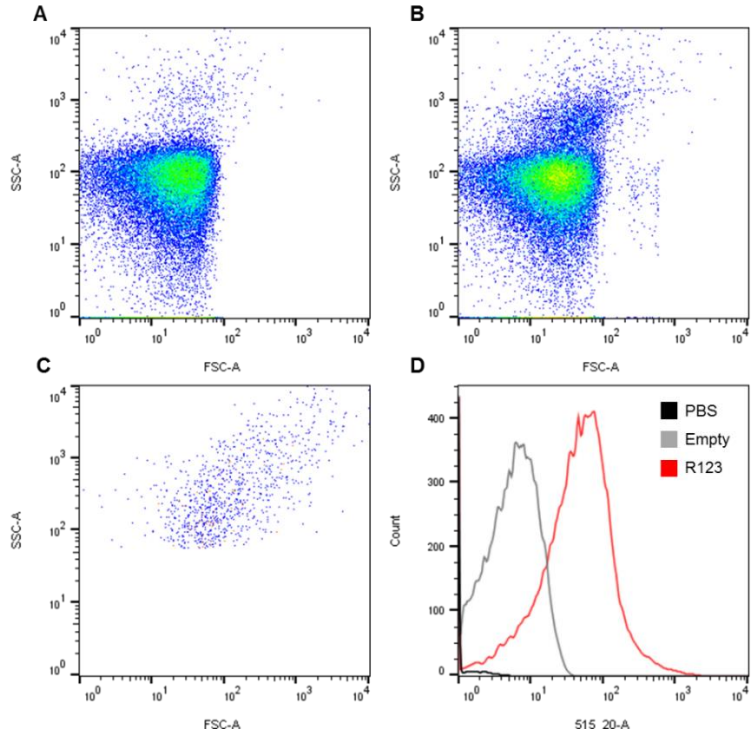

Figure 2.14: Detection of R123-loaded liposomes by flow cytometry. (**A**) Empty or (**B**) rhodamine-123 (R123)-loaded liposomes were analysed by flow cytometry using a 515 band-pass filter for detection of rhodamine. (**C**) PBS was used to adjust the threshold for the detection of particles and to minimise signal noise. (**D**) Fluorescent signal of R123 was detected as a peak shift relative to empty liposomes and PBS samples. Data are representative from n = 3 samples. FSC, forward scatter; SSC, side scatter.

Once it was confirmed that liposomes could be detected by flow cytometry using the optimised settings, micelles composed of 0%, 10% or 30% FITC-labelled phospholipid (FITC-PEG-DSPE; 30% of total micelle phospholipid) were incubated with preformed empty liposomes as per the post-insertion method of targeted liposome preparation (Allen et al. 2002). DLS analysis revealed a small increase in average liposome diameter for all three preparations following the post-insertion step relative to liposomes that had not been incubated with micelles (Table 2.6). The PDI of the three post-insertion preparations increased slightly, but peak intensity remained at 100%, indicating the absence of

unincorporated micelles in the liposome preparations. Analysis of the liposomes by flow cytometry revealed a significant increase ($P < 0.01$) in the mean fluorescence intensity (MFI) for liposomes that had been incubated with 10% or 30% FITC-labelled micelles compared to liposomes incubated with non-fluorescent micelles (Fig. 2.15). There was no significant difference in MFI between the 10% FITC and 30% FITC liposome preparations.

Table 2.6: Characterisation of FITC-labelled liposomes. Liposomes were prepared by the thin film hydration method, and micelles composed of 0%, 10% or 30% FITC-PEG2000-DSPE were incorporated into the liposomes using the post-insertion method. Liposomes were analysed by dynamic light scattering. Values are means ± s.d. (n = 3).

Liposome	Diameter (nm)	Polydispersity index	Intensity (%)
No micelle	136.0 ± 2.1	0.055 ± 0.033	100
0% FITC micelle	140.6 ± 2.4	0.089 ± 0.003	100
10% FITC micelle	140.1 ± 2.4	0.086 ± 0.041	100
30% FITC micelle	143.1 ± 2.7	0.079 ± 0.021	100

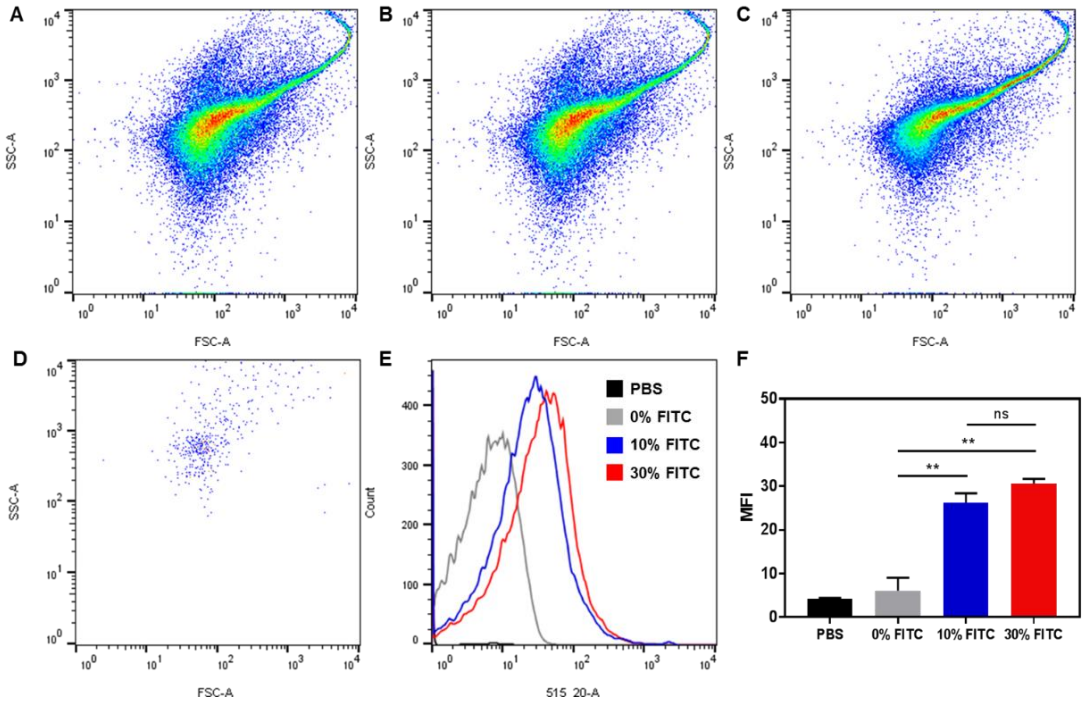

Figure 2.15: Detection of post-insertion of FITC micelles into liposomes. Liposomes were incubated with (**A**) 0% FITC micelles, (**B**) 10% FITC micelles or (**C**) 30% FITC micelles and analysed by flow cytometry (FSC = forward scatter; SSC = side scatter). (**D**) PBS only was used to select an appropriate voltage to minimise the signal from small non-liposome particles and noise signal. (**E**) Histograms of the mean fluorescence intensity (MFI) of the samples. (**F**) MFI values for each sample. Values are means ± s.e.m. (n = 3). ns = not significant; ** = $P < 0.01$. FSC, forward scatter; SSC, side scatter; FITC, fluorescein isothiocyanate.

2.4 Discussion

In this chapter, *N*-AI-loaded PAI-2-functionalised (*N*-AI PAI-2) liposomes were prepared and characterised for the first time using optimisations to previously reported methods. *N*-AI PAI-2 liposomes were 141.1 ± 5.0 nm in diameter, monodisperse (PDI of 0.086 ± 0.030), had a zeta potential of –4.66 ± 0.52 mV and contained *N*-AI at a concentration of 2.2 mM, equating to 43.1% encapsulation efficiency. PAI-2 conjugation to the surface of *N*-AI-loaded liposomes was achieved using conventional and post-insertion methods of liposome functionalisation and was confirmed using SEC and Western blotting. A PAI-2 inhibitory activity assay confirmed that PAI-2 attached to the surface of liposomes remained active against its target uPA after conjugation, which indicated that *N*-AI PAI-2 liposomes are suitable for further *in vitro* and *in vivo* evaluation against breast cancer cells.

The empty (non-drug-loaded), empty PAI-2-functionalised, *N*-AI-loaded and *N*-AI-loaded PAI-2-functionalised liposomes prepared in this work ranged between 130 nm and 150 nm in diameter, which is in the size range of previously reported PEGylated phosphatidylcholine liposomes (Chang & Yeh 2012). This liposome size range has been reported to avoid rapid clearance by the mononuclear phagocyte system (MPS) in circulation and to utilise the enhanced permeability and retention effect to extravasate and accumulate at the site of tumours for drug delivery (Maeda 2015). The zeta potential, or surface charge, of liposomes is dependent on a number of factors, including the composition of the liposome (Smith et al. 2017). It has been reported that while PEG itself does not affect the surface charge of liposomes, PEG-DSPE introduces a negative surface potential due to the phosphate diester moiety (Barenholz 2012). This is reflected by the zeta potential measurements of the four liposome formulations reported in this chapter, which ranged between –3.63 mV and –4.66 mV (Tables 2.1 and 2.2). This indicates that the liposomes have a slightly negative, but near-neutral, surface charge, which did not vary greatly with *N*-AI encapsulation and/or PAI-2 conjugation to the liposome surface, although it was noted that PAI-2-functionalised liposomes had a slightly more negative surface charge than non-functionalised liposomes (Tables 2.1 and 2.2). This is expected, given that PAI-2 has a predicted isoelectric point of 5.4 and therefore a negative charge at physiological pH (Croucher et al. 2007). Liposomes with mildly charged or near-neutral surfaces have a propensity to aggregate faster than liposomes with a strong surface

charge as the latter have greater particle-particle repulsion and hence are more electrostatically stabilised in suspension (Safhi et al. 2017). However, strongly positively charged particles lead to rapid elimination by the MPS (Litzinger et al. 1996), whereas near-neutral liposomes have an increased circulation half-life (Allen & Cullis 2013). Importantly, histological analysis of the localisation of liposomes within *in vivo* tumours has shown that negatively charged and neutral liposomes are able to extravasate at the site of the tumour, while positively charged liposomes remain associated with the vascular endothelium, limiting their suitability for tumour targeting applications (Krasnici et al. 2003).

The successful encapsulation of a hydrophobic drug into liposomes can greatly enhance the aqueous solubility and bioavailability of the molecule, and therefore increase the suitability for its use in drug delivery applications. In this work, the thin film hydration method was used to load *N*-AI into the bilayer of soy phosphatidylcholine PEGylated liposomes. The *N*-AI loading into liposomes appeared to be stable and not crystallise out of the liposomes (Fig. 2.3), and the encapsulation efficiency was determined to be approximately 43.1% of the starting amount of *N*-AI used in the formulation. Drug loading into liposomes depends on many factors, and in the case of loading into the bilayer, liposome size is a key factor (Swenson et al. 2001). One of the drawbacks of the thin film method is the typically low drug loading, as compared to other methods, as the space in the bilayer limits how much drug can be loaded (Pattni et al. 2015). In this work, *N*-AI was substituted for cholesterol in the formulation of *N*-AI-loaded liposomes in order to increase the drug-loading capacity of the bilayer. As the molecular weights of *N*-AI and cholesterol are similar (425.07 g/mol and 386.65 g/mol, respectively) and both are hydrophobic molecules that act to stabilise the liposome bilayer (Leonenko et al. 2004), a greater encapsulation of *N*-AI in the liposomes was achieved without affecting liposome size or surface charge (Table 2.1). Alternative methods can be used to load drugs into the liposome core, which typically has a larger volume and therefore a greater capacity for drug loading (Gubernator 2011). For example, the commonly used anticancer drug docetaxel, which is strongly hydrophobic and poorly water soluble, has previously been loaded into the bilayer of liposomes. This was achieved by creating a weak base derivative of the drug molecule, and the use of ion gradients in the liposome formulation were used to actively load the drug into the liposome core, increasing the trapping efficiency to close

to 100% at a drug-to-lipid ratio of up to 0.4 mg/mg (Zhigaltsev et al. 2010). Such an approach could be explored in the future to increase the loading of *N*-AI in liposomes if required.

The main advantage of the thin film method is that it is relatively straightforward and easy to produce reasonable and consistent quantities of liposomes for laboratory testing. However, upscaling of liposome production – as required for clinical use – is challenging since lab-based liposome production methods are generally not amenable to scale up beyond the millilitre scale. The formation of liposome thin films via the use of rotary evaporation is limited by the size of the flask used to create the film, and flask overloading may increase liposome polydispersity and alter other physicochemical characteristics of the resultant sample (Wagner & Vorauer-Uhl 2011). The extrusion of liposomes through membranes as required to achieve a desired size distribution is another labour-intensive step in the production process as preparations need to be passed repeatedly across a membrane and usually on a 1-20 millilitre scale. In the laboratory setting, the preparation of multiple separate batches of liposomes can be used to overcome these issues, although batch-to-batch variability must be considered. This is particularly important for ligand-functionalised liposome formulations as variations in the physicochemical characteristics of the preparation may influence stability, *in vivo* circulation time, clearance properties, tumour uptake, therapeutic efficacy and toxicity (Honary & Zahir 2013). Therefore, adequate characterisation of liposomes intended for further *in vitro* and *in vivo* evaluation is essential.

The conjugation of PAI-2 to the surface of empty and *N*-AI-loaded liposomes via PEG was performed using standard coupling chemistry as described previously (Vine et al. 2014). Removal of unconjugated PAI-2 was achieved using SEC, as is standard in the liposome field (Grimaldi et al. 2016). When unconjugated PAI-2 was removed from PAI-2 liposomes following the conjugation step by SEC, the absorbance at 280 nm revealed the presence of two distinct peaks (Fig. 2.5). The first peak corresponded to the largest particles eluting from the column: PAI-2-functionalised liposomes. The second peak corresponded to the smaller, unconjugated PAI-2 molecules, which had a longer elution time. This pattern was also observed in the OD350 readout, where liposome phospholipid, but not protein, showed absorption. Phospholipid signal was observed for the first peak

(fractions 4-9) but not in the second peak (fractions 34-40), corroborating the OD280 readout and suggesting that liposomes eluted from the column first, followed by unconjugated protein (Fig. 2.5). However, due to the broad absorbance spectrum of phospholipids, including at 280 nm (Appendix A), it was impossible to determine whether PAI-2 was covalently attached to those liposomes.

The quantification of covalently attached PAI-2 in the liposome samples was attempted using two biochemical copper-based protein assays. However, protein could not be detected due to the following factors: 1) liposomal phospholipid interferes in both Lowry and BCA assays, resulting in an overestimation of protein concentration (Kessler & Fanestil 1986) (Fig. 2.6); 2) the amount of protein in the liposome sample is expected to be low and therefore is likely below the limit of detection (the minimum amount of protein that can be detected in the Lowry and BCA assays is reported as 5 µg/mL and 8 µg/mL, respectively); and 3) after SEC, the liposome sample is diluted considerably, further compounding the former two factors. Therefore, Western blotting of the size-exclusion fractions was performed to detect PAI-2 in those fractions as an indirect measure of successful PAI-2 conjugation to the liposomes.

Western blot detection of PAI-2 in fractions from the two size-exclusion peaks confirmed that PAI-2 was conjugated to the liposome phospholipid (PEG-DSPE) in the first peak, while the second peak contained unconjugated PAI-2 (Fig. 2.7). The latter peak presented as a band at 45 kDa, the same as the molecular weight observed for purified PAI-2 (positive control). In the liposome fraction, PAI-2 presented at a molecular weight higher than 45 kDa. This shift upwards in the gel is the consequence of a lag in migration of the PAI-2-PEG-DSPE molecules through the gel due to steric hindrance of the PEG and interaction with SDS. Therefore, PAI-2-PEG-DSPE does not migrate through the gel as quickly as free PAI-2, resulting in a higher apparent molecular weight (Vine et al. 2014). The appearance of a second higher molecular weight band in the liposome sample suggests the presence of PAI-2 bound to two or more PEG-DSPE molecules, which is possible since PAI-2 has four available cysteine residues that can bind to the maleimide group of PEG-DSPE (Chapter 1, Section 1.5.1). Native PAGE eliminates the PEG-SDS interaction and provides a higher band resolution, so this technique could be used as an

alternative to SDS-PAGE for further analysis of ligand-functionalised PEG liposomes (Zheng et al. 2007).

The Western blot of size-exclusion samples showed that there was no detectable band at 45 kDa, indicating that unconjugated PAI-2 was successfully removed from the liposome sample by SEC (Fig. 2.7). Quantification of PAI-2 on liposomes was attempted using densitometry of Western blots, and although an approximate ratio of bound and unbound PAI-2 was determined to be 50:50 (Appendix C), the irregular pattern of the liposome PAI-2 band on the blot indicated that densitometry was not a reliable tool to quantify PAI-2 conjugation. However, as outlined above, Western blotting was successful in qualitatively confirming the conjugation of PAI-2 to liposomes and in confirming the absence of unconjugated PAI-2 in the purified liposome sample prior to further testing. These findings highlight a distinct limitation in the research field of actively targeted liposomes: the lack of robust methodology to quantify small amounts of liposome-bound protein in liposome formulations (Belfiore, L. et al. 2018). In this chapter, quantifying small amounts of PAI-2 was not achieved using biochemical assays due to phospholipid interference, although it is important to note that even if such methods were successful, they could only provide a quantification of the total protein in a liposome sample rather than a quantification of the average number of protein ligands bound to each liposome. This lack of published methods necessitates the development of alternative methods to quantify protein conjugation of actively targeted liposome formulations.

As outlined in Chapter 1, Section 1.6, the majority of clinically approved nanotherapies are arguably quite simplistic in their composition and structure. In the context of ligand-directed liposomes, controlling for batch-to-batch variability is difficult without effective methods for characterisation, and the inability to control or correct for variability in ligand attachment to liposomes may become an issue in the regulatory processes required for clinical translation of a novel formulation. Without robust methods to enable detection of ligand conjugation and quantification of surface ligands, variation between batches may lead to deviations in the physicochemical characteristics of the preparation, which would ultimately influence stability, *in vivo* circulation time, clearance properties, tumour uptake, therapeutic efficacy and toxicity of a targeted liposome formulation (Honary & Zahir 2013). Adequate methods for the confirmation and quantification of ligand

attachment to liposomes have not been developed (Saul et al. 2006), which poses a larger challenge for dual-ligand and multi-ligand liposomes, where the determination of stoichiometry of ligand attachment, in addition to density, is an important step in the characterisation process. Theoretical values of ligand conjugation and ligand ratios have been reported, but this has not been demonstrated empirically for most liposome formulations as the methods used to generate such data are technically challenging. The development of new methods to quantify ligand attachment to liposomes will enable a more complete characterisation of targeted liposome formulations to facilitate optimisation and assist with standardising nanoparticle characterisation in the research field more broadly (Faria et al. 2018). This concept is explored further in Chapter 5, where single-molecule fluorescence microscopy was evaluated as a method to quantify ligands attached to the surface of liposomes.

An important step in characterising ligand-functionalised liposomes is to confirm whether the targeting ligand(s) conjugated to the liposome surface retain activity against the target receptor once bound to the liposome surface and following all the processes of production and purification. In a fluorogenic activity assay, PAI-2 liposomes successfully inhibited the enzymatic activity of uPA, while non-functionalised liposomes did not show inhibition, as expected (Fig. 2.8). While there was no observed uPA inhibitory effect due to liposome phospholipid alone, there was an observed interference effect from the presence of the liposome phospholipid in the assay for both non-functionalised and PAI-2-functionalised liposomes, which was revealed as a positive shift from the baseline in both samples. Despite this, the rate of inhibition as indicated by fluorescence (RFLU) of 4026.9 ± 206.2 FLU/min for non-functionalised liposomes was significantly reduced to 43.5 ± 24.9 FLU/min for PAI-2 liposomes, which confirms that PAI-2 bound to the surface of liposomes retains its inhibitory action against uPA. This is a crucial aspect for utilising PAI-2 liposomes for uPA/uPAR targeting *in vitro* and *in vivo*.

Given that SEC results in considerable dilution of liposome samples, centrifugation was explored as a potential method to concentrate liposomes and remove unconjugated protein from liposomes in a high-throughput manner. Centrifugation of liposomes is reported in the literature, particularly in the context of removing unencapsulated soluble drug from liposomes, such as in protocols for the active-loading method of drug

encapsulation (Gubernator 2011). In this study, centrifugation of liposomes for up to 4 h showed a time-dependent pelleting of liposomes, with a plateau after 2 h of centrifugation at 20,000 x g (Fig. 2.9). In the supernatant of these samples, DLS revealed that while the pelleted liposome diameter remained relatively constant, the average diameter of the liposomes remaining in the supernatant decreased over time. As centrifugation causes the largest particles in a solution to pellet before the smallest particles, the largest liposomes pelleting between 0 h and 2 h of centrifugation corresponded with the smallest liposomes remaining in solution, shifting the size distribution considerably. DLS analysis of pelleted liposomes after 4 h of centrifugation revealed a small but not significant ($P > 0.05$) increase in the average diameter compared to non-centrifuged liposomes (153.9 ± 5.9 nm and 148.0 ± 4.2 nm, respectively) and a 77.1% retention of liposomes after 4 h of centrifugation (Table 2.3). The centrifuged liposomes appeared to remain intact and had not aggregated as determined by nanoparticle tracking analysis (Fig. 2.10). While these results indicate that centrifugation of empty liposomes does not change the liposome population significantly, it is unknown whether prolonged centrifugation of *N*-AI-loaded liposomes would affect drug loading. This would need to be determined specifically for *N*-AI-loaded liposomes prior to adopting centrifugation as a standard purification method for drug-loaded liposomes. Additionally, the development of a robust method to quantify PAI-2 attachment to liposomes is needed in order to elucidate whether centrifugation results in changes to PAI-2 ligand attachment on the surface of liposomes.

As outlined in Section 2.1.2, the post-insertion method is an alternative method of conjugating ligands to the surface of liposomes, with the greatest advantage of this method being the ease with which a range of dual-ligand or multi-ligand liposomes can be produced from a single batch of liposomes (Moreira et al. 2002). Previous work comparing these two methods indicates that liposomes prepared by conventional and post-insertion methods are equivalent (Iden & Allen 2001). In this chapter, PAI-2-functionalised liposomes prepared via the post-insertion method were significantly larger ($P < 0.05$) in diameter than those prepared by the conventional method (154.1 ± 1.3 nm and 141.1 ± 5.0 nm, respectively) (Fig. 2.13). This appears to be a result of the post-insertion step specifically, as *N*-AI liposomes incubated with maleimide-PEG micelles alone (145.0 ± 1.7 nm) or with a mixture of micelles that contained non-maleimide-functionalised PEG and PAI-2 (145.4 ± 4.7 nm) did not show a significant increase in

diameter compared to the liposome diameter prior to the post-insertion step (141.2 ± 4.7 nm). It is possible that the post-insertion method led to more efficient conjugation of PAI-2 and mal-PEG compared to the conventional method, perhaps due to the higher temperature of the conjugation step, meaning that the observed increase in liposome size could be due to post-insertion liposomes having a greater average number of PAI-2 proteins attached to the surface than conventional liposomes. This was further explored in Chapter 5 (Section 5.3.6). DLS analysis of micelles alone prior to the post-insertion step showed small amounts of aggregation in the sample (Fig. 2.11). However, following the post-insertion step and SEC of liposomes, DLS analysis revealed 100% peak intensity (Fig. 2.12), indicating the absence of unincorporated micelles or aggregates.

Flow cytometry was used as an indirect confirmation that post-insertion of micelle phospholipids (and any covalently conjugated ligands) into the liposome outer leaflet was successful, as per previously reported methods (Mack et al. 2012). Rhodamine-123-loaded liposomes showed a 20.7-fold increase in MFI (43.8 ± 0.5) relative to non-fluorescent liposomes (2.1 ± 1.3), indicating that fluorescently labelled liposomes could be detected by flow cytometry (Fig. 2.14). Analysis of post-insertion liposomes by flow cytometry revealed a significant increase ($P < 0.01$) in MFI for liposomes that had been incubated with 10% or 30% FITC-PEG-DSPE micelles compared to liposomes incubated with non-fluorescent micelles (Fig. 2.15). This work detected the association of fluorescent micelle phospholipids in liposomes after the post-insertion step, indirectly confirming successful post-insertion. However, as this method is only semi-qualitative, it remains unknown if and how well protein ligands are transferred into the outer liposome bilayer using the post-insertion method.

As the post-insertion method requires the extra step of firstly preparing ligand-functionalised micelles, the conventional method is more straightforward for preparing single-ligand liposomes. The post-insertion step also involves heating, which may affect the structure or activity of some protein ligands, so this would need to be determined for the individual ligands used. The main advantage of the post-insertion method is in the context of creating dual-ligand liposomes to target multiple tumour cell receptors, such as in the case of liposomes targeting tumour heterogeneity (Chapter 1, Section 1.6). As dual-ligand liposomes can increase the number of targetable receptors at the cell surface,

a greater number of liposomes can bind to tumour cells to enhance the therapeutic efficacy of the encapsulated drug (Laginha et al. 2005). Therefore, the findings presented in this chapter can be considered in future work exploring the creation of dual-ligand liposomes using the post-insertion method.

2.5 Conclusion

The work presented in this chapter demonstrates the successful preparation and characterisation of liposomes encapsulating the *N*-AI cytotoxin, with PAI-2 covalently attached to the liposome surface as a targeting ligand for binding to uPAR-positive cells. Previously published liposome analysis methods were optimised in order to allow the successful characterisation of liposomes as required for *in vitro* and *in vivo* evaluation. *N*-AI-loaded PAI-2-functionalised liposomes were monodisperse, contained encapsulated *N*-AI, had PAI-2 successfully conjugated to the liposome surface, and importantly, were active in inhibiting target uPA in an activity assay. Therefore, further testing of these liposomes against uPAR-positive breast cancer cells using *in vitro* and *in vivo* models is warranted.

Chapter 3:

In Vitro Evaluation of *N*-alkylisatin-Loaded Liposomes Targeting the Urokinase Plasminogen Activator System

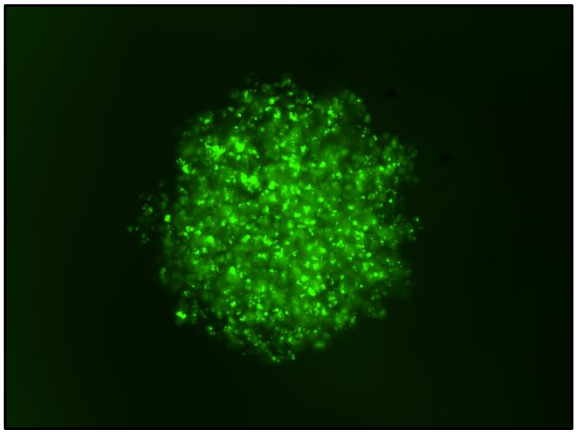

N-AI-loaded liposome-mediated destruction of a multicellular tumour spheroid

Portions of this chapter have been included in the following work for publication:

Belfiore, L, Saunders, DN, Ranson, M & Vine, KL 2019, '*N*-alkylisatin-loaded liposomes targeting the urokinase plasminogen activator system in breast cancer', manuscript in preparation.

Author contributions: LB, DNS, MR and KLV designed the experiments; LB and KLV performed the experiments and analysed the data; LB wrote the manuscript; DNS, MR and KLV edited the manuscript for submission.

3.1 Introduction

The work described in Chapter 2 of this thesis detailed the preparation and characterisation of *N*-alkylisatin (*N*-AI)-loaded plasminogen activator inhibitor-2 (PAI-2)-functionalised (*N*-AI PAI-2) liposomes. In order to evaluate how these liposomes interact with and affect breast cancer cells, *N*-AI PAI-2 liposomes were tested against breast cancer cells *in vitro*. This is an important step to confirm the cellular uptake, cellular localisation and cytotoxicity of *N*-AI PAI-2 liposomes before evaluating their potential as an anticancer therapeutic using more complex *in vivo* models of breast cancer.

3.1.1 Cell-based models of cancer

A diverse range of cancer cell lines derived from tumour biopsies have been established in the laboratory and retain many – but not all – of the genotypic and phenotypic properties of the original tumour cells, making them useful representative models for testing targeted therapies (Holliday & Speirs 2011; Subik et al. 2010) and for studying mechanisms of therapeutic resistance (Boulbes et al. 2015). Cells grown on dishes are amenable to high-throughput approaches for determining morphological changes and cytotoxicity resulting from treatment with novel drugs, and endpoint cell viability assays can be used to measure changes in cell proliferation and metabolism in a high-throughput manner. *In vitro* cell-based models of cancer are also useful for measuring the targeting ability of novel nanotherapies and the localisation of nanoparticles within cells.

Cancer cells can be grown as two-dimensional (2D) cell monolayers or three-dimensional (3D) cell aggregates or spheroid structures. While 2D cell culture is high-throughput, robust and widely validated, 3D cell culture better recapitulates several key elements of *in vivo* tumours, including tumour architecture, tumour cell interactions, tumour-stroma interactions, and the various proliferative and metabolic gradients that form when tumour cells exist as a 3D structure (Li & Lu 2011). Multicellular tumour cell spheroids are cancer cells that are grown in a large spherical association, resembling small tumours and micrometastases (Senavirathna et al. 2013) (Fig. 3.1). The ability of cancer cells to form spheroids is strongly related to the expression of several cell-cell adhesion molecules (Ivascu & Kubbies 2007), and spheroid formation can be facilitated by culturing cells in conditions that prevent adherence to cell culture plates (Friedrich et al. 2009). Changes in

spheroid morphology and diameter in response to a drug treatment can be measured using manual or automated imaging techniques (Karacali et al. 2007), and end-point biochemical assays allow for the determination of cell viability (Friedrich et al. 2007). As drug sensitivities of cell lines can vary depending on whether the cells are grown in 2D or 3D (Godugu et al. 2013), it is important to utilise 3D cell culture models in the screening of novel drug formulations.

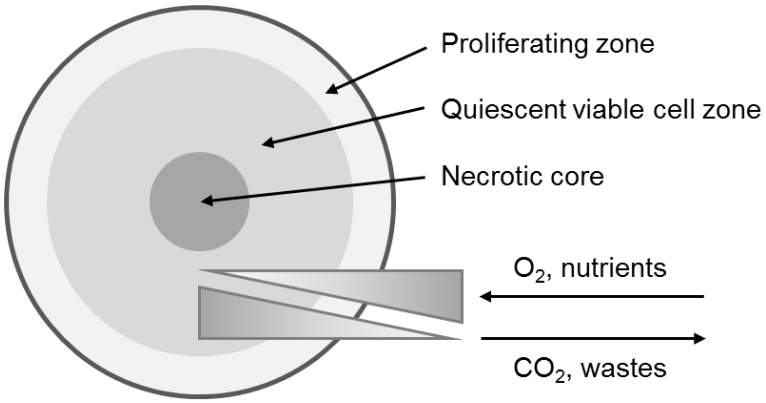

Figure 3.1: Cross-section view of a multicellular tumour cell spheroid. Spheroids recapitulate several key elements of *in vivo* tumours, including three-dimensional (3D) tumour architecture, cell-cell interactions and the various proliferative and metabolic gradients that form when tumour cells exist as a 3D structure. Figure adapted from Lin et al. 2008.

3.1.2 Experimental rationale

The targeting ability, cellular localisation and cytotoxicity of *N*-AI PAI-2 liposomes can be determined using 2D monolayer cell culture and 3D multicellular tumour spheroid models (Thoma et al. 2014). The commonly used breast cancer cell lines MCF-7 (Soule et al. 1973) and MDA-MB-231 (Olivé et al. 1974) serve as representative urokinase plasminogen activator receptor (uPAR)-negative and uPAR-positive cells (Huber et al. 2016), respectively, for the testing of uPAR-targeted liposomes. The *in vitro* evaluation of *N*-AI PAI-2 liposomes will serve to justify and guide further evaluation *in vivo*.

3.1.3 Aims

This chapter tested the hypothesis that *N*-AI-loaded PAI-2-functionalised (*N*-AI PAI-2) liposomes exhibit increased cellular uptake and increased cytotoxic effect in uPAR-positive breast cancer cells relative to uPAR-negative breast cancer cells. Therefore, the

overall aim of this chapter was to evaluate the *in vitro* properties of *N*-AI PAI-2 liposomes in two breast cancer cell lines that vary in expression of uPAR. The specific aims of this chapter were to:

1. Determine the cellular uptake of *N*-AI PAI-2 liposomes in breast cancer cells;
2. Elucidate the cellular localisation of *N*-AI PAI-2 liposomes in breast cancer cells; and
3. Characterise the cytotoxicity of *N*-AI PAI-2 liposomes against breast cancer cells grown as either monolayers or multicellular tumour spheroids.

3.2 Methods

3.2.1 Cell lines and culture conditions

The human mammary epithelial invasive ductal carcinoma cell lines MCF-7 and MDA-MB-231 were originally purchased from the American Type Culture Collection (ATCC, VA, USA). Cells were cultured in RPMI-1640 medium (Life Technologies, CA, USA) containing 24 mM $NaHCO_3$ and supplemented with 10% (v/v) heat-inactivated fetal bovine serum (FBS; Thermo Fisher Scientific, MA, USA). Cells were maintained in culture at 37°C in a 95% humidified atmosphere with 5% CO_2 in a HERAcell incubator (Kendro Laboratory Products, Germany). For passaging, cells were harvested by treatment with 0.05% trypsin-EDTA (Life Technologies, CA, USA), followed by centrifugation at 300 x g for 5 min. For experiments, cells were harvested by treatment with PBS containing 5 mM EDTA (pH 7.4), followed by centrifugation at 300 x g for 5 min. Viable cells were counted with a haemocytometer using the Trypan Blue (Sigma-Aldrich, MO, USA) exclusion method. Cell lines were routinely tested and confirmed negative for mycoplasma contamination (in-house testing conducted by the IHMRI Technical Services Unit). Cell lines were confirmed negative for cross contamination by short-tandem repeat (STR) sequencing (performed by the Garvan Institute of Medical Research, Darlinghurst, Australia).

3.2.2 Cell surface uPA and uPAR expression

Expression of urokinase plasminogen activator (uPA) and uPAR on the surface of MCF-7 and MDA-MB-231 cells was determined by flow cytometry. Cells (1×10^5) in 100 µL PBS (pH 7.4, with 1% w/v BSA) were incubated with mouse anti-human uPA

monoclonal antibody (ADI #394; Alpha Diagnostic International, TX, USA) at 10 µg/mL, mouse anti-human uPAR monoclonal antibody (DAKO #7294; Agilent Technologies, CA, USA) at 10 µg/mL or mouse IgG_1 monoclonal antibody (isotype control) (Merck #MABC002; Merck, Germany) at 10 µg/mL for 45 min on ice, followed by three washes with ice-cold PBS (with 1% w/v BSA) and centrifugation at 300 x g for 5 min after each wash. Cells were then incubated with donkey anti-mouse IgG-Alexa Fluor 488 polyclonal antibody at 2 µg/mL for 45 min on ice, followed by three washes with ice-cold PBS (with 1% w/v BSA) as above. Cells were resuspended in 100 µL PBS and the fluorescence intensity of the Alexa-488-conjugated antibody analysed by flow cytometry (LSR II; BD Biosciences, CA, USA) (excitation 488 nm, emission collected with 515/20 band-pass filter). FlowJo software (version 10; Tree Star Inc., OR, USA) was used to evaluate cell-surface expression of uPA and uPAR relative to the IgG isotype control to account for non-specific antibody binding to cells.

3.2.3 Cellular uptake of liposomes by flow cytometry

Uptake of fluorescently labelled non-functionalised and PAI-2-functionalised liposomes by MCF-7 and MDA-MB-231 cells was assessed using flow cytometry. Cells (2×10^5 cells per well) were seeded into 12-well plates and allowed to attach for 24 h at 37°C. Liposomes containing 1% (mol/mol) FITC-PEG_{2000}-DSPE were prepared as described in Chapter 2, Section 2.2 and added to cells in culture media (RPMI-1640 + 10% (v/v) FBS) at dilutions ranging from 1:20 to 1:5. At specified time intervals ranging between 15 min and 60 min, the supernatant was removed, cells washed once with PBS and then harvested using PBS containing 5 mM EDTA (pH 7.4). Cells were then centrifuged (300 x g for 5 min) and washed three times with PBS before being resuspended in 200 µL PBS for analysis. The fluorescence intensity was determined by flow cytometry (LSR II flow cytometer; BD Biosciences, CA) (excitation 488 nm, emission collected with 515/20 band-pass filter). FlowJo software (V10; Tree Star Inc., OR, USA) was used to evaluate the mean fluorescence intensity (MFI) to determine cellular uptake of liposomes.

3.2.4 Cellular localisation of liposomes by confocal microscopy

Uptake and cellular localisation of fluorescently labelled liposomes were determined by confocal microscopy as reported previously (Ducat et al. 2011). For monolayer cell

culture experiments, 50,000 cells per well were seeded into 8-well µ-Slide chambered coverslips (ibidi, Germany) and incubated for 24 h at 37°C. Cells were allowed to reach 80% confluence before the addition of liposomes. Liposomes containing 1% or 10% (mole % of liposome phospholipid) FITC-PEG_{2000}-DSPE, or 0.625% (mole % of liposome phospholipid) octadecyl rhodamine B chloride (R18; Invitrogen, CA, USA) were prepared as described in Chapter 2, Section 2.2. Liposomes were added to cells in culture media (RPMI-1640 + 10% (v/v) FBS) at dilutions ranging from 1:5 to 1:10 and incubated for 30 min to 2 h at 37°C. Supernatant was removed and wells were rinsed three times with PBS before LysoTracker Green DND-26 (excitation/emission 504/511 nm) or LysoTracker Red DND-99 (excitation/emission 577/590 nm) (Thermo Fisher Scientific, MA, USA) was added to each well (50 nM final concentration) immediately prior to imaging. Live imaging of cells in PBS was performed using a Leica TCS SP5 Confocal Microscope (Leica Microsystems, Germany) and images were acquired using a 63X oil immersion lens. Images were analysed using Leica Application Suite (V10; Leica Microsystems, Germany).

3.2.5 2D monolayer cytotoxicity assays

In vitro cytotoxicity assays were performed in 96-well flat-bottom microtitre plates as described previously (Vine et al. 2016). MCF-7 or MDA-MB-231 cells were seeded at a density of 5000 cells per well into sterile 96-well flat-bottom plates and incubated at 37°C for 24 h in an IncuCyte Zoom automated imaging instrument (Essen BioScience, MI, USA). Empty and *N*-AI-loaded liposomes were prepared as outlined in Chapter 2, Section 2.2 and were serially diluted in PBS before being added to cells (each concentration tested in triplicate). Liposomes were incubated with cells for 72 h and wells were imaged every 24 h by the automated IncuCyte imaging system. To determine cell viability at the experimental endpoint, CellTiter 96 Aqueous One Solution Cell Proliferation Assay MTS reagent (3-(4,5-dimethylthiazol-2-yl)-5-(3-carboxymethoxyphenyl)-2-(4-sulfophenyl)-2H-tetrazolium; Promega Corporation, WI, USA) was added to each well at a final concentration of 10% (v/v). Plates were incubated at 37°C for 3 h and the absorbance at 490 nm was measured using a Spectramax spectrophotometer (Molecular Devices, CA, USA). The IC_{50} (dose required to inhibit the metabolic activity of 50% of the cell population) was calculated from logarithmic sigmoidal dose-response curves fitted to the data using GraphPad Prism V7 for Windows (GraphPad Software, CA, USA). The

absorbance readings of wells containing media only were subtracted from sample readings to correct for background absorbance. Data were normalised to absorbance readings for cells treated with PBS only (positive control).

3.2.6 3D multicellular tumour spheroid cytotoxicity assays

MCF-7 or MDA-MB-231 cells were seeded into ultra-low attachment 96-well plates (Sigma-Aldrich, MO, USA) at a density ranging between 625 and 5000 cells per well and incubated at 37°C to promote spheroid formation. Empty and *N*-AI-loaded liposomes were serially diluted in PBS and incubated with cells for up to 96 h (each concentration tested in triplicate). To determine cell viability at the experimental endpoint, an acid phosphatase (APH) assay (Friedrich et al. 2007) or calcein staining (Leary et al. 2016) was performed. For the APH assay, spheroids were carefully washed twice with PBS and the spheroid plate centrifuged at 400 x g for 10 min after each wash step. The supernatant was replaced with 100 µL APH assay buffer (2 mg/mL para-Nitrophenylphosphate and 0.1% (v/v) Triton-X-100 in 0.1 M sodium acetate). The plate was incubated at 37°C for 90 min and then 10 µL 1 M sodium hydroxide was added to each well. The absorbance of each well at 405 nm was then measured using a Spectramax spectrophotometer (Molecular Devices, CA, USA). For calcein staining, calcein-AM (Thermo Fisher Scientific, MA, USA) was added to spheroids at a final concentration of 1 µM per well. The plate was incubated at 37°C for 30 min and images were acquired using an IncuCyte Zoom automated imaging instrument (Essen BioScience, MI, USA), with a 10X objective and green filter (excitation 440-480 nm, emission 504-544 nm) to detect calcein fluorescence associated with viable cells.

3.2.7 Data analysis

All data analysis, including the generation of graphs and statistical tests, was performed using GraphPad Prism software (version 7), unless stated otherwise. Data are presented as the mean ± standard deviation (s.d.) or standard error of the mean (s.e.m.) as stated. Pairwise comparisons were made using Student's t-test and multiple comparisons were made using one-way ANOVA with Tukey's post-test.

3.3 Results

3.3.1 Profiling MCF-7 and MDA-MB-231 cells for uPA/uPAR expression

Two commonly used breast cancer cell lines, MCF-7 and MDA-MB-231, were profiled for cell surface uPA and uPAR expression by flow cytometry prior to liposome testing (Fig. 3.2). MDA-MB-231 cells showed positive expression of uPAR, with a significantly ($P < 0.001$) higher (46-fold) MFI (11.82 ± 0.90) than that of uPAR-negative MCF-7 cells (0.26 ± 0.03). Both cell lines showed positive expression of uPA, with uPA levels significantly ($P < 0.05$) higher (2.7-fold) for MDA-MB-231 cells compared to MCF-7 cells (MFI values of 6.66 ± 0.97 and 2.49 ± 0.10, respectively).

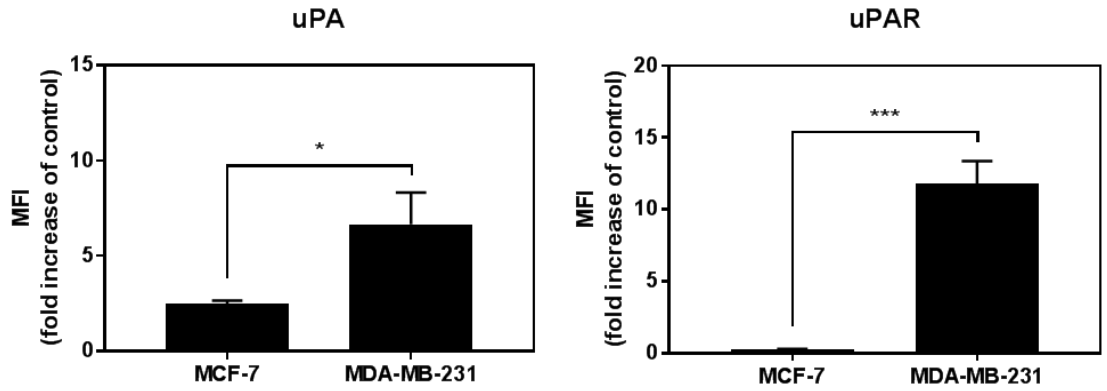

Figure 3.2: Flow cytometry analysis of surface uPA and uPAR expression. MCF-7 cells and MDA-MB-231 cells were incubated with antibodies against human urokinase plasminogen activator (uPA), human uPAR (urokinase plasminogen activator receptor) or an isotype control antibody (IgG) and analysed by flow cytometry to detect fluorescence of Alexa-488-conjugated secondary antibody. MFI = mean fluorescence intensity (fold-increase of IgG control). Data are the mean ± s.d. (n = 3). * = $P < 0.05$; *** = $P < 0.001$.

3.3.2 Measuring cellular uptake of PAI-2 liposomes by flow cytometry

The cellular uptake of fluorescently labelled liposomes can be determined by flow cytometry (Ducat et al. 2011). To decide on an appropriate fluorophore for liposome detection by flow cytometry in subsequent experiments, liposomes loaded with either *N*-AI (in the liposome bilayer) or rhodamine 123 (in the liposome core), as well as FITC-labelled liposomes (FITC-PEG-DSPE incorporated into the liposome bilayer), were incubated with MDA-MB-231 cells at equivalent phospholipid concentrations (20 mM) for 15 min or 60 min before analysis by flow cytometry (Fig. 3.3). Compared to untreated control MDA-MB-231 cells, all fluorescently labelled liposomes showed an increase in

MFI after 15 min and 60 min, although this difference was only significant for R123 liposomes. While the percentage of viable cells remained high after 15 min, the percentage of cells in the viable gate dropped significantly from that of the untreated control cells following the 60 min incubation, with a percentage of 46.8 ± 5.5 %. The drop in cell viability was most pronounced for the *N*-AI and R123 liposomes, with the percentage of viable cells at 60 min dropping to 1.5 ± 0.9 % and 0.07 ± 0.02 %, respectively. The percentage of viable cells for cells treated with FITC-labelled liposomes dropped to 25.6 ± 1.1 % at 60 min, indicating that FITC liposomes were the least cytotoxic to cells out of the three fluorescently labelled liposomes.

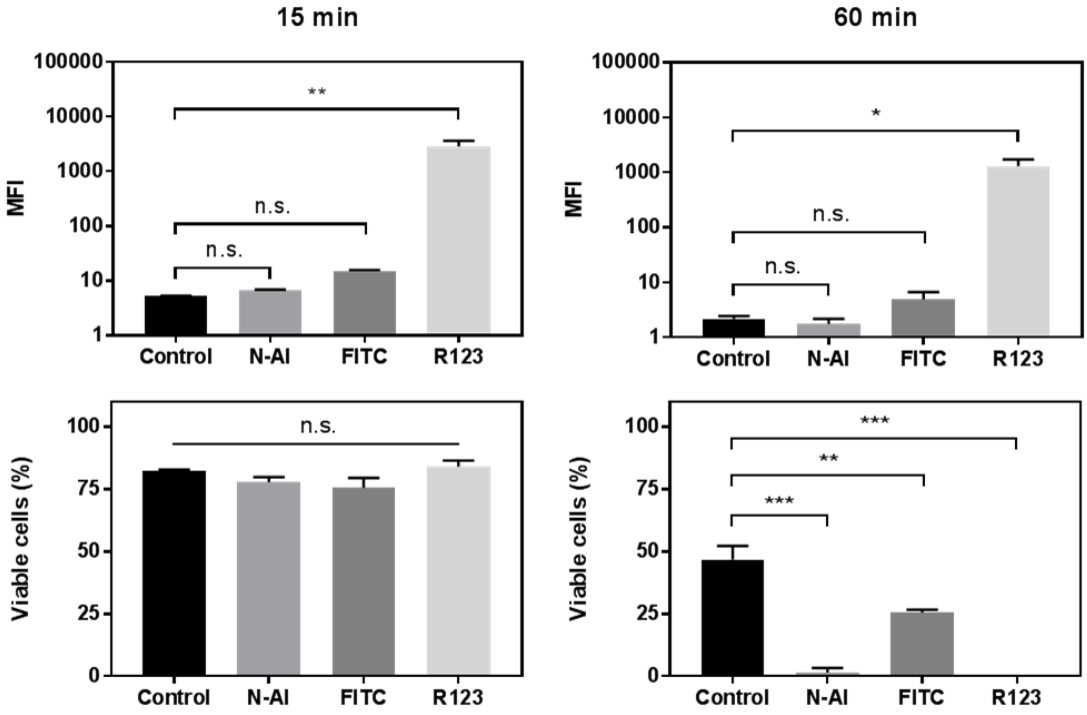

Figure 3.3: Cellular uptake of fluorescently labelled liposomes. Liposomes were fluorescently labelled with either *N*-AI, FITC or R123 and were incubated with MDA-MB-231 cells at an equivalent phospholipid concentration (20 mM) for 15 min (left) or 60 min (right). Cells were analysed by flow cytometry to determine the mean fluorescence intensity (MFI) (top) and percentage of cells within the viable gate (bottom). Control cells were not treated with liposomes. Data are the mean ± s.d. (n = 3). *** = $P < 0.001$, ** = $P < 0.01$, * = $P < 0.05$, n.s. = not significant ($P > 0.05$).

As the FITC-labelled liposomes were shown to be the least cytotoxic to MDA-MB-231 cells at the 60 min time point, FITC-labelled liposomes were further investigated to determine the effect of liposome concentration and incubation time on MFI and on cell viability. FITC-labelled liposomes (or non-FITC control liposomes at an equivalent

phospholipid concentration) were incubated with MDA-MB-231 cells at concentrations between 0 mM and 10 mM for either 15 min or 60 min and analysed by flow cytometry (Fig. 3.4). The results showed a dose-dependent and time-dependent increase in MFI, with significant ($P < 0.05$) increases in MFI between the 15 min and 60 min time points for each concentration of FITC liposome tested. Cell viability was not significantly ($P > 0.05$) different at any FITC liposome concentration after either the 15 min or 60 min incubation, indicating that MDA-MB-231 cells remained viable after 60 min treatment with liposomes up to and including 10 mM concentration.

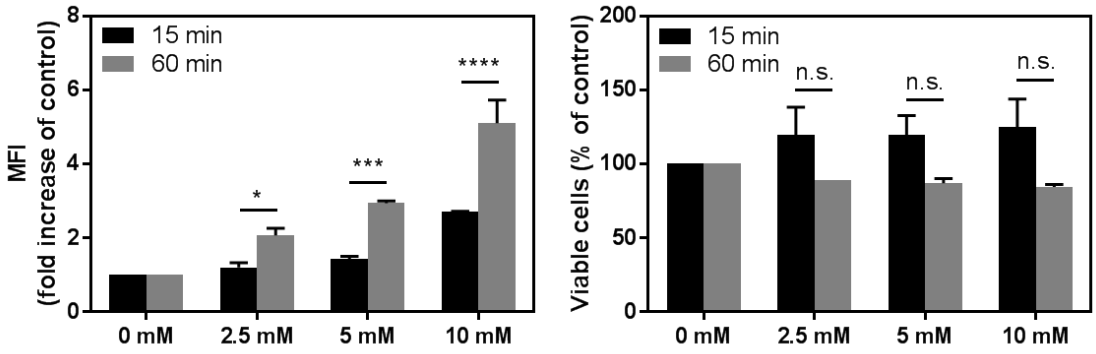

Figure 3.4: Cellular uptake of non-functionalised FITC-labelled liposomes. MDA-MB-231 cells were incubated with FITC-labelled liposomes (or non-FITC control liposomes at an equivalent phospholipid concentration) for 15 min or 60 min and analysed by flow cytometry. Data are the mean ± s.d. (n = 3). MFI = mean fluorescence intensity. **** = $P < 0.0001$, *** = $P < 0.001$, * = $P < 0.05$, n.s. = not significant ($P > 0.05$).

In order to detect differences in the uptake of PAI-2-functionalised liposomes between MCF-7 cells (low uPAR) and MDA-MB-231 cells (high uPAR), non-functionalised (NF) FITC liposomes and PAI-2-functionalised FITC liposomes (152.6 ± 8.7 nm and 152.8 ± 11.7 nm, respectively) were incubated with MCF-7 and MDA-MB-231 cells for 45 min and liposome uptake was determined by flow cytometry (Fig. 3.5). For MDA-MB-231 cells, there was a significant increase in FITC PAI-2 liposome uptake at the 5 mM and 2.5 mM liposome concentrations ($P < 0.0001$ and $P < 0.001$, respectively) relative to NF PAI-2 liposomes, but not at the 1.25 mM liposome concentration. For MCF-7 cells, no significant differences were observed between the uptake of NF and PAI-2 liposomes at any liposome concentrations ($P > 0.05$).

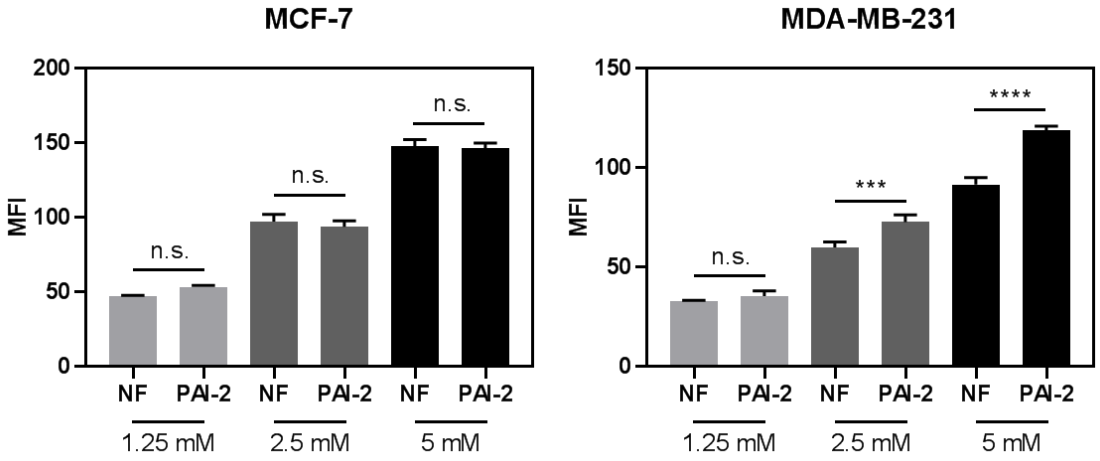

Figure 3.5: Uptake of PAI-2 FITC-labelled liposomes in breast cancer cells. MCF-7 cells (left) and MDA-MB-231 cells (right) were incubated with non-functionalised (NF) FITC liposomes and PAI-2-functionalised (PAI-2) FITC liposomes for 45 min and analysed by flow cytometry. Data are the mean ± s.d. (n = 3). **** = $P < 0.0001$, *** = $P < 0.001$, n.s. = not significant ($P > 0.05$).

3.3.3 Cellular localisation of PAI-2 liposomes by confocal microscopy

Confocal microscopy can be used to detect the uptake and cellular localisation of fluorescently labelled liposomes (Ducat et al. 2011). In initial experiments, 1% and 10% (mol/mol) FITC liposomes were used, but the fluorescent signal was too low (data not shown). Therefore, the intensely fluorescent fluorophore R18 was used to label liposomes for the detectable accumulation of liposomes in cells. Non-functionalised (NF) and PAI-2-functionalised liposomes containing 0.625% (mol %) R18 in the lipid bilayer were prepared as outlined in Chapter 2, Section 2.2. Liposomes were analysed by dynamic light scattering, which revealed average diameters of 131.3 ± 2.5 nm and 131.2 ± 6.6 nm for NF and PAI-2 liposomes, respectively. Liposomes were incubated with MCF-7 and MDA-MB-231 cells at a 2.5 mM phospholipid concentration at 37°C for 60 min prior to imaging by confocal microscopy. Imaging showed a strong fluorescent signal from R18-labelled liposomes, which was present at the cell membrane, within the cytoplasm and within lysosomes (indicated by colocalisation of liposome and LysoTracker) for both cell lines (Fig. 3.6).

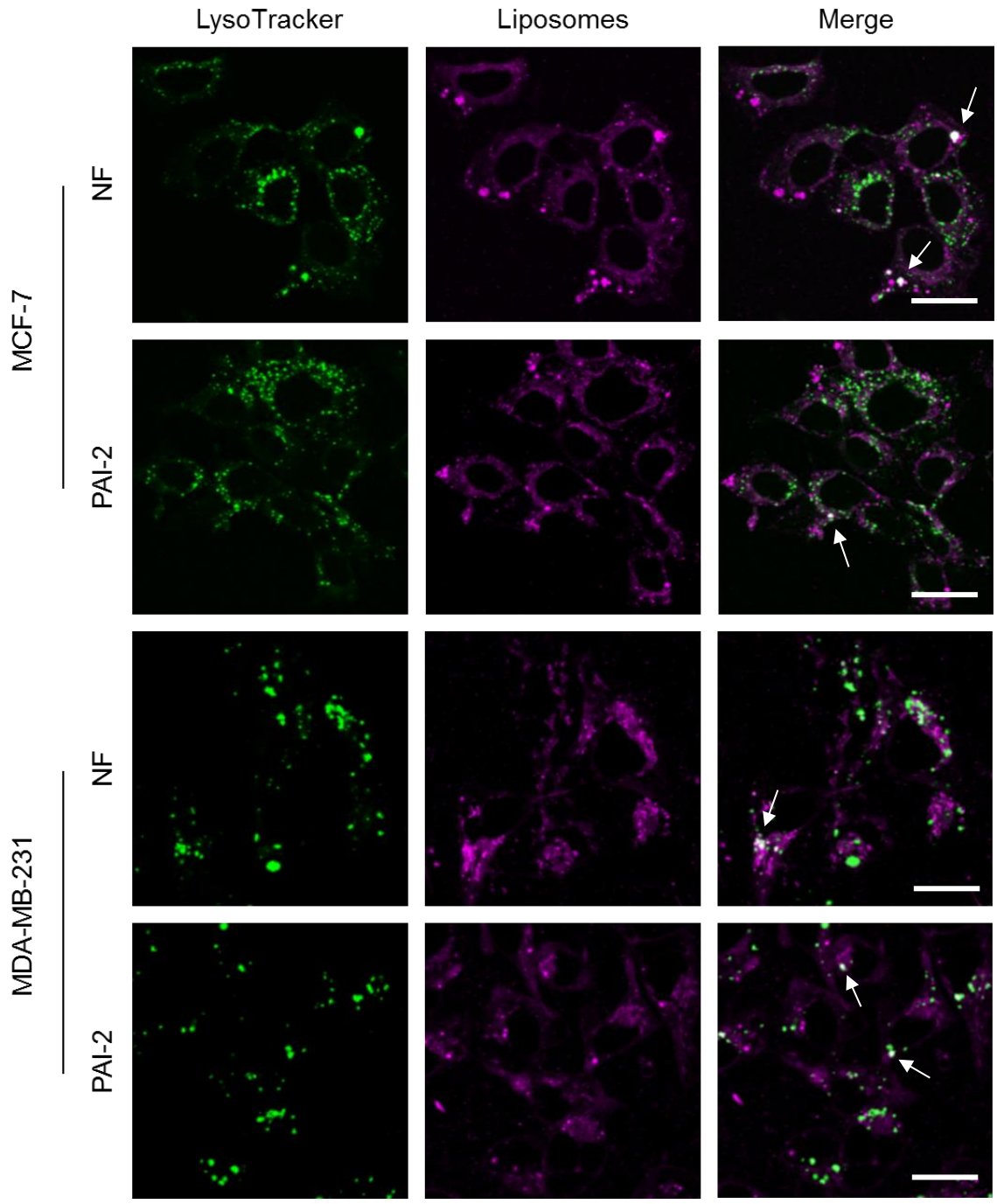

Figure 3.6: Cellular uptake and localisation of R18-labelled liposomes. Non-functionalised (NF) and PAI-2-functionalised (PAI-2) liposomes were labelled with octadecyl rhodamine B chloride (R18) and incubated with cells at a liposome concentration of 2.5 mM for 1 h. LysoTracker green was added immediately prior to imaging via confocal microscopy to visualise lysosomes. Arrows indicate white foci which indicate colocalisation of green and magenta signals. Representative images are shown. Scale bars are 25 µm.

3.3.4 Cytotoxicity of *N*-AI PAI-2 liposomes against breast cancer cells

To determine the cytotoxicity of *N*-AI-loaded PAI-2-functionalised (*N*-AI PAI-2) liposomes against breast cancer cells *in vitro*, *N*-AI PAI-2 liposomes and empty (EMP) PAI-2 liposomes at an equivalent phospholipid concentration were tested against MCF-7 and MDA-MB-231 cells. Treatment with *N*-AI PAI-2 liposomes showed changes in cell morphology for both cell lines, consistent with intracellular delivery of the cytotoxic *N*-AI (Fig. 3.7). Treatment with EMP PAI-2 liposomes did not induce a change in cell morphology in either cell line. After incubating EMP PAI-2 liposomes or *N*-AI PAI-2 liposomes with MCF-7 and MDA-MB-231 cells for a period of 72 h, an endpoint MTS cell viability assay showed a dose-dependent cytotoxic effect of the *N*-AI PAI-2 liposomes against both cell lines. The cytotoxic effect of *N*-AI PAI-2 liposomes against MDA-MB-231 cells (IC_{50} of 5.40 ± 1.14 µM) was significantly greater ($P < 0.01$) than that against MCF-7 cells (IC_{50} of 31.84 ± 8.20 µM). EMP PAI-2 liposomes did not elicit a dose-dependent cytotoxic response but showed some degree of cytotoxicity in both cell lines at the highest liposome concentrations tested.

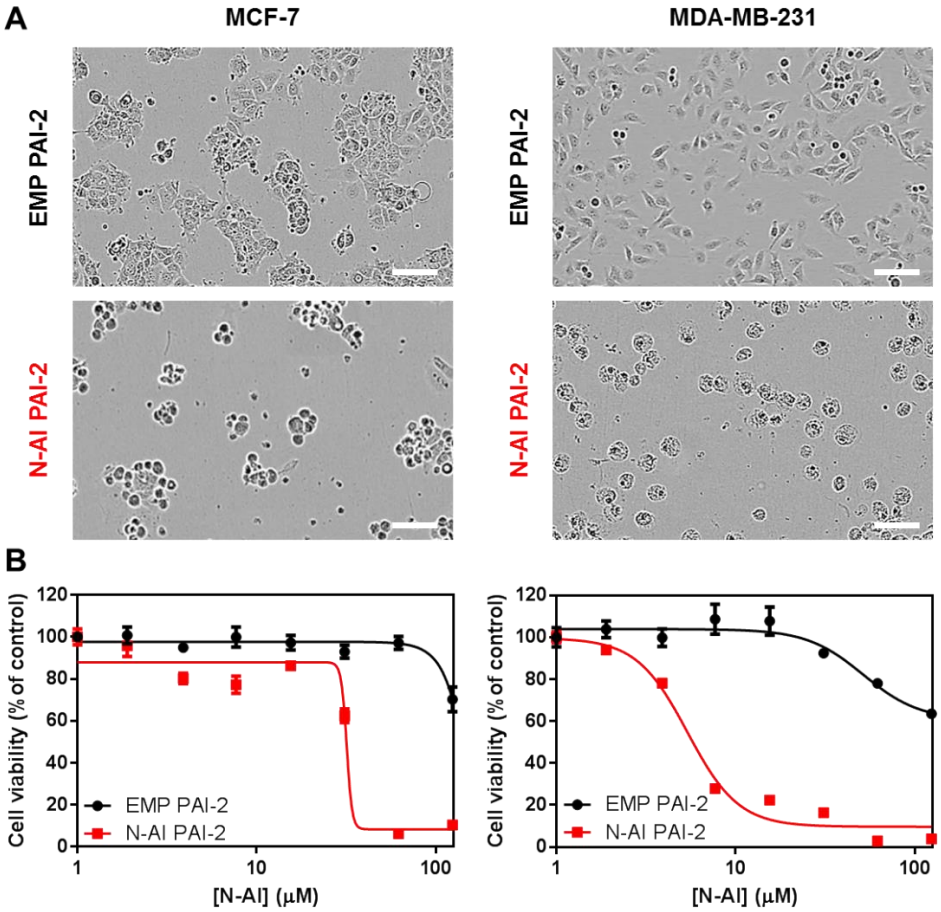

Figure 3.7: Cytotoxicity of *N*-AI PAI-2 liposomes. *In vitro* cytotoxicity testing of empty (EMP) PAI-2 liposomes and *N*-AI PAI-2 liposomes against MCF-7 (low uPAR) and MDA-MB-231 (high uPAR) breast cancer cell lines. (**A**) Representative images showing changes in cell growth and morphology 72 h after treatment with liposomes at 62.0 μM *N*-AI or equivalent phospholipid concentration (scale bars are 100 μm). (**B**) Dose-response cell viability curves via MTS assay at 72 h post-treatment. Data are the mean ± s.d. (n = 3).

3.3.5 Cytotoxicity of *N*-AI PAI-2 liposomes against breast cancer spheroids

A range of cancer cell lines have been reported to spontaneously form spheroids under low-attachment growth conditions (Friedrich et al. 2009). To determine whether MCF-7 and MDA-MB-231 cells could form multicellular tumour spheroids for testing of *N*-AI PAI-2 liposomes, MCF-7 and MDA-MB-231 cells were seeded into ultra-low attachment 96-well plates at 5000, 2500, 1250 or 625 cells per well. Cells were incubated at 37°C for 5 days and bright-field images acquired every 24 h (Fig. 3.8). Imaging revealed that both MCF-7 and MDA-MB-231 cells formed spheroids at all cell densities tested and spheroid diameter at each cell density was comparable between the two cell lines. There were notable differences in spheroid morphology between the two cell lines. MCF-7 cells

formed tight spheroids with well-defined edges and high circularity compared to MDA-MB-231 spheroids, which appeared looser with less definition of the spheroid surface. At 48 h post-cell seeding, the average spheroid diameters for 5000 cells were 488.0 ± 11.3 µm and 484.3 ± 9.3 µm for MCF-7 and MDA-MB-231 cells, respectively. For 625 seeded cells at 48 h, the average spheroid diameters were 285.0 ± 7.6 µm and 230 ± 22.1 µm for MCF-7 and MDA-MB-231 cells, respectively. Spheroid diameter measurements revealed that MCF-7 spheroids continued to grow in diameter in a linear fashion over the experiment. In contrast, MDA-MB-231 spheroid growth was less rapid at the higher cell densities tested, and an initial decrease in diameter of the MDA-MB-231 spheroids coincided with the observed slower spheroid formation relative to MCF-7 spheroids.

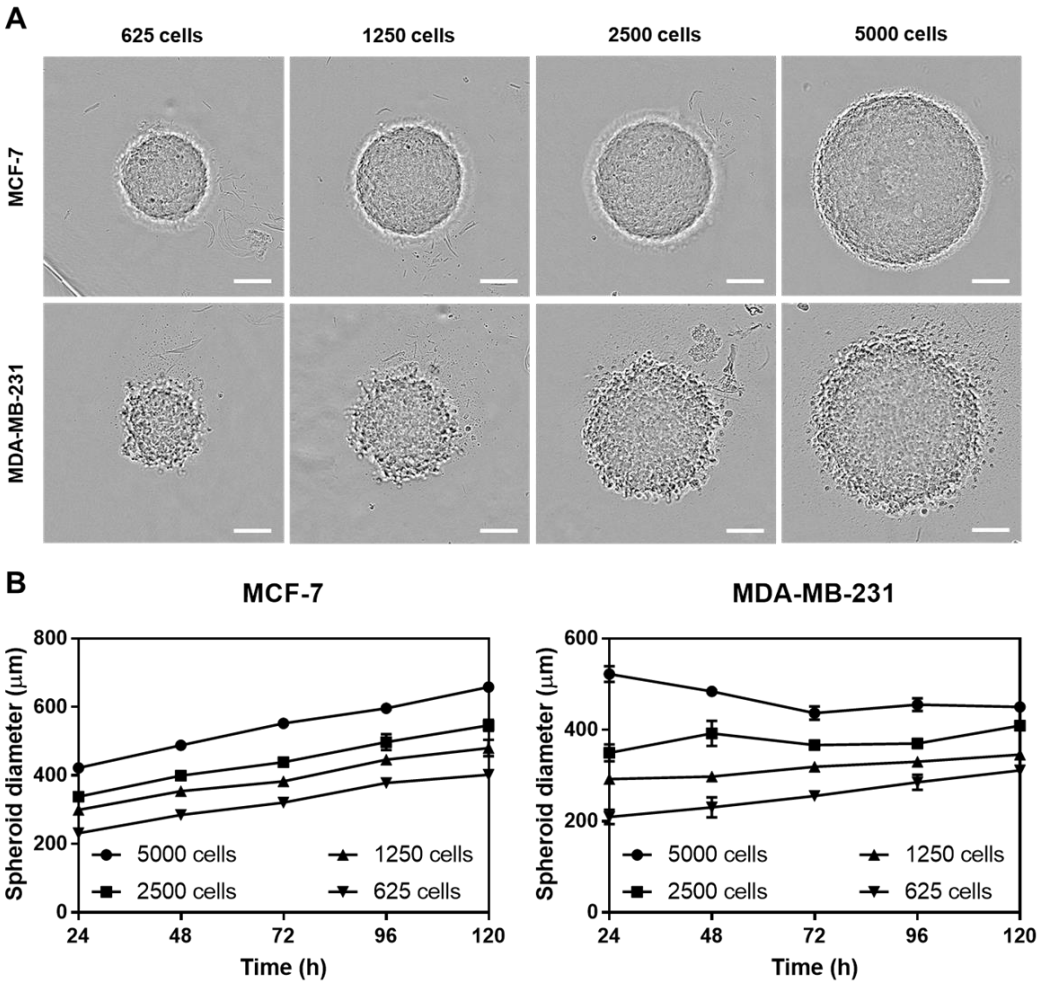

Figure 3.8: Cell titre for establishing breast tumour spheroids. MCF-7 and MDA-MB-231 cells were seeded at different cell densities (5000, 2500, 1250 and 625 cells per well) to optimise conditions for growing spheroids. Spheroids were imaged using light microscopy. (**A**) Representative spheroid images at 48 h post-cell seeding (once all wells had formed spheroids). Scale bars are 100 µm. (**B**) Spheroid diameter measurements for MCF-7 and MDA-MB-231 spheroids over time. Graphs are representative from two experimental repeats. Presented data are the mean ± s.d. (n = 3).

Once MCF-7 and MDA-MB-231 cells were confirmed to form spheroids, cells were seeded in ultra-low attachment 96-well plates at a density of 1000 cells per well and incubated at 37°C for 48 h to promote the formation of multicellular tumour spheroids prior to liposome testing. As per Section 3.3.4, EMP PAI-2 and *N*-AI PAI-2 liposomes at equivalent phospholipid concentrations were incubated with the preformed spheroids at 37°C for a period of 72 h, with spheroids imaged every 24 h (Fig. 3.9). MCF-7 and MDA-MB-231 spheroids treated with *N*-AI PAI-2 liposomes showed a time-dependent and concentration-dependent dissemination of the spheroid structure, with the complete destruction of the spheroid by 96 h at *N*-AI concentrations above 62.5 µM for both cell lines. At the 24 h time point, MDA-MB-231 spheroids treated with *N*-AI PAI-2 liposomes appeared to be more greatly dissociated than MCF-7 spheroids. In contrast, MCF-7 and MDA-MB-231 spheroids treated with EMP liposomes showed continued growth and an increase in spheroid diameter over time.

At the experiment endpoint, an acid phosphatase assay was used to measure the metabolic activity of the cells comprising the spheroids to determine the cytotoxic effect of the EMP PAI-2 and *N*-AI PAI-2 liposomes after 72 h. The assay confirmed the cytotoxicity of the *N*-AI PAI-2 liposomes on these spheroids in a dose-dependent manner, and also for the EMP PAI-2 liposomes (Fig. 3.10). The IC_{50} values for *N*-AI PAI-2 liposomes tested against MCF-7 and MDA-MB-231 spheroids were 30.9 ± 5.4 µM and 59.3 ± 7.5 µM, respectively, and significantly different ($P < 0.01$). IC_{50} values for EMP PAI-2 liposomes could not be determined as sigmoidal dose-response curves could not be fitted to the data, but the trends indicated a dose-dependent decrease in cell viability with empty liposome concentrations equal to and greater than a phospholipid concentration of 375 µM.

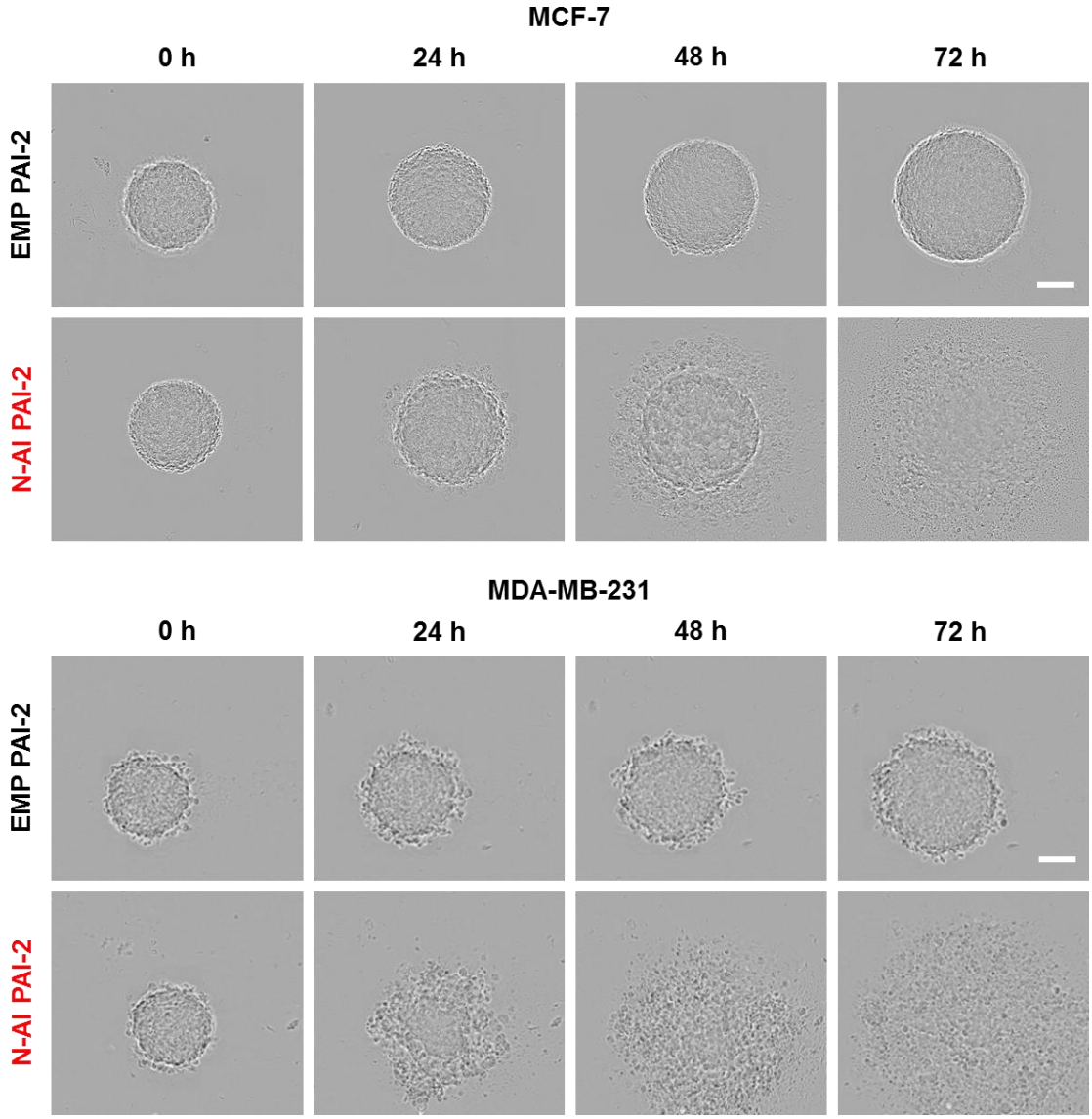

Figure 3.9: Imaging of breast cancer spheroids treated with *N*-AI PAI-2 liposomes. Testing of empty (EMP) PAI-2 and *N*-AI PAI-2 liposomes against MCF-7 and MDA-MB-231 multicellular tumour spheroids over a period of 72 h at 62.0 µM *N*-AI or equivalent phospholipid concentration. Representative images were captured at the same magnification (n = 3). Scale bars are 100 µm.

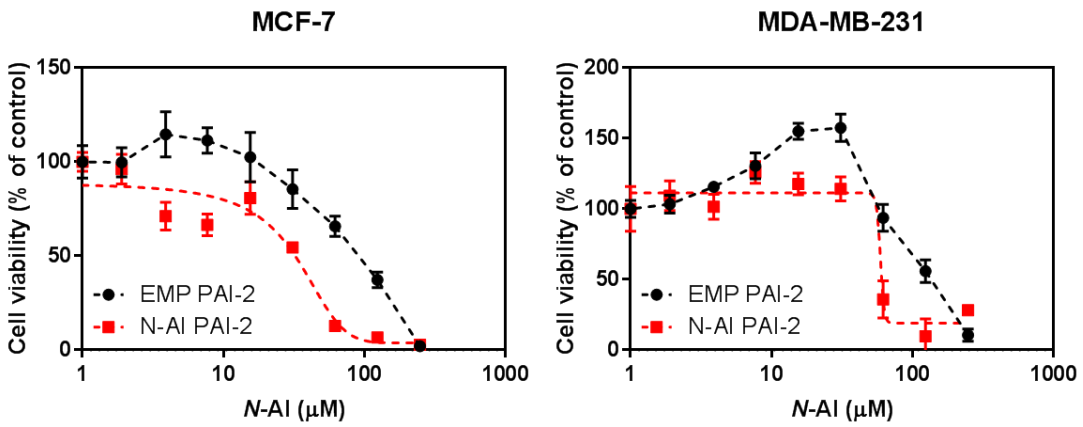

Figure 3.10: Cytotoxic effect of *N*-AI PAI-2 liposomes on breast cancer spheroids. Empty (EMP) PAI-2 liposomes and *N*-AI PAI-2 liposomes were tested against MCF-7 and MDA-MB-231 multicellular tumour spheroids over a period of 72 h. An endpoint acid phosphatase assay was used to determine cell viability. Data are the mean ± s.d. (n = 3).

As the 2D and 3D cell testing revealed a cytotoxic effect of EMP PAI-2 liposomes at high phospholipid concentrations, additional testing was conducted using non-functionalised liposomes alongside PAI-2-functionalised liposomes at equivalent phospholipid concentrations. MCF-7 and MDA-MB-231 spheroids were treated with empty liposomes (EMP), empty PAI-2-functionalised liposomes (EMP PAI-2), *N*-AI-loaded liposomes (*N*-AI) and *N*-AI-loaded PAI-2-functionalised liposomes (*N*-AI PAI-2) for 96 h. Images indicated that *N*-AI and *N*-AI PAI-2 liposomes showed similar effects on spheroid morphology, with destruction of the spheroid structure at the experimental endpoint (Fig. 3.11). EMP and EMP PAI-2 liposomes had a similar effect on spheroids.

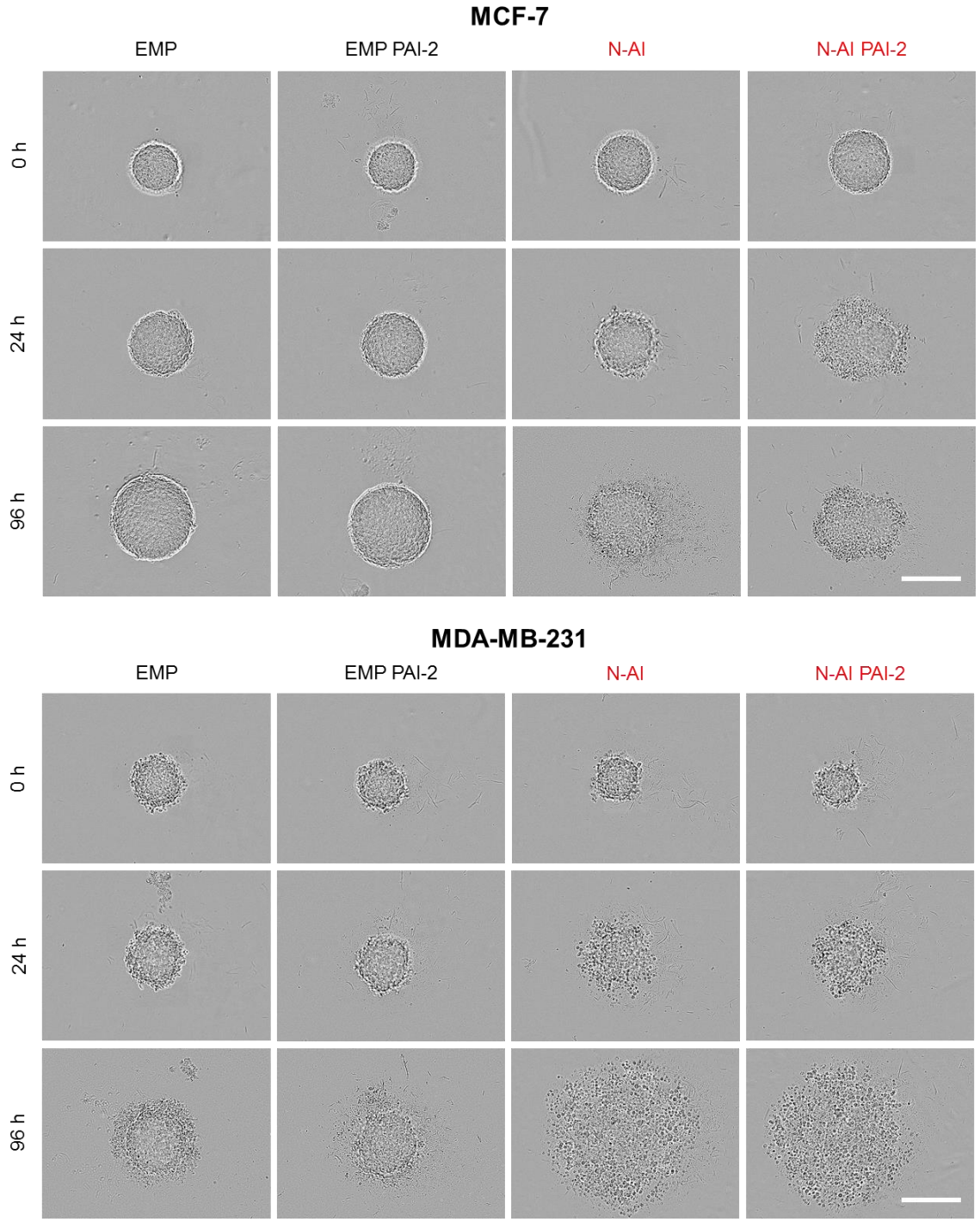

Figure 3.11: Morphological effect of *N*-AI PAI-2 liposomes on spheroids. Testing of empty (EMP), empty PAI-2 (EMP PAI-2), *N*-AI and *N*-AI PAI-2 liposomes against MCF-7 and MDA-MB-231 multicellular tumour spheroids over a period of 96 h. Representative images (n = 3) of treatment with 25 µM *N*-AI liposomes (or empty liposomes at equivalent phospholipid concentration). All images were captured at the same magnification. Scale bar is 100 µm.

Spheroid diameter was measured every 24 h where spheroids were still intact and had a distinct border (Fig. 3.12). Relative to control (untreated) spheroids, MCF-7 and MDA-

MB-231 spheroids showed a stable or slight increase in diameter over 96 h when treated with EMP or EMP PAI-2 liposomes. For MCF-7 spheroids, a time-dependent decrease in diameter was observed with treatment of 6.25 µM *N*-AI or *N*-AI PAI-2 liposomes. For MDA-MB-231 spheroids, there was no trend of diameter decrease for spheroids treated with 6.25 µM *N*-AI or *N*-AI PAI-2 liposomes. At the 24 h time point, there was a significant ($P < 0.01$) difference in diameter for MDA-MB-231 spheroids treated with *N*-AI PAI-2 liposomes (74.5 ± 3.4 µm) relative to *N*-AI liposomes (91.8 ± 5.1 µm). Significant differences in diameter between *N*-AI and *N*-AI PAI-2 liposomes were not observed at any other time points at the 6.25 µM *N*-AI concentration, and no significant differences were observed at any time points for MCF-7 spheroids.

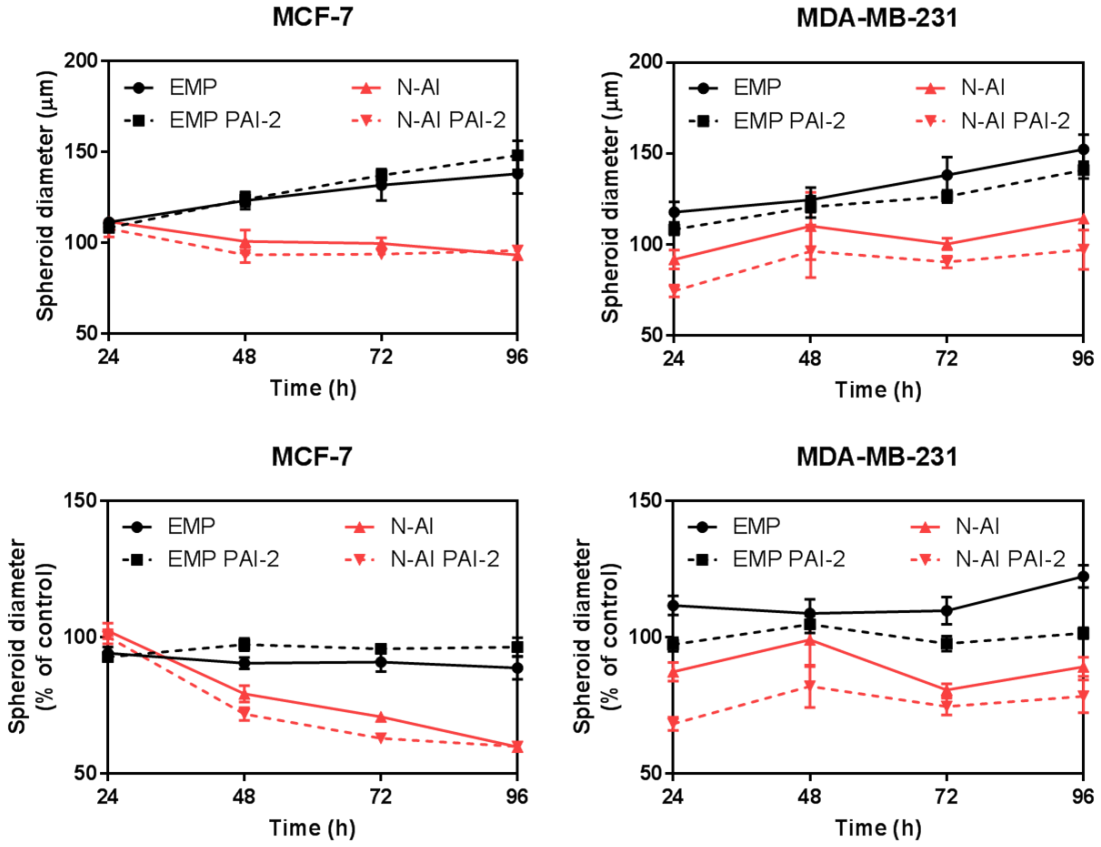

Figure 3.12: Diameter of liposome-treated breast cancer spheroids over 96 hours. MCF-7 spheroids and MDA-MB-231 spheroids were treated with empty (EMP) liposomes, empty PAI-2-functionalised (EMP PAI-2) liposomes, *N*-AI-loaded (*N*-AI) liposomes and *N*-AI-loaded PAI-2-functionalised (*N*-AI PAI-2) liposomes for 96 h. Images were taken every 24 h and spheroid diameter measured at each time point. Data are shown for treatment with a 6.25 µM concentration of liposomal *N*-AI (or equivalent liposome phospholipid concentration for empty liposomes). Data are means ± s.d. (n = 3).

To determine the viability of the spheroids at the experimental endpoint, spheroids were incubated with calcein-AM at the 96 h time point and imaged to detect calcein fluorescence (Fig. 3.13). Images indicated a change in cell viability across the different liposome concentrations tested, with disseminated but viable clusters of MCF-7 and MDA-MB-231 cells after treatment with 100 µM *N*-AI or *N*-AI PAI-2 liposomes. EMP and EMP PAI-2 liposomes at an equivalent phospholipid concentration also showed noticeable changes in the distribution of calcein staining for both cell lines.

Dose-response curves derived from the calcein staining revealed similar trends between *N*-AI and *N*-AI PAI-2 liposomes for both cell lines, with no significant difference between the two liposome treatments (Fig. 3.14). The IC_{50} values for both *N*-AI and *N*-AI PAI-2 liposomes were not significantly different between MCF-7 and MDA-MB-231 spheroids (Table 3.1). The IC_{50} value for spheroids treated with EMP PAI-2 liposomes was significantly ($P < 0.05$) lower for MCF-7 cells (80.3 ± 7.2 µM) relative to MDA-MB-231 cells (105.6 ± 12.3 µM).

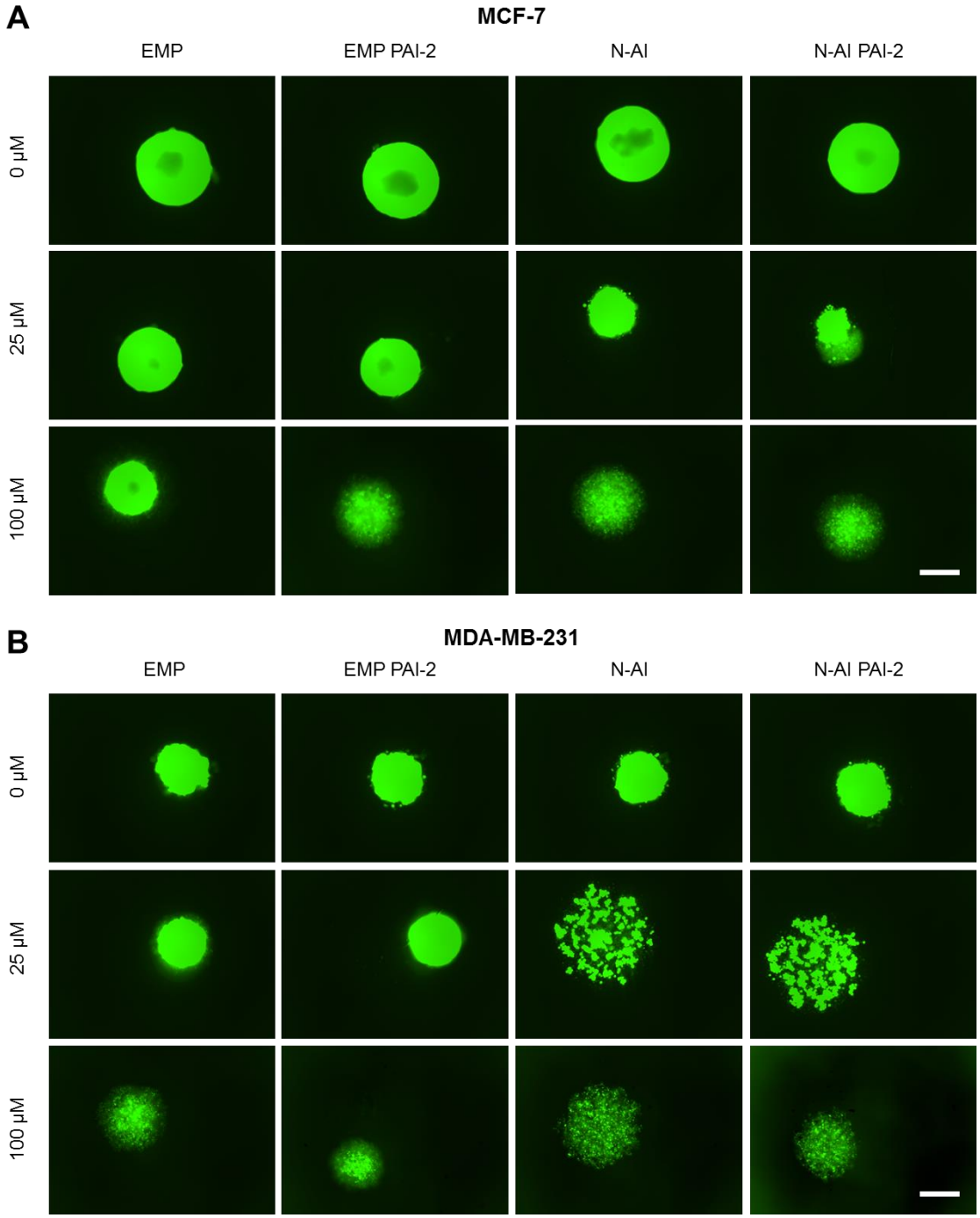

Figure 3.13: Calcein imaging of liposome-treated breast cancer spheroids. (**A**) MCF-7 spheroids and (**B**) MDA-MB-231 spheroids were treated with empty (EMP) liposomes, empty PAI-2-functionalised (EMP PAI-2) liposomes, *N*-AI-loaded (*N*-AI) liposomes and *N*-AI-loaded PAI-2-functionalised (*N*-AI PAI-2) liposomes for 96 h. Calcein-AM was added to spheroids to visualise viable cells. Images are representative of triplicate samples of liposomes tested at three different concentrations (0, 25 or 100 µM *N*-AI, or empty liposomes at equivalent phospholipid concentration). Scale bars are 100 µm.

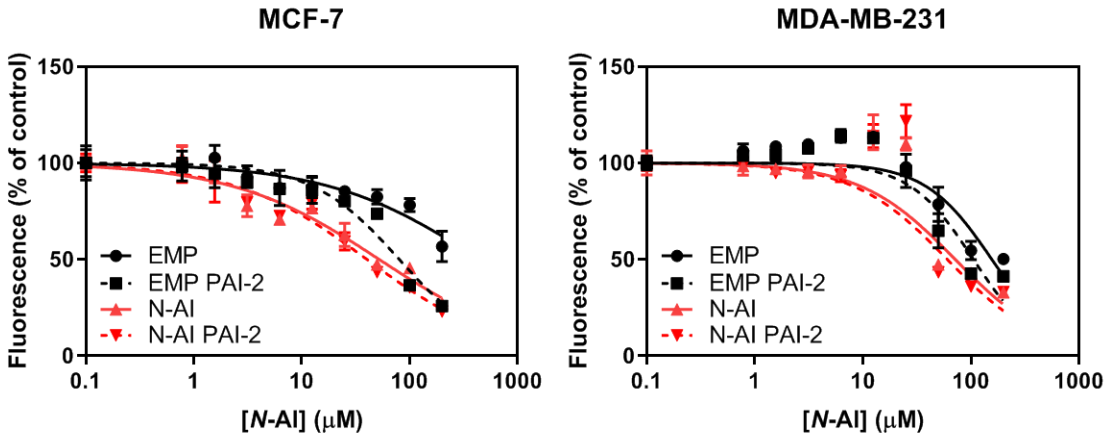

Figure 3.14: Calcein viability of liposome-treated breast cancer spheroids. MCF-7 spheroids and MDA-MB-231 spheroids were treated with empty (EMP) liposomes, empty PAI-2-functionalised (EMP PAI-2) liposomes, *N*-AI-loaded (*N*-AI) liposomes and *N*-AI-loaded PAI-2-functionalised (*N*-AI PAI-2) liposomes for 96 h. Calcein-AM was added to spheroids to visualise viable cells. Data are green fluorescence intensity means ± s.d. (n = 3).

Table 3.1: IC_{50} values for liposome-treated breast cancer spheroids. MCF-7 spheroids and MDA-MB-231 spheroids were treated with empty (EMP) liposomes, empty PAI-2-functionalised (EMP PAI-2) liposomes, *N*-AI-loaded (*N*-AI) liposomes and *N*-AI-loaded PAI-2-functionalised (*N*-AI PAI-2) liposomes for 96 h. Calcein-AM was added to spheroids to visualise viable cells. Total fluorescence was used to determine viability and IC_{50} values (μM). Data are means ± s.d. (n = 3). * = $P < 0.05$ (relative to MCF-7 EMP PAI-2 value).

	EMP	**EMP PAI-2**	***N*-AI**	***N*-AI PAI-2**
MCF-7	not reached	80.3 ± 7.2	52.2 ± 6.2	40.2 ± 4.0
MDA-MB-231	156.1 ± 20.5	105.6 ± 12.3*	71.5 ± 7.6	60.4 ± 7.1

3.4 Discussion

Determining the *in vitro* properties of novel nanotherapies using cell-based models is important for initially evaluating the cellular effects of a nanoparticle formulation before proceeding to *in vivo* studies. In this chapter, the cellular uptake, localisation and cytotoxicity of *N*-AI-loaded PAI-2-functionalised (*N*-AI PAI-2) liposomes were determined using two breast cancer cell lines that vary in their expression of cell surface uPAR. PAI-2-functionalised liposomes showed a significantly greater uptake than non-functionalised (NF) liposomes in MDA-MB-231 cells (uPAR-positive) but not in MCF-7 cells (uPAR-negative). Confocal microscopy revealed uptake of both NF and PAI-2 liposomes into both cell lines, with localisation in the cytoplasm and some accumulation within lysosomes. *N*-AI PAI-2 liposomes showed a significantly increased cytotoxic

effect against MDA-MB-231 cells compared to MCF-7 cells after 72 h when grown in 2D culture. *N*-AI PAI-2 liposomes were also cytotoxic to MCF-7 and MDA-MB-231 multicellular tumour spheroids, resulting in dissemination of the 3D structure and cytotoxic effect, but with no significant differences in IC_{50} between the two cell lines after 96 h. Collectively, the results presented in this chapter form a basis for understanding the *in vitro* properties of *N*-AI PAI-2 liposomes to guide further *in vivo* evaluation.

As reported previously, uPA and uPAR expression is low in MCF-7 cells and high in MDA-MB-231 cells (Huber et al. 2016; Ma et al. 2001). The profiling results in this chapter corroborated this, with MDA-MB-231 cells showing significantly greater uPAR expression than MCF-7 cells and the IgG control (Fig. 3.2). This difference in uPAR expression was associated with a significant increase in fluorescently labelled PAI-2 liposome uptake relative to non-functionalised liposomes by MDA-MB-231 cells, but not by MCF-7 cells (Fig. 3.5). In these experiments, FITC-labelled empty liposomes were used as *N*-AI is slightly fluorescent (Fig. 3.3) and empty liposomes do not have a significantly different size or surface charge as compared to *N*-AI-loaded liposomes (Chapter 2, Section 2.3.1). In addition, both *N*-AI (Vine et al. 2016) and rhodamine-123 (Krag et al. 1989) have been shown to be cytotoxic against tumour cells, and this was observed as a decrease in the viable cell population after 60 min treatment with *N*-AI and R123-loaded liposomes by flow cytometry (Fig. 3.3). This cytotoxic profile of *N*-AI and R123 make their use in uptake studies unfavourable. In contrast to *N*-AI and R123 liposomes, FITC-labelled liposomes did not have a strong cytotoxic effect against MDA-MB-231 cells at a 20 mM phospholipid concentration, and FITC liposomes at 10 mM did not show a significant decrease in cell viability after incubation with cells for 60 min (Fig. 3.4). Therefore, this fluorophore was chosen to label liposomes for subsequent flow cytometry experiments.

Liposomes can be taken into cells via several different mechanisms, including adsorption, lipid exchange, intracellular membrane fusion and receptor-mediated endocytosis (RME) (Ducat et al. 2011). The presence of a fluorescent signal from cells treated with non-functionalised (NF) fluorescently labelled liposomes (Fig. 3.3) indicates that NF liposomes were taken up by cells, most likely by fusion or other non-specific mechanisms, rather than by RME. In contrast, the uptake of PAI-2 liposomes by MDA-MB-231 cells

was greater than the uptake of NF liposomes in MDA-MB-213 cells (Fig. 3.5). As the average liposome diameters of the FITC-labelled NF and PAI-2 liposomes were equivalent (152.6 ± 8.7 nm and 152.8 ± 11.7 nm, respectively), this difference in uptake is likely due to the presence of PAI-2 at the liposome surface and interaction with uPA/uPAR overexpressed on the surface of MDA-MB-231 cells. Competition binding studies using excess PAI-2 or uPAR antibody could be used to further confirm this (Willis & Forssen 1998; Xiao et al. 2011).

Confocal microscopy indicated that both NF and PAI-2 liposomes were internalised by MCF-7 and MDA-MB-231 cells, which further supports the above flow cytometry uptake results. Colocalisation of liposome signal with lysosomes in both cell lines confirmed that liposomes were internalised by cells and accumulated in lysosomes, in addition to being present elsewhere in the cell (Fig. 3.6). The R18 signal was also observed at the cell membrane and within the cytoplasm, with the dispersed signal suggesting that some degree of liposome fusion with the cell membrane occurred. This is not an unexpected result given that the liposomes were incubated with cell monolayers at a high liposome concentration, making it likely that liposomes in solution will passively fuse with cells over time (Ducat et al. 2011). Collectively, the results indicate that NF and PAI-2 liposomes are taken into cells by fusion and potentially also by RME in the case of PAI-2 liposomes. This could be further explored by using inhibitors of endocytosis to elucidate mechanisms of liposome uptake (Lu et al. 2017; Un et al. 2012).

The work presented in this chapter highlights the need for adequate characterisation of liposome ligand density to guide and interpret *in vitro* uptake experiments. For example, for the *N*-AI PAI-2 liposome formulation, the exact number of PAI-2 ligands present at the liposome surface and the proportion of liposomes that have one or more PAI-2 ligands attached for cell binding is unknown. These factors will affect how the liposome formulation behaves *in vitro*. Previous studies have demonstrated that modulating the liposome ligand density by changing the starting maleimide-PEG concentration of the formulation affects cellular binding and uptake (Chu et al. 2016; Gayong et al. 2016; Li, H et al. 2016). As discussed in Chapter 2, Section 2.4, robust methods to quantify the number of ligands present at the liposome surface are needed in order to optimise ligand density for cell uptake and functional effect. Chapter 5 reports a novel single-molecule

fluorescence microscopy method to quantify liposome ligand density, which could be used in future experiments to determine the optimal number of ligands for maximal receptor binding, cellular uptake and therapeutic effect (Belfiore, Lisa et al. 2018).

In the cytotoxicity testing against breast cancer cells grown as monolayers, *N*-AI PAI-2 liposomes showed a dose-dependent cytotoxic effect that was significantly ($P < 0.01$) more potent against MDA-MB-231 cells compared to MCF-7 cells, with IC_{50} values of 5.40 ± 1.14 µM and 31.84 ± 8.20 µM, respectively. This appears to indicate PAI-2-mediated targeting and an increased cytotoxic effect of PAI-2-functionalised liposomes against uPAR-positive MDA-MB-231 cells (Fig. 3.7), which correlates with the flow cytometric uptake data showing increased uptake of PAI-2 liposomes relative to NF liposomes in MDA-MB-231 cells (Fig. 3.5). The less potent but still cytotoxic effect of *N*-AI PAI-2 liposomes against the uPAR-negative MCF-7 cells indicates that the liposomes were still taken up by cells via receptor-independent pathways in this cell line, which correlates with the flow cytometry and confocal microscopy findings (Fig. 3.6). In addition, EMP PAI-2 liposomes showed a cytotoxic effect against both cell lines at the highest liposome concentrations tested, which is likely due to empty liposomes fusing with cell membranes at high concentrations, resulting in cell lysis (Lu et al. 2017).

In the multicellular tumour spheroid experiments, imaging of spheroids over the course of the experiment indicated a concentration-dependent and time-dependent destruction of both MCF-7 spheroids and MDA-MB-231 spheroids when treated with *N*-AI PAI-2 liposomes (Fig. 3.9). Treatment with EMP PAI-2 liposomes did not result in morphological changes to the spheroid structure. However, the effect of EMP PAI-2 liposomes on the viability of cells grown in 3D appeared to be greater than that observed in the 2D experiments. EMP PAI-2 liposomes showed a dose-dependent cytotoxic effect against both cell lines grown as spheroids, as revealed by an acid phosphatase (APH) endpoint viability assay (Fig. 3.10). To determine whether this effect was due to the phospholipid concentration or the presence of PAI-2 at the liposome surface, both EMP (non-functionalised) and EMP PAI-2 liposomes were tested against MCF-7 and MDA-MB-231 spheroids in a subsequent experiment, which revealed similar effects (Fig. 3.11). An endpoint calcein viability stain revealed that the IC_{50} of spheroids treated with EMP PAI-2 was significantly ($P < 0.05$) lower for MCF-7 spheroids (80.3 ± 7.2 µM) relative

to MDA-MB-231 spheroids (105.6 ± 12.3 μM), but no significant differences in IC_{50} were observed for the other liposome treatments (Table 3.1).

MCF-7 and MDA-MB-231 cells have been previously shown to form spheroids, with the former developing into compact and highly rounded spheroids, and the latter forming looser spheroid structures (Ivascu & Kubbies 2007). Similar findings were observed in the cell titre experiment reported in this chapter (Fig. 3.8), with phase-contrast imaging revealing that MCF-7 spheroids formed tighter and more circular spheroids, whereas MDA-MB-231 spheroids appeared looser and less defined, despite both cell lines forming spheroids of similar diameters. This difference in spheroid morphology was further highlighted by the calcein imaging of spheroids (Fig. 3.13). Untreated MCF-7 spheroids showed a decrease in fluorescence at the spheroid centre, indicative of a necrotic core with few viable cells (Fig. 3.1). In contrast, untreated MDA-MB-231 spheroids were smaller than MCF-7 spheroids and did not show evidence of a necrotic core via calcein imaging. These observed differences in spheroid morphology may have effects on liposome penetration and drug performance (Ivascu & Kubbies 2007). While MDA-MB-231 spheroids treated with *N*-AI PAI-2 liposomes showed greater destruction of the spheroid architecture than MCF-7 spheroids at the 24 h time point (Fig. 3.9), this increased spheroid dissociation did not correlate with an increased cytotoxic effect (Fig. 3.11). The increased destructive effect may be the result of the weaker cell-cell junctions that hold the spheroid together, as reported previously for MDA-MB-231 spheroids (Ivascu & Kubbies 2007). In order to negate the effect of these inherent differences between breast cancer cell lines, it would be advantageous to generate a stably transfected cell line that overexpresses uPAR, or a knockout of a uPAR overexpressing line, and compare spheroid testing with the parent cell line (Moirangthem et al. 2016).

The APH and calcein viability assays revealed an increase in MDA-MB-231 viability above untreated control spheroids at mid-range liposome concentrations. At lower *N*-AI concentrations, it appears that the liposomes did not kill the majority of MDA-MB-231 cells, but reduced the integrity of the spheroid. It is possible that these cells were still able to proliferate in small clusters of the aggregate and remained viable even though the spheroid was no longer intact. This light microscopy imaging of spheroids treated with liposomes (Fig. 3.11) appears to indicate that the cells are not viable, but the calcein

imaging at the experimental endpoint (Fig. 3.14) reveals that viable cell clusters are present for MDA-MB-231 spheroids treated with liposomes at a 25 µM *N*-AI concentration. Therefore, at lower *N*-AI concentrations, there may have been a greater number of viable cells than in the untreated spheroids, since the cells were more spread out and cell proliferation was not slowed down by the spheroid growing larger in size.

There was a high degree of corroboration between the APH assay and calcein-AM staining in the determination of IC_{50} values for *N*-AI PAI-2 liposomes tested against MCF-7 spheroids and MDA-MB-231 spheroids. The IC_{50} values for MCF-7 spheroids treated with *N*-AI PAI-2 liposomes were 30.9 ± 5.4 µM (APH assay) and 40.2 ± 4.0 µM (calcein staining). The IC_{50} values for MDA-MB-231 spheroids treated with *N*-AI PAI-2 liposomes were 59.3 ± 7.5 µM (APH assay) and 60.4 ± 7.1 µM (calcein staining). While the 2D testing indicated that *N*-AI PAI-2 liposomes are approximately 6-fold more potent against MDA-MB-231 cells relative to MCF-7 cells, the 3D testing did not reveal a significant difference in potency for *N*-AI PAI-2 liposomes between the two cell lines (Fig. 3.7). The observed differences in IC_{50} values between 2D and 3D testing is not unexpected given the different pathways of liposome diffusion and uptake by cells grown in 2D versus 3D (Katt et al. 2016), and the reported differences in cell morphology and gene expression in 2D versus 3D cultures that can result in different responses to drug treatment (Kenny et al. 2007). For example, the sensitivity of breast cancer cells to trastuzumab, pertuzumab and lapatinib changes depending on whether the cells are grown as 2D or 3D cultures (Weigelt et al. 2010), and the apparent differences in HER2 signalling observed between 2D and 3D cell culture models of breast cancer suggest that 3D models better recapitulate *in vivo* HER2 signalling pathways (Pickl & Ries 2009). While uPAR profiling of other cancer cell lines has indicated that uPAR expression remains similar between 2D and 3D culture (Ertongur et al. 2004), it remains unknown whether the expression of uPA and uPAR by MCF-7 and MDA-MB-231 cells changes when cells are grown as 3D structures.

Despite flow cytometry revealing an increase in the uptake of PAI-2-functionalised liposomes over non-functionalised liposomes by MDA-MB-231 cells, the endpoint viability assays revealed no significant differences in IC_{50} values between non-functionalised and PAI-2-functionalised *N*-AI liposomes. It is possible that at the

experimental endpoints of 72 h or 96 h, any differences in cytotoxicity were masked as remaining viable cells continued to proliferate over time. There appeared to be a greater destruction of the spheroid structure for MDA-MB-231 spheroids than MCF-7 spheroids after treatment with *N*-AI PAI-2 liposomes at the 24 h time point (Fig. 3.9), and a significant decrease ($P < 0.01$) in the diameter of MDA-MB-231 spheroids treated with *N*-AI PAI-2 liposomes (74.5 ± 3.4 µm) compared to *N*-AI liposomes (91.8 ± 5.1 µm) at the 24 h time point (Fig. 3.12). However, these differences were lost at later time points and at the experimental endpoints of 72 h and 96 h. As the flow cytometric uptake showed a significant difference in the uptake of PAI-2 liposomes over NF liposomes after a 45 min incubation, differences in liposome uptake and cytotoxic effect may be apparent initially but lost over time. For this reason, analysis of spheroid viability at earlier time points and the use of real-time analysis of cell viability rather than (or in addition to) endpoint viability assays would be advantageous in future experiments in order to determine different mechanisms of liposome uptake into tumour spheroids. This could be achieved by using fluorescent dyes that track viable cells to detect differences in viability at various time points after liposome treatment (Tario et al. 2018; Yumoto et al. 2014).

A limitation of multicellular tumour spheroid models for testing new drug-loaded nanotherapies is that these static models do not reproduce the complex vascular network, hypoxia, interstitial fluid pressure and fluid shear observed in the *in vivo* tumour microenvironment. Importantly, static spheroid models do not account for drug transport across the vascular endothelium but rely exclusively on passive diffusion of liposomes through the culture medium to permeate the spheroid (Li & Lu 2011). The use of high local concentrations of drug-loaded liposomes to elicit a dose-dependent cytotoxic effect on spheroids grown *in vitro* is not the best representation of the *in vivo* context, where the enhanced permeability and retention (EPR) effect is at play and vascular permeability is a relevant factor in liposome accumulation at the tumour site (Maeda 2015). The development and validation of *in vitro* models that recapitulate aspects of the EPR effect is an emerging field of research. Static 3D co-culture models comprised of vascular network structures and breast tumour spheroids can be used for incorporating the effect of vascularisation in drug testing experiments (Swaminathan et al. 2017). Microfluidic-based platforms can be used for monitoring nanoparticle delivery in a 3D environment that recapitulates circulation, extravasation and delivery to the tumour across the

interstitial space (Li et al. 2018). These models also permit examination of tumour cell and vascular cell interactions and how these interactions affect drug delivery. For example, in a microfluidic drug delivery model recapitulating the EPR effect, MDA-MB-231 cells were shown to increase vascular permeability to liposomes compared to MCF-7 cells, likely through the release of VEGF (Tang et al. 2017). The creation of clinically relevant models to study the interactions between distinct cell types in the tumour microenvironment and to test the effects of novel targeted therapies is vital for improving the translation of results from the *in vitro* to the *in vivo* setting (Herrmann et al. 2014).

3.5 Conclusion

The work presented in this chapter confirmed the cellular uptake, cellular localisation and cytotoxicity of *N*-AI PAI-2 liposomes. Liposomes were shown to be taken up by MCF-7 and MDA-MB-231 cells, with PAI-2-functionalised liposomes showing increased uptake over non-functionalised liposomes by the uPAR-positive, but not uPAR-negative, MDA-MB-231 breast cancer cell line by flow cytometry after 45 min incubation. Liposomes were shown to be internalised by MCF-7 and MDA-MB-231 cells, with localisation at the cell membrane, within the cytoplasm and some accumulation in the lysosomes. *N*-AI-loaded liposomes were cytotoxic to breast cancer cells grown in both 2D and 3D, with increased cytotoxicity against MDA-MB-231 cells over MCF-7 cells in 2D culture and early time points (24 h) in 3D culture. Collectively, the *in vitro* results reported in this chapter provide a rationale to proceed with pharmacokinetic, biodistribution and efficacy testing of *N*-AI PAI-2 liposomes using clinically relevant *in vivo* models of uPAR-positive breast cancer.

Chapter 4:

In Vivo Evaluation of *N*-alkylisatin-Loaded Liposomes Targeting the Urokinase Plasminogen Activator System

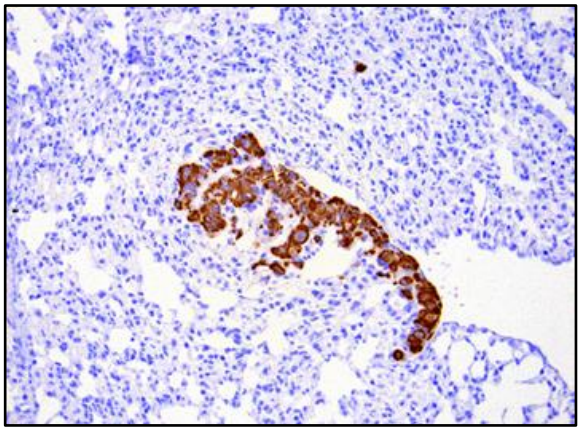

Metastatic human tumour cells in mouse lung tissue

Portions of this chapter have been included in the following work for publication:

Belfiore, L, Saunders, DN, Ranson, M & Vine, KL 2019, '*N*-alkylisatin-loaded liposomes targeting the urokinase plasminogen activator system in breast cancer', manuscript in preparation.

Author contributions: LB, DNS, MR and KLV designed the experiments; LB and KLV performed the experiments and analysed the data; LB wrote the manuscript; DNS, MR and KLV edited the manuscript for submission.

4.1 Introduction

The work described in Chapter 3 of this thesis explored the cellular uptake and cytotoxic effect of *N*-alkylisatin (*N*-AI)-loaded plasminogen activator inhibitor-2 (PAI-2)-functionalised (*N*-AI PAI-2) liposomes on uPAR-positive breast cancer cells grown in monolayer culture and multicellular tumour spheroid culture. Despite the approximations of these cell models to *in vivo* tumours, there are limitations to how accurately cells grown on tissue culture plates can represent the characteristics of real tumours. In particular, modelling of the enhanced permeability and retention (EPR) effect – the primary means by which liposomes are thought to accumulate at tumour sites – is not possible in the *in vitro* setting. Additionally, metastatic disease cannot be adequately modelled and studied without the use of whole organisms. Therefore, there is a need to use animal models to better understand and validate the efficacy of novel anticancer nanotherapeutics *in vivo*.

4.1.1 *In vivo* tumour models

In vitro tumour cell models are informative insofar as they can be physiologically relevant, but in certain respects, their utility is limited since they cannot adequately replicate the complete nature of actual tumours (Katt et al. 2016). For example, *in vitro* cell models are static models that rely on passive diffusion for drugs to reach and permeate tumour cells or spheroids, which does not account for transport across the vascular endothelium as happens *in vivo*. Notably for nanoparticle testing, *in vitro* models cannot reproduce the complex vascular network, hypoxia, interstitial fluid pressure and fluid shear observed in the *in vivo* tumour environment (Velasco-Velazquez et al. 2011). Additionally, in order to understand the impact of the complexity of the tumour microenvironment, including the extracellular matrix, stromal cells and immune cells, on the performance of new drugs, models as similar to the *in vivo* situation as possible are required. While *ex vivo* tumour models have been reported, such as microfluidic-based platforms that recapitulate circulation, extravasation and drug delivery to tumours across the interstitial space (Tang et al. 2017), evaluation of new nanotherapies and other drugs in whole animals remains the standard for preclinical testing.

In vivo, the EPR effect enables the passive accumulation of liposomes to tumour sites, although this effect is reported to be highly variable between different tumour types and

is not observed for all solid tumours (Hansen et al. 2015; Wang 2015). Generally, the nanoparticle targeting of haematological and lymphoid tumours, particularly for ligand-directed liposomes, has shown greater success in *in vivo* tumour models since tumour cells in circulation are more directly accessible to liposomes than large solid tumours immersed in complex microenvironments (Buxton 2009; Cho & Lee 2014). However, the application of nanoparticles in the treatment of some solid tumours may have greater potential for use in the adjuvant setting to target vascularised micrometastases rather than (or in addition to) the primary tumour (Zhao, M et al. 2017).

Currently, metastatic disease is the leading cause of cancer mortality, accounting for approximately 90% of cancer-related deaths, and remains untreatable (Sledge 2016). Metastatic disease cannot be adequately modelled and studied without the use of whole organisms. Modelling metastatic disease using mice is necessary to evaluate the potential effect of a nanotherapeutic on the spread of cancer and growth rates of secondary tumours (Fantozzi & Christofori 2006). The generation of such models usually involves the injection of human cells into an immunocompromised mouse, forming a xenograft, and after primary tumour formation, those human cells may metastasise. Many established human cancer cell lines have a low metastatic potential, with the likelihood of spontaneous metastasis in an animal being dependent on the model used. For example, the standard MDA-MB-231 breast cancer cell line routinely used *in vitro* has been shown to metastasise in an intraductal NODScidIL2gamma$^{-/-}$ (NSG) mouse model (Young et al. 2016) but remains poorly metastatic in a mammary fat pad BALB/c nude mouse model (Stutchbury et al. 2007). This highlights the importance of selecting appropriate tumour models for the evaluation of nanotherapies *in vivo*.

While mouse models are the most frequently used animal models of tumours and other disease states, given the high degree of similarity between mice and humans, there are several known differences between mouse tumour models and the human context. For example, the rate of mouse model tumour growth and resultant angiogenesis is much greater than the formation of a tumour in humans, which tends to increase the EPR effect (Maeda 2015). Additionally, the lack of an adaptive immune system in immunocompromised xenograft mouse models used to study nanotherapies means that known immune system effects on tumour growth and metastasis are absent from testing

(Budhu et al. 2014). Despite their limitations, mouse models enable the determination of key characteristics of new nanotherapies, such as potential toxicity and off-target effects. Importantly, mouse models allow the evaluation of pharmacokinetics to determine how quickly a nanoparticle formulation is cleared from the bloodstream (plasma half-life), which is an important indicator of how likely it is that the nanoparticle will successfully reach the site of the tumour. Similarly, biodistribution studies provide information about where the nanoparticle localises in the body and how the nanoparticle is cleared. These characteristics can be measured by radiolabelling the nanoparticles and then detecting the presence of radiolabel in plasma and tissues at various time points post-injection (Vine et al. 2014). This information can then guide dosing for efficacy experiments, which can help elucidate the effects of repeated nanoparticle treatments on primary tumour growth rate and tumour metastases to major organs, giving an indication of potential therapeutic effect in a clinical setting.

4.1.2 Experimental rationale

To better understand the behaviour and potential anti-tumour effects of PAI-2-functionalised liposomes containing *N*-AI (*N*-AI PAI-2 liposomes) *in vivo*, it is necessary to evaluate the properties of the liposomes in animal models of breast cancer. Toxicology studies previously performed by our laboratory have shown that *N*-AI-loaded liposomes are non-toxic in mice, with up to 100 mg/kg total dose of liposomal *N*-AI showing no adverse effects (Appendix D). PAI-2 has also been shown to be safe and non-toxic in mice when administered intravenously (Hang et al. 1998; Vine et al. 2012). The biodistribution and pharmacokinetic properties of *N*-AI PAI-2 liposomes need to be determined to guide treatment schedules for efficacy experiments in mouse breast tumour models, which can be used to evaluate the potential therapeutic effect of *N*-AI PAI-2 liposomes in uPAR-positive breast cancer.

4.1.3 Aims

This chapter tested the hypothesis that *N*-AI-loaded PAI-2-functionalised liposomes (*N*-AI PAI-2 liposomes) enhance the tumour cell uptake into and cytotoxic effect of *N*-AI against uPAR-positive breast tumours. Therefore, the overall aim of this chapter was to determine the pharmacokinetics, biodistribution and anti-tumour efficacy of *N*-AI PAI-2

liposomes in human xenograft models of primary and metastatic uPAR-positive triple-negative breast cancer (TNBC) in order to evaluate the scope for future preclinical analysis and clinical application of *N*-AI PAI-2 liposomes. The specific aims of this chapter were to:

1. Determine the pharmacokinetic and biodistribution profiles of *N*-AI PAI-2 liposomes in female BALB/c nude mice bearing MDA-MB-231 orthotopic breast tumour xenografts;
2. Determine the anti-tumour (primary tumour) efficacy of multiple doses of *N*-AI PAI-2 liposomes in female BALB/c nude mice bearing MDA-MB-231 orthotopic breast tumour xenografts; and
3. Determine the anti-tumour (primary tumour and metastatic tumour) efficacy of multiple doses of *N*-AI PAI-2 liposomes in NOD-SCID-IL2gamma$^{-/-}$ mice bearing MDA-MB-231 intraductal breast tumour xenografts.

4.2 Methods

4.2.1 Pharmacokinetics and biodistribution of *N*-AI PAI-2 liposomes

4.2.1.1 Preparation of ^{3}H-CHE-labelled liposomes

Liposome components (20 mM soy L-α-phosphatidylcholine (124.0 mg), 0.8 mM mPEG-DSPE (18.7 mg), 0.2 mM mal-PEG-DSPE (4.7 mg), 5 mM hydroxymethylbenzyl-isatin (17.0 mg)) were weighed out into glass vials and dissolved in chloroform/methanol (2:1 v/v). All solutions were transferred to a round-bottom flask using a glass pipette and 400 µCi tritiated cholesteryl hexadecyl ether [cholesteryl-1,2-3H(N)] (^{3}H-CHE) (PerkinElmer, MA, USA) (50 µCi per mL liposome) was added to the solution. Solvents were removed by rotary evaporation. The flask was then filled with nitrogen, sealed with parafilm and transferred to 4°C overnight. To reconstitute the thin film, 8 mL degassed endotoxin-free PBS (pH 7.4; Sigma-Aldrich, MO, USA) was added to the flask. The flask was placed in a shaking water bath at room temperature (RT) and left for 1 h to reconstitute. The solution was filtered through a 0.22 µm PVDF membrane and extruded through a 0.1 µm membrane a total of 11 times at RT using a syringe-driven mini-extruder (Avanti Polar Lipids). Liposomes were characterised by dynamic light scattering (DLS) analysis (NanoSight) to determine size and monodispersity. *N*-AI-loaded non-functionalised liposomes (*N*-AI) and *N*-AI-loaded PAI-2-functionalised liposomes (*N*-AI

PAI-2) were prepared by adding 704 µL of either PBS (pH 7.4) or PAI-2 (2.3 mg/mL in PBS, pH 7.4), respectively, to 3 mL of liposome solution and incubating at RT for 4 h. The radioactivity of the preparations was measured using a scintillation counter (Tri-Carb 2810 TR Liquid Scintillation Counter; PerkinElmer, MA, USA) (10 µL liposome + 6 mL Ultima Gold). Prior to injection, the liposome preparations were sterile-filtered through a 0.22 µm pore PVDF filter and kept sterile for subsequent *in vivo* studies.

4.2.1.2 Mice

Female BALB/c-Fox1nu/Ausb nude immunocompromised mice (5 weeks old) (Australian BioResources, Moss Vale) were housed in isolator cages at the University of Wollongong animal facility. Mice were given food and water ad libitum and kept on a 12 h light/dark cycle for the duration of the experiment. Mice were allowed to acclimatise for 2 weeks before commencement of the experiment. All experiments were conducted in accordance with the 'NHMRC Australian Code for the Care and Use of Animals for Scientific Purposes', which requires 3R compliance (replacement, reduction and refinement) at all stages of animal care and use, and the approval of the Animal Ethics Committee of the University of Wollongong (Australia) under protocol AE13/18. MDA-MB-231 cells (ATCC; mycoplasma negative and STR profiled) were cultured in RPMI-1640 medium with 10% heat-inactivated FBS (incubated at 37°C). Cells were detached from flasks with 0.05% trypsin/EDTA solution (Gibco, MA, USA) and incubated for 3-5 min at 37°C. Cells were collected in RPMI-1640 medium with 10% FBS and centrifuged at 1200 rpm (~300 x g) for 5 min at RT. Cells were resuspended in PBS with Ca/Mg (pH 7.4; Sigma-Aldrich, MO, USA) and centrifuged again as above. Cells were then resuspended in PBS (no Ca/Mg; pH 7.4; Sigma-Aldrich, MO, USA) and counted using Trypan blue (Sigma-Aldrich, MO, USA) and a haemocytometer. A cell suspension at a concentration of 4 x 10^7 cells/mL was prepared to give 2 x 10^6 cells in a 50 µL injection volume. Cell viability was checked after injections had been completed and was found to be approximately 90%.

Mice were weighed prior to cell injection. Insulin syringe needles (29-gauge; BD Biosciences, NJ, USA) were used to inject 50 µL of cell suspension (containing 2 x 10^6 cells) into the upper left mammary fat pad. Mice were injected one cage at a time and the injection order of cages was randomised. Mice were monitored closely following

injection of cells, and tumours were observed to form at approximately 3 weeks post-injection.

4.2.1.3 Treatment with liposomes

All mice were monitored and weighed prior to the start of treatments. Mice did not show signs of distress or weight loss in the weeks prior to treatment commencement. Tumours were apparent in most mice and were small (< 100 mm^3) upon commencement of liposome treatment. Mice were randomly allocated to treatment (*N*-AI liposome or *N*-AI PAI-2 liposome) and time point (10 min, 3 h, 6 h, 24 h, 48 h or 96 h) groups (4 mice per cohort). Treatments were administered intravenously via a single lateral tail vein injection. Tails were warmed using a heat lamp to dilate the tail vein before injecting 100 µL (4 µCi) of liposome solution. Following injection, a small amount of pressure was placed on the injection site to stem any bleeding. Mice that were deemed significantly (± 10%) smaller or larger in weight than their cage mates had their dose volume adjusted proportionally based on their weight relative to the average of their cage mates.

Cohorts were euthanised at designated time points post-treatment (10 min (0.17 h), 3 h, 6 h, 24 h, 48 h or 96 h) via CO_2 inhalation. Immediately after sacrifice, whole blood was collected by cardiac puncture using 29-gauge insulin syringes and transferred into 1 mL EDTA animal collection tubes (Greiner, Austria). Blood was centrifuged at 500 x g for 15 min at RT and 0.1 mL of plasma was transferred to a pre-weighed 7 mL glass scintillation vial. Kidneys, liver, spleen, lungs and tumour, as well as the tail (to subtract activity remaining at injection site) were removed from each animal and transferred to individual pre-weighed 20 mL glass scintillation vials. Vials were sealed and stored at 4°C until tissues were processed.

4.2.1.4 Blood and tissue analysis

The ^{3}H-CHE radioactivity (liposome) in the plasma, kidneys, liver, spleen, lungs, tumour and tail (for injection correction) was quantified using previously published methods (Vine et al. 2014). Vials were equilibrated to RT and the weight of each tissue was determined by subtracting the pre-recorded weights of each empty vial. Solvable (PerkinElmer, MA, USA) was added to each vial to dissolve the tissues: 0.4 mL for plasma; 2 mL for kidneys, spleen, lungs and tail; 5 mL for liver; and 1 mL for tumours

(where present). Vials were sealed and incubated at 60°C for 1-3 h with occasional agitation to dissolve tissues. Vials were then cooled to RT and hydrogen peroxide (30% v/v) was added to bleach the samples: 0.2 mL for plasma, kidneys, spleen, lungs and tail; 0.5 mL for liver; and 0.1 mL for tumour. Samples were allowed to stand for 30 min at RT to complete the reaction. Vials were then sealed tightly and incubated at 60°C for 1 h. Vials were cooled to RT and 0.5 mL of each sample (0.25 mL for liver due to residual intense colouration) was transferred to a 7 mL glass scintillation vial. To this, 5 mL of Ultima Gold LSC (PerkinElmer, MA, USA) was added, vials were inverted to mix and samples were temperature-adapted (25°C) and dark-adapted for 1 h prior to counting. Samples were analysed using a Tri-Carb 2810 TR Liquid Scintillation Counter (PerkinElmer, MA, USA). Separate control vials for each tissue were prepared in parallel and contained the same volumes of each reagent but in the absence of tissue. The raw counts for each sample were corrected for the amount of radioactivity remaining in the tail and are presented as the percentage of injected dose (ID) per gram of tissue (% ID/g) or percentage of ID in the whole tumour (% ID). Pharmacokinetic profiles were determined by plotting the % ID/mL remaining in the plasma over time and fitted to a one phase decay model using GraphPad Prism V7 for Windows (GraphPad Software, CA, USA).

4.2.2 Efficacy of *N*-AI PAI-2 liposomes in a primary tumour model

4.2.2.1 Liposome preparation

Liposomes were prepared as outlined in Section 4.2.1.1 in the absence of ^{3}H-CHE. Empty non-functionalised (EMP) liposomes were composed of 20 mM soy PC, 1 mM mPEG-DSPE and 5 mM cholesterol. *N*-AI-loaded non-functionalised (*N*-AI) and *N*-AI-loaded PAI-2-functionalised (*N*-AI PAI-2) liposomes were composed of 20 mM soy PC, 0.8 mM mPEG-DSPE, 0.2 mM mal-PEG-DSPE and 5 mM 5,7-dibromo-*N*-(*p*-hydroxymethylbenzyl)isatin (*N*-AI). Liposomes were serially extruded through a 0.1 µm pore PVDF membrane using a thermobarrel batch extruder (Lipex) and characterised by DLS (NanoSight).

4.2.2.2 Mice

Female BALB/c-Fox1nu/Ausb nude immunocompromised mice (5 weeks old) (Australian BioResources, Moss Vale) were housed in isolator cages at the University of

Wollongong Animal Facility. Mice were given food and water ad libitum and kept on a 12 h light/dark cycle for the duration of the experiment. Mice were allowed to acclimatise for 3 weeks before commencement of the experiment. All experiments were conducted in accordance with the 'NHMRC Australian Code for the Care and Use of Animals for Scientific Purposes', which requires 3R compliance (replacement, reduction and refinement) at all stages of animal care and use, and approval of the Animal Ethics Committee of the University of Wollongong (Australia) under protocol AE13/18. Mice were inoculated with MDA-MB-231 tumour cells as outlined in Section 4.2.1.2.

4.2.2.3 Treatment with liposomes

All mice were monitored and weighed prior to the start of treatments. Mice did not show signs of distress or weight loss in the weeks prior to treatment commencement. Tumours were apparent in most mice and were large (~200 mm^3) at the start of treatments. Mice were randomly allocated to one of three treatment groups (EMP, *N*-AI and *N*-AI PAI-2) (8 mice per treatment group). Treatments (100 µL) were administered intravenously via the lateral tail vein as described in Section 4.2.1.3 for a total of 6 injections over 2 weeks (average total dose = 68.1 mg/kg *N*-AI). Mice that were deemed significantly (± 10%) smaller or larger in weight than their cage mates had their dose volume adjusted proportionally based on their weight relative to the average of their cage mates. Tumour dimensions were measured three times per week using callipers and tumour volume was calculated using the equation: volume (mm^3) = (length (mm) x width (mm) x width (mm)) / 2. Animals were weighed triweekly for the duration of the experiment. Mice were sacrificed by CO_2 inhalation upon reaching tumour end point (tumour dimensions of 15 mm x 15 mm) or at the experimental end point. Immediately after sacrifice, the kidneys, liver, spleen, heart and lungs, and tumour were removed and weighed.

4.2.3 Efficacy of *N*-AI PAI-2 liposomes in a metastatic tumour model

4.2.3.1 Liposome preparation

Liposomes were prepared as outlined in Section 4.2.2.1 in the absence of ^{3}H-CHE. The four liposome preparations, empty non-functionalised (EMP), empty PAI-2-functionalised (EMP PAI-2), *N*-AI non-functionalised (*N*-AI) and *N*-AI PAI-2-functionalised (*N*-AI PAI-2) liposomes, were sterile-filtered through a 0.22 µm PVDF membrane and kept sterile until treatment.

4.2.3.2 Mice

Female immunocompromised NOD-SCID-IL2gamma$^{-/-}$ mice (5 weeks old) were housed in the Biological Testing Facility at the Garvan Institute of Medical Research. Mice were given food and water ad libitum and kept on a 12 h light/dark cycle for the duration of the experiment. All animal procedures were approved by the Garvan/St Vincent's Animal Ethics and Experimentation Committee (approval number 14/27) according to the Animal Research Act 1985, Animal Research Regulation 2010 and the Australian Code of Practice for the Care and Use of Animals for Scientific Purposes, which requires 3R compliance (replacement, reduction and refinement) at all stages of animal care and use. Intraductal injections of MDA-MB-231 cells were performed by Samantha Oakes at The Kinghorn Cancer Centre. 80,000 MDA-MB-231 cells were injected directly into the right mammary duct in a total volume of 10 µL, as described previously (Young et al. 2016). Mice were monitored twice weekly and tumour growth was measured for the duration of the experiment. Tumours were measured immediately prior to each injection and volume was calculated using the equation: volume (mm^3) = (length (mm) x width (mm) x width (mm)) / 2.

4.3.3.3 Treatment with liposomes

At 5 weeks post-tumour cell inoculation, mice were randomised into one of four treatment groups (5 mice per treatment cohort): EMP (empty liposomes), EMP PAI-2 (empty PAI-2-functionalised liposomes), *N*-AI (*N*-AI-loaded liposomes) or *N*-AI PAI-2 (*N*-AI-loaded PAI-2-functionalised liposomes). Treatments (100 µL, dose of 4.7 mg/kg *N*-AI) were administered intravenously via the lateral tail vein using a 25-gauge needle on a triweekly schedule for a total of 3.5 weeks (11 injections in total; total dose of 51.7 mg/kg *N*-AI). At 9 weeks post-tumour cell inoculation, mice were euthanised by CO_2 inhalation and cervical dislocation. The mammary glands, tumours, lungs and livers were harvested and fixed for 4 h in 10% buffered formalin at RT for subsequent histology and/or immunohistochemistry analysis.

4.3.3.4 Tissue analysis

All analyses were performed at The Kinghorn Cancer Centre histology laboratory. Mammary glands were whole mounted and processed for histology. After fixation, lungs and livers were sectioned and stained with vimentin (1:800; Leica NCL-L-VIM-V9), and

tumours were sectioned and stained with cleaved caspase-3 (1:100; CST ASP175 9664) using DAKO immunohistochemistry as per the manufacturer's instructions. Images were captured using a Leica DFC 450 microscope using 20X magnification. Images were analysed using ImageJ (version 1.51s) with automated algorithms designed for IHC analysis (Law et al. 2017).

4.2.4 Data analysis

All data analysis, including the generation of graphs and statistical tests, was performed using GraphPad Prism software (version 7), unless stated otherwise. Data are presented as the mean ± standard deviation (s.d.) or standard error of the mean (s.e.m.) as stated. Pairwise comparisons were made using Student's t-test, and multiple comparisons were made using one-way ANOVA with Tukey's post-test, or two-way ANOVA for grouped comparisons.

4.3 Results

4.3.1 Pharmacokinetics and biodistribution

To determine the pharmacokinetic and organ distribution profiles of *N*-AI-loaded non-functionalised liposomes (*N*-AI) and *N*-AI-loaded PAI-2-functionalised liposomes (*N*-AI PAI-2) in tumour-bearing mice, liposomes were labelled with tritiated cholesteryl hexadecyl ether (^{3}H-CHE) to enable the detection of liposomes in plasma and tissues by liquid scintillation counting. Following preparation, liposomes were characterised by DLS, which revealed monodisperse populations with average diameters of 115 ± 34 nm and 117 ± 39 nm for *N*-AI and *N*-AI PAI-2 liposomes, respectively. Scintillation counts of the two liposome stock preparations were 319,698 CPM and 312,163 CPM for *N*-AI and *N*-AI PAI-2 liposomes, respectively. The plasma half-life was determined to be 5.63 h and 5.82 h for *N*-AI and *N*-AI PAI-2 liposomes, respectively (Fig. 4.1). The plasma clearance profiles of the two liposomes and the pharmacokinetic parameters from curve fitting analysis were not significantly different ($P > 0.05$) (Table 4.1). *N*-AI and *N*-AI PAI-2 showed no significant differences in the average final weight of the kidneys, liver, spleen or lungs (Appendix E).

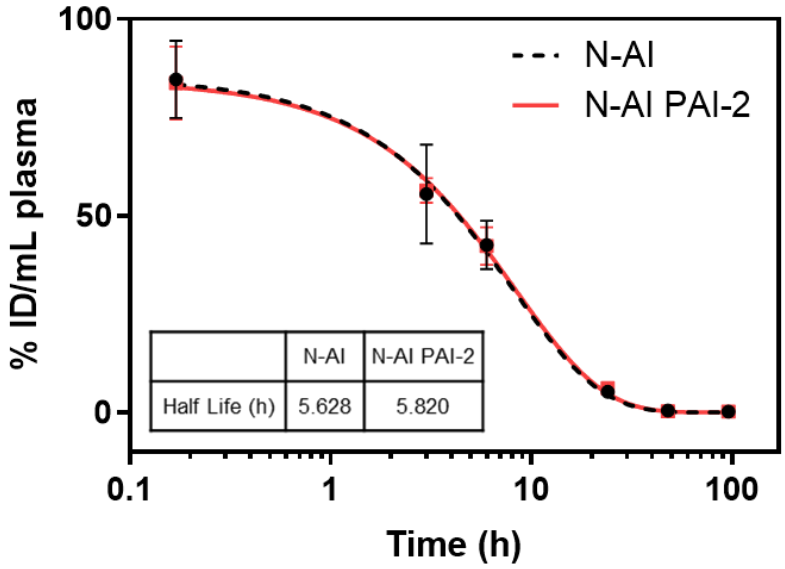

Figure 4.1: Detection of radiolabelled liposomes in the plasma of mice over time. *N*-AI and *N*-AI PAI-2 liposomes were labelled with tritiated cholesteryl hexadecyl ether and administered intravenously as a single bolus dose. Tritiated signal was measured in plasma at each time point. Results are expressed as the percentage of injected dose (ID) per mL of plasma (%ID/mL). Error bars are s.d. (n = 4).

Table 4.1: Pharmacokinetic parameters of *N*-AI and *N*-AI PAI-2 liposomes. *N*-AI and *N*-AI PAI-2 liposomes were labelled with tritiated cholesteryl hexadecyl ether and administered intravenously as a single bolus dose. Tritiated signal was measured in plasma at each time point.

PK Parameter	***N*-AI**	***N*-AI PAI-2**
C_{max} (% ID/mL)	84.66 (± 9.79)	83.76 (± 9.25)
K_{elim} α (fast) min^{-1}	0.061	0.058
K_{elim} β (slow) min^{-1}	0.002	0.002
$T_{1/2}$ α (fast) min	11.419	12.050
$T_{1/2}$ β (slow) min	408.152	410.843
Correlation coefficient (R^2)	0.9629	0.9836
AUC (% ID/min/mL)	860.3 (± 66.89)	873.4 (± 50.79)

Liposome accumulation in the kidneys, liver, spleen and lungs at each time point was similar between *N*-AI and *N*-AI PAI-2 liposomes (Fig. 4.2). The trends indicated increased clearance via the liver and spleen over time and decreased clearance via the kidneys and lungs over time. There was no significant difference ($P > 0.05$) in clearance via the kidneys, liver or lungs between the two liposomes at any time point. Clearance via the spleen was significantly higher ($P < 0.05$) at the 48 h time point for *N*-AI liposomes (78.5 ± 32.2 % ID/g tissue) compared to *N*-AI PAI-2 liposomes (44.2 ± 6.7 % ID/g tissue).

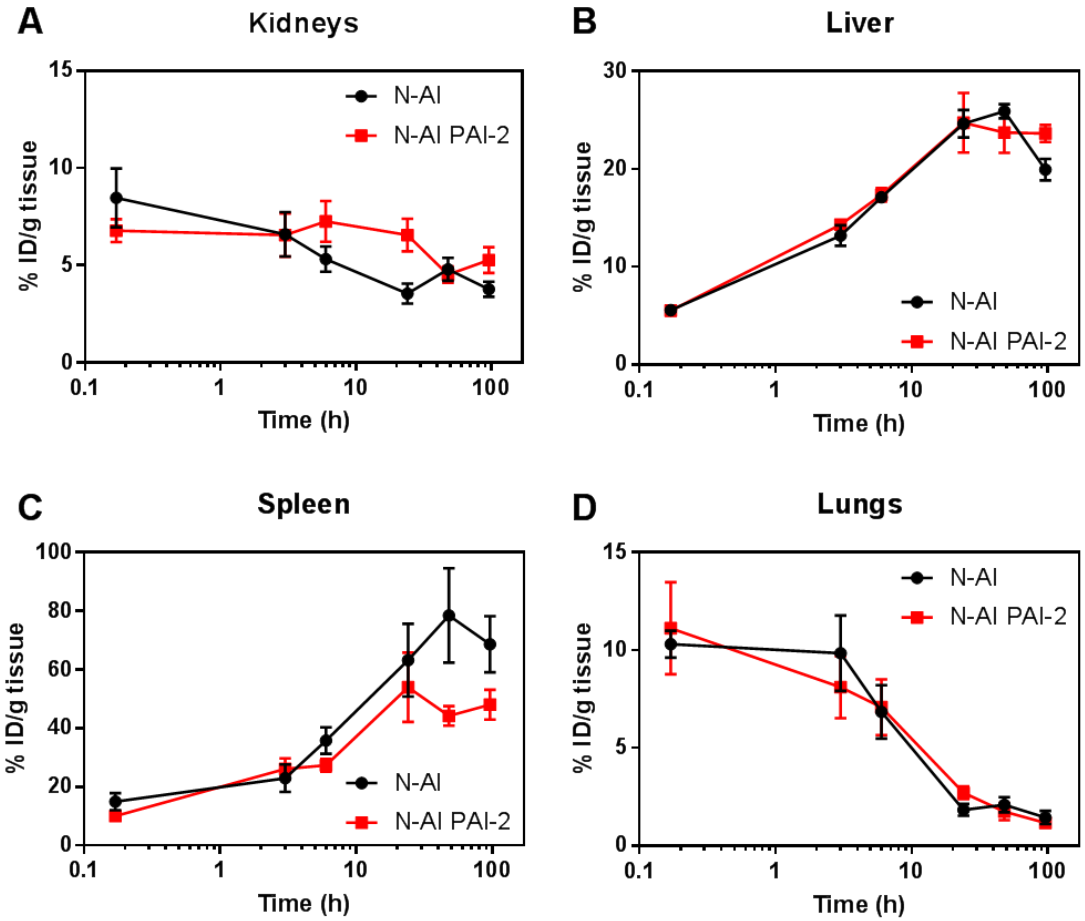

Figure 4.2: Detection of radiolabelled liposomes in clearance organs. *N*-AI and *N*-AI PAI-2 liposomes were labelled with tritiated cholesteryl and administered intravenously as a single bolus dose. Tritiated signal was measured in the (**A**) kidneys, (**B**) liver, (**C**) spleen and (**D**) lungs at each time point. Results are expressed as the percentage of injected dose (ID) per gram of tissue (%ID/g). Values are means ± s.e.m. (n = 4).

Comparison of the different clearance organs revealed similar patterns between *N*-AI and *N*-AI PAI-2 liposomes (Fig. 4.3). The primary route of clearance after the 10 min time point was via the spleen for both liposome formulations, which was 68.6 ± 19.3 % ID/g tissue and 48.1 ± 10.1 % ID/g tissue at the 96 h time point for *N*-AI and *N*-AI PAI-2 liposomes, respectively. Clearance via the liver was also high, with 20.0 ± 2.2 % ID/g tissue and 23.6 ± 1.8 % ID/g at the 96 h time point for *N*-AI and *N*-AI PAI-2 liposomes, respectively. Clearance via the kidneys and accumulation in the lungs were minimal for both liposome formulations.

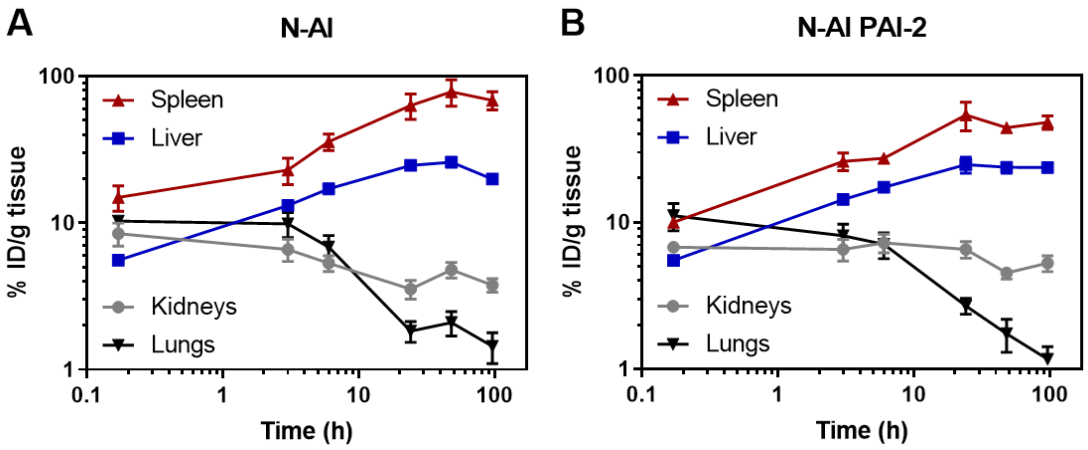

Figure 4.3: Comparison of *N*-AI and *N*-AI PAI-2 liposome clearance. *N*-AI and *N*-AI PAI-2 liposomes were labelled with tritiated cholesteryl and administered intravenously as a single bolus dose. Tritiated signal was measured in the kidneys, liver, spleen and lungs at each time point. Results are expressed as the percentage of injected dose (ID) per gram of tissue (%ID/g). Values are means ± s.e.m. (n = 4).

Where present, tumours were removed from mice and analysed for tritiated liposome signal in the same manner as for tissues (Fig. 4.4). The results showed rapid accumulation of *N*-AI PAI-2 liposome signal in tumours compared to *N*-AI liposomes, as indicated by significantly increased %ID at 10 min, 3 h and 6 h post-injection ($P < 0.001$). At 24 h, 48 h and 96 h, tumour uptake of *N*-AI and *N*-AI PAI-2 liposomes was not significantly different ($P > 0.05$).

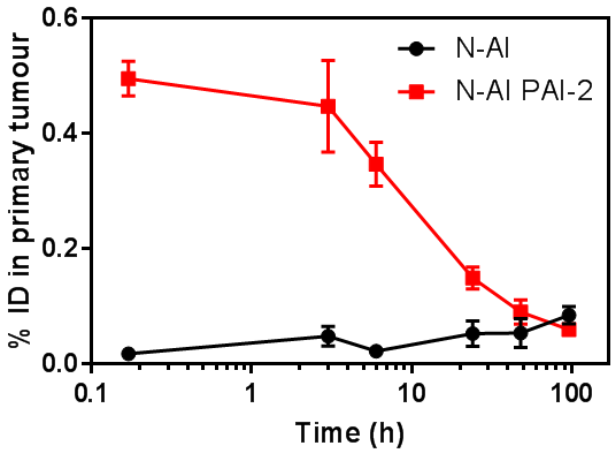

Figure 4.4: Accumulation of liposomes in uPAR-positive breast tumours. *N*-AI and *N*-AI PAI-2 liposomes were labelled with tritiated cholesteryl hexadecyl ether and administered intravenously as a single bolus dose. Tritiated signal was measured in whole collected tumour (where present) for each time point. Results are expressed as the percentage of the injected dose (ID) in the whole analysed primary tumour. Error bars are s.e.m. (n = 4).

4.3.2 Efficacy in a primary breast tumour model

In order to determine the potential effect of *N*-AI PAI-2 liposomes on primary tumour growth, mice bearing MDA-MB-231 tumours were treated with empty liposomes (EMP), *N*-AI-loaded liposomes (*N*-AI) or *N*-AI-loaded PAI-2-functionalised (*N*-AI PAI-2) liposomes three times per week for two weeks. Mice in all cohorts continued to gain weight for the duration of the experiment, suggesting no toxic effects of the multiple dose schedule of the liposomes (Fig. 4.5). While average animal weights were not significantly different between the three cohorts over the course of the experiment, the *N*-AI PAI-2 cohort showed a trend of a higher percentage weight gain compared to the other cohorts, although this was not statistically significant ($P > 0.05$).

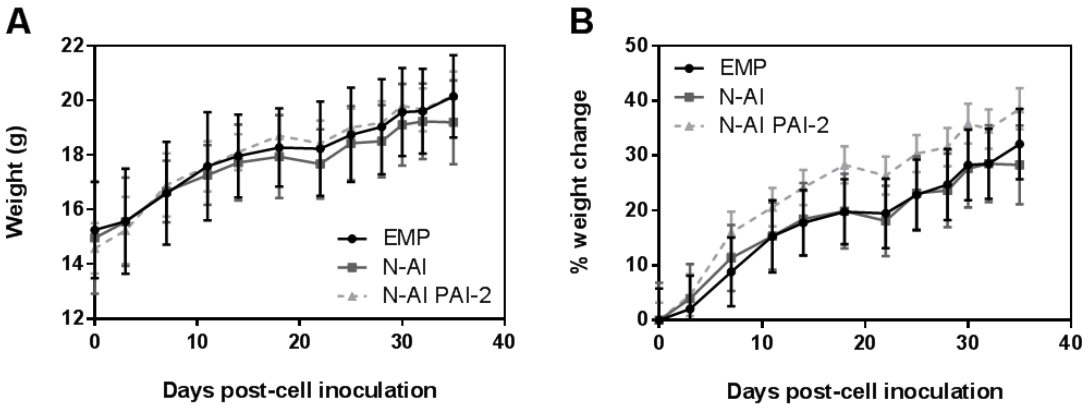

Figure 4.5: Animal weights over the duration of liposome treatment. Mice bearing MDA-MB-231 uPAR-positive tumours were administered with EMP, *N*-AI or *N*-AI PAI-2 liposomes on a triweekly schedule for two weeks. (**A**) Average weight and (**B**) percentage weight change (relative to experiment start) for each cohort for the duration of the experiment. Values are means ± s.e.m. (n = 8).

To assess the effect of the liposome treatments on primary tumour growth, tumours were measured using callipers three times a week and tumour volume was calculated using the equation: volume (mm^3) = (length (mm) x width (mm) x width (mm)) / 2. Tumours showed relatively linear growth across all cohorts, and the average tumour volume and percentage change in tumour volume between the three cohorts was not significantly different ($P > 0.05$) at any experimental time point (Fig. 4.6).

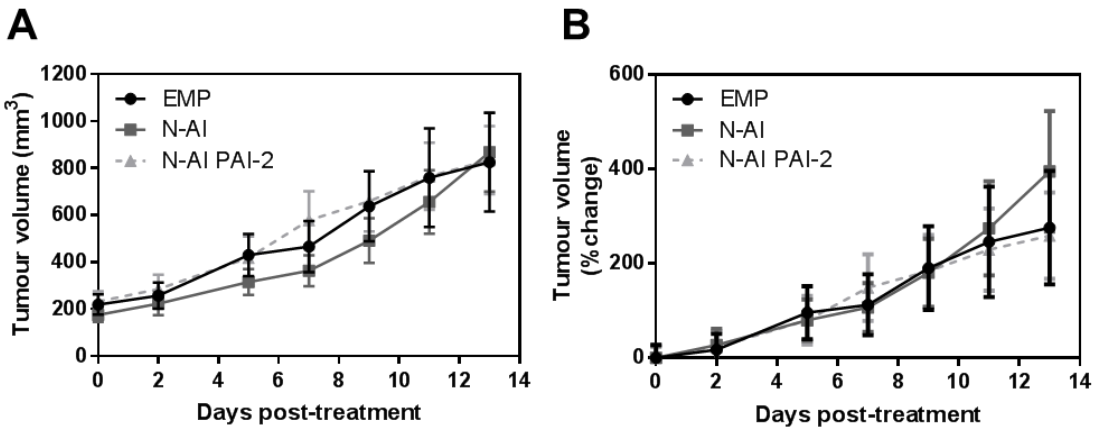

Figure 4.6: Primary tumour volume measurements. Mice bearing MDA-MB-231 uPAR-positive tumours were administered with EMP, *N*-AI or *N*-AI PAI-2 liposomes on a triweekly schedule for two weeks. (**A**) Tumour volume and (**B**) percentage change in tumour volume (relative to day 0 of treatment) for each cohort for the duration of the experiment. Values are means ± s.e.m. (n = 8).

At the end of the experiment, the kidneys, liver, spleen, and heart and lungs of each mouse were removed in whole and weighed. The final organ weights between the three cohorts were not significantly different ($P > 0.05$), indicating no toxicity from the multiple dosing schedule of the treatments (Fig. 4.7).

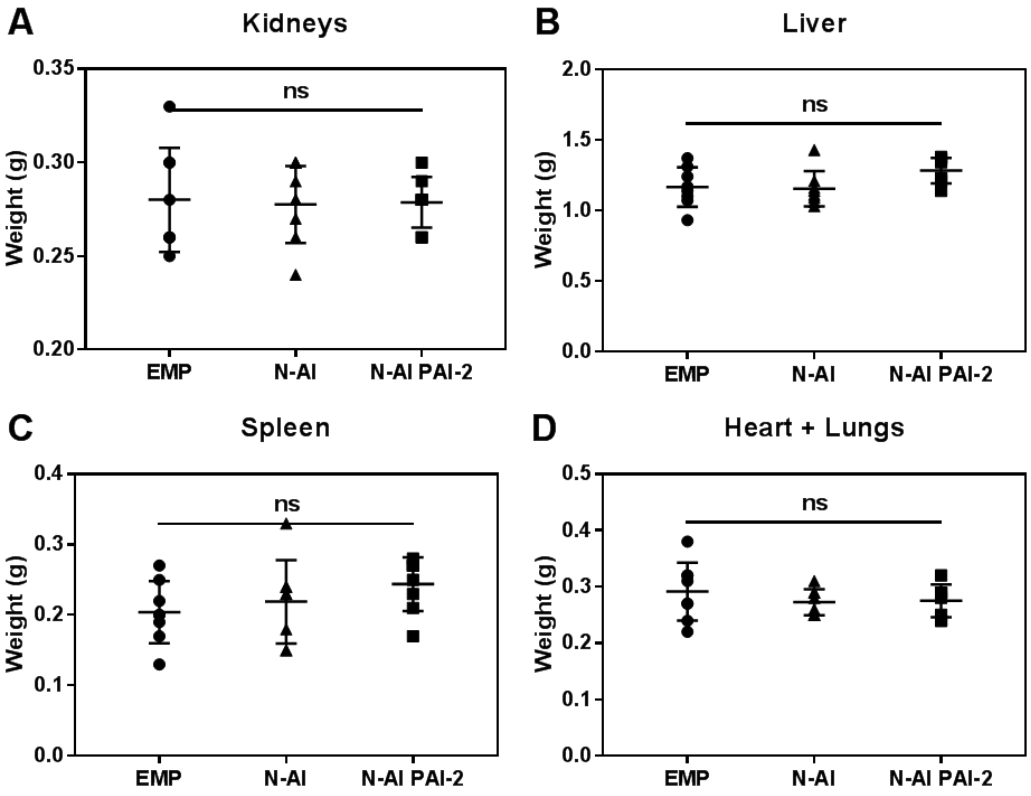

Figure 4.7: Final organ weights of liposome-treated mice. Mice bearing MDA-MB-231 uPAR-positive tumours were administered with EMP, *N*-AI or *N*-AI PAI-2 liposomes on a triweekly schedule for two weeks. At the experimental endpoint, mice were euthanised and (**A**) kidneys, (**B**) liver, (**C**) spleen and (**D**) heart and lungs were removed in whole and weighed. Values are means ± s.e.m. (n = 8). ns = not significant ($P > 0.05$).

Primary tumours were removed in whole and weighed. Primary tumour weights varied greatly between individuals within each cohort, but the average primary tumour weight between the three cohorts was not significantly different (Fig. 4.8). Comparison of primary tumour weights and primary tumour volume (calculated from calliper measurements) showed a high level of corroboration, but also showed no significant differences between the three treatment cohorts.

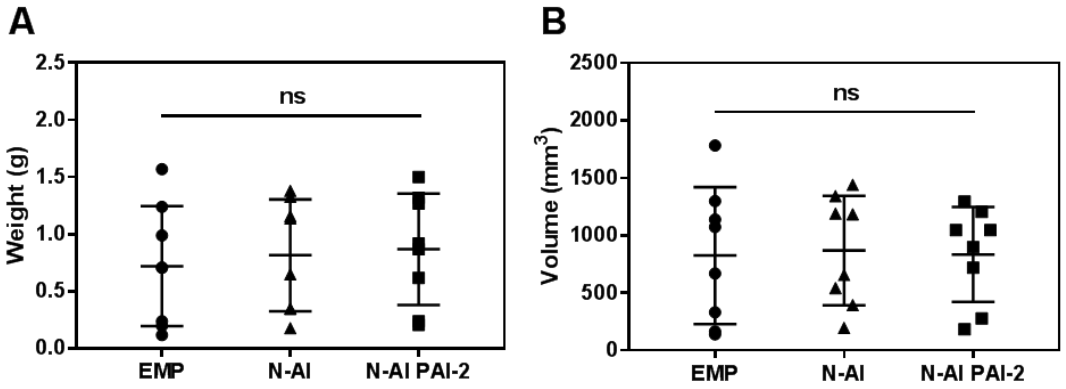

Figure 4.8: Final primary tumour measurements of liposome-treated mice. Mice bearing MDA-MB-231 uPAR-positive tumours were administered with EMP, *N*-AI or *N*-AI PAI-2 liposomes three times per week for two weeks. (**A**) At the experimental endpoint, mice were euthanised and primary tumours were removed in whole and weighed. (**B**) Final primary tumour volume as determined by calliper measurements. Values are means ± s.e.m. (n = 8). ns = not significant ($P > 0.05$).

4.3.3 Efficacy in a metastatic breast tumour model

To investigate the effect of *N*-AI PAI-2 liposomes on metastatic tumours, liposomes were tested in a metastatic intraductal breast tumour model with mice bearing MDA-MB-231 tumours. Empty non-functionalised liposomes (EMP), empty PAI-2-functionalised liposomes (EMP PAI-2), *N*-AI-loaded non-functionalised liposomes (*N*-AI) and *N*-AI-loaded PAI-2-functionalised liposomes (*N*-AI PAI-2) were administered intravenously from 5 weeks post-tumour cell inoculation when tumours were small (palpable, not measurable) on a triweekly schedule. Tumour volume increased steadily over time in all cohorts, with a more rapid increase observed from 20 days post-treatment (Fig. 4.9). Primary tumour growth was not significantly different between the four treatment cohorts, although mice treated with EMP PAI-2, *N*-AI or *N*-AI PAI-2 liposomes showed a trend of decreased tumour growth relative to the EMP treatment cohort.

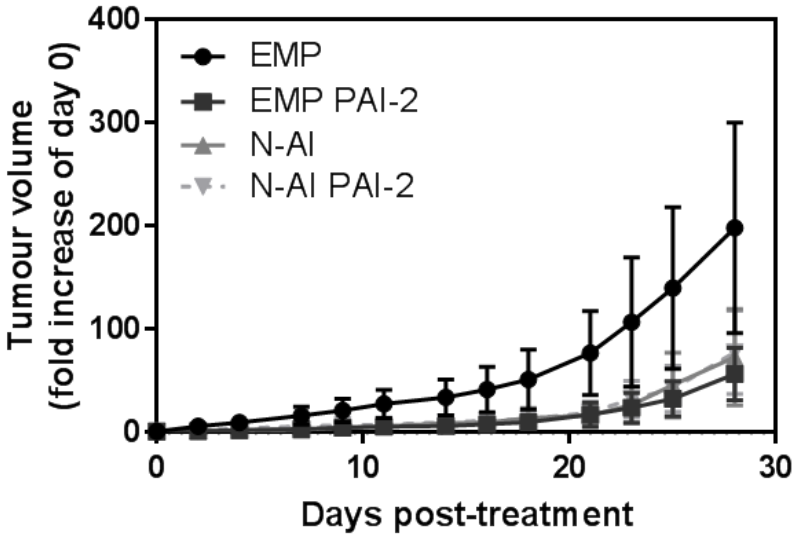

Figure 4.9: Primary tumour measurements in an intraductal tumour model. Mice bearing intraductal MDA-MB-231 tumours were treated with empty liposomes (EMP), empty PAI-2-functionalised liposomes (EMP PAI-2), *N*-AI-loaded liposomes (*N*-AI) or *N*-AI-loaded PAI-2-functionalised liposomes (*N*-AI PAI-2) (at equivalent *N*-AI and/or PAI-2 concentrations, where applicable) 3 times a week for 5 weeks. Values are means ± s.e.m. (n = 5).

Animal weights fluctuated throughout the course of the experiment but did not significantly change with progression of liposome treatment (Fig. 4.10). At the final time point (25 days post-treatment), the average percentage weight change of the *N*-AI PAI-2 cohort was significantly higher than that of the other three cohorts ($P < 0.05$).

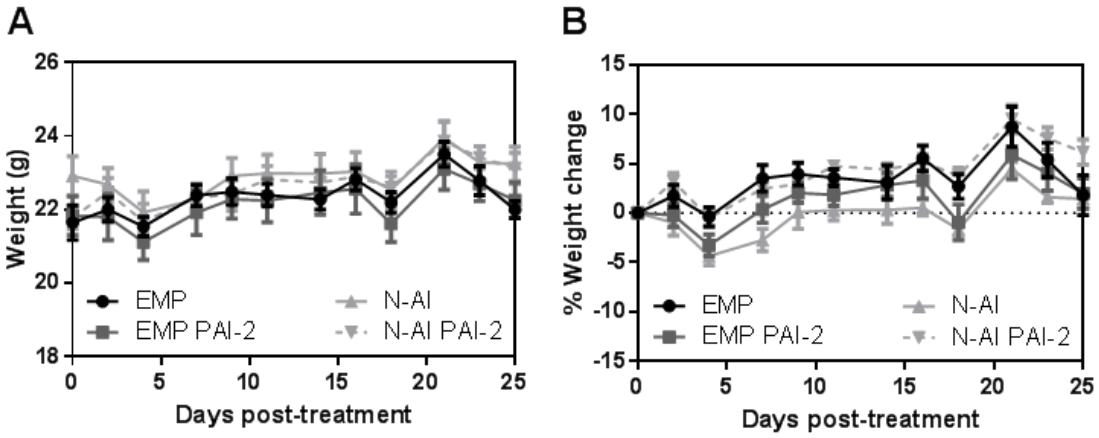

Figure 4.10: Animal weights in an intraductal model over duration of treatment. Mice bearing intraductal MDA-MB-231 tumours were treated with empty liposomes (EMP), empty PAI-2-functionalised liposomes (EMP PAI-2), *N*-AI-loaded liposomes (*N*-AI) or *N*-AI-loaded PAI-2-functionalised liposomes (*N*-AI PAI-2). (**A**) Animals were weighed prior to each treatment. (**B**) Animal weights normalised to day 0 post-treatment. Values are means ± s.e.m. (n = 5).

At the experimental end point, primary tumours (where present; n = 18), mammary glands (where possible; n = 15), lungs and livers were removed in whole. Mammary glands were stained with carmine as described previously (Young et al. 2016) and imaged for secondary tumour detection in the mammary gland once the primary tumour was removed (Fig. 4.11). The proportion of mammary glands with secondary tumours present was highest for the EMP cohort (4/5) and lowest for the *N*-AI PAI-2 cohort (0/2). There were no significant differences ($P > 0.05$) in average positive tumour area between the cohorts where secondary tumours were present (EMP, EMP PAI-2 and *N*-AI).

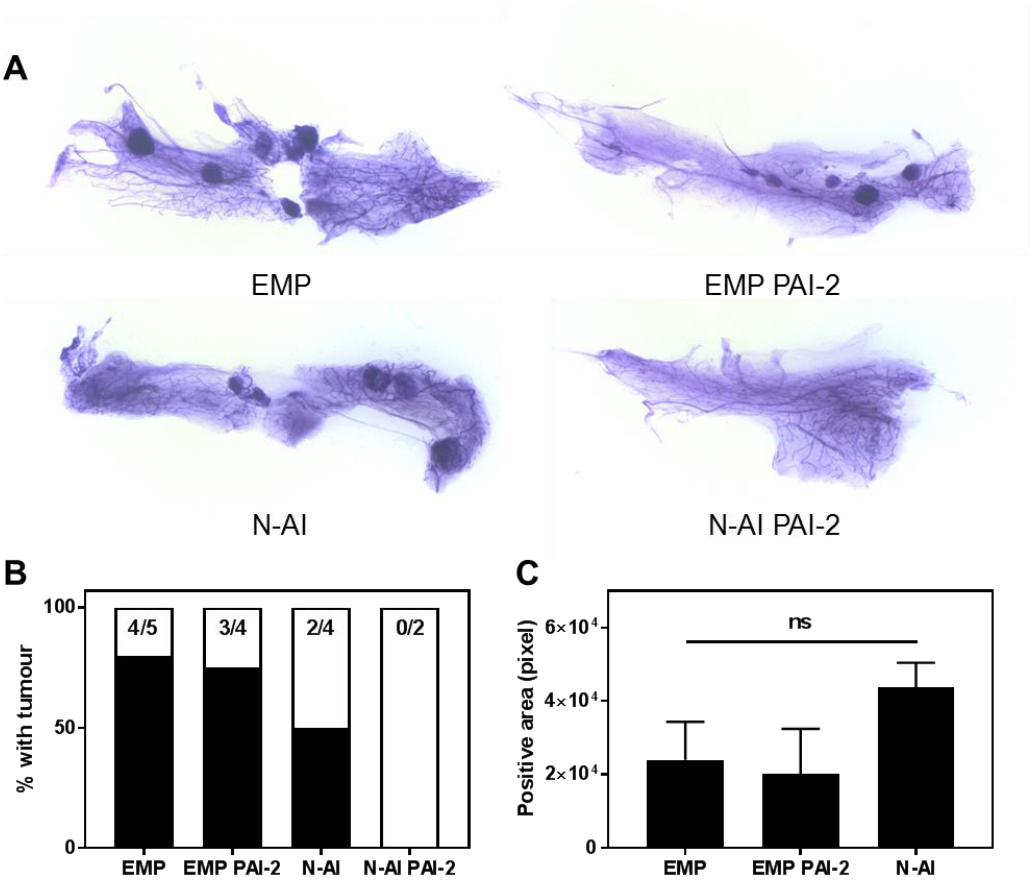

Figure 4.11: Mammary gland whole-mount analysis. Mice bearing intraductal MDA-MB-231 tumours were treated with empty liposomes (EMP), empty PAI-2-functionalised liposomes (EMP PAI-2), *N*-AI-loaded liposomes (*N*-AI) or *N*-AI-loaded PAI-2-functionalised liposomes (*N*-AI PAI-2). At the experimental endpoint, mammary glands were removed in whole where possible and mounted for carmine staining. (**A**) Representative carmine-stained mammary gland images. (**B**) Percentage of mice with tumour(s) present in mammary gland at experimental endpoint. (**C**) Tumour area (positive stain) of mammary glands where tumours were present. Values are means ± s.e.m. (n = 2-4). n.s. = not significant ($P > 0.05$).

To determine the potential cytotoxic anti-tumour cell effect of the *N*-AI and *N*-AI PAI-2 liposome treatments on primary tumours, primary tumour sections were stained with cleaved caspase-3 to detect apoptotic cells (Fig. 4.12). Automated imaging analysis of positively stained cells showed a considerable degree of variability between individuals within each treatment cohort, but no significant differences ($P > 0.05$) in the average positive area between the four cohorts in terms of cleaved caspase-3-positive cells.

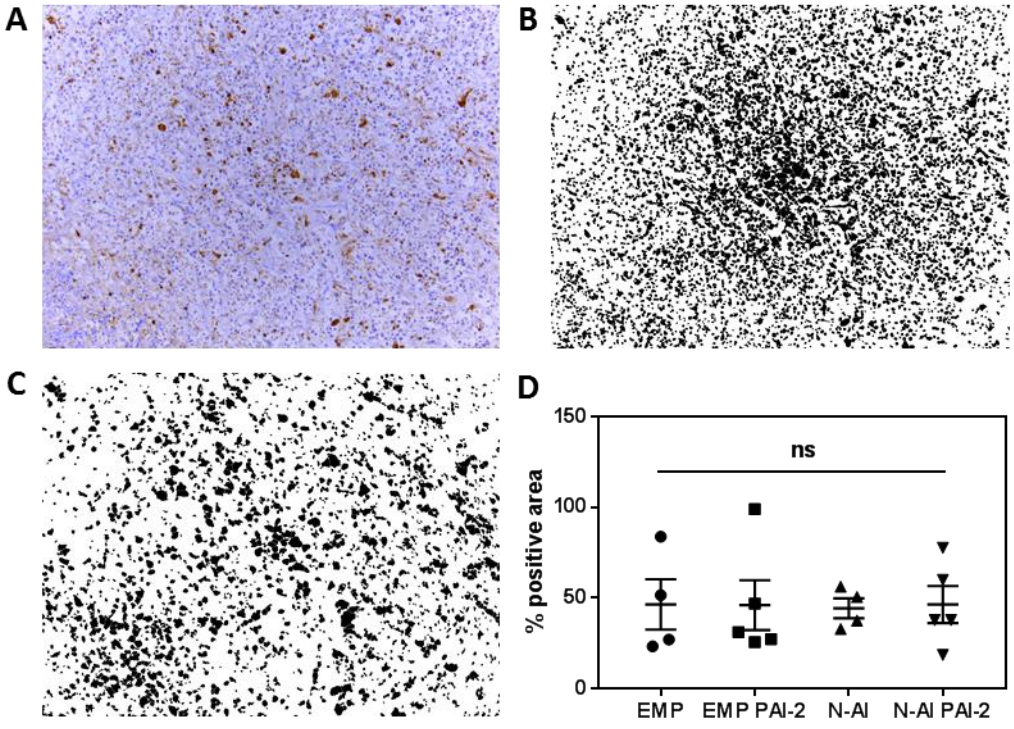

Figure 4.12: Immunohistochemistry analysis of primary tumours. Mice bearing intraductal MDA-MB-231 tumours were treated with empty liposomes (EMP), empty PAI-2-functionalised liposomes (EMP PAI-2), *N*-AI-loaded liposomes (*N*-AI) or *N*-AI-loaded PAI-2-functionalised liposomes (*N*-AI PAI-2). (**A**) Tumour sections were stained with cleaved caspase-3 (apoptotic cells). (**B**) Representative total mask (all cells) using automated imaging analysis. (**C**) Representative positive mask (apoptotic cells) using automated imaging analysis. (**D**) Percentage of cleaved caspase-3-positive area (apoptotic cells) relative to total cell area. Values are means ± s.e.m. (n = 5). n.s. = not significant ($P > 0.05$).

To determine the effect of the four liposome treatments on metastasis to the lungs and liver, lung and liver sections were stained with vimentin to detect metastatic cells (Fig. 4.13). Automated imaging analysis of positively stained cells showed a high degree of variability between individuals within each cohort, but no significant differences ($P > 0.05$) in average positive area between the four cohorts in terms of vimentin-positive cells.

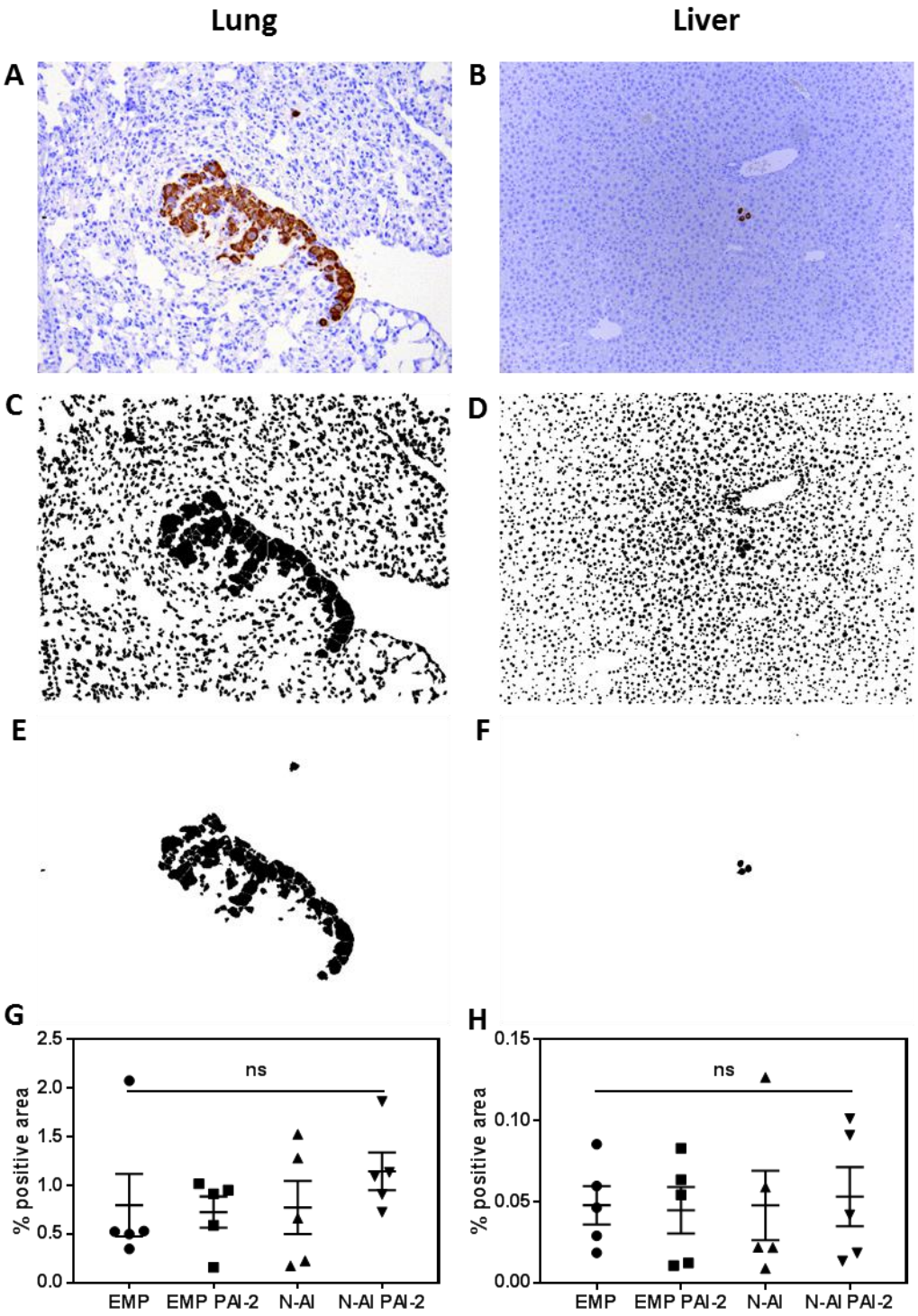

Figure 4.13: Immunohistochemistry analysis of lung and liver metastasis. Mice bearing intraductal MDA-MB-231 tumours were treated with empty liposomes (EMP), empty PAI-2-functionalised liposomes (EMP PAI-2), *N*-AI-loaded liposomes (*N*-AI) or *N*-AI-loaded PAI-2-functionalised liposomes (*N*-AI PAI-2). (**A-B**) Lung and liver sections were stained with vimentin (metastatic cells). (**C-D**) Representative total masks (all cells) using automated imaging analysis. (**E-F**) Representative positive masks (metastatic cells) using automated imaging analysis. (**G-H**) Percentage of vimentin-positive area (metastatic cells) relative to total cell area. Values are means ± s.e.m. (n = 5). n.s. = not significant ($P > 0.05$).

4.4 Discussion

Determining the *in vivo* properties of novel nanotherapies using animal models is important for evaluating how a new nanoparticle formulation can be expected to perform in humans. In this chapter, the pharmacokinetics, biodistribution and anti-tumour efficacy of *N*-AI-loaded PAI-2-functionalised (*N*-AI PAI-2) liposomes were evaluated using two different breast cancer xenograft mouse models. The addition of PAI-2 to the surface of *N*-AI-loaded liposomes did not significantly alter the *in vivo* clearance properties of the formulation but did appear to increase accumulation of liposomes at the primary tumour site in an orthotopic MDA-MB-231 BALB/c-Fox1nu/Ausb xenograft mouse model relative to non-functionalised liposomes. Despite this increase in tumour uptake, the anti-tumour efficacy of *N*-AI PAI-2 liposomes relative to non-functionalised *N*-AI-loaded liposomes and empty control liposomes was not significantly different in the two mouse models used.

Understanding the pharmacokinetic properties and tissue distribution of nanoparticle formulations is essential to determine circulation time, clearance mechanisms and how well the nanoparticle reaches and accumulates at the site of primary and metastatic tumours (Allen & Cullis 2013). Importantly, the pharmacokinetic profile reveals the circulation half-life of a nanoparticle, a characteristic of particular importance for nanotherapies as the enhanced permeability and retention (EPR) effect is the primary mechanism by which nanoparticles are thought to target tumours and exhibit anti-tumour effects (Maeda 2015). The plasma circulation time of liposomes has been shown to be dependent on their lipid composition, size, surface charge, morphology and other physicochemical characteristics, as the dominant mechanism by which liposomes are typically cleared from the bloodstream is based on interactions with phagocytic cells of the mononuclear phagocyte system (MPS). The inclusion of PEG at the outer surface of the liposome can increase the *in vivo* circulation time by reducing recognition and clearance by the MPS (Uster et al. 1996). Therefore, PEGylated liposomes reportedly have decreased rates of clearance as PEG at the nanoparticle surface helps to shield the nanoparticle from the innate immune response.

In this work, *N*-AI and *N*-AI PAI-2 PEGylated liposomes both exhibited an average plasma half-life in mice of approximately 6 hours (5.63 h and 5.82 h, respectively) (Fig.

4.1). This plasma half-life is comparable to other reports of PEGylated liposomes, which typically exhibit a plasma half-life of several hours (Krishna et al. 2001; Vijayakumar et al. 2016). The organ accumulation of *N*-AI and *N*-AI PAI-2 liposomes was in accordance with the general clearance pattern typically seen for nanoparticles, with high degrees of clearance from the spleen, liver and kidneys (Dams et al. 2000) (Fig. 4.2). The biodistribution profile of the two liposome preparations correlates with the known general patterns of clearance of PEGylated liposomes from the blood, with a drop in liposome plasma concentration at the 6 h time point correlating with increased liposome clearance primarily by the spleen (indicative of clearance via the MPS), in addition to the liver, and comparatively low clearance by the kidneys and lungs (Litzinger et al. 1996) (Fig. 4.3). Clearance via the spleen was significantly higher ($P < 0.05$) at the 48 h time point for *N*-AI liposomes (78.5 ± 32.2 % ID/g tissue) compared to *N*-AI PAI-2 liposomes (44.2 ± 6.7 % ID/g tissue), which is not unexpected given that the presence of functional groups on the surface of nanoparticles can affect clearance via the MPS (Alexis et al. 2008). While the *N*-AI and *N*-AI PAI-2 liposomes were equivalent in diameter (115 ± 34 nm and 117 ± 39 nm, respectively), the observed difference in spleen accumulation may be due to the difference in surface charge between the liposomes (–3.64 ± 0.59 mV and –4.66 ± 0.52 mV, respectively) (Chapter 2, Section 2.3.3). However, the result obtained in this study contrasts with the general trend observed in previous studies, which report that nanoparticles with a greater negative charge show greater clearance via the spleen (He et al. 2010) and liver (Xiao et al. 2011). The decreased spleen accumulation of *N*-AI PAI-2 liposomes relative to *N*-AI liposomes at the 48 h time point may be due to the increased tumour accumulation of *N*-AI PAI-2 liposomes at earlier time points.

The accumulation of nanoparticles in tumours via the EPR effect is dependent on a number of factors, including interstitial fluid pressure, vascularity of the tumour and the *in vivo* circulation time of the nanoparticle formulation (Nichols & Bae 2014). The results presented here indicate a trend of increased tumour uptake of *N*-AI PAI-2 liposomes over *N*-AI liposomes. Tumour accumulation of *N*-AI PAI-2 liposomes was significantly higher ($P < 0.001$) than *N*-AI liposomes at the 10 min, 3 h and 6 h time points (Fig. 4.4). After the 6 h time point, the tumour accumulation of *N*-AI and *N*-AI PAI-2 liposomes was not significantly different. As the plasma half-lives of the two liposomes were equivalent (Fig. 4.1), the presence of PAI-2 at the liposome surface may have affected liposome

extravasation and uptake at the tumour site. This may have been due to PAI-2 liposomes binding to uPAR expressed by tumour cells, as was observed in Chapter 3 in the *in vitro* uptake and cytotoxicity testing of non-functionalised and PAI-2-functionalised liposomes. The difference in uptake may also be due to other differences between *N*-AI and *N*-AI PAI-2 liposomes. For example, as mentioned above, *N*-AI PAI-2 liposomes had a slightly more negative surface charge than *N*-AI liposomes, and surface charge has been shown to affect tumour uptake of nanoparticles (Xiao et al. 2011).

The maximum tumour accumulation of the liposomes was 0.5% of the ID at the 10 min time point for *N*-AI PAI-2 liposomes and 0.02% for *N*-AI liposomes (Fig. 4.4). These values are comparable to other PEGylated nanoparticles, which typically show approximately 1% or less of the total ID reaching the site of the primary tumour. Generally, the percentage of the total ID of nanoparticles administered intravenously reaching the target site is quite low: the median value has been reported as 0.7% (Wilhelm et al. 2016). While the circulation time of nanoparticles is typically much longer than that of small molecules (as would be expected for free *N*-AI), a longer half-life is optimal for achieving tumour targeting, as the EPR effect relies on the nanoparticles remaining in circulation long enough to reach tumours and extravasate at those sites, which in turn drives enhanced tumour uptake, and accumulation and retention of liposomes for anti-tumour effect (Grimaldi et al. 2016). Notably, the high tumour accumulation of Doxil® in humans (reported as high as 10% of the ID) is due in large part to the very long circulation half-life (up to 45 h) of the formulation (Gabizon et al. 1994).

The biodistribution and pharmacokinetics experiment indicated that *N*-AI PAI-2 nanoparticles reached the site of the primary tumour from a single intravenous injection, with an apparent increase in tumour localisation of the *N*-AI PAI-2 liposomes compared to *N*-AI liposomes. To determine whether this tumour accumulation of *N*-AI PAI-2 liposomes would translate into a reduction in primary tumour growth rates, mice bearing large tumours (approximately 200 mm^3) were injected three times per week for 2 weeks and tumour volume was measured to detect any changes to the tumour growth rate (Fig. 4.6). Final organ weights were the same across all treatment cohorts (Fig. 4.7), supporting the results of a previous toxicology study that showed *N*-AI-loaded liposomes were not toxic at the multiple dosing schedule used, and that the maximum tolerated dose (MTD)

of *N*-AI-loaded liposomes was not reached at 100 mg/kg, the highest dose tested (Appendix D). Despite the lack of toxicity, in this study, no significant differences were observed in tumour growth rates, final tumour size or final tumour weight between the EMP liposome, *N*-AI liposome and *N*-AI PAI-2 liposome treatments (Fig. 4.6 and Fig. 4.8). There may be several reasons for this observation.

In contrast to the biodistribution study, where the starting tumour volume was approximately 100 mm^3, tumours in this cohort were higher at the commencement of treatment, which may have meant that treatment started too late to result in any significant primary tumour growth delay. There was also a large degree of variability between tumour volume and growth rates among individual animals within the same cohorts, which made it difficult to determine differences between treatments, even with a sample size of 8 animals per treatment cohort (Fig. 4.8). Additionally, it is unknown whether primary tumours were sufficiently vascularised during the treatment timeframe, which would be needed to allow the liposomes to enter and reach the tumour area to exert an anti-tumour effect (Nichols & Bae 2014). This is an important factor, because for solid tumours that are poorly vascularised, any significant accumulation of nanoparticles in the vicinity of the tumour via the EPR effect is unlikely (Bahrami et al. 2017). The high degree of variability in starting tumour size may have meant differing degrees of tumour vascularisation, which may have translated to different degrees of the EPR effect and therefore varied liposome delivery to the tumours. While *N*-AI and *N*-AI PAI-2 liposomes were shown to accumulate at the site of primary tumours in this mouse model, given that the plasma half-life of the liposomes was 6 h, the liposomes may not have accumulated at the primary tumour site in large enough numbers to have a significant anti-tumour effect at the biweekly dosing schedule used. Therefore, an increased frequency of liposome administration may have been more suitable in increasing *N*-AI at the tumour site for an anti-tumour effect. However, in addition to being impractical for the researcher, frequent intravenous injections via the lateral tail veins may bring up ethical issues, as the injection site should be allowed to heal adequately before additional injections are made (Turner et al. 2011).

As uPAR-positive breast cancer cells have a high propensity to metastasise (Chapter 1, Section 1.5), a mouse model of metastatic uPAR-positive breast cancer was used to assess

the potential anti-tumour effect of *N*-AI PAI-2 liposomes on both primary tumours and on micrometastases (Young et al. 2016). Mice were treated with EMP, EMP PAI-2, *N*-AI and *N*-AI PAI-2 liposomes on a triweekly injection schedule for a total of 5 weeks. Previous work has shown that free *N*-AI has a potent anti-tumour effect on primary tumours at a dose of 10 mg/kg (Vine et al. 2012). In this experiment, *N*-AI or *N*-AI PAI-2 liposomes administered at a total dose of 51.7 mg/kg did not demonstrate an anti-tumour effect on primary tumours (Fig. 4.9). Further, the *N*-AI PAI-2 liposome treatment did not differ significantly from *N*-AI liposomes or EMP PAI-2 liposomes, indicating that under the treatment conditions used, the combination of *N*-AI and PAI-2 does not have a synergistic anti-tumour effect in this model. As observed in the orthotopic breast tumour xenograft model described in Section 4.3.2, this intraductal breast tumour xenograft model also showed a high degree of variability in primary tumour growth and formation of metastases of individual animals within each cohort (Fig. 4.9 and Fig. 4.13). Original reports of this model using a variant of the MDA-MB-231 cell line also showed a high degree of variability among tumour growth of mice within treatment cohorts, which was reflected by a high variability (approximately 3 weeks) of the time to detection of initial primary tumour development in control mice (Young et al. 2016). Therefore, the statistical power of this model may have been limited by a high degree of biological variability.

Previous experiments using the MDA-MB-231 intraductal xenograft model showed that antagonism of the survival factor myeloid cell leukemia-1 suppressed metastasis in TNBC xenografts (Young et al. 2016). Analysis of the mammary whole mounts in the current work showed no significant differences in secondary tumour formation in the mammary gland where the primary tumour was located (Fig. 4.11). This may be due to the fact that mammary glands could not be dissected from all mice, only from those where the primary tumour had not taken over entire mammary gland, limiting the total numbers available for analysis. No significant differences between treatment cohorts were found when primary tumours were stained with cleaved caspase-3 (Fig. 4.12), likely because the tumours were large at the experimental endpoint and the majority of the tumour core contained apoptotic cells. Vimentin was used to detect metastatic human cells in the lungs and liver, the tissues where MDA-MB-231 cells have been reported to metastasise in this mouse model (Young et al. 2016). While metastatic human cells were detected in the

lungs and liver of some mice, the low levels of metastasis in the control mice (EMP liposome treated) at the experimental endpoint meant that the number of vimentin-positive cells detected per animal was relatively low (Fig. 4.13). Due to this, as well as the high degree of variability between individual animals in this model, significant differences between treatment groups could not be detected. If experiments using this model are repeated, an extended time frame should be used to ensure sufficient metastatic burden to the lungs and liver in control mice in order to detect potential changes in the number of metastatic cells of mice in the treatment groups. A superior way to conduct these experiments would be to utilise bioluminescent live imaging techniques (for example, using luciferase-tagged tumour cells) so that tumour growth and metastatic burden could be monitored in real time, helping to inform the decisions of when to start and end liposome treatments (Tung et al. 2016).

An additional rationale for the use of non-invasive imaging techniques in *in vivo* experiments for testing liposomes is to elucidate the degree to which the EPR effect is occurring in these models (Chapter 1, Section 1.6). This is important as the EPR effect is reported to be highly variable and is not observed for all solid tumours, especially poorly vascularised tumours (Nichols & Bae 2014; Wang 2015). The EPR effect is also known to be highly variable between different animal models, different disease models, and between animals and humans (Hare et al. 2017). As the rate of animal tumour growth and resultant angiogenesis are reportedly much greater than the formation of tumours in humans (Maeda 2015), this results in a more pronounced EPR effect in animal models, which may partially explain why many nanotherapies that show promise in *in vivo* studies fail in clinical trials (Nichols & Bae 2014). Further research is required to better understand the EPR effect and elucidate the differences in this phenomenon between animal and human tumours, and between different tumour types, in order to increase the translation of nanoparticle-based therapeutics into the clinic (Lammers et al. 2016). This could be achieved via imaging methods, such as the radionuclide imaging of liposomes to determine their fate *in vivo* (van der Geest et al. 2016). Single photon emission computed tomography (SPECT) and positron emission tomography (PET) have previously been used to quantify the *in vivo* distribution of nanoparticles, including accumulation of nanoparticles at the tumour site, in a non-invasive manner (Harrington et al. 2001). The use of nanoparticles in conjunction with such imaging techniques may

also have theranostic applications, whereby both diagnostic and therapeutic agents are utilised in order to better guide and monitor treatment (Chen et al. 2017).

While the biophysical properties of a nanoparticle formulation affect the plasma circulation time, clearance properties, and therefore tumour accumulation *in vivo*, it is important for future research to consider and evaluate the interactions of nanoparticles with cells of the immune system and clearance organs, since nanoparticles that are filtered out of the blood and end up in liver and spleen do not reach their intended target, which limits the therapeutic effect. The frequent use of xenograft models to allow the study of human cancer cells in mouse models means that immunocompromised mice are used in order to prevent rejection of the human xenografts. Given the known effect of the adaptive immune system in tumour growth and metastasis (Kitamura et al. 2015), there is a need for tumour models in immunocompetent animals in addition to the often used immunocompromised models that eliminate potential effects of the immune system in the evaluation of new anticancer therapies (Gomez-Cuadrado et al. 2017). The increasing use of such models lends itself to the improved assessment of targeted therapies in the context of cancer treatment (Budhu et al. 2014).

Previous studies have shown that the plasma circulation time is dependent not only on the biophysical properties of the liposome formulation but also on the number of injections administered (Dams et al. 2000). This phenomenon is relevant to efficacy studies, which typically involve administration of multiple doses of a nanoparticle formulation to maximise therapeutic effect. The accelerated blood clearance (ABC) phenomenon describes how the first dose of a PEGylated nanoparticle may affect the pharmacokinetic properties of subsequent doses. Specifically, ABC describes an increased clearance rate of PEGylated nanoparticles from the blood with second and subsequent intravenous injections of the nanoparticle formulation (Laverman et al. 2001; Oussoren & Storm 1999), and is dependent on the lipid dose administered and duration of the administration interval (Gabizon et al. 2008; Laverman et al. 2001). In this context, reduced circulation time correlates with increased liver and spleen accumulation (Laverman et al. 2001). The ABC phenomenon has been described for PEGylated liposomes, polymeric nanoparticles and PEGylated solid lipid nanoparticles delivered intravenously (Szebeni & Storm 2015). While the exact mechanism of the ABC phenomenon remains unknown, a key identified

mechanism is the production of anti-PEG IgM following the first injection, which selectively binds to the surface of subsequently injected PEGylated particles and acts to accelerate clearance by substantial complement activation (Szebeni 2014). In immunocompromised mice, this mechanism is unlikely. However, Doxil® has been reported to activate the complement system (innate immune system) in animals and humans, leading to a hypersensitivity reaction known as complement activation-related pseudoallergy (CARPA), which can impact upon the pharmacokinetic and pharmacodynamic properties of the drug (Szebeni et al. 2016). Such research demonstrates that the ABC phenomenon is an important factor to consider in the design and development of PEGylated liposomes and other nanoformulations for repeat dosing therapeutic applications.

Another key consideration for testing new nanotherapies, particularly those that are actively targeted, is the use of models that recapitulate intratumoural heterogeneity. The injection of a human cancer cell line into an animal to create an *in vivo* tumour model largely fails to represent the heterogeneity observed in human tumours since cells within a cell line are clonally similar (Alizadeh et al. 2015). This means that any treatment tested is expected to affect most, if not all, cells in that model in the same way, which is not representative of the clinical situation (Zardavas et al. 2015). Therefore, the use of these models in developing and testing novel therapies, especially dual-targeted therapies that are designed to address intratumoural heterogeneity, is limited as they do not permit evaluation of the effects of differential cell targeting and therapeutic resistance when determining anti-tumour efficacy. Patient-derived xenografts can be more representative of the clinical situation as they capture some elements of intratumoural heterogeneity, as well as the diversity observed between patients with cancer (Gomez-Cuadrado et al. 2017). In addition to intratumoural heterogeneity, the interpatient heterogeneity observed in cancer also warrants the development and utilisation of patient-derived cell lines to more accurately assess patient responses to novel therapies, particularly in cases where resistance to currently used therapies is frequently observed (Shafaee & Ellis 2017).

A final consideration in the testing of novel ligand-functionalised liposomes involves the question of what happens to liposome integrity, ligand attachment, ligand function, and therefore the biophysical properties of a liposome formulation after intravenous

administration, which affects *in vivo* circulation time and clearance properties. For example, the well-documented propensity of biological molecules, especially proteins, present in the bloodstream to associate non-specifically with the surface of liposomes *in vivo* and the subsequent formation of a protein corona around the liposome may affect numerous biophysical properties of a liposome formulation (Caracciolo et al. 2017). In the case of ligand-functionalised liposomes, the physical presence of a protein shield around the surface of the liposome, including association of plasma proteins with liposome ligands, may act to inhibit binding of the liposome targeting ligand with its target receptor, which would affect the targeting success *in vivo* (Shi et al. 2017). These potential changes to the liposome are usually unaccounted for but could have significant effects on the anticipated biodistribution, pharmacokinetic and efficacy profiles of a liposome formulation, and are therefore important factors to consider when testing liposomes in biological systems (Walkey & Chan 2012).

4.5 Conclusion

The work presented in this chapter reports novel data on the pharmacokinetics and biodistribution of *N*-AI and *N*-AI PAI-2 liposomes, as well as the efficacy of multiple doses of *N*-AI PAI-2 liposomes in two mouse models bearing orthotopic uPAR-positive breast tumour xenografts. While increased tumour uptake of *N*-AI PAI-2 liposomes over *N*-AI liposomes was observed, further research is needed to clarify if and how the potency of *N*-AI as a cytotoxin can be translated into an anti-tumour growth effect by targeting uPAR-positive tumours. The utilisation of more advanced preclinical models and methods will enable enhanced evaluation of *N*-AI PAI-2 liposomes in the *in vivo* context.

Chapter 5:
Quantification of Ligand Density and Stoichiometry on the Surface of Liposomes by Single-Molecule Fluorescence Microscopy

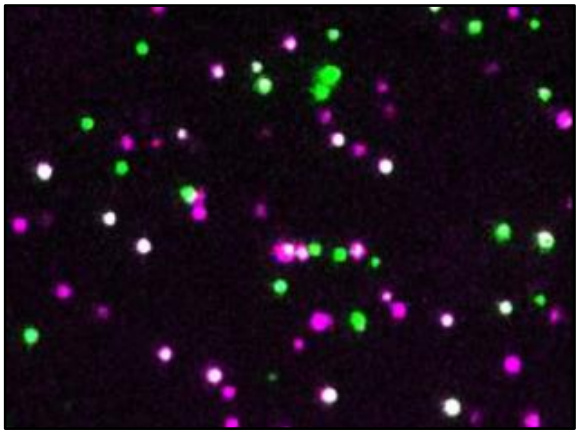

Single-molecule fluorescence imaging of liposomes

Portions of this chapter have been published in the following work:

Belfiore, L, Spenkelink, LM, Ranson, M, van Oijen, AM & Vine, KL 2018, 'Quantification of ligand density and stoichiometry on the surface of liposomes using single-molecule fluorescence imaging', *Journal of Controlled Release*, vol. 278, pp. 80-86.

Author contributions: LB, LMS, MR, AMvO and KLV designed the experiments; LB and LMS performed the experiments and analysed the data; LB and LMS wrote the manuscript; MR, AMvO and KLV edited the manuscript for submission.

5.1 Introduction

The work described in Chapter 2 of this thesis detailed the preparation and characterisation of novel *N*-alkylisatin (*N*-AI)-loaded, plasminogen activator inhibitor-2 (PAI-2)-functionalised liposomes. The confirmation and quantification of PAI-2 ligand attachment to the surface of liposomes were attempted using biochemical protein assays, size-exclusion chromatography and Western blotting, but these methods could not provide direct and robust quantification of the average number of ligands attached to the surface of each liposome. This characteristic of an actively targeted liposome formulation is essential to enable the optimisation of ligand density to ensure optimal tumour cell uptake, as well as for quality control purposes such as accounting for batch-to-batch variability. Ligand quantification is particularly important for dual-ligand liposomes, for which the quantification of both the number and ratio of multiple different ligands attached to the liposome surface is needed to achieve optimal target cell effect. Currently, there are no methods to comprehensively characterise actively targeted liposomes in terms of precise surface ligand quantification. Therefore, there is a need to develop new methods to quantify the density and stoichiometry of ligands on the surface of ligand-functionalised liposomes to facilitate their preclinical evaluation, pharmaceutical scale-up and manufacture, and ultimately, their utilisation in clinical applications.

5.1.1 Current approaches for liposome ligand quantification

Liposomes have been utilised as delivery systems for drugs and other molecules *in vivo* for several decades (Grimaldi et al. 2016). Despite extensive research into the development of nanoparticle-based therapeutics, all clinically approved liposome formulations are non-ligand-directed, with efficacies relying solely on passive targeting and accumulation (Estanqueiro et al. 2014). A comprehensive list can be found in Chapter 1, Table 1.2, and in the published literature (Shi et al. 2017). Active targeting strategies using liposomes have been extensively explored in the preclinical setting, particularly liposomes targeting tumour-associated receptors, with many reported formulations demonstrating improved efficacy over non-ligand-directed liposomes (Lukyanov et al. 2004; Park et al. 2001). Given the general movement in the field towards actively targeted nanotherapeutics, the lack of translation of ligand-directed liposome formulations into clinical practice is somewhat surprising (Anchordoquy et al. 2017). Previous reviews

have identified some of the likely reasons for this phenomenon, ranging from methodological difficulties involved in the large-scale preparation of ligand-directed liposomes, to the limitations of evaluating their efficacy in preclinical models that fail to adequately recapitulate human tumours (Hare et al. 2017). For example, once liposomes are administered intravenously, non-specific interactions of liposomes with a range of plasma proteins may result in the formation of a protein 'corona' at the liposome surface, effectively shielding liposome-bound targeting ligands from interacting with their target receptors and therefore negating their intended tumour cell targeting ability (Caracciolo et al. 2017).

The absence of molecular tools for the robust characterisation of complex liposomes may also be contributing to the lack of clinically approved ligand-directed liposomes. Specifically, no methodology exists to quantify the number of ligands covalently bound to the surface of liposomes. Estimation of ligand conjugation is possible based on preparation parameters, but direct measurement of total surface-bound protein using standard biochemical assays has inherent limitations. For example, measurement of surface-bound protein in an actively targeted liposome formulation using colourimetric biochemical methods is challenging due to phospholipid interference in the measurement of very low protein concentrations (Klegerman et al. 2002). Flow cytometric methods that detect the insertion of fluorescently labelled micelles into liposomes as a proxy for successful liposome functionalisation (Chapter 2, Section 2.3.9) have been reported but are indirect and semi-quantitative (Mack et al. 2012). While current methods could potentially be used to quantify the total amount of protein in a sample, they cannot provide information about the average number of ligands bound to each liposome in a formulation. Thus, there is a need for fine-scale, single nanoparticle resolution.

The lack of quantitative methodology poses a particular challenge for the development of liposomes with more than one surface-bound ligand, since the determination of ligand stoichiometry is important to control for batch-to-batch variability in the laboratory and for clinical production (Belfiore, L. et al. 2018). The absence of rigorous quantification protocols hinders high-quality large-scale manufacturing of ligand-directed liposome formulations, which may introduce regulatory barriers and slow down their introduction to the clinic. This is because without quantification methods, it is difficult to ascertain the

effects of different liposome preparation or purification methods on the resultant ligand density of the liposome formulation. For example, in the laboratory setting, size-exclusion chromatography (SEC) is commonly used to remove unconjugated ligands from liposomes but is not high-throughput. Alternative methods more amenable to scaling up, such as high-speed centrifugation, are more favourable, but it remains unknown whether centrifugation changes the ligand density of the final preparation. Such questions may be answered using a robust quantitative methodology.

5.1.2 Single-molecule fluorescence microscopy

Single-molecule fluorescence microscopy is a high-resolution imaging technique that removes ensemble averaging, allowing the direct visualisation of population distributions and the precise characterisation of subpopulations (Monachino et al. 2017). The single-molecule fluorescence microscope removes out-of-focus background fluorescence of the imaged sample by utilising total internal reflection fluorescence (TIRF), enabling the detection of individual fluorescently labelled molecules. Laser light of a specific wavelength is coupled into the microscope objective, and the fluorescent signal from the sample is detected with an electron-multiplying charge-coupled device (EMCCD) camera (Fig. 5.1). By tracking the photobleaching steps of individual fluorescently labelled molecules, the number of fluorophores per molecule and the total number of molecules can be determined.

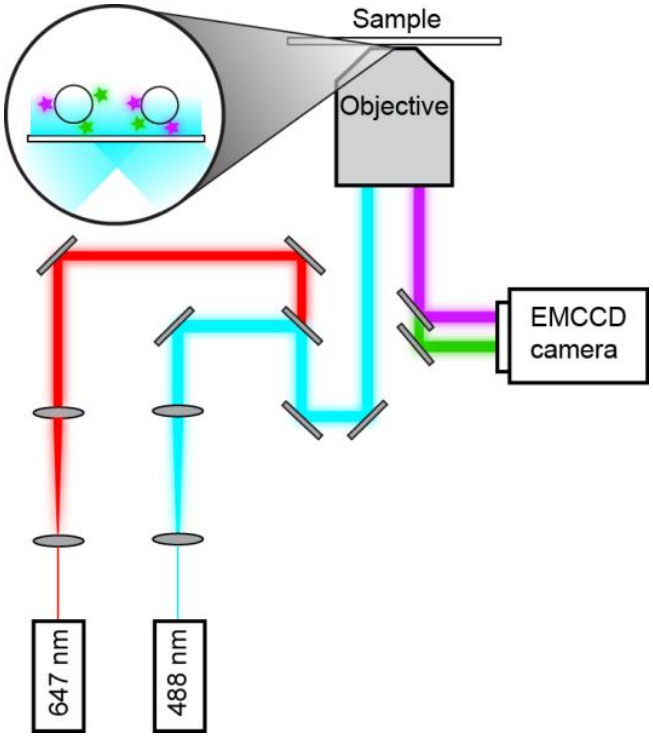

Figure 5.1: Schematic overview of the single-molecule fluorescence microscope. Laser light of a specific wavelength is coupled into the microscope objective. The fluorescent signal from the sample is detected with an electron-multiplying charge-coupled device (EMCCD) camera.

Single-molecule methods have already proven to be important biophysical tools for studying a wide variety of biological processes (Shashkova & Leake 2017), including mechanisms of DNA replication (Ticau et al. 2017), conformational changes of enzymes (Marchetti et al. 2017) and the composition and assembly of various multiprotein complexes (Aggarwal & Ha 2016). However, single-molecule microscopy remains an under-utilised technique in therapeutics development. Based on how the technique has been previously used to quantify proteins that have been fluorescently labelled with fluorophores (Choi et al. 2012; Tessler & Mitra 2011), it should be possible to use the technique to count protein ligands bound to liposomes. Liposomes can be labelled with fluorescent dyes, such as octadecyl rhodamine B chloride (R18), which only fluoresce when bound to lipid membranes (Nunes-Correia et al. 2002). Lipid vesicles have previously been imaged using single-molecule fluorescence microscopy in the context of studying protein-membrane interactions (Chadda & Robertson 2016; Liu et al. 2010). In a similar way, liposomes and other nanoparticles that have surface-attached protein (or other) ligands can be studied using this high-resolution imaging technique.

5.1.3 Experimental rationale

Despite the longstanding existence of liposome technology in drug delivery applications, there have been no ligand-directed liposome formulations approved for clinical use to date. This lack of translation is due in part to the absence of molecular tools available for the robust quantification of ligands on the surface of liposomes, which is necessary for optimising liposome preparation in the preclinical context, and eventually, to comprehensively characterise an actively targeted liposome formulation as required for clinical application. The successful development of a new and accurate method to quantify liposome ligands should help facilitate the production of actively targeted liposomes and their improved preclinical characterisation.

5.1.4 Aims

This chapter tested the hypothesis that single-molecule fluorescence microscopy can be used to determine the number of protein ligands bound to functionalised liposomes. Therefore, the overarching aim of this chapter was to develop single-molecule fluorescence microscopy as a tool for the quantification of ligands bound to the surface of liposomes. Specifically, the aims of this chapter were to:

1. Quantify the ligand density and stoichiometry of both single-ligand and dual-ligand liposomes using single-molecule fluorescence microscopy;
2. Determine the effect of size-exclusion chromatography and centrifugation on the resultant ligand density of actively targeted liposome formulations; and
3. Determine the effect of conventional and post-insertion functionalisation methods on the resultant ligand density of actively targeted liposome formulations.

5.2 Methods

5.2.1 Labelling proteins with fluorophores

Human recombinant plasminogen activator inhibitor-2 (PAI-2), produced in-house by previously published methods (Cochran et al. 2009), and trastuzumab (TZ, Herceptin®; Genentech, CA, USA) were labelled with CF488 or CF647 succinimidyl ester fluorescent dyes (Sigma-Aldrich, MO, USA) as per the manufacturer's instructions. Absorbance at 280 nm (protein) and 488 nm or 647 nm (dye) was used to calculate the protein

concentration and degree of labelling (DOL). DOL was further confirmed by electrospray ionisation mass spectrometry (ESI-MS).

5.2.2 Electrospray ionisation mass spectrometry

Positive ion mass spectra of unlabelled and labelled proteins were acquired on a quadrupole time of flight mass spectrometer (Micromass Q-TOF Ultima; Waters, MA, USA) fitted with a Z-spray ionisation source. Samples in phosphate-buffered saline (PBS; pH 7.4) were exchanged into deionised water containing 0.1% formic acid and made up to a final concentration of approximately 10 μM. The mass spectra were acquired with a capillary voltage of 2.6 kV, a cone voltage of 50 V, a source block temperature of 40 °C, and a resolution power of 5000 Hz. Caesium iodide was used for external calibration. Mass was calculated using MassLynx MS V4.1 (Waters, MA, USA).

5.2.3 Liposome preparation

Liposomes were prepared using the thin film hydration method as described previously (Uster et al. 1996). Dipalmitoylphosphatidylcholine (DPPC), cholesterol, 1,2-distearoyl-*sn*-glycero-3-phosphoethanolamine-*N*-[(polyethylene glycol)-2000] (mPEG$_{2000}$-DSPE) and 1,2-distearoyl-*sn*-glycero-3-phosphoethanolamine-*N*-[maleimide(polyethylene glycol)-2000] (mal-PEG$_{2000}$-DSPE) (Avanti Polar Lipids, AL, USA) in a 20:10:0.8:0.2 molar ratio (conventional (CO) method), or DPPC, cholesterol and mPEG$_{2000}$-DSPE in a 20:10:0.6 molar ratio (post-insertion (PI) method), were dissolved in chloroform/methanol (2:1 v/v). For colocalisation experiments, liposomes were labelled with octadecyl rhodamine B chloride (R18; Invitrogen, CA, USA) by adding R18 to the chloroform/methanol solution in a 160:1 molar ratio (liposome phospholipid:R18). Organic solvents were removed by rotary evaporation and subsequent freeze-drying to form a lipid film.

Phospholipids were reconstituted in degassed HEPES buffer (115 mM NaCl, 20 mM HEPES, 2.4 mM K_2PO_4, 1.2 mM $CaCl_2$, 1.2 mM $MgCl_2$; pH 7.4) at a concentration of 20 mM. Once reconstituted, liposomes were passed once through a 0.22 μm polyvinylidene fluoride (PVDF) membrane (Merck Millipore, MA, USA) and then serially extruded 11 times through a 0.1 μm PVDF membrane using a syringe-driven extruding apparatus

(Avanti Polar Lipids, AL, USA) at a temperature of 50°C (above the phase-transition temperature of DPPC). Liposomes were analysed by dynamic light scattering (DLS) to determine particle diameter using a Zetasizer APS (Malvern Instruments, Malvern, UK). Liposomes were surface-functionalised with CF647 labelled PAI-2 and CF488 labelled PAI-2 or TZ using either the CO method or the PI method (Fig. 5.2) (Iden & Allen 2001).

For the CO method, preformed liposomes were incubated with thiolated CF dye labelled PAI-2 or TZ (at a molar ratio of 3333:1 liposome phospholipid:protein) for 2 h at room temperature. For the PI method, micelles composed of 0.8 mM mal-PEG_{2000}-DSPE and 0.2 mM $mPEG_{2000}$-DSPE were prepared as per previously reported methods (Moreira et al. 2002), and CF dye labelled PAI-2 or TZ was added to the micelles (at a molar ratio of 10:1, mal-PEG_{2000}-DSPE:protein) to form functionalised micelles. Functionalised micelles were added to preformed liposomes and heated to 60°C for 1 h to facilitate the post-insertion of micelle lipids into the outer leaflet of the liposomes. Following the liposome functionalisation steps, unbound protein was removed from liposomes via either size exclusion chromatography (SEC) using Sepharose CL-4B (Sigma-Aldrich, MO, USA) or repeated centrifugation at 20,000 x g for 1.5 h at 4°C. Liposomes were resuspended in HEPES buffer (pH 7.4) for single-molecule fluorescence imaging.

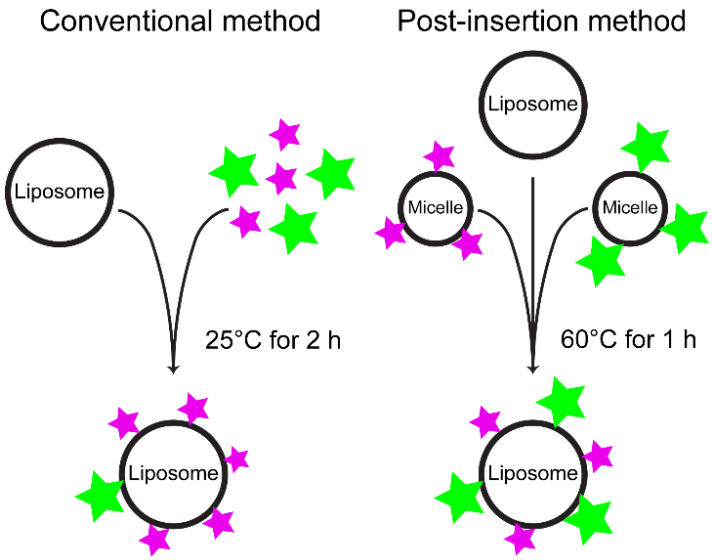

Figure 5.2: Conventional and post-insertion methods for ligand conjugation. The conventional method involves incubation of preformed liposomes with thiolated proteins (represented by green and magenta stars), which attach covalently to the liposome surface via terminal maleimide functional groups. The post-insertion method involves attaching thiolated proteins to maleimide-functionalised micelles, which are then incubated with preformed liposomes at 60°C to facilitate the transfer of micelle phospholipids with covalently attached proteins into the outer leaflet of the liposome bilayer.

5.2.4 Intensity measurements for labelled proteins

Microscope coverslips were thoroughly cleaned to remove any hydrophobic and hydrophilic contaminants that could cause background fluorescence from the glass. They were first sonicated for 30 min in ethanol (Chem-Supply, SA, AUS) and then rinsed with deionised water. Subsequently, they were sonicated for 30 min in 1 M potassium hydroxide (KOH; Sigma-Aldrich, MO, USA) and rinsed with deionised water again. After these sonication steps were repeated, the coverslips were dried with N_2 (Tanner & van Oijen 2010). CF dye-labelled proteins were diluted to a concentration of approximately 10 pM and immobilised on the surface of the cleaned microscope coverslip for visualisation on an inverted microscope (Nikon Eclipse Ti-E) with a CFI Apo Total Internal Reflection Fluorescence (TIRF) 100X oil-immersion TIRF objective (NA 1.49, Nikon). The green- and red-labelled proteins were excited at 1.5 W cm^{-2} with 488 nm (Coherent, Sapphire 488-200 CW) and 647 nm (Coherent, Obis 647-100 CW) lasers, respectively (Fig. 5.1). The signals were separated via dichroic mirrors (Photometrics, DVΛ Multichannel Imaging System) and appropriate filter sets (Chroma). The imaging was performed with an EMCCD camera (Photometics, Evolve 512 Delta).

For each measurement, at least two coverslips were used. For each coverslip, multiple (5-10) fields of view were imaged. Using ImageJ (National Institutes of Health, USA) with in-house built plugins, the integrated intensity for single CF dyes over time was calculated after applying a local background subtraction. Using a change-point step-fitting algorithm, the intensity distributions for a single CF fluorophore were calculated (Fig. 5.3B) (Duderstadt et al. 2016; Watkins & Yang 2005). The histograms obtained were fit with either a Gaussian or Poisson distribution function using MATLAB 2014b to give a mean intensity of $3 \pm 0.1 \times 10^3$ for CF647 (Fig. 5.3C) and $1.2 \pm 0.6 \times 10^4$ for CF488. To measure the number of fluorophores per protein, the initial fluorescence intensity per protein was divided by the intensity of a single fluorophore.

5.2.5 Measurement of protein density on liposomes

To determine the average number of proteins per liposome, liposomes were imaged under the same conditions as the proteins, and the fluorescence intensity per liposome was

calculated analogously. The number of proteins per liposome was obtained by dividing the liposome intensities by the intensity of a single protein.

5.2.6 Data analysis

All data analysis, including the generation of graphs and statistical tests, was performed using GraphPad Prism software (version 7), unless stated otherwise. Data are presented as the mean ± standard deviation (s.d.) or standard error of the mean (s.e.m.) as stated. Pairwise comparisons were made using Student's t-test, and multiple comparisons were made using one-way ANOVA with Tukey's post-test.

5.3 Results

5.3.1 Imaging CF647-labelled PAI-2

To first visualise PAI-2 using single-molecule fluorescence microscopy, the 45 kDa protein was labelled with a small red fluorophore (CF647) and imaged using TIRF microscopy, which allowed for the selective excitation of only the fluorescent species on the coverslip surface and imaging of fluorescence from surface-immobilised proteins with high contrast and low background (Fig. 5.3A). The intensity of the signal of every individual protein was measured over time (Fig. 5.3B, black line). The fluorescence intensity trajectories showed a stepwise decay towards zero due to photobleaching of the fluorophores attached to the protein. As the height of a single step corresponds to the intensity of a single fluorophore, the number of fluorophores per protein was determined by counting the number of steps. Analysis of numerous spots enabled a distribution to be fitted for the number of fluorophores per protein and for the fluorescence intensity per fluorophore. The intensity of a single fluorophore was determined using an unbiased change-point step-fitting algorithm (Fig. 5.3B, red line) (Duderstadt et al. 2016). The mean intensity of a single CF647 fluorophore was $3 \pm 0.1 \times 10^3$ (mean ± s.e.m., n = 962) (Fig. 5.3C). By dividing the total intensity per protein by the intensity of a single fluorophore, it was calculated that there are 1.5 ± 0.4 (mean ± s.d., n = 291) CF647 fluorophores per protein (Fig. 5.3D), with the width of the distribution in line with that expected for a Poisson distribution. The measurements were repeated using the same batch of protein measured in subsequent experiments, which found 2.0 ± 0.6 fluorophores

per protein (data not shown). ESI-MS analysis found an average of 3 fluorophores per protein for CF647-labelled PAI-2 (Appendix F).

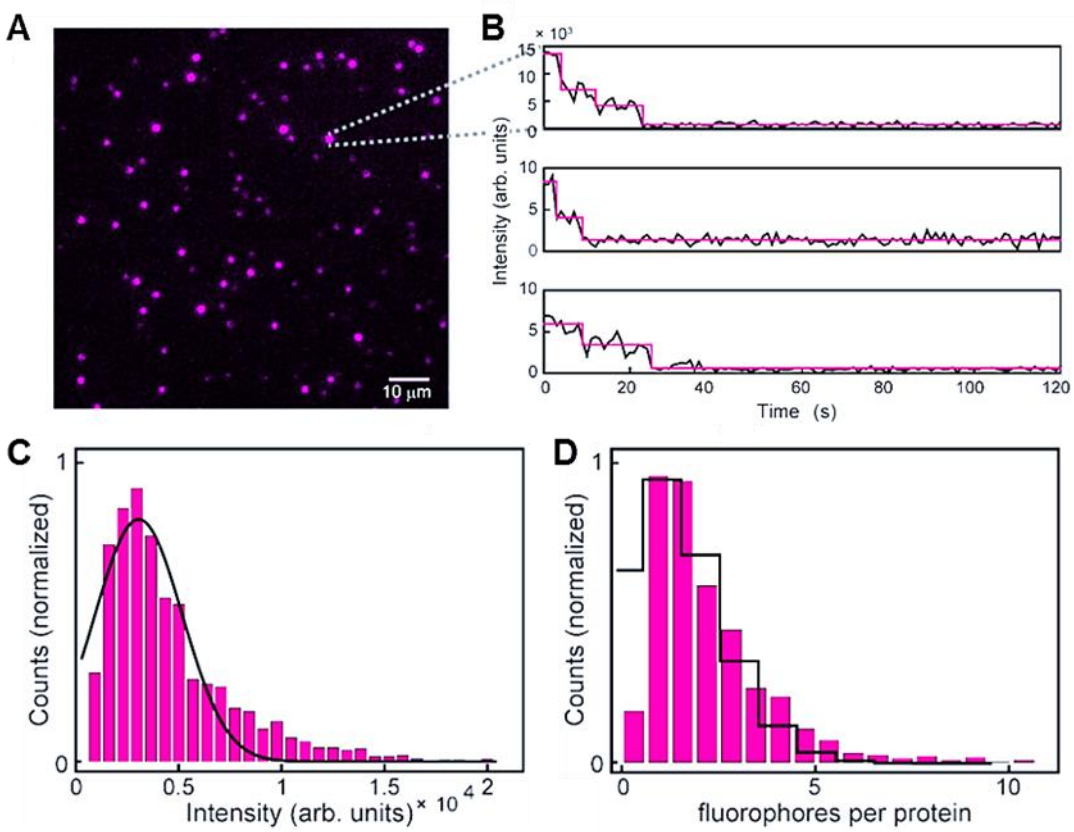

Figure 5.3: Single-molecule imaging of CF647-labelled PAI-2. (**A**) Representative field of view of CF647-labelled plasminogen activator inhibitor-2 (PAI-2) proteins immobilised on a cleaned coverslip. (**B**) Example fluorescence intensity trajectories of individual proteins (black line) and individual steps identified using a change-point algorithm (magenta line). (**C**) Histogram of the intensity of a single CF647 fluorophore (fitted with a Gaussian distribution): $3 \pm 0.1 \times 10^3$ (mean ± s.e.m., n = 962). (**D**) Histogram of the number of CF647 fluorophores per protein (fitted with a Poisson distribution): 1.5 ± 0.4 (mean ± s.d., n = 291).

5.3.2 Imaging CF647-labelled PAI-2-functionalised liposomes

To quantify the number of PAI-2 proteins attached to liposomes using single-molecule fluorescence microscopy, liposomes were functionalised with CF647-labelled PAI-2 via the PI method and visualised using TIRF microscopy under the same conditions that were used to image the CF647-labelled PAI-2. To confirm that the fluorescence signal observed in the imaging experiments originated from proteins bound to single liposomes, liposomes were pre-labelled with the fluorophore R18 so that the encapsulated R18 acted as a marker for liposomes that had an intact lipid bilayer (Serro et al. 2012). Using optics

that split the image into a yellow and a red channel, the R18-labelled liposomes and attached CF647-labelled PAI-2 proteins were visualised simultaneously but each on different areas of the camera sensor to visualise the R18 fluorescence and the signal from the red-labelled proteins, with a merge of the two signals revealing colocalisation as indicated by white spots (Fig. 5.4A, top panel). Analysis of these images revealed that 88% of R18-labelled liposomes had at least one CF647-labelled PAI-2 protein attached. The number of proteins per liposome was determined by dividing the average CF647 fluorescence intensity per liposome by the intensity of a single CF647-labelled PAI-2 protein, obtained previously (Section 5.3.1). The protein density was calculated to be 11 ± 4 (mean ± s.d.) proteins per liposome (Fig. 5.4B). DLS analysis of the liposomes indicated a liposome diameter of 153 ± 56 nm (mean ± s.d.) and a polydispersity index of 0.041 ± 0.017 (mean ± s.d.) (Fig. 5.4C). R18-labelled liposomes prepared in parallel using non-maleimide-functionalised micelles did not show colocalisation with CF647-labelled PAI-2 when imaged by single-molecule fluorescence microscopy (Fig. 5.4A, bottom panel).

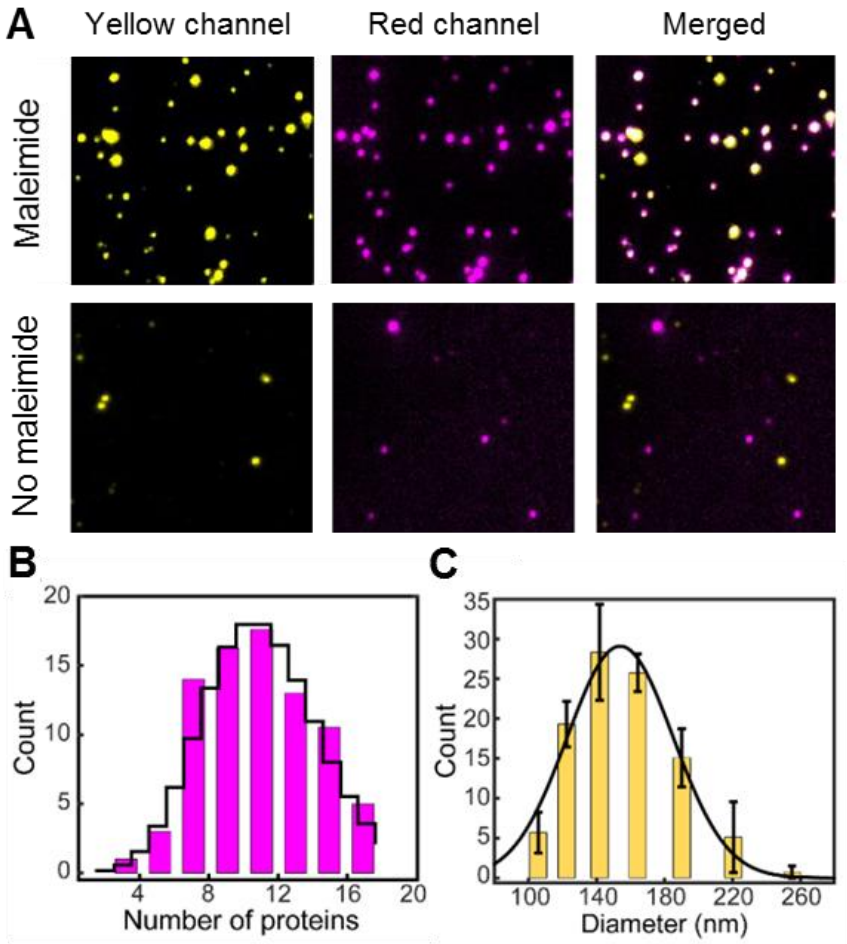

Figure 5.4: Imaging CF647-labelled PAI-2-functionalised liposomes. (**A**) Liposomes labelled with octadecyl rhodamine B chloride (R18) (left) and CF647-labelled plasminogen activator inhibitor-2 (PAI-2) (middle) were imaged simultaneously (n = 14 fields of view, ~30 liposomes per field of view). A merge of the two channels (right) showed a high degree of colocalisation (white spots). Liposomes prepared in parallel using non-maleimide-micelles showed no colocalisation with protein signal (n = 14 fields of view, with ~10 liposomes per field of view). (**B**) Histogram of the number of proteins per liposome, fitted with a Poisson distribution (black line): 11 ± 4 (mean ± s.d.). (**C**) Histogram of liposome diameter measured by dynamic light scattering, fitted with a Gaussian distribution (black line): 153 ± 56 (mean ± s.d.). Bars represent the mean ± s.d. (n = 3).

5.3.3 Inhibitory activity of CF647-labelled PAI-2 liposomes

A fluorogenic urokinase plasminogen activator (uPA) activity assay was performed to determine whether quantification of PAI-2 by single-molecule imaging would enable appropriate liposome sample dilution in the assay to achieve inhibition of uPA activity by the PAI-2-functionalised liposomes. The assay was performed for the CF647-labelled PAI-2-functionalised liposome sample before and after single-molecule quantification at a molar ratio of 2:1 PAI-2:uPA. PAI-2 concentration of the liposome sample was informed by either estimation based on preparation parameters (1.78 µM) or by single-

molecule data (45 nM). The single-molecule quantification (proteins per particle) combined with liposome concentration (particles per mL) as determined by nanoparticle tracking analysis (NTA; Chapter 2, Section 2.2.3.2) enabled calculation of the average PAI-2 protein concentration of the liposome sample.

The result of the assay performed before single-molecule quantification indicated no significant difference between the PAI-2 liposome treatment and positive control (uninhibited uPA), indicating no measurable inhibitory effect of the PAI-2 liposomes (Fig. 5.5A). When single-molecule quantification was performed on the sample to guide the concentration of sample to be used in the assay, the PAI-2 liposome sample showed significant ($P < 0.01$) inhibitory activity relative to the positive control (Fig. 5.5B), indicating that PAI-2 bound to liposomes retained inhibitory activity against uPA when combined with uPA at a true molar ratio of 2:1, as informed by single-molecule fluorescence imaging.

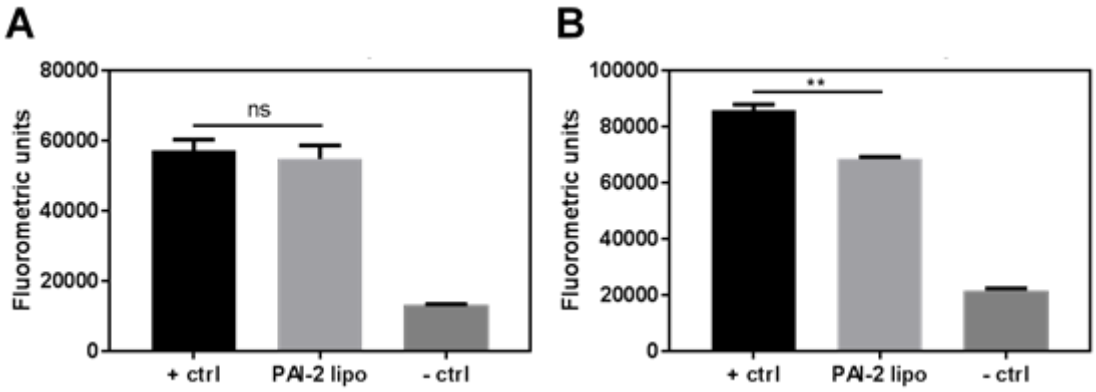

Figure 5.5: Activity-based profiling of PAI-2-functionalised liposomes. The inhibitory activity of plasminogen activator inhibitor-2 (PAI-2)-functionalised liposomes was determined using a fluorogenic urokinase plasminogen activator (uPA) assay. (**A**) Prior to determination of PAI-2 ligand density via single-molecule imaging, estimation of PAI-2 concentration was 1.78 µM. This estimate was used to dilute the liposome sample to give a 2:1 PAI-2:uPA (inhibitor:enzyme) molar ratio. (**B**) After single-molecule imaging was performed, a PAI-2 concentration of 45 nM was indicated for the liposome preparation, which was used to dilute the liposome sample to yield a 2:1 molar ratio of PAI-2:uPA. Data are the mean ± s.d. (n = 3). ** = $P < 0.01$, ns = not significant.

5.3.4 Ligand stoichiometry of dual-functionalised liposomes

To explore the ability of single-molecule fluorescence imaging to quantify small differences in protein density, the stoichiometry of two fluorescently-labelled proteins

was varied during the preparation of a series of dual-functionalised liposomes and their ratio quantified. To negate potential confounding effects that could arise from using two different proteins, such as protein size and reactivity, PAI-2 was labelled with either CF647 or CF488 (0.9 kDa; intensity of a single CF488 fluorophore 1.2 ± 0.6 x 10^4 (mean ± s.e.m., n = 796); 4.5 ± 2.2 (mean ± s.d., n = 104) fluorophores per protein) to enable imaging of the two differently labelled (i.e. red and green) proteins. Liposomes were functionalised via the PI method using red-labelled (CF647) and green-labelled (CF488) PAI-2 at molar ratios of 1:1, 2:1, 5:1 and 10:1 (red:green) while keeping the total amount of protein constant for each liposome preparation. The two proteins were visualised simultaneously using dual-colour imaging and the protein density was determined as above. At a 1:1 molar ratio, 51 ± 2 % of the total number of proteins per liposome had a red label and 49 ± 2 % had a green label. Analysis of the other preparations revealed that changing the ratios of the two labelled proteins during preparation similarly altered the ratios of proteins incorporated into the liposome, as quantified by single-molecule fluorescence microscopy (Fig. 5.6A). This relationship was linear, with an R^2 value of 0.9655 (Fig. 5.6B). Imaging of the 1:1 dual-functionalised liposomes showed high levels of colocalisation of red and green spots (white spots), indicating that a high proportion of liposomes were indeed dual-functionalised (Fig. 5.6C).

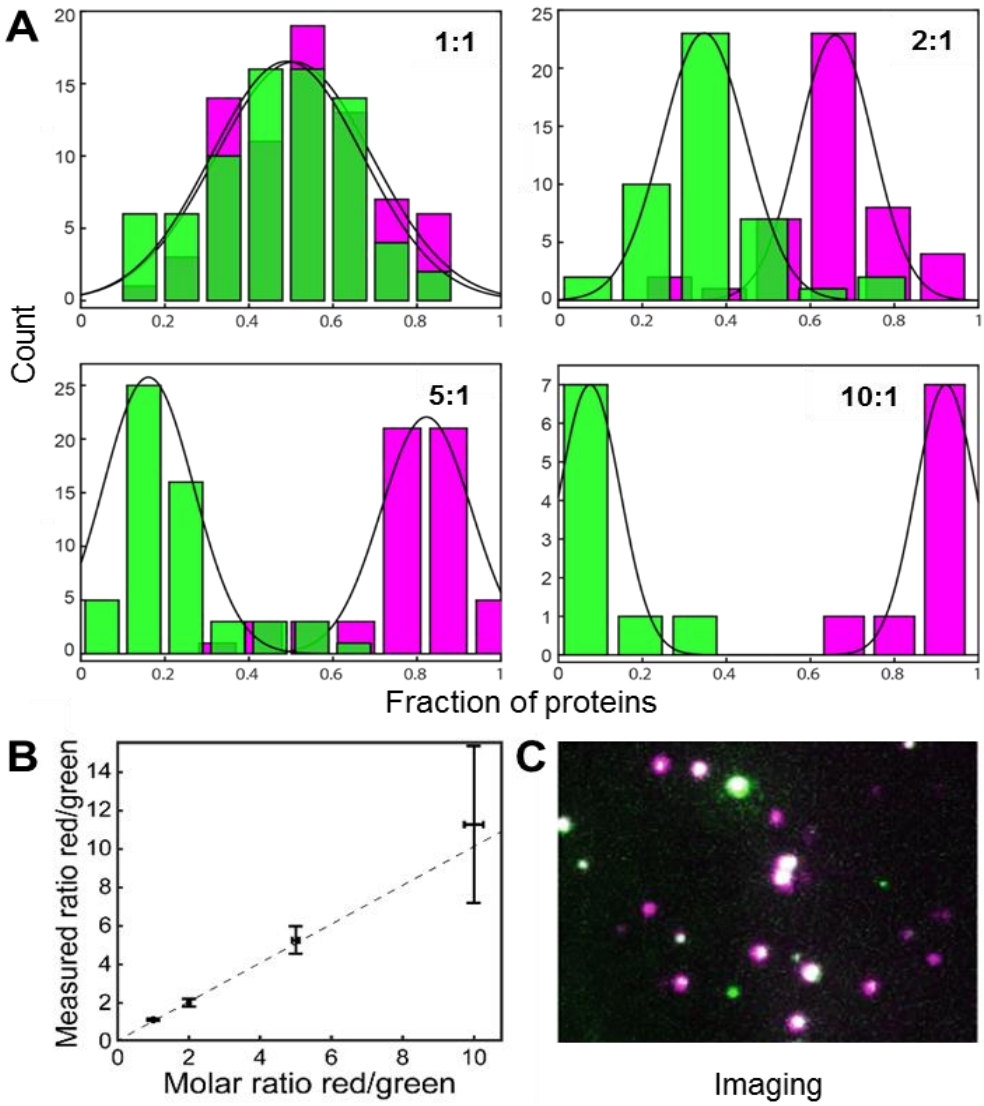

Figure 5.6: Ligand stoichiometry of dual-functionalised liposomes. (**A**) Histograms of the measured fraction of red-labelled (magenta) and green-labelled (green) proteins per liposome, where 1:1 (n = 146), 2:1 (n = 111), 5:1 (n = 232) and 10:1 (n = 137) molar ratios of red to green proteins were used during liposome preparation. Black lines represent Gaussian fits to the data. (**B**) Measured ratio of the fraction of red-labelled proteins over the fraction of green-labelled proteins as a function of the molar ratio used during preparation (mean ± s.e.m.). The errors in the molar ratio are pipetting errors calculated from the manufacturer-published imprecision ranges of the pipettes used to add the micelle volumes to the liposomes during preparation. (**C**) Representative field of view showing merge of red and green channels of the 1:1 liposome sample, with colocalisation indicated by white spots.

5.3.5 Centrifugation of liposomes to remove unbound ligands

Size-exclusion chromatography (SEC) is a commonly used but low-throughput method for functionalised liposome preparation, whereas alternative methods, such as high-speed centrifugation, may be an option to streamline the production process of functionalised liposomes for preclinical testing. In Chapter 2, high-speed centrifugation was tested as a

method to efficiently remove unconjugated PAI-2 protein from PAI-2-functionalised liposome samples. The results indicated that free PAI-2 protein could be removed from liposomes, with a high recovery of liposomes in the sample following repeated centrifugation. However, the effect of repeated high-speed centrifugation on PAI-2 protein attachment to the liposome in the final formulation remained unknown. To test the effect of this method on the final degree of PAI-2 attachment to liposomes, dual-functionalised PAI-2 liposomes were prepared and functionalised via the PI method as per Section 5.3.4 using a 1:1 molar ratio of CF647-labelled PAI-2 and CF488-labelled PAI-2. Following the functionalisation step, any unconjugated PAI-2 was removed from the liposomes using either SEC or repeated high-speed centrifugation (5 cycles for 90 min at 20,000 x g). Single-molecule imaging of the two final liposome samples revealed similar numbers of red and green proteins attached to the liposomes (Fig. 5.7). The total number of attached PAI-2 proteins per liposome was 10.8 and 14.8 for SEC and centrifugation liposomes, respectively.

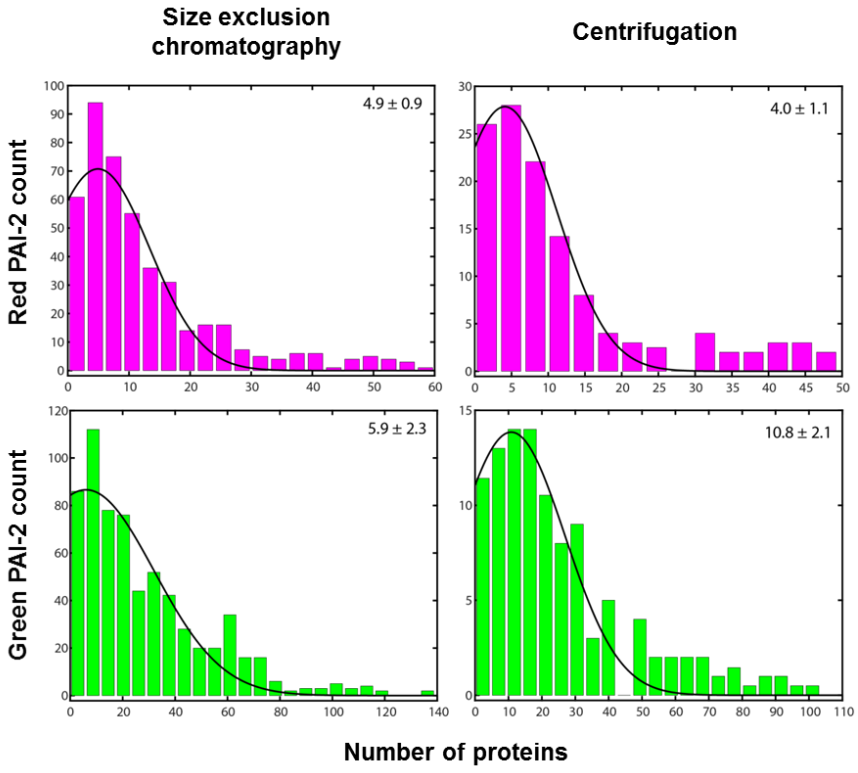

Figure 5.7: Size-exclusion chromatography and centrifugation of liposomes. Liposomes functionalised with both CF647-PAI-2 and CF488-PAI-2 in a 1:1 molar ratio were purified using either size-exclusion chromatography (left) or repeated centrifugation at 20,000 x g (right) to remove any unbound PAI-2. Single-molecule fluorescence microscopy of the liposomes was performed to quantify the number of CF647-labelled PAI-2 proteins and CF488-labelled PAI-2 proteins attached to the purified liposomes. The black lines represent Gaussian fits to the data. Values are means ± s.e.m.

5.3.6 Characterisation of PAI-2-TZ dual-functionalised liposomes

Quantification of ligand density and stoichiometry on the surface of dual-functionalised liposomes is important to optimise preparation parameters and select the most appropriate method of ligand conjugation to the liposome surface, to enable the production of a dual-ligand targeted liposome that is optimally effective in its intended application. In the context of tumour targeting, liposomes bearing two different targeting ligands need to be able to bind successfully to their respective target cell receptors to enable liposome internalisation into the target cell. However, the current lack of methodology to determine the number and ratio of two different ligands on the surface of liposomes means that the development and optimisation of dual-functionalised liposome formulations is limited. To explore the utility of single-molecule quantification in the characterisation of novel clinically relevant ligand-directed liposomes, dual-ligand liposomes were prepared via both the CO and the PI methods of liposome functionalisation (Fig. 5.1). PAI-2 and trastuzumab (TZ, Herceptin®; 145 kDa) were labelled with red and green CF fluorophores, respectively, and conjugated to preformed liposomes using a 1:1 molar ratio of PAI-2:TZ. DLS showed a small but significant increase in liposome diameter following functionalisation for PI, but not CO, liposomes (Appendix G). Single-molecule fluorescence imaging and data analysis of the dual-functionalised liposomes were performed as outlined in Section 5.3.4. Using single-molecule imaging, the ratio of PAI-2 to TZ of the dual-functionalised liposomes was 17 ± 18 (n = 115) for liposomes prepared via the CO method and 2.1 ± 2.5 (n = 167) for liposomes prepared via the PI method (Fig. 5.8). Imaging of the samples indicated that liposomes prepared via the PI method showed higher levels of colocalisation than the CO method.

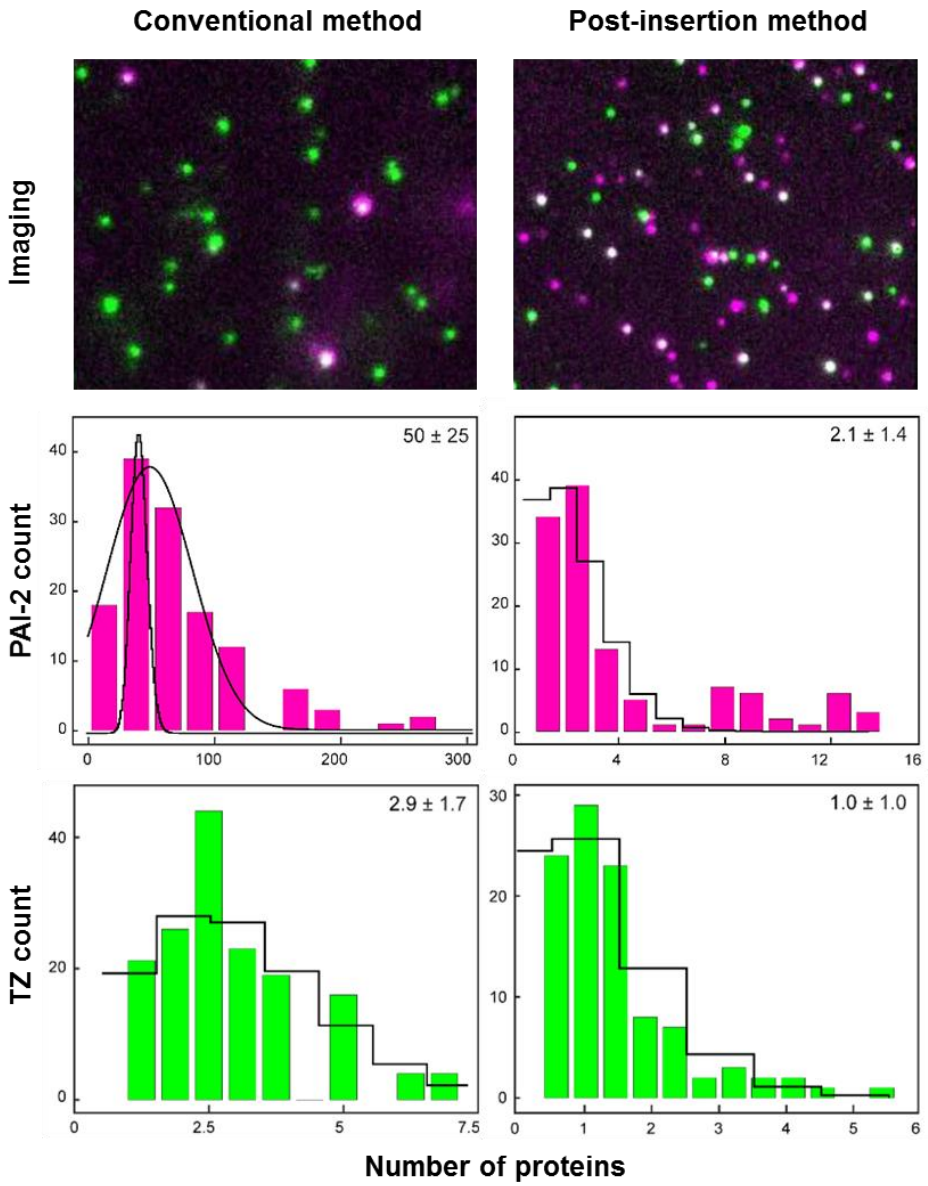

Figure 5.8: Imaging of PAI-2-TZ dual-functionalised liposomes. (**A**) Representative field of view during single-molecule imaging of plasminogen activator inhibitor-2 (PAI-2)/trastuzumab (TZ) liposomes prepared via the conventional (left) and post-insertion (right) methods. (**B**) Histograms of the number of proteins per liposome. The black lines represent Poisson distribution fits to the histograms. Due to the large number of PAI-2 proteins in the conventional sample, heterogeneities within the sample broadened the histogram and obscured the Poisson distribution. Therefore, this histogram was fitted with a Gaussian distribution.

5.4 Discussion

The quantification of ligands attached to the surface of liposomes is important for the comprehensive characterisation, production optimisation and quality control of ligand-functionalised liposome formulations. The overarching aim of this chapter was to use single-molecule fluorescence microscopy as a tool for the quantification of ligands bound to the surface of liposomes, which was ultimately successful. In this chapter, the quantification of proteins attached to the surface of liposomes was achieved for the first time using single-molecule fluorescence imaging to count the photobleaching steps of fluorescently labelled proteins bound to liposomes. Liposome and protein signals showed a high degree of colocalisation, indicating that proteins were bound to intact liposomes and that proteins could be visualised successfully using the single-molecule fluorescence microscope. The average number of attached proteins per liposome was determined to be 11 ± 4, and imaging of dual-functionalised liposomes revealed stoichiometries of two attached proteins in accordance with the molar ratios of protein added during preparation. Single-molecule quantification indicated that centrifugation of liposomes slightly increased the final ligand density of liposomes relative to SEC due to the selection of a highly monodisperse population of liposomes in a particular size range, as expected. Single-molecule imaging revealed that the PI method generated dual-functionalised liposomes with a more equal representation of two differently sized protein ligands than the CO method, demonstrating the ability of the former method to enable superior control of the final liposome protein densities (Allen & Cullis 2013). Overall, this chapter has demonstrated the utility of single-molecule fluorescence imaging in the quantification of the density and stoichiometry of ligands attached to the surface of liposomes, which enables superior characterisation of functionalised liposomes in the preclinical testing context.

The lipophilic dye R18 has been previously used in single-molecule fluorescence imaging experiments (Otterstrom et al. 2014) and was used in this work to visualise intact liposomes and image proteins conjugated to liposomes, rather than imaging free proteins in the sample. Liposomes prepared without maleimide-PEG were used to confirm that only covalently attached proteins colocalised with liposomes in imaging experiments. The lack of observed colocalisation (Fig. 5.4) demonstrates that non-specific binding of PAI-2 proteins to liposomes is minimal, as would be expected given the mechanism of

covalent conjugation of ligands to the liposome surface (Iden & Allen 2001) and given that the methods used for purification were suitable. The fluorescence intensity of the R18-labelled liposomes was variable during imaging and this coincided with a mix of larger and smaller spots observed in the field of view (Fig. 5.4). Given that the R18 molecule partitions in lipid membranes and more R18 molecules can associate with the bilayers of larger liposomes, this correlation is expected. Similarly, the calculated average number of attached PAI-2 proteins per liposome was variable, ranging from 3 to 17 proteins. When the same batch of liposomes was analysed by DLS to determine the average liposome diameter of the sample, the relative width of the liposome size distribution (0.36) was found to correlate with the relative width of the distribution of the number of proteins per liposome (0.37) as determined by single-molecule imaging (Fig. 5.4). This suggests that the width of the distribution for the number of proteins per liposome is a result of the heterogeneity in liposome size, as larger liposomes have a greater number of attached proteins than smaller liposomes due to the greater number of mal-PEG moieties available for ligand conjugation to the liposome surface (Allen et al. 1995).

The addition of a 1:1 molar ratio of red-labelled and green-labelled PAI-2 to the liposomes during the liposome preparation step resulted in a 1:1 measured ratio via single-molecule imaging in the liposome formulation (Fig. 5.6). This observation indicated that the two different fluorophores did not affect protein attachment to the liposome surface, and that the two proteins were incorporated into the liposome in the same 1:1 ratio as their input stoichiometry in the formulation process. In contrast to preliminary experiments in which a 1:4 ratio of maleimide-PEG:methoxy-PEG was used in the liposome formulation, resulting in an average of 2-3 attached proteins per liposome (data not shown), the maleimide-PEG:methoxy-PEG ratio was changed to 4:1 for the ratiometric experiment in order to increase the total available sites for protein conjugation. Increasing the number of total proteins bound to the liposome surface enabled better detection of the variation between the different protein ratios used and a more robust calculation of ratios. This change resulted in the attachment of 8-12 proteins per liposome, corresponding to an approximate 4-fold increase in attached protein when the maleimide concentration was also increased 4-fold. The increased total protein of the liposomes was particularly important for the 10:1 liposome sample due to the fact that only dual-functionalised

liposomes were analysed (i.e. only liposomes that had at least one red-labelled and one green-labelled protein attached), resulting in a much lower number of dual-functionalised liposomes available in the sample for analysis than for the 1:1 sample. This explains the larger calculated error in the measured ratio of the 10:1 sample (Fig. 5.6). Nonetheless, the ratiometric experiment showed a linear correlation between input and measured ratio as determined by single-molecule fluorescence imaging, highlighting the ability of the single-molecule method to quantify small changes in protein attachment in dual-functionalised liposomes.

In Chapter 2, high-speed centrifugation was explored as an alternative to the conventionally used but low-throughput SEC to remove unconjugated PAI-2 from PAI-2-functionalised liposomes. Centrifugation is commonly used to remove unencapsulated soluble drug and other small molecules from liposomes (Yalcin et al. 2018), as liposomes and other nanoparticles pellet under conditions of high speed centrifugation, while soluble small molecules remain in solution for removal. Following centrifugation of dual-ligand liposomes to remove unconjugated red- and green-labelled PAI-2, single-molecule quantification determined that the total number of attached proteins was higher for centrifuged liposomes relative to size-exclusion purified liposomes (14.8 and 10.8 proteins, respectively) (Fig. 5.7). However, the ratio of the two attached proteins was similar to liposomes purified using SEC. While it is encouraging that repeated high-speed centrifugation did not remove the proteins from the liposome surface, the small difference in protein attachment observed between the two methods is likely due to the fact that centrifugation selects for larger liposomes. As larger liposomes pellet before smaller liposomes when centrifuged, the distribution of the liposome population is narrowed with each centrifugation step as the larger pelleted liposomes are recovered and the smallest liposomes that remain in solution are removed in the wash steps. Indeed, in Chapter 2 it was noted that the average diameter of a liposome sample increased from 148.0 nm to 153.9 nm following repeated centrifugation, with 77.1% retention of particles following centrifugation (Chapter 2, Table 2.3).

In the case of ligand-functionalised liposomes, larger liposomes containing more phospholipid groups and liposome constituents have a greater number of maleimide-PEG functional groups in the liposome bilayer and therefore have a greater number of proteins

attached to the liposome surface. Since centrifugation selects for larger liposomes with greater numbers of attached proteins, the centrifuged sample of liposomes had a higher average number of proteins per liposome. This observation is also supported by the R18 liposome experiment (Section 5.3.2), which found a direct correlation between average liposome size and total number of attached PAI-2 proteins. Therefore, centrifugation did not appear to remove conjugated PAI-2 from the surface of liposomes, although the final liposome population obtained was slightly altered for this reason. While the centrifugation method is high-throughput, allows for the production of multiple different liposome preparations in series and results in a high recovery of liposomes (Chapter 2, Section 2.3.7), the inherent selection towards larger liposomes and resultant narrowing of the final liposome distribution should be considered as a factor in the production process.

Single-molecule fluorescence microscopy was used to compare the effect of the conventional and post-insertion functionalisation methods on the resultant ligand density of actively targeted liposome formulations. Previous research has indicated that there are no significant differences between single-functionalised liposomes produced via the two methods in terms of uptake or cytotoxic effect *in vitro* and *in vivo* (Iden & Allen 2001). However, the effect of these functionalisation methods on dual-functionalised liposomes has not been determined due to the lack of methodology to quantify the density and stoichiometry of two different proteins attached to the surface of liposomes. In this chapter, PAI-2/TZ dual-functionalised liposomes prepared using two different functionalisation methods revealed notable differences in the final composition of the liposomes as measured by single-molecule fluorescent imaging (Fig. 5.8). When a 1:1 molar ratio of PAI-2 and TZ was used in the conventional preparation method, the calculated number of attached PAI-2 proteins per liposome was 17 times higher than the number of TZ antibodies. In contrast, the incorporation of PAI-2 and TZ was more balanced (~2:1 PAI-2:TZ) when the post-insertion method was used to prepare the liposomes.

The differences between the two liposomes are unsurprising when the differences between the two functionalisation methods are considered (Fig. 5.2). The conventional method involves incubation of a small protein (45 kDa) and a large antibody (150 kDa) with preformed liposomes, where differences in protein size (i.e. steric hindrance on rates

of reaction) and reactivity (i.e. the number of available sites for conjugation) may affect their equal incorporation into the liposomes. The incorporation of these two proteins of different sizes introduces a degree of competition between them for binding to the maleimide-PEG at the liposome surface. For conventional liposomes, it was observed that the degree of colocalisation of the two proteins (indicating dual-functionalised liposomes) was lower than that of post-insertion liposomes, which may indicate that the presence of the larger TZ antibody at the liposome surface caused a degree of steric hindrance to PAI-2 attachment, resulting in fewer dual-functionalised liposomes and a larger proportion of liposomes with only TZ attached (i.e. TZ-functionalised liposomes).

In contrast, the post-insertion method showed a high degree of colocalisation between PAI-2 and TZ, indicating that a greater number of dual-functionalised liposomes were successfully produced using this method. The post-insertion method negates the effects of protein differences through the simultaneous insertion of two separate preformed protein-functionalised micelles into the liposomes (Iden & Allen 2001). This means that each protein is given the opportunity to covalently attach to all available micelle maleimide-PEG groups without competition from the other protein before all groups are then transferred into the liposome outer leaflet. Theoretically, this would result in liposomes with a more even distribution of the two proteins at the liposome surface, and this is corroborated by the single-molecule quantification method used in this chapter. The quantification of PAI-2 and TZ at the surface of liposomes as outlined in this chapter provides a rationale for the use of the post-insertion method in the production of dual-functionalised liposomes, in particular for those that have two (or more) very disparate proteins attached in terms of their size and/or reactivity. This aspect is relevant to the clinical setting, where liposomes used to target heterogeneous tumour cell populations would likely bear two different targeting ligands (Chapter 1, Sections 1.4 and 1.6.3). Therefore, the application of single-molecule quantification enables optimisation of the preparation protocol in order to allow for a better control of the stoichiometry of the two ligands at the liposome surface.

Single-molecule fluorescence imaging enabled, for the first time, quantification of the average number of PAI-2 proteins per liposome for PAI-2-functionalised liposomes, which enabled a more accurate determination of the PAI-2 concentration of liposome

samples. The analysis of liposomes by nanoparticle tracking analysis (Chapter 2, Section 2.2.3.2) allowed the determination of liposome concentration (number of particles per mL), and this value combined with the single-molecule quantification (number of PAI-2 proteins per particle) enabled the calculation of the average PAI-2 protein concentration of the liposome sample, which was 45 nM. Prior estimation of the average PAI-2 protein concentration of the liposome sample without the single-molecule data and based only on preparation parameters, including estimated sample loss and dilution factors, indicated a PAI-2 concentration of 1.78 µM. The fluorogenic uPA activity assay was performed for the CF647-labelled PAI-2-functionalised liposome sample both before and after single-molecule quantification at a molar ratio of 2:1 PAI-2:uPA, with the PAI-2 concentration of the sample informed by either estimation or single-molecule data. Prior to single-molecule quantification, the assay indicated no significant difference between the PAI-2 liposome treatment and positive control (uninhibited uPA), indicating no measurable inhibitory effect of the PAI-2 liposomes (Fig. 5.5). When single-molecule quantification was performed on the sample to guide the concentration of sample to be used in the assay, the PAI-2 liposome sample showed significant ($P < 0.01$) inhibitory activity relative to the positive control, indicating that PAI-2 bound to liposomes retained inhibitory activity against uPA when combined with uPA at a true molar ratio of 2:1, as informed by single-molecule fluorescence imaging. This highlights the ability of single-molecule quantification to enable more accurate determination of the effect of liposome ligand density on liposome ligand function, as reflected in a sensitive functional assay.

To further demonstrate the applicability of single-molecule fluorescence microscopy as a quantification tool for ligand-targeted nanomedicine development, future work could utilise the methods reported here to demonstrate correlations between the number of targeting ligands at the liposome surface and functional cellular effects. For example, single-molecule quantification of liposome ligand density could help determine the optimal number of ligands for maximum receptor binding, target cellular uptake and therapeutic effect, or could determine the functional effects of targeted liposomes produced by different methods. Previous studies have demonstrated that the modulation of liposome ligand density, achieved by changing the starting maleimide-PEG concentration of the formulation, affects cellular binding and uptake (Chu et al. 2016; Gayong et al. 2016; Li, H et al. 2016). The single-molecule method described here could

be used in future work to further confirm such findings, and also to elucidate additional characteristics of ligand-directed liposomes. For example, the method could be used to determine inner and outer leaflet labelling of liposomes produced by the post-insertion method where heat is used, since it is possible that proteins may insert into the inner leaflet of the liposomes and therefore not be available for cell targeting. The quantification of inner and outer leaflet labelling of liposomes could be elucidated by single-molecule imaging using dyes (e.g. pH-sensitive dyes) as per previously reported methods (Otterstrom et al. 2014).

The single-molecule quantification technique reported in this chapter appears to be an accurate and high-throughput method, with the ratiometric experiment demonstrating the reproducibility of the method across different batches of liposomes. The number of fluorophores attached per protein (degree of labelling) using the same protein sample was measured in independent experiments, which found no variation between the calculated values. PAI-2 protein labelled with CF647 dye was determined to have 1.5 ± 0.4 fluorophores per protein, and when this measurement was repeated several months later with the same labelled protein, the single-molecule method found 2.0 ± 0.6 fluorophores per protein (data not shown). In addition, single-molecule measurements from two different coverslips for the same batch of liposomes found 11.0 ± 2.2 and 13.0 ± 2.1 PAI-2 proteins per liposome (data not shown). As described in Section 5.2.5, the single-molecule method requires determination of the degree of fluorescent labelling of the protein via single-molecule imaging in addition to imaging of the functionalised liposomes. This procedure is straightforward, only needs to be done once for a newly labelled ligand, and can be done at the same time as imaging of the liposome samples. Once determined, multiple liposome samples that have been functionalised with that ligand can then be imaged and the data analysed using established protocols. Data acquisition can easily be further scaled up and automated, and the analysis pipeline can readily be converted to an automated process to improve the throughput of the method (Monachino et al. 2017).

While the work presented in this chapter explored the quantification of a small protein ligand and a whole antibody on the surface of liposomes, in principle, the single-molecule approach reported in this thesis could also be applied to other surface ligand types and

nanoparticle systems. Quantification of other commonly used nanoparticle ligand types, such as antibody fragments, small peptides and aptamers, is possible, provided that the ligands can be fluorescently labelled for single-molecule imaging. Indeed, previous studies have utilised single-molecule imaging for quantifying fluorescently labelled peptides (Liu et al. 2010). Single-molecule fluorescence imaging techniques have been used to quantitatively characterise peptide-binding to lipid bilayers in order to understand the structure and function of membrane-bound proteins (Fox et al. 2009). More recently, single-molecule imaging was used to visualise the three-dimensional motions of membrane peptides in supported lipid bilayers by taking advantage of the surface-induced fluorescence attenuation of single emitting fluorophores (Li, Y et al. 2016). In addition to liposomes, single-molecule imaging could also be utilised in the quantification of ligands attached to the surface of other types of nanoparticles (Shashkova & Leake 2017), as previous research has shown successful application of single-molecule fluorescence microscopy analysis with various nanoparticle types, such as solid lipid nanoparticles (Zoubari et al. 2017), polymeric nanoparticles (Langdon et al. 2015), micelles (Cheng et al. 2013) and dendrimers (Younghoon et al. 2013). Such studies further support the suitability of single-molecule fluorescence microscopy for the characterisation of a wide variety of ligand types for ligand-functionalised nanoparticle development.

The single-molecule quantification method reported in this chapter is not without limitations. For example, the formation of a protein corona around the surface of systemically administered nanoparticles represents a potential problem for the ability of functionalised liposomes to successfully bind to their target cells *in vivo*. Quantifying non-specific protein adsorption to the surface of nanoparticles to determine the effect of this on nanoparticle functionality cannot be achieved using the single-molecule approach as this method simply counts the number of fluorescently labelled ligands covalently attached to the liposome surface. Proteins in biological media that may adsorb to the liposome surface and ‘shield’ ligands by forming a protein corona would not change the number of ligands covalently bound to the liposome, only (potentially) the functional activity of the ligands, which the single-molecule imaging method does not measure. How the liposome ligand density changes after exposure to biological media is a question that cannot be answered by single-molecule imaging, but it is an important question for the nanomedicine field more broadly. Therefore, the development of additional

characterisation methods for ligand-functionalised liposomes within the biological context is necessary to facilitate successful preclinical evaluation and clinical translation.

5.5 Conclusion

The work presented in this chapter demonstrates the practical utility of single-molecule fluorescence microscopy to quantify the number of protein ligands bound to the surface of liposomes, which represents a key step forward in the characterisation and evaluation of actively targeted nanotherapies. Using this technique, ligand quantification was achieved for single-ligand and dual-ligand liposomes, and the methods used to prepare and functionalise actively targeted liposomes were successfully characterised for their effect on resultant liposome ligand attachment. By enabling the quantification of surface-bound ligands, this single-molecule imaging technique can be used to optimise liposome preparation protocols, assist with the scale up of liposome preparation processes, and allow for batch-to-batch quality control in a preclinical or commercial production setting. Therefore, the comprehensive characterisation of preclinical ligand-functionalised liposomes using single-molecule fluorescence imaging may help improve the preclinical development of novel actively targeted liposomal drug delivery systems for cancer therapy and facilitate the translation of such nanotherapies from the laboratory through to clinical use.

Chapter 6:
Conclusions and Future Directions

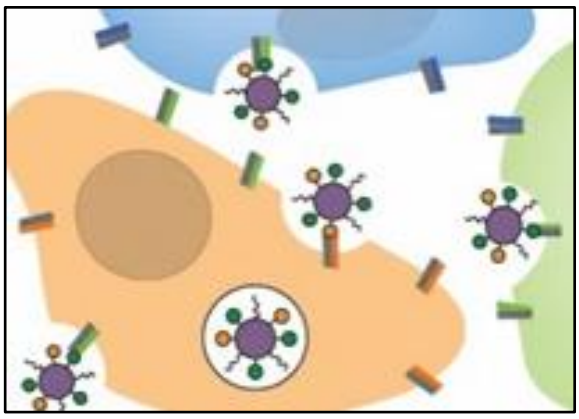

Dual-targeted drug-loaded liposomes

Portions of this chapter have been published in the following work:

Belfiore, L, Saunders, DN, Ranson, M, Thurecht, KJ, Storm, G & Vine, KL 2018, 'Towards clinical translation of dual-ligand liposomes in cancer therapy: Challenges and opportunities', *Journal of Controlled Release*, vol. 277, pp. 1-13.

Author contributions: LB wrote the manuscript; DNS, MR, KJT, GS and KLV edited the manuscript for submission.

6.1 Introduction

The development of more effective treatments for metastatic breast cancer remains an important area of research since it is a global health problem and there is currently no cure for metastatic disease. The urokinase plasminogen activator system has been recognised to play an important role in the ability of cancer cells to escape the primary site of the tumour and colonise other parts of the body. This system is particularly relevant in breast cancer metastasis, including in the human epidermal growth factor receptor 2 (HER2)-positive subtype and the triple-negative breast cancer (TNBC) subtype, both of which have an aggressive disease profile and poor prognosis. Hence, targeting this system using novel approaches may be effective in the treatment of metastatic breast cancer. Plasminogen activator inhibitor-2 (PAI-2) has previously been used to target the urokinase plasminogen activator receptor (uPAR) and deliver cytotoxins to breast cancer cells. The work described in this thesis aimed to build upon this concept by attaching PAI-2 to the surface of PEGylated liposomes containing the potent cytotoxin *N*-alkylisatin (*N*-AI), for increased and selective drug delivery to uPAR-positive breast cancer cells. Therefore, the work presented in this thesis explored the preparation, characterisation, *in vitro* evaluation and *in vivo* evaluation of novel *N*-AI-loaded PAI-2-functionalised liposomes for targeting uPAR in breast cancer.

6.2 *N*-AI PAI-2 liposomes can be prepared by conventional methods

In order to facilitate the uPAR-mediated uptake of *N*-AI-loaded liposomes into breast cancer cells, previously reported methods were optimised to create novel *N*-AI-loaded liposomes that were surface-functionalised with PAI-2. Novel *N*-AI-loaded PAI-2-functionalised (*N*-AI PAI-2) liposomes were successfully prepared and characterised. *N*-AI PAI-2 liposomes were 141.1 ± 5.0 nm in diameter, were monodisperse (polydispersity index of 0.086 ± 0.030) and had a zeta potential of –4.66 ± 0.52 mV. The liposomes contained *N*-AI at a concentration of 2.2 mM, significantly enhancing the aqueous solubility of *N*-AI for drug delivery applications. PAI-2 conjugation to the surface of *N*-AI-loaded liposomes was confirmed using size-exclusion chromatography and Western blotting. A PAI-2 inhibitory activity assay confirmed that PAI-2 attached to the surface of liposomes remained active against urokinase plasminogen activator (uPA) after

conjugation, making *N*-AI PAI-2 liposomes suitable for further *in vitro* and *in vivo* evaluation against breast cancer cells.

The methods used to prepare *N*-AI PAI-2 liposomes could be further improved to facilitate high-throughput production for subsequent testing and analysis. The continual development of new methods and technologies to prepare liposomes is expected to help facilitate their clinical development. In order to meet the demands for the large-scale preparation of liposomes as required for clinical use, microfluidic approaches have recently emerged as a way to produce large quantities of liposomes of a uniform size and consistent physicochemical properties, which may be a way forward for efficient and cost-effective liposome preparation (Jahn et al. 2004).

Recent technological developments have contributed to a shift away from conventional covalent coupling methods of attaching ligands to the surface of liposomes and towards the specific engineering of antibodies and aptamers for cellular targeting applications. The use of short-chain antibody fragments as targeting ligands, as opposed to whole antibodies, is a promising strategy for creating actively targeted liposomes, as the ligands can be engineered to optimise binding affinity and other physical properties for improved tumour cell targeting and uptake. As antibody fragments are smaller than whole antibodies, the immunogenicity may be lower and the *in vivo* circulation time of the resultant targeted liposomes more appropriate (i.e. more prolonged) for tumour targeting (Cheng & Allen 2010). Protocols to develop bispecific immunoliposome formulations using two different single-chain FV fragments on the liposome surface to target two different tumour cell populations have been reported, where each ligand shows a retention of binding activity for its target receptor (Mack et al. 2012). Multivalent liposomal therapeutic antibody constructs that bind to more than one antigen have been reported (Chiu et al. 2007), as well as PEGylated hyper-branched polymers bearing two different targeting ligands (Pearce et al. 2016).

The use of bispecific antibodies bound to the surface of liposomes may facilitate the recognition of multiple antigens to achieve the same effect attained with conventionally prepared dual-ligand liposomes (Howard et al. 2016). The successful development of a liposome with a single surface-attached bispecific antibody that can recognise and bind

to both endoglin and fibroblast activation protein demonstrates the feasibility of this approach in dual-targeting (Rabenhold et al. 2015). These approaches allow for more control in the stoichiometry of the two targeting ligands (i.e. always 1:1) compared to the traditional conjugation of two separate ligands, and for this reason may aid the production and regulatory processes required for clinical use of actively targeted liposomes. Such developments in antibody engineering mean that future nanoparticle-based drug delivery strategies can more easily permit targeting of multiple cell types, including genetically distinct tumour cells, but also key cells of the tumour microenvironment that are known to play a role in supporting tumour growth and spread, including immune cells and cancer stem cells (Angelova et al. 2017).

6.3 *N*-AI PAI-2 liposomes are cytotoxic to breast cancer cells

The cellular uptake, localisation and cytotoxicity of *N*-AI PAI-2 liposomes were successfully evaluated *in vitro* using breast cancer cells grown in monolayers and as multicellular tumour spheroids. As the binding of extracellular PAI-2 to uPAR-bound uPA results in the receptor-mediated endocytosis of the PAI-2/uPA/uPAR complex, PAI-2 can be used as a targeting ligand for the intracellular delivery of covalently attached cytotoxin to uPAR-positive tumour cells (Cochran et al. 2011). The cellular uptake of fluorescently labelled PAI-2 liposomes into MDA-MB-231 breast cancer cells (uPAR-positive) was significantly increased ($P < 0.01$) relative to MCF-7 breast cancer cells (uPAR-negative), as measured by flow cytometry. Confocal microscopy confirmed the uptake of PAI-2 liposomes and localisation within the cytoplasm and lysosomes of cells. *N*-AI PAI-2 liposomes showed a potent cytotoxic effect against both MCF-7 and MDA-MB-231 cells grown in 2D (IC_{50} values of 31.84 ± 8.20 μM and 5.40 ± 1.14 μM, respectively) and in 3D as multicellular tumour spheroids (IC_{50} values of 40.2 ± 4.0 μM and 60.4 ± 7.1 μM, respectively), which supports the use of uPAR as a therapeutic target and warranted further evaluation of *N*-AI PAI-2 liposomes *in vivo*.

The gradual movement away from simplistic monolayer and monoculture cell models and towards the utilisation of models that better recapitulate *in vivo* tumours, including computer simulated models (Dionysiou et al. 2006), *ex vivo* multicellular tumour spheroid models (Jiang et al. 2017), co-culture models (Lee et al. 2014), biomimetic microfluidic tumour microenvironment models (Tang et al. 2017) and patient-derived xenografts

(Shafaee & Ellis 2017), will allow for the inclusion of some aspects of tumoural heterogeneity and factor in the contribution of the tumour microenvironment in the evaluation of novel nanotherapies. As current *in vitro* models do not reproduce the complex vascular network, hypoxia, interstitial fluid pressure and fluid shear observed in the *in vivo* tumour microenvironment (Li & Lu 2011), a key limitation of multicellular tumour spheroid models for testing new drug-loaded nanotherapies is that these static models do not account for transport across the vascular endothelium (Maeda 2015). The development and validation of *in vitro* models that recapitulate aspects of the enhanced permeability and retention (EPR) effect is an emerging field of research. Static 3D co-culture models comprised of vascular network structures and tumour spheroids can be used for incorporating the effect of vascularisation in drug testing experiments (Swaminathan et al. 2017). Microfluidic-based platforms can be used for monitoring nanoparticle delivery in a 3D environment that recapitulates circulation, extravasation and delivery to the tumour across the interstitial space (Li et al. 2018). These models also enable the examination of tumour cell and vascular cell interactions and how these interactions affect drug delivery, which is an important aspect of evaluating novel liposome formulations (Tang et al. 2017). These approaches are expected to help guide nanotherapy research in its early stages and provide a more accurate understanding of the expected efficacy should the formulation progress to *in vivo* studies or clinical trials.

6.4 PAI-2 enhances the tumour accumulation of liposomes *in vivo*

Following the *in vitro* evaluation of *N*-AI PAI-2 liposomes, the biodistribution, pharmacokinetic profile and anti-tumour efficacy of the liposomes were explored *in vivo* using mouse models of breast cancer. *N*-AI PAI-2 liposomes were found to have a plasma circulation half-life of 5.82 hours, with clearance predominately via the spleen, yet significantly increased tumour uptake of *N*-AI PAI-2 liposomes relative to *N*-AI liposomes was observed. No significant differences were noted in primary or metastastic anti-tumour growth in two mouse models of TNBC. Further research is needed to clarify if and how the potency of *N*-AI as a cytotoxin can be translated into an anti-tumour growth effect by targeting uPAR-positive tumour cells *in vivo* using PAI-2-functionalised liposomes.

Tumour targeting by liposomes is primarily mediated by the enhanced permeability and retention (EPR) effect, which is dependent on a number of factors, including interstitial fluid pressure and vascularity of the tumour, as well as the physical properties of the liposome formulation (Nichols & Bae 2014). It is well established that liposomes need to be relatively small and have a long circulation time to take advantage of the EPR effect for tumour targeting (Perche & Torchilin 2013). While Doxil® is comprised of liposomes of approximately 80-100 nm in diameter (Soundararajan et al. 2009), other clinically used liposome formulations for cancer therapy are slightly larger in size, including Onivyde™ with a mean diameter of 110 nm, and Myocet® with a diameter of 150-250 nm (Bulbake et al. 2017). Endosomes, which are 50-150 nm in diameter, show promise in drug delivery applications, but their utility faces the same challenges as liposomes with regards to clearance from the plasma and poor tumour targeting specificity (Si et al. 2019). Notably, the high tumour accumulation of Doxil® in humans is due in large part to the very long circulation half-life (up to 45 hours) of the formulation, which is comprised of PEGylated liposomes to reduce the rate of plasma clearance (Gabizon et al. 1994). Neutral or negatively charged liposomes (as in the case of Doxil®) have been shown to be better suited for drug delivery to solid tumours as they associate less with angiogenic blood vessels than positively charged liposomes, and are therefore more likely to extravasate (Krasnici et al. 2003). To increase the specificity of tumour targeting, ligand-targeted liposomes can be combined with the application of pH, temperature or magnetic field triggers to enable the controlled release of drug cargo at the tumour site and reduce off-target effects (Han et al. 2016). While there are general optimal liposome properties for tumour targeting, liposomes should be designed for the specific tumour type to be targeted, with consideration of the tumour microenvironment and the EPR effect (Rosenblum et al. 2018).

The development of animal models that recapitulate the EPR effect at a level more analogous to the human condition would be of benefit in the initial evaluation of novel targeted nanotherapies. Further research is required to better understand the EPR effect and elucidate the differences in this phenomenon between animal and human tumours, and between different tumour types, in order to increase translation of nanoparticle-based therapeutics into the clinic (Lammers et al. 2016). This could be achieved via imaging methods, such as the radionuclide imaging of liposomes to determine their fate *in vivo*

(van der Geest et al. 2016). Intravital imaging techniques can be used to assess the depth of nanoparticle (and drug cargo) penetration into the tumour and the movement of nanoparticles away from the major blood vessels that vascularise the tumour (Puttick et al. 2015; Zhao, Y et al. 2017). Single photon emission computed tomography (SPECT) and positron emission tomography (PET) can also be used to quantify the *in vivo* distribution of nanoparticles, including the accumulation of nanoparticles at the tumour site, in a non-invasive manner (Harrington et al. 2001).

The use of models that recapitulate intratumoural heterogeneity is important in the evaluation of dual-ligand liposomes designed to target multiple tumour cell receptors. Patient-derived xenografts are more representative of the clinical situation as they capture some elements of intratumoural heterogeneity, as well as the diversity observed between patients with cancer (Gomez-Cuadrado et al. 2017). In addition to intratumoural heterogeneity, the interpatient heterogeneity observed in cancer also warrants the development and utilisation of patient-derived xenografts and patient-derived cell lines to more accurately assess patient responses to novel therapies, particularly in cases where resistance to currently used therapies is frequently observed (Shafaee & Ellis 2017). Additionally, the use of tumour models in immunocompetent animals is important given the known effect of the adaptive immune system on tumour growth and metastasis (Kitamura et al. 2015). The increasing use of such models lends itself to the improved assessment of targeted therapies in the context of cancer treatment (Budhu et al. 2014).

6.5 Single-molecule imaging can be used to quantify liposome ligands

Due to the lack of robust methods to quantify liposome ligands, single-molecule fluorescence microscopy techniques were successfully developed to quantify the density and stoichiometry of protein ligands attached to the surface of targeted liposomes. As reported in Chapter 5, single-molecule imaging confirmed that PAI-2 molecules were attached to the liposome surface, with an average of 11 ± 4 PAI-2 molecules per liposome. This was the first direct confirmation and quantification of PAI-2 attached to the surface of liposomes and marks an important first step in utilising these high resolution technologies in nanomedicine-based therapeutics development (Pujals et al. 2019). The method enabled the quantification of ligands after liposomes had been purified using two alternative methods and revealed the effects of these methods on the resultant liposome

ligand density. It was also demonstrated that the post-insertion method is more favourable for creating dual-ligand liposomes than the conventional method, as single-molecule imaging was able to quantify the density and ratio of PAI-2 and trastuzumab ligands attached to clinically relevant dual-functionalised liposomes. Therefore, this work has demonstrated the utility of single-molecule fluorescence imaging in the quantification of the density and stoichiometry of ligands attached to the surface of liposomes, which enables superior characterisation of functionalised liposomes in the preclinical testing context.

Future work using single-molecule fluorescence imaging could help to elucidate additional characteristics of ligand-directed liposomes. For example, the quantification of ligands by single-molecule imaging could determine inner and outer leaflet labelling of liposomes produced by the post-insertion method, since it is possible that ligands may insert into the inner leaflet of the liposomes and not be available for cell targeting. The quantification of inner and outer leaflet labelling of liposomes could be elucidated by single-molecule imaging using pH-sensitive dyes as per previously reported methods (Otterstrom et al. 2014). The work described in this thesis explored differences in the ligand density of liposomes produced specifically by the conventional and post-insertion methods, but the single-molecule imaging method could also be used to explore the functionalisation of liposomes produced by a range of methods, in addition to controlling for batch-to-batch variability in liposome production.

Single-molecule quantification can be used to help address the issues surrounding the standardisation of liposome characterisation in the broader field of nanomedicine research (Faria et al. 2018). There are currently no FDA guidelines or associated documentation outlining the requirements for the determination of target ligand density on liposomes or other nanoparticle-based formulations. Approximations for ligand density and the number of ligands per nanoparticle have been determined by making assumptions, such as that the nanoparticle is spherical, contains a certain number of functional groups and that the bioconjugation reaction is 100% efficient. Notably, the ligand density of single-chain anti-HER2 antibodies conjugated to the surface of doxorubicin-loaded liposomes (MM-302) has never been quantified, as traditional methods for characterisation were not

applicable to functionalised liposomes (Hendriks et al. 2013; Nellis, Ekstrom, et al. 2005; Nellis, Giardina, et al. 2005).

To further demonstrate the applicability of single-molecule fluorescence microscopy as a quantification tool for ligand-targeted nanomedicine development, future work could utilise the methods reported here to demonstrate correlations between the number of targeting ligands at the liposome surface and functional cellular effects. For example, the single-molecule quantification of liposome ligand density could help determine the optimal number of ligands for maximum receptor binding, target cellular uptake or therapeutic effect, or could determine the functional effects of targeted liposomes produced by different methods. Previous studies have demonstrated that the modulation of liposome ligand density, achieved by changing the starting maleimide-PEG concentration of the formulation, affects cellular binding and uptake (Chu et al. 2016; Gayong et al. 2016; Li, H et al. 2016). The single-molecule method described here could be used in future work to further confirm such findings.

Given the utility of single-molecule imaging in the characterisation of ligand-directed liposomes, the method reported in this thesis could be further developed to make the quantification process more high-throughput. Data acquisition could be further scaled up and automated, and the analysis pipeline could readily be converted into an automated process (Monachino et al. 2017). To further improve the method, a fluorescent antibody detection system could be used to bypass the need to pre-label ligands with fluorescent dyes. This would allow characterisation and analysis of liposomes at any point during or after their production. The recent development of a high-resolution optical nanoscopy technique to determine the number and distribution of functional moieties on the surface of nanoparticles without the need for fluorescent labelling is another promising method for characterising actively targeted liposomes in the preclinical setting (Delcanale et al. 2018).

6.6 Conclusion

The first clinically approved liposome, Doxil®, has been in use for over 20 years and is still used as an effective treatment for several cancers. However, the liposome field has not yet evolved into translating effective targeted liposomes. Ligand-directed liposomes

have the potential to increase the selectivity of therapy, and dual-ligand liposomes may additionally address intratumoural heterogeneity to overcome patient resistance to targeted therapies. The work described in this thesis demonstrated the successful development and characterisation of a novel ligand-directed uPAR-targeted liposome containing the potent anti-mitotic cytotoxin *N*-AI for the treatment of metastatic breast cancer. Cellular uptake and cytotoxicity of the liposomes were demonstrated *in vitro* against breast cancer cell lines varying in uPAR expression. *In vivo*, increased tumour uptake was demonstrated for ligand-directed liposomes relative to non-ligand directed liposomes, although no obvious anti-tumour benefit was observed in the models described. A single-molecule fluorescence microscopy method was successfully developed to enable future characterisation of ligand-directed liposomes to help guide their production and evaluation in the preclinical setting.

Together, the findings in this thesis support the rationale for targeting uPAR-positive breast cancer cells using *N*-AI-loaded PAI-2-functionalised liposomes. The results also provide a basis for the further development of dual-ligand liposomes that can target heterogeneous tumour cells within the HER2-positive and TNBC subtypes, in which uPAR has been shown to play a key role in driving metastasis. Despite the hurdles left to overcome in the production, evaluation and translation of ligand-directed liposomes towards clinical use in the context of cancer therapy, the utility of liposome technologies is promising. The continued development of better methodologies and models to comprehensively characterise novel ligand-directed liposomes and assess the likelihood of their performance in humans, including the recapitulation of intratumoural heterogeneity, will likely improve the translation of novel targeted nanotherapies from preclinical models through to the clinic.

References

Abdalla, A, Xiao, L, Ullah, M, Yu, M, Ouyang, C & Yang, G 2018, 'Current challenges of cancer anti-angiogenic therapy and the promise of nanotherapeutics', *Theranostics*, vol. 8, pp. 533-48.

Abraham, J & Staffurth, J 2016, 'Systemic therapy: Hormonal therapy for cancer', *Medicine*, vol. 44, pp. 30-3.

Aggarwal, V & Ha, T 2016, 'Single-molecule fluorescence microscopy of native macromolecular complexes', *Current Opinion in Structural Biology*, vol. 41, pp. 225-32.

Ahn, ER & Vogel, CL 2012, 'Dual HER2-targeted approaches in HER2-positive breast cancer', *Breast Cancer Research and Treatment*, vol. 131, no. 2, pp. 371-83.

Al-Mahmood, S, Sapiezynski, J, Garbuzenko, OB & Minko, T 2018, 'Metastatic and triple-negative breast cancer: challenges and treatment options', *Drug Delivery and Translational Research*, vol. 8, no. 5, pp. 1483-507.

Alexis, F, Pridgen, E, Molnar, LK & Farokhzad, OC 2008, 'Factors affecting the clearance and biodistribution of polymeric nanoparticles', *Molecular Pharmaceutics*, vol. 5, no. 4, pp. 505-15.

Alizadeh, AA, Aranda, V, Bardelli, A, Blanpain, C, Bock, C, Borowski, C, Caldas, C, Califano, A, Doherty, M, Elsner, M, Esteller, M, Fitzgerald, R, Korbel, JO, Lichter, P, Mason, CE, Navin, N, Pe'er, D, Polyak, K, Roberts, CWM, Siu, L, Snyder, A, Stower, H, Swanton, C, Verhaak, RGW, Zenklusen, JC, Zuber, J & Zucman-Rossi, J 2015, 'Toward understanding and exploiting tumor heterogeneity', *Nature Medicine*, vol. 21, no. 8, pp. 846-53.

Allen, TM & Cullis, PR 2013, 'Liposomal drug delivery systems: From concept to clinical applications', *Adv. Drug Delivery Rev.*, vol. 65, no. 1, pp. 36-48.

Allen, TM, Hansen, CB, Kao, GY, Brandeis, E & Zalipsky, S 1995, 'A new strategy for attachment of antibodies to sterically stabilized liposomes resulting in efficient targeting to cancer cells', *BBA - Biomembranes*, vol. 1237, no. 2, pp. 99-108.

Allen, TM, Sapra, P & Moase, E 2002, 'Use of the post-insertion method for the formation of ligand-coupled liposomes', *Cellular & Molecular Biology Letters*, vol. 7, no. 3, pp. 889-94.

Anchordoquy, TJ, Barenholz, Y, Boraschi, D, Chorny, M, Decuzzi, P, Dobrovolskaia, MA, Farhangrazi, ZS, Farrell, D, Gabizon, A, Ghandehari, H, Godin, B, La-Beck, NM, Ljubimova, J, Moghimi, SM, Pagliaro, L, Park, J-H, Peer, D, Ruoslahti, E, Serkova, NJ & Simberg, D 2017, 'Mechanisms and Barriers in Cancer Nanomedicine: Addressing Challenges, Looking for Solutions', *ACS Nano*, vol. 11, no. 1, pp. 12-8.

Angelova, A, Garamus, VM, Angelov, B, Tian, Z, Li, Y & Zou, A 2017, 'Historical perspective: Advances in structural design of lipid-based nanoparticle carriers for delivery of macromolecular drugs, phytochemicals and anti-tumor agents', *Advances in Colloid and Interface Science*, vol. 249, pp. 331-45.

Ariazi, EA, Ariazi, JL, Cordera, F & Jordan, VC 2006, 'Estrogen receptors as therapeutic targets in breast cancer', *Current Topics in Medicinal Chemistry*, vol. 6, no. 3, pp. 181-202.

Asuthkar, S, Stepanova, V, Lebedeva, T, Holterman, AL, Estes, N, Cines, DB, Rao, JS & Gondi, CS 2013, 'Multifunctional roles of urokinase plasminogen activator (uPA) in cancer stemness and chemoresistance of pancreatic cancer', *Molecular Biology of the Cell*, vol. 24, no. 17, pp. 2620-32.

Aubele, M, Huber, MC, Falkenberg, N, Gross, E, Braselmann, H, Walch, AK & Schmitt, M 2015, 'uPA receptor and its interaction partners: Impact as potential therapeutic targets in triple-negative breast cancer', *Journal of Clinical Oncology*, vol. 33, no. 28_suppl, p. 150.

Bahrami, A, Khazaei, M, Bagherieh, F, Ghayour-Mobarhan, M, Maftouh, M, Hassanian, SM & Avan, A 2017, 'Targeting stroma in pancreatic cancer: Promises and failures of targeted therapies', *Journal of Cellular Physiology*, vol. 232, no. 11, pp. 2931-7.

Bailey, P, Chang, DK, Nones, K, Johns, AL, Patch, AM, Gingras, MC, Miller, DK, Christ, AN, Bruxner, TJ, Quinn, MC, Nourse, C, Murtaugh, LC, Harliwong, I, Idrisoglu, S, Manning, S, Nourbakhsh, E & Wani, S 2016, 'Genomic analyses identify molecular subtypes of pancreatic cancer', *Nature*, vol. 531, no. 7592, pp. 47-52.

Barenholz, Y 2012, 'Doxil(R)--the first FDA-approved nano-drug: lessons learned', *Journal of Controlled Release*, vol. 160, no. 2, pp. 117-34.

Basile, D, Cinausero, M, Iacono, D, Pelizzari, G, Bonotto, M, Vitale, MG, Gerratana, L & Puglisi, F 2017, 'Anti-Tumour Treatment: Androgen receptor in estrogen receptor positive breast cancer: Beyond expression', *Cancer Treatment Reviews*, vol. 61, pp. 15-22.

Belfiore, L, Saunders, DN, Ranson, M, Thurecht, KJ, Storm, G & Vine, KL 2018, 'Towards clinical translation of ligand-functionalized liposomes in targeted cancer therapy: Challenges and opportunities', *Journal of Controlled Release*, vol. 277, pp. 1-13.

Belfiore, L, Spenkelink, LM, Ranson, M, van Oijen, AM & Vine, KL 2018, 'Quantification of ligand density and stoichiometry on the surface of liposomes using single-molecule fluorescence imaging', *Journal of Controlled Release*, vol. 278, pp. 80-6.

Berg, D, Wolff, C, Malinowsky, K, Tran, K, Walch, A, Bronger, H, Schuster, T, Hofler, H & Becker, KF 2012, 'Profiling signalling pathways in formalin-fixed and paraffin-embedded breast cancer tissues reveals cross-talk between EGFR, HER2, HER3 and uPAR', *Journal of Cellular Physiology*, vol. 227, no. 1, pp. 204-12.

Bianchi, E, Cohen, RL, Thor, AT, Todd, RF, Mizukami, IF, Lawrence, DA, Ljung, BM, Shuman, MA & Smith, HS 1994, 'The urokinase receptor is expressed in

invasive breast cancer but not in normal breast tissue', *Cancer Research*, vol. 54, no. 4, pp. 861-6.

Bobo, D, Robinson, KJ, Islam, J, Thurecht, KJ & Corrie, SR 2016, 'Nanoparticle-Based Medicines: A Review of FDA-Approved Materials and Clinical Trials to Date', *Pharmaceutical Research*, vol. 33, no. 10, pp. 2373-87.

Boshuizen, J, Koopman, LA, Krijgsman, O, Shahrabi, A, van den Heuvel, EG, Ligtenberg, MA, Vredevoogd, DW, Kemper, K, Kuilman, T, Song, JY, Pencheva, N, Mortensen, JT, Foppen, MG, Rozeman, EA, Blank, CU, Janmaat, ML, Satijn, D, Breij, ECW, Peeper, DS & Parren, P 2018, 'Cooperative targeting of melanoma heterogeneity with an AXL antibody-drug conjugate and BRAF/MEK inhibitors', *Nature Medicine*, vol. 24, no. 2, pp. 203-12.

Boulbes, DR, Chauhan, GB, Jin, Q, Bartholomeusz, C & Esteva, FJ 2015, 'CD44 expression contributes to trastuzumab resistance in HER2-positive breast cancer cells', *Breast Cancer Research and Treatment*, vol. 151, no. 3, pp. 501-13.

Bracci, L, Schiavoni, G, Sistigu, A & Belardelli, F 2014, 'Immune-based mechanisms of cytotoxic chemotherapy: implications for the design of novel and rationale-based combined treatments against cancer', *Cell Death and Differentiation*, vol. 21, no. 1, pp. 15-25.

Budhu, S, Wolchok, J & Merghoub, T 2014, 'The importance of animal models in tumor immunity and immunotherapy', *Current Opinion in Genetics and Development*, vol. 24, pp. 46-51.

Bulbake, U, Doppalapudi, S, Kommineni, N & Khan, W 2017, 'Liposomal Formulations in Clinical Use: An Updated Review', *Pharmaceutics*, vol. 9, no. 2.

Burris, HA, Rugo, HS, Vukelja, SJ, Vogel, CL, Borson, RA, Limentani, S, Tan-Chiu, E, Krop, IE, Michaelson, RA, Girish, S, Amler, L, Zheng, M, Chu, YW, Klencke, B & O'Shaughnessy, JA 2011, 'Phase II study of the antibody drug conjugate trastuzumab-DM1 for the treatment of human epidermal growth factor receptor 2 (HER2)-positive breast cancer after prior HER2-directed therapy', *Journal of Clinical Oncology*, vol. 29, no. 4, pp. 398-405.

Buxton, DB 2009, 'Nanomedicine for the management of lung and blood diseases', *Nanomedicine (Lond)*, vol. 4, no. 3, pp. 331-9.

Caracciolo, G, Farokhzad, OC & Mahmoudi, M 2017, 'Review: Biological Identity of Nanoparticles In Vivo: Clinical Implications of the Protein Corona', *Trends in Biotechnology*, vol. 35, pp. 257-64.

Carriero, MV & Stoppelli, MP 2011, 'The urokinase-type plasminogen activator and the generation of inhibitors of urokinase activity and signaling', *Current Pharmaceutical Design*, vol. 17, no. 19, pp. 1944-61.

Chadda, R & Robertson, JL 2016, 'Measuring Membrane Protein Dimerization Equilibrium in Lipid Bilayers by Single-Molecule Fluorescence Microscopy', *Methods in Enzymology*, vol. 581, pp. 53-82.

Chang, HI & Yeh, MK 2012, 'Clinical development of liposome-based drugs: formulation, characterization, and therapeutic efficacy', *International Journal of Nanomedicine*, vol. 7, pp. 49-60.

Chen, H, Zhang, W, Zhu, G, Xie, J & Chen, X 2017, 'Rethinking cancer nanotheranostics', *Nature Reviews Materials*, vol. 2, p. 17024.

Chen, K, Huang, YH & Chen, JL 2013, 'Understanding and targeting cancer stem cells: therapeutic implications and challenges', *Acta Pharmacologica Sinica*, vol. 34, no. 6, pp. 732-40.

Cheng, M-C, Leske, AT, Matsuoka, T, Kim, BC, Lee, J, Burns, MA, Takayama, S & Biteen, JS 2013, 'Super-resolution imaging of PDMS nanochannels by single-molecule micelle-assisted blink microscopy', *The Journal Of Physical Chemistry. B*, vol. 117, no. 16, pp. 4406-11.

Cheng, WW & Allen, TM 2010, 'The use of single chain Fv as targeting agents for immunoliposomes: an update on immunoliposomal drugs for cancer treatment', *Expert Opin Drug Deliv*, vol. 7, no. 4, pp. 461-78.

Chiu, GN, Edwards, LA, Kapanen, AI, Malinen, MM, Dragowska, WH, Warburton, C, Chikh, GG, Fang, KY, Tan, S, Sy, J, Tucker, C, Waterhouse, DN, Klasa, R & Bally, MB 2007, 'Modulation of cancer cell survival pathways using multivalent liposomal therapeutic antibody constructs', *Molecular Cancer Therapeutics*, vol. 6, no. 3, pp. 844-55.

Cho, HS, Mason, K, Ramyar, KX, Stanley, AM, Gabelli, SB, Denney, DW & Leahy, DJ 2003, 'Structure of the extracellular region of HER2 alone and in complex with the Herceptin Fab', *Nature*, vol. 421, no. 6924, pp. 756-60.

Cho, HY & Lee, YB 2014, 'Nano-sized drug delivery systems for lymphatic delivery', *J Nanosci Nanotechnol*, vol. 14, no. 1, pp. 868-80.

Choi, UB, Weninger, KR & Bowen, ME 2012, 'Immobilization of proteins for single-molecule fluorescence resonance energy transfer measurements of conformation and dynamics', *Methods in Molecular Biology*, vol. 896, pp. 3-20.

Chu, C, Xu, P, Zhao, H, Chen, Q, Chen, D, Hu, H, Zhao, X & Qiao, M 2016, 'Effect of surface ligand density on cytotoxicity and pharmacokinetic profile of docetaxel loaded liposomes', *Asian Journal of Pharmaceutical Sciences*, vol. 11, no. 5, pp. 655-61.

Cochran, BJ, Croucher, DR, Lobov, S, Saunders, DN & Ranson, M 2011, 'Dependence on endocytic receptor binding via a minimal binding motif underlies the differential prognostic profiles of SerpinE1 and SerpinB2 in cancer', *Journal of Biological Chemistry*, vol. 286, no. 27, pp. 24467-75.

Cochran, BJ, Gunawardhana, LP, Vine, KL, Lee, JA, Lobov, S & Ranson, M 2009, 'The CD-loop of PAI-2 (SERPINB2) is redundant in the targeting, inhibition and clearance of cell surface uPA activity', *BMC Biotechnology*, vol. 9, p. 43.

Collins, AT, Berry, PA, Hyde, C, Stower, MJ & Maitland, NJ 2005, 'Prospective identification of tumorigenic prostate cancer stem cells', *Cancer Research*, vol. 65, no. 23, pp. 10946-51.

Croucher, DR, Iconomou, M, Hastings, JF, Kennedy, SP, Han, JZR, Shearer, RF, McKenna, J, Wan, A, Lau, J, Aparicio, S & Saunders, DN 2016, 'Bimolecular complementation affinity purification (BiCAP) reveals dimer-specific protein interactions for ERBB2 dimers', *Science Signaling*, vol. 9, no. 436, p. ra69.

Croucher, DR, Saunders, DN, Lobov, S & Ranson, M 2008, 'Revisiting the biological roles of PAI2 (SERPINB2) in cancer', *Nature Reviews: Cancer*, vol. 8, no. 7, pp. 535-45.

Croucher, DR, Saunders, DN, Stillfried, GE & Ranson, M 2007, 'A structural basis for differential cell signalling by PAI-1 and PAI-2 in breast cancer cells', *The Biochemical journal*, vol. 408, no. 2, pp. 203-10.

Dalerba, P, Dylla, SJ, Park, I-K, Liu, R, Wang, X, Cho, RW, Hoey, T, Gurney, A, Huang, EH, Simeone, DM, Shelton, AA, Parmiani, G, Castelli, C & Clarke, MF 2007, 'Phenotypic characterization of human colorectal cancer stem cells', *Proceedings of the National Academy of Sciences*, vol. 104, no. 24, p. 10158.

Dams, ETM, Laverman, P, Oyen, WJG, Storm, G, Scherphof, GL, Van Der Meer, JWM, Corstens, FHM & Boerman, OC 2000, 'Accelerated blood clearance and altered biodistribution of repeated injections of sterically stabilized liposomes', *Journal of Pharmacology and Experimental Therapeutics*, vol. 292, no. 3, pp. 1071-9.

Dass, K, Ahmad, A, Azmi, AS, Sarkar, SH & Sarkar, FH 2008, 'Evolving role of uPA/uPAR system in human cancers', *Cancer Treatment Reviews*, vol. 34, no. 2, pp. 122-36.

De Marchi, T, Foekens, JA, Umar, A & Martens, JWM 2016, 'Review: Endocrine therapy resistance in estrogen receptor (ER)-positive breast cancer', *Drug Discovery Today*, vol. 21, pp. 1181-8.

Delcanale, P, Miret-Ontiveros, B, Arista-Romero, M, Pujals, S & Albertazzi, L 2018, 'Nanoscale Mapping Functional Sites on Nanoparticles by Points Accumulation for Imaging in Nanoscale Topography (PAINT)', *ACS Nano*, vol. 12, no. 8, pp. 7629-37.

Denkert, C, Liedtke, C, Tutt, A & von Minckwitz, G 2017, 'Molecular alterations in triple-negative breast cancer—the road to new treatment strategies', *The Lancet*, vol. 389, no. 10087, pp. 2430-42.

Didiasova, M, Wujak, L, Wygrecka, M & Zakrzewicz, D 2014, 'From Plasminogen to Plasmin: Role of Plasminogen Receptors in Human Cancer', *International Journal of Molecular Sciences*, vol. 15, no. 11, p. 21229.

Diéras, V, Pierga, J-Y, Vincent-Salomon, A, Beuzeboc, P, Pouillart, P & de Cremoux, P 2003, 'Targeting epidermal growth factor receptor in cancer of the breast', *Bulletin du Cancer*, vol. 90, pp. S257-62.

Dionysiou, DD, Stamatakos, GS, Uzunoglu, NK & Nikita, KS 2006, 'A computer simulation of in vivo tumour growth and response to radiotherapy: New algorithms and parametric results', *Computers in Biology and Medicine*, vol. 36, no. 5, pp. 448-64.

Dolznig, H, Walzl, A, Kramer, N, Rosner, M, Garin-Chesa, P & Hengstschläger, M 2011, 'Organotypic spheroid cultures to study tumor–stroma interaction during cancer development', *Drug Discovery Today: Disease Models*, vol. 8, no. 2–3, pp. 113-9.

Doolittle, E, Peiris, PM, Doron, G, Goldberg, A, Tucci, S, Rao, S, Shah, S, Sylvestre, M, Govender, P, Turan, O, Lee, Z, Schiemann, WP & Karathanasis, E 2015, 'Spatiotemporal Targeting of a Dual-Ligand Nanoparticle to Cancer Metastasis', *ACS Nano*, vol. 9, no. 8, pp. 8012-21.

Dos Anjos Pultz, B, Da Luz, FAC, De Faria, PR, Oliveira, APL, De Araújo, RA & Silva, MJB 2014, 'Far Beyond the Usual Biomarkers in Breast Cancer: A Review', *Journal of Cancer*, vol. 5, no. 7, pp. 559-71.

Ducat, E, Evrard, B, Peulen, O & Piel, G 2011, 'Cellular uptake of liposomes monitored by confocal microscopy and flow cytometry', *Journal of Drug Delivery Science and Technology*, vol. 21, no. 6, pp. 469-77.

Duderstadt, KE, Geertsema, HJ, Stratmann, SA, Punter, CM, Kulczyk, AW, Richardson, CC & van Oijen, AM 2016, 'Simultaneous Real-Time Imaging of Leading and Lagging Strand Synthesis Reveals the Coordination Dynamics of Single Replisomes', *Molecular Cell*, vol. 64, no. 6, pp. 1035-47.

Duffy, MJ, McGowan, PM, Harbeck, N, Thomssen, C & Schmitt, M 2014, 'uPA and PAI-1 as biomarkers in breast cancer: validated for clinical use in level-of-evidence-1 studies', *Breast Cancer Research*, vol. 16, no. 4, p. 428.

Eirew, P, Steif, A, Khattra, J, Ha, G, Yap, D, Farahani, H, Gelmon, K, Chia, S, Mar, C, Wan, A, Laks, E, Biele, J, Shumansky, K, Rosner, J, McPherson, A, Nielsen, C, Roth, AJL, Lefebvre, C, Bashashati, A, de Souza, C, Siu, C, Aniba, R, Brimhall, J, Oloumi, A, Osako, T, Bruna, A, Sandoval, JL, Algara, T, Greenwood, W, Leung, K, Cheng, H, Xue, H, Wang, Y, Lin, D, Mungall, AJ, Moore, R, Zhao, Y, Lorette, J, Nguyen, L, Huntsman, D, Eaves, CJ, Hansen, C, Marra, MA, Caldas, C, Shah, SP & Aparicio, S 2015, 'Dynamics of genomic clones in breast cancer patient xenografts at single-cell resolution', *Nature*, vol. 518, no. 7539, pp. 422-6.

Emens, LA & Middleton, G 2015, 'The Interplay of Immunotherapy and Chemotherapy: Harnessing Potential Synergies', *Cancer immunology research*, vol. 3, no. 5, pp. 436-43.

Ertongur, S, Lang, S, Mack, B, Wosikowski, K, Muehlenweg, B & Gires, O 2004, 'Inhibition of the invasion capacity of carcinoma cells by WX-UK1, a novel synthetic inhibitor of the urokinase-type plasminogen activator system', *International Journal of Cancer*, vol. 110, no. 6, pp. 815-24.

Espelin, CW, Leonard, SC, Geretti, E, Wickham, TJ & Hendriks, BS 2016, 'Dual HER2 Targeting with Trastuzumab and Liposomal-Encapsulated Doxorubicin (MM-302) Demonstrates Synergistic Antitumor Activity in Breast and Gastric Cancer', *Cancer Research*, vol. 76, no. 6, pp. 1517-27.

Estanqueiro, M, Amaral, MH, Conceição, J & Lobo, JMS 2014, 'Evolution of liposomal carriers intended to anticancer drug delivery: an overview', *Int. J. Curr. Pharm. Res.*, vol. 6, no. 4, p. 8.

Fantozzi, A & Christofori, G 2006, 'Mouse models of breast cancer metastasis', *Breast Cancer Research*, vol. 8, no. 4, p. 212.

Faria, M, Björnmalm, M, Thurecht, KJ, Kent, SJ, Parton, RG, Kavallaris, M, Johnston, APR, Gooding, JJ, Corrie, SR, Boyd, BJ, Thordarson, P, Whittaker, AK, Stevens, MM, Prestidge, CA, Porter, CJH, Parak, WJ, Davis, TP, Crampin, EJ & Caruso, F 2018, 'Minimum information reporting in bio–nano experimental literature', *Nature Nanotechnology*, vol. 13, no. 9, pp. 777-85.

Fox, CB, Wayment, JR, Myers, GA, Endicott, SK & Harris, JM 2009, 'Single-Molecule Fluorescence Imaging of Peptide Binding to Supported Lipid Bilayers', *Analytical Chemistry*, vol. 81, no. 13, pp. 5130-8.

Friedrich, J, Eder, W, Castaneda, J, Doss, M, Huber, E, Ebner, R & Kunz-Schughart, LA 2007, 'A reliable tool to determine cell viability in complex 3-d culture: the acid phosphatase assay', *J Biomol Screen*, vol. 12, no. 7, pp. 925-37.

Friedrich, J, Seidel, C, Ebner, R & Kunz-schughart, LA 2009, 'Spheroid-based drug screen: considerations and practical approach', *Nature Protocols*, vol. 4, no. 3, pp. 309-24.

Gabizon, A, Isacson, R, Libson, E, Kaufman, B, Uziely, B, Catane, R, Ben-Dor, CG, Rabello, E, Cass, Y, Peretz, T, Sulkes, A, Chisin, R & Barenholz, Y 1994, 'Clinical Studies of Liposome-Encapsulated Doxorubicin', *Acta Oncologica*, vol. 33, no. 7, pp. 779-86.

Gabizon, A, Isacson, R, Rosengarten, O, Tzemach, D, Shmeeda, H & Sapir, R 2008, 'An open-label study to evaluate dose and cycle dependence of the pharmacokinetics of pegylated liposomal doxorubicin', *Cancer Chemotherapy and Pharmacology*, vol. 61, no. 4, pp. 695-702.

Gao, H, Hu, Y, Xiong, Y, Zhang, S, Yang, J, Yu, L & Jiang, X 2014, 'Glioma targeting and anti-glioma effect of interleukin 13 peptide and RGD peptide dual

functionalized nanoparticles', *Current Pharmaceutical Biotechnology,* vol. 14, no. 13, pp. 1118-26.

Gao, H, Yang, Z, Zhang, S, Pang, Z, Liu, Q & Jiang, X 2014, 'Study and evaluation of mechanisms of dual targeting drug delivery system with tumor microenvironment assays compared with normal assays', *Acta Biomaterialia*, vol. 10, no. 2, pp. 858-67.

Garg, K, Maurer, M, Griss, J, Bruggen, MC, Wolf, IH, Wagner, C, Willi, N, Mertz, KD & Wagner, SN 2016, 'Tumor-associated B cells in cutaneous primary melanoma and improved clinical outcome', *Human Pathology,* vol. 54, pp. 157-64.

Gayong, S, Yong Hee, Y, Soondong, L, Jinyoung, K & Yu-Kyoung, O 2016, 'Surface-modified liposomes for syndecan 2–targeted delivery of edelfosine', *Asian Journal of Pharmaceutical Sciences,* vol. 11, no. 5, pp. 596-602.

Gerlinger, M, Rowan, AJ, Horswell, S, Larkin, J, Endesfelder, D, Gronroos, E, Martinez, P, Matthews, N, Stewart, A, Tarpey, P, Varela, I, Phillimore, B, Begum, S, McDonald, NQ, Butler, A, Jones, D, Raine, K, Latimer, C, Santos, CR, Nohadani, M, Eklund, AC, Spencer-Dene, B, Clark, G, Pickering, L, Stamp, G, Gore, M, Szallasi, Z, Downward, J, Futreal, PA & Swanton, C 2012, 'Intratumor heterogeneity and branched evolution revealed by multiregion sequencing', *New England Journal of Medicine,* vol. 366, no. 10, pp. 883-92.

Gerlowski, LE & Jain, RK 1986, 'Microvascular permeability of normal and neoplastic tissues', *Microvascular Research*, vol. 31, no. 3, pp. 288-305.

Ghosh, A & Heston, WD 2004, 'Tumor target prostate specific membrane antigen (PSMA) and its regulation in prostate cancer', *Journal of Cellular Biochemistry*, vol. 91, no. 3, pp. 528-39.

Giannopoulou, I, Mylona, E, Kapranou, A, Mavrommatis, J, Markaki, S, Zoumbouli, C, Keramopoulos, A & Nakopoulou, L 2007, 'The prognostic value of the topographic distribution of uPAR expression in invasive breast carcinomas', *Cancer Letters*, vol. 246, no. 1-2, pp. 262-7.

Gillies, RJ, Verduzco, D & Gatenby, RA 2012, 'Evolutionary dynamics of carcinogenesis and why targeted therapy does not work', *Nature Reviews: Cancer*, vol. 12, no. 7, pp. 487-93.

Gluz, O, Liedtke, C, Gottschalk, N, Pusztai, L, Nitz, U & Harbeck, N 2009, 'Triple-negative breast cancer - Current status and future directions', *Annals of Oncology*, vol. 20, no. 12, pp. 1913-27.

Godugu, C, Patel, AR, Desai, U, Andey, T, Sams, A & Singh, M 2013, 'AlgiMatrix™ Based 3D Cell Culture System as an In-Vitro Tumor Model for Anticancer Studies', *PloS One*, vol. 8, no. 1, p. e53708.

Gomez-Cuadrado, L, Tracey, N, Ma, R, Qian, B & Brunton, VG 2017, 'Mouse models of metastasis: progress and prospects', vol. 10, no. 9, pp. 1061-74.

Gonias, SL & Hu, J 2015, 'Urokinase receptor and resistance to targeted anticancer agents', *Frontiers in Pharmacology*, vol. 6, p. 154.

Grimaldi, N, Andrade, F, Segovia, N, Ferrer-Tasies, L, Sala, S, Veciana, J & Ventosa, N 2016, 'Lipid-based nanovesicles for nanomedicine', *Chemical Society Reviews*, vol. 45, no. 23, pp. 6520-45.

Grondahl-Hansen, J, Peters, HA, van Putten, WL, Look, MP, Pappot, H, Ronne, E, Dano, K, Klijn, JG, Brunner, N & Foekens, JA 1995, 'Prognostic significance of the receptor for urokinase plasminogen activator in breast cancer', *Clinical Cancer Research*, vol. 1, no. 10, pp. 1079-87.

Gubernator, J 2011, 'Active methods of drug loading into liposomes: recent strategies for stable drug entrapment and increased in vivo activity', *Expert Opin Drug Deliv*, vol. 8, no. 5, pp. 565-80.

Gulati, V & Wallace, R 2012, 'Rafts, Nanoparticles and Neural Disease', *Nanomaterials*, vol. 2, no. 3, p. 217.

Han, Q, Wang, W, Jia, X, Qian, Y, Li, Q, Wang, Z, Zhang, W, Yang, S, Jia, Y & Hu, Z 2016, 'Switchable Liposomes: Targeting-Peptide-Functionalized and pH-Triggered Cytoplasmic Delivery', *ACS Appl Mater Interfaces*, vol. 8, no. 29, pp. 18658-63.

Hanahan, D & Weinberg, Robert A 2011, 'Hallmarks of Cancer: The Next Generation', *Cell*, vol. 144, no. 5, pp. 646-74.

Hang, MTN, Ranson, M, Saunders, DN, Liang, XM, Bunn, CL & Baker, MS 1998, 'Pharmacokinetics and biodistribution of recombinant human plasminogen activator inhibitor type 2 (PAI-2) in control and tumour xenograft-bearing mice', *Fibrinolysis and Proteolysis*, vol. 12, no. 3, pp. 145-54.

Hansen, AE, Petersen, AL, Henriksen, JR, Boerresen, B, Rasmussen, P, Elema, DR, Rosenschöld, PMa, Kristensen, AT, Kjær, A & Andresen, TL 2015, 'Positron Emission Tomography Based Elucidation of the Enhanced Permeability and Retention Effect in Dogs with Cancer Using Copper-64 Liposomes', *ACS Nano*, vol. 9, no. 7, pp. 6985-95.

Hare, JI, Lammers, T, Ashford, MB, Puri, S, Storm, G & Barry, ST 2017, 'Challenges and strategies in anti-cancer nanomedicine development: An industry perspective', *Advanced Drug Delivery Reviews*, vol. 108, pp. 25-38.

Harrington, KJ, Mohammadtaghi, S, Uster, PS, Glass, D, Peters, AM, Vile, RG & Stewart, JS 2001, 'Effective targeting of solid tumors in patients with locally advanced cancers by radiolabeled pegylated liposomes', *Clinical Cancer Research*, vol. 7, no. 2, pp. 243-54.

Harris, L, Fritsche, H, Mennel, R, Norton, L, Ravdin, P, Taube, S, Somerfield, MR, Hayes, DF & Bast, RC 2007, 'American Society of Clinical Oncology 2007 update of recommendations for the use of tumor markers in breast cancer', *Journal of Clinical Oncology*, vol. 25, no. 33, pp. 5287-312.

Haun, RS, Fan, CY, Mackintosh, SG, Zhao, H & Tackett, AJ 2014, 'CD109 Overexpression in Pancreatic Cancer Identified by Cell-Surface Glycoprotein Capture', *J Proteomics Bioinform,* vol. Suppl 10, p. S10003.

Hayes, DF 2016, 'Is Breast Cancer a Curable Disease?', *Journal of Oncology Practice,* vol. 12, no. 1, pp. 13-6.

He, C, Hu, Y, Yin, L, Tang, C & Yin, C 2010, 'Effects of particle size and surface charge on cellular uptake and biodistribution of polymeric nanoparticles', *Biomaterials,* vol. 31, no. 13, pp. 3657-66.

Hendriks, BS, Klinz, SG, Reynolds, JG, Espelin, CW, Gaddy, DF & Wickham, TJ 2013, 'Impact of tumor HER2/ERBB2 expression level on HER2-targeted liposomal doxorubicin-mediated drug delivery: multiple low-affinity interactions lead to a threshold effect', *Molecular Cancer Therapeutics,* vol. 12, no. 9, pp. 1816-28.

Hermann, PC, Huber, SL, Herrler, T, Aicher, A, Ellwart, JW, Guba, M, Bruns, CJ & Heeschen, C 2007, 'Distinct populations of cancer stem cells determine tumor growth and metastatic activity in human pancreatic cancer', *Cell Stem Cell,* vol. 1, no. 3, pp. 313-23.

Herrmann, D, Conway, JRW, Vennin, C, Magenau, A, Hughes, WE, Morton, JP & Timpson, P 2014, 'Three-dimensional cancer models mimic cell–matrix interactions in the tumour microenvironment', *Carcinogenesis,* vol. 35, no. 8, pp. 1671-9.

Higa, GM & Abraham, J 2007, 'Lapatinib in the treatment of breast cancer', *Expert Review of Anticancer Therapy,* vol. 7, no. 9, pp. 1183-92.

Holliday, D & Speirs, V 2011, 'Choosing the right cell line for breast cancer research', *Breast Cancer Research,* vol. 13, no. 4, p. 215.

Holohan, C, Van Schaeybroeck, S, Longley, DB & Johnston, PG 2013, 'Cancer drug resistance: an evolving paradigm', *Nature Reviews Cancer,* vol. 13, no. 10, pp. 714-26.

Honary, S & Zahir, F 2013, 'Effect of Zeta Potential on the Properties of Nano-Drug Delivery Systems - A Review (Part 2)', *Tropical Journal of Pharmaceutical Research,* vol. 12, no. 2, pp. 265-73.

Howard, CB, Fletcher, N, Houston, ZH, Fuchs, AV, Boase, NR, Simpson, JD, Raftery, LJ, Ruder, T, Jones, ML, de Bakker, CJ, Mahler, SM & Thurecht, KJ 2016, 'Overcoming Instability of Antibody-Nanomaterial Conjugates: Next Generation Targeted Nanomedicines Using Bispecific Antibodies', *Adv Healthc Mater,* vol. 5, no. 16, pp. 2055-68.

Howlader, N, Altekruse, SF, Li, CI, Chen, VW, Clarke, CA, Ries, LAG & Cronin, KA 2014, 'US incidence of breast cancer subtypes defined by joint hormone receptor and HER2 status', *Journal of the National Cancer Institute,* vol. 106, no. 5, p. dju055.

Huber, MC, Mall, R, Braselmann, H, Feuchtinger, A, Molatore, S, Lindner, K, Walch, A, Gross, E, Schmitt, M, Falkenberg, N & Aubele, M 2016, 'uPAR enhances malignant potential of triple-negative breast cancer by directly interacting with uPA and IGF1R', *BMC Cancer*, vol. 16, no. 1, p. 615.

Iden, DL & Allen, TM 2001, 'In vitro and in vivo comparison of immunoliposomes made by conventional coupling techniques with those made by a new post-insertion approach', *BBA - Biomembranes*, vol. 1513, no. 2, pp. 207-16.

Indira Chandran, V, Eppenberger-Castori, S, Venkatesh, T, Vine, KL & Ranson, M 2015, 'HER2 and uPAR cooperativity contribute to metastatic phenotype of HER2-positive breast cancer', *Oncoscience*, vol. 2, no. 3, pp. 207-24.

Ishida, T, Iden, DL & Allen, TM 1999, 'A combinatorial approach to producing sterically stabilized (Stealth) immunoliposomal drugs', *FEBS Letters*, vol. 460, no. 1, pp. 129-33.

Ivascu, A & Kubbies, M 2007, 'Diversity of cell-mediated adhesions in breast cancer spheroids', *International Journal of Oncology*, vol. 31, no. 6, pp. 1403-13.

Jahn, A, Gaitan, M, Vreeland, WN & Locascio, LE 2004, 'Controlled Vesicle Self-Assembly in Microfluidic Channels with Hydrodynamic Focusing', *Journal of the American Chemical Society*, vol. 126, no. 9, pp. 2674-5.

Jemal, A, Bray, F, Center, MM, Ferlay, J, Ward, E & Forman, D 2011, 'Global cancer statistics', *CA: A Cancer Journal for Clinicians*, vol. 61, no. 2, pp. 69-90.

Jiang, T, Munguia-Lopez, JG, Flores-Torres, S, Grant, J, Vijayakumar, S, Leon-Rodriguez, AD & Kinsella, JM 2017, 'Directing the Self-assembly of Tumour Spheroids by Bioprinting Cellular Heterogeneous Models within Alginate/Gelatin Hydrogels', *Scientific Reports*, vol. 7, no. 1, p. 4575.

Jo, M, Eastman, BM, Webb, DL, Stoletov, K, Klemke, R & Gonias, SL 2010, 'Cell signaling by urokinase-type plasminogen activator receptor induces stem cell-like properties in breast cancer cells', *Cancer Research*, vol. 70, no. 21, pp. 8948-58.

Kang, MH, Yoo, HJ, Kwon, YH, Yoon, HY, Lee, SG, Kim, SR, Yeom, DW, Kang, MJ & Choi, YW 2015, 'Design of Multifunctional Liposomal Nanocarriers for Folate Receptor-Specific Intracellular Drug Delivery', *Molecular Pharmaceutics*, vol. 12, no. 12, pp. 4200-13.

Karacali, B, Vamvakidou, A & Tozeren, A 2007, 'Automated recognition of cell phenotypes in histology images based on membrane- and nuclei-targeting biomarkers', *BMC Medical Imaging*, vol. 7, no. 1, p. 7.

Katt, ME, Placone, AL, Wong, AD, Xu, ZS & Searson, PC 2016, 'In Vitro Tumor Models: Advantages, Disadvantages, Variables, and Selecting the Right Platform', *Frontiers in Bioengineering and Biotechnology*, vol. 4, p. 12.

Keam, B, Im, SA, Kim, HJ, Oh, DY, Kim, JH, Lee, SH, Chie, EK, Han, W, Kim, DW, Moon, WK, Kim, TY, Park, IA, Noh, DY, Heo, DS, Ha, SW & Bang, YJ 2007, 'Prognostic impact of clinicopathologic parameters in stage II/III breast cancer treated with neoadjuvant docetaxel and doxorubicin chemotherapy: paradoxical features of the triple negative breast cancer', *BMC Cancer*, vol. 7, p. 203.

Kenny, PA, Lee, GY, Myers, CA, Neve, RM, Semeiks, JR, Spellman, PT, Lorenz, K, Lee, EH, Barcellos-Hoff, MH, Petersen, OW, Gray, JW & Bissell, MJ 2007, 'The morphologies of breast cancer cell lines in three-dimensional assays correlate with their profiles of gene expression', *Molecular Oncology*, vol. 1, no. 1, pp. 84-96.

Kessler, RJ & Fanestil, DD 1986, 'Interference by lipids in the determination of protein using bicinchoninic acid', *Analytical Biochemistry*, vol. 159, no. 1, pp. 138-42.

Kitamura, T, Qian, BZ & Pollard, JW 2015, 'Immune cell promotion of metastasis', *Nature Reviews: Immunology*, vol. 15, no. 2, pp. 73-86.

Klegerman, ME, Hamilton, AJ, Huang, S-L, Tiukinhoy, SD, Khan, AA, MacDonald, RC & McPherson, DD 2002, 'Quantitative Immunoblot Assay for Assessment of Liposomal Antibody Conjugation Efficiency', *Analytical Biochemistry*, vol. 300, no. 1, p. 46.

Klein, CA 2008, 'Cancer. The metastasis cascade', *Science*, vol. 321, no. 5897, pp. 1785-7.

Kluza, E, van der Schaft, DWJ, Hautvast, PAI, Mulder, WJM, Mayo, KH, Griffioen, AW, Strijkers, GJ & Nicolay, K 2010, 'Synergistic Targeting of αvβ3 Integrin and Galectin-1 with Heteromultivalent Paramagnetic Liposomes for Combined MR Imaging and Treatment of Angiogenesis', *Nano Letters*, vol. 10, no. 1, pp. 52-8.

Koudelka, Š & Turánek, J 2012, 'Liposomal paclitaxel formulations', *Journal of Controlled Release*, vol. 163, no. 3, pp. 322-34.

Krag, DN, Theon, AP, Gan, L, Wardell, J & Shi Zhen, T 1989, 'Relationship between cellular accumulation of rhodamine 123 (R123) and cytotoxicity in B16 melanoma cells', *Journal of Surgical Research*, vol. 46, no. 4, pp. 361-5.

Krasnici, S, Werner, A, Eichhorn, ME, Schmitt-Sody, M, Pahernik, SA, Sauer, B, Schulze, B, Teifel, M, Michaelis, U, Naujoks, K & Dellian, M 2003, 'Effect of the surface charge of liposomes on their uptake by angiogenic tumor vessels', *International Journal of Cancer*, vol. 105, no. 4, pp. 561-7.

Krishna, R, Webb, MS, St Onge, G & Mayer, LD 2001, 'Liposomal and nonliposomal drug pharmacokinetics after administration of liposome-encapsulated vincristine and their contribution to drug tissue distribution properties', *Journal of Pharmacology and Experimental Therapeutics*, vol. 298, no. 3, pp. 1206-12.

Krueger, S, Kalinski, T, Wolf, H, Kellner, U & Roessner, A 2005, 'Interactions between human colon carcinoma cells, fibroblasts and monocytic cells in coculture--

regulation of cathepsin B expression and invasiveness', *Cancer Letters*, vol. 223, no. 2, pp. 313-22.

Kulkarni, SB, Singh, M & Betageri, GV 1997, 'Encapsulation, stability and in-vitro release characteristics of liposomal formulations of colchicine', *Journal of Pharmacy and Pharmacology*, vol. 49, no. 5, pp. 491-5.

Lackner, MR, Wilson, TR & Settleman, J 2012, 'Mechanisms of acquired resistance to targeted cancer therapies', *Future Oncology*, vol. 8, no. 8, pp. 999-1014.

Laginha, K, Mumbengegwi, D & Allen, T 2005, 'Liposomes targeted via two different antibodies: Assay, B-cell binding and cytotoxicity', *BBA - Biomembranes*, vol. 1711, pp. 25-32.

Lale, SV, Aswathy, RG, Aravind, A, Kumar, DS & Koul, V 2014, 'AS1411 aptamer and folic acid functionalized pH-responsive ATRP fabricated pPEGMA–PCL–pPEGMA polymeric nanoparticles for targeted drug delivery in cancer therapy', *Biomacromolecules*, vol. 15, no. 5, pp. 1737-52.

Lammers, T, Kiessling, F, Ashford, M, Hennink, W, Crommelin, D & Storm, G 2016, 'Cancer nanomedicine: Is targeting our target?', *Nature Reviews Materials*, vol. 1, no. 9, p. 16069.

Langdon, BB, Mirhossaini, RB, Mabry, JN, Sriram, I, Lajmi, A, Zhang, Y, Rojas, OJ & Schwartz, DK 2015, 'Single-Molecule Resolution of Protein Dynamics on Polymeric Membrane Surfaces: The Roles of Spatial and Population Heterogeneity', *ACS Applied Materials & Interfaces*, vol. 7, no. 6, pp. 3607-17.

Laverman, P, Carstens, MG, Boerman, OC, Dams, ET, Oyen, WJ, van Rooijen, N, Corstens, FH & Storm, G 2001, 'Factors affecting the accelerated blood clearance of polyethylene glycol-liposomes upon repeated injection', *Journal of Pharmacology and Experimental Therapeutics*, vol. 298, no. 2, pp. 607-12.

Law, AMK, Yin, JXM, Castillo, L, Young, AIJ, Piggin, C, Rogers, S, Caldon, CE, Burgess, A, Millar, EKA, O'Toole, SA, Gallego-Ortega, D, Ormandy, CJ & Oakes, SR 2017, 'Andy's Algorithms: new automated digital image analysis pipelines for FIJI', *Scientific Reports*, vol. 7, no. 1, p. 15717.

Leary, E, Rhee, C, Wilks, B & Morgan, JR 2016, 'Accurate quantitative wide-field fluorescence microscopy of 3-D spheroids', *Biotechniques*, vol. 61, no. 5, pp. 237-47.

LeBeau, AM, Duriseti, S, Murphy, ST, Pepin, F, Hann, B, Gray, JW, VanBrocklin, HF & Craik, CS 2013, 'Targeting uPAR with antagonistic recombinant human antibodies in aggressive breast cancer', *Cancer Research*, vol. 73, no. 7, pp. 2070-81.

Lee, HW, Kook, Y-M, Lee, HJ, Park, H & Koh, W-G 2014, 'A three-dimensional co-culture of HepG2 spheroids and fibroblasts using double-layered fibrous scaffolds incorporated with hydrogel micropatterns', *RSC Advances*, vol. 4, no. 105, pp. 61005-11.

Lee, YT 1983, 'Breast carcinoma: pattern of metastasis at autopsy', *Journal of Surgical Oncology*, vol. 23, no. 3, pp. 175-80.

Leonenko, ZV, Finot, E, Ma, H, Dahms, TES & Cramb, DT 2004, 'Investigation of Temperature-Induced Phase Transitions in DOPC and DPPC Phospholipid Bilayers Using Temperature-Controlled Scanning Force Microscopy', *Biophysical Journal*, vol. 86, no. 6, pp. 3783-93.

Li, C, Cao, S, Liu, Z, Ye, X, Chen, L & Meng, S 2010, 'RNAi-mediated downregulation of uPAR synergizes with targeting of HER2 through the ERK pathway in breast cancer cells', *International Journal of Cancer*, vol. 127, no. 7, pp. 1507-16.

Li, H, Yuan, D, Sun, M & Ping, Q 2016, 'Effect of ligand density and PEG modification on octreotide-targeted liposome via somatostatin receptor in vitro and in vivo', *Drug Delivery*, vol. 23, no. 9, pp. 3562-72.

Li, L & Lu, Y 2011, 'Optimizing a 3D Culture System to Study the Interaction between Epithelial Breast Cancer and Its Surrounding Fibroblasts', *Journal of Cancer*, vol. 2, pp. 458-66.

Li, W, Khan, M, Mao, S, Feng, S & Lin, J-M 2018, 'Advances in tumor-endothelial cells co-culture and interaction on microfluidics', *Journal of pharmaceutical analysis*, vol. 8, no. 4, pp. 210-8.

Li, XP, Zhang, XW, Zheng, LZ & Guo, WJ 2015, 'Expression of CD44 in pancreatic cancer and its significance', *International Journal of Clinical and Experimental Pathology*, vol. 8, no. 6, pp. 6724-31.

Li, Y, Qian, Z, Ma, L, Hu, S, Nong, D, Xu, C, Ye, F, Lu, Y, Wei, G & Li, M 2016, 'Single-molecule visualization of dynamic transitions of pore-forming peptides among multiple transmembrane positions', *Nature Communications*, vol. 7, p. 12906.

Liedtke, C & Kiesel, L 2012, 'Breast cancer molecular subtypes – Modern therapeutic concepts for targeted therapy of a heterogeneous entity', *Maturitas*, vol. 73, no. 4, pp. 288-94.

Lin, R-Z & Chang, H-Y 2008, 'Recent advances in three-dimensional multicellular spheroid culture for biomedical research', *Biotechnology Journal*, vol. 3, no. 9-10, pp. 1172-84.

Litzinger, DC, Brown, JM, Wala, I, Kaufman, SA, Van, GY, Farrell, CL & Collins, D 1996, 'Fate of cationic liposomes and their complex with oligonucleotide in vivo', *Biochimica et Biophysica Acta*, vol. 1281, no. 2, pp. 139-49.

Liu, B, Mazouchi, A & Gradinaru, CC 2010, 'Trapping single molecules in liposomes: surface interactions and freeze-thaw effects', *Journal of Physical Chemistry. B*, vol. 114, no. 46, pp. 15191-8.

Liu, FT & Rabinovich, GA 2005, 'Galectins as modulators of tumour progression', *Nature Reviews: Cancer*, vol. 5, no. 1, pp. 29-41.

Lu, J, Yan, D, Shen, L, Sun, Y, Hu, H & Chen, D 2017, 'Cellular uptake mechanism and clearance kinetics of fluorescence-labeled glycyrrhetinic acid and glycyrrhetinic acid–modified liposome in hepatocellular carcinoma cells', *Environmental Toxicology and Pharmacology*, vol. 53, pp. 46-56.

Ludyga, N, Anastasov, N, Rosemann, M, Seiler, J, Lohmann, N, Braselmann, H, Mengele, K, Schmitt, M, Hofler, H & Aubele, M 2013, 'Effects of simultaneous knockdown of HER2 and PTK6 on malignancy and tumor progression in human breast cancer cells', *Molecular Cancer Research*, vol. 11, no. 4, pp. 381-92.

Lukyanov, AN, Elbayoumi, TA, Chakilam, AR & Torchilin, VP 2004, 'Tumor-targeted liposomes: doxorubicin-loaded long-circulating liposomes modified with anti-cancer antibody', *Journal of Controlled Release*, vol. 100, no. 1, pp. 135-44.

Ma, Z, Webb, DJ, Jo, M & Gonias, SL 2001, 'Endogenously produced urokinase-type plasminogen activator is a major determinant of the basal level of activated ERK/MAP kinase and prevents apoptosis in MDA-MB-231 breast cancer cells', *Journal of Cell Science*, vol. 114, no. 18, pp. 3387-96.

Mack, K, Rüger, R, Fellermeier, S, Seifert, O & Kontermann, RE 2012, 'Dual Targeting of Tumor Cells with Bispecific Single-Chain Fv-Immunoliposomes', *Antibodies*, vol. 1, no. 2, pp. 199-214.

Maeda, H 2015, 'Toward a full understanding of the EPR effect in primary and metastatic tumors as well as issues related to its heterogeneity', *Advanced Drug Delivery Reviews*, vol. 91, pp. 3-6.

Marchetti, M, Malinowska, A, Heller, I & Wuite, GJL 2017, 'How to switch the motor on: RNA polymerase initiation steps at the single-molecule level', *Protein Science*, vol. 26, no. 7, pp. 1003-13.

Masoud, V & Pages, G 2017, 'Targeted therapies in breast cancer: New challenges to fight against resistance', *World Journal of Clinical Oncology*, vol. 8, no. 2, pp. 120-34.

Matesic, L, Locke, JM, Bremner, JB, Pyne, SG, Skropeta, D, Ranson, M & Vine, KL 2008, 'N-Phenethyl and N-naphthylmethyl isatins and analogues as in vitro cytotoxic agents', *Bioorganic and Medicinal Chemistry*, vol. 16, no. 6, pp. 3118-24.

Matsumura, Y & Maeda, H 1986, 'A new concept for macromolecular therapeutics in cancer chemotherapy: mechanism of tumoritropic accumulation of proteins and the antitumor agent smancs', *Cancer Research*, vol. 46, no. 12, pp. 6387-92.

Matthews, H 2011, 'Synthesis and biological evaluation of plasminogen activation inhibitors as antitumour/antimetastasis agents', Doctor of Philosophy thesis, University of Wollongong.

Mazar, AP, Ahn, RW & O'Halloran, TV 2011, 'Development of Novel Therapeutics Targeting the Urokinase Plasminogen Activator Receptor (uPAR) and Their Translation Toward the Clinic', *Current Pharmaceutical Design*, vol. 17, no. 19, pp. 1970-8.

McCarty, OJ, Mousa, SA, Bray, PF & Konstantopoulos, K 2000, 'Immobilized platelets support human colon carcinoma cell tethering, rolling, and firm adhesion under dynamic flow conditions', *Blood*, vol. 96, no. 5, pp. 1789-97.

Mehnert, JM, McCarthy, MM, Aziz, SA, Sznol, M, Flaherty, KT, Camp, RL, Rimm, DL & Kluger, HM 2007, 'VEGF, VEGFR1, and VEGFR2 expression in melanoma', *Journal of Clinical Oncology*, vol. 25, no. 18_suppl, p. 8520.

Meng, S, Tripathy, D, Shete, S, Ashfaq, R, Saboorian, H, Haley, B, Frenkel, E, Euhus, D, Leitch, M, Osborne, C, Clifford, E, Perkins, S, Beitsch, P, Khan, A, Morrison, L, Herlyn, D, Terstappen, LW, Lane, N, Wang, J & Uhr, J 2006, 'uPAR and HER-2 gene status in individual breast cancer cells from blood and tissues', *Proceedings of the National Academy of Sciences of the United States of America*, vol. 103, no. 46, pp. 17361-5.

Menyhart, O, Santarpia, L & Gyorffy, B 2015, 'A Comprehensive Outline of Trastuzumab Resistance Biomarkers in HER2 Overexpressing Breast Cancer', *Current Cancer Drug Targets*, vol. 15, no. 8, pp. 665-83.

Messerschmidt, SK, Kolbe, A, Muller, D, Knoll, M, Pleiss, J & Kontermann, RE 2008, 'Novel single-chain Fv' formats for the generation of immunoliposomes by site-directed coupling', *Bioconjugate Chemistry*, vol. 19, no. 1, pp. 362-9.

Miller, K, Cortes, J, Hurvitz, SA, Krop, IE, Tripathy, D, Verma, S, Riahi, K, Reynolds, JG, Wickham, TJ, Molnar, I & Yardley, DA 2016, 'HERMIONE: a randomized Phase 2 trial of MM-302 plus trastuzumab versus chemotherapy of physician's choice plus trastuzumab in patients with previously treated, anthracycline-naive, HER2-positive, locally advanced/metastatic breast cancer', *BMC Cancer*, vol. 16, p. 352.

Moirangthem, A, Bondhopadhyay, B, Mukherjee, M, Bandyopadhyay, A, Mukherjee, N, Konar, K, Bhattacharya, S & Basu, A 2016, 'Simultaneous knockdown of uPA and MMP9 can reduce breast cancer progression by increasing cell-cell adhesion and modulating EMT genes', *Scientific Reports*, vol. 6, p. 21903.

Monachino, E, Spenkelink, LM & van Oijen, AM 2017, 'Watching cellular machinery in action, one molecule at a time', *Journal of Cell Biology*, vol. 216, no. 1, pp. 41-51.

Moreira, JN, Gaspar, R, Ishida, T & Allen, TM 2002, 'Use of the post-insertion technique to insert peptide ligands into pre-formed stealth liposomes with retention of binding activity and cytotoxicity', *Pharmaceutical Research*, vol. 19, no. 3, pp. 265-9.

Nahta, R & Esteva, FJ 2006, 'HER2 therapy: molecular mechanisms of trastuzumab resistance', *Breast Cancer Research*, vol. 8, no. 6, p. 215.

Nellis, DF, Ekstrom, DL, Kirpotin, DB, Zhu, J, Andersson, R, Broadt, TL, Ouellette, TF, Perkins, SC, Roach, JM, Drummond, DC, Hong, K, Marks, JD, Park, JW & Giardina, SL 2005, 'Preclinical manufacture of an anti-HER2 scFv-PEG-DSPE, liposome-inserting conjugate. 1. Gram-scale production and purification', *Biotechnology Progress*, vol. 21, no. 1, pp. 205-20.

Nellis, DF, Giardina, SL, Janini, GM, Shenoy, SR, Marks, JD, Tsai, R, Drummond, DC, Hong, K, Park, JW, Ouellette, TF, Perkins, SC & Kirpotin, DB 2005, 'Preclinical manufacture of anti-HER2 liposome-inserting, scFv-PEG-lipid conjugate. 2. Conjugate micelle identity, purity, stability, and potency analysis', *Biotechnology Progress*, vol. 21, no. 1, pp. 221-32.

Nichols, JW & Bae, YH 2014, 'EPR: Evidence and fallacy', *Journal of Controlled Release*, vol. 190, pp. 451-64.

Nielsen, A, Scarlett, CJ, Samra, JS, Gill, A, Li, Y, Allen, BJ & Smith, RC 2005, 'Significant overexpression of urokinase-type plasminogen activator in pancreatic adenocarcinoma using real-time quantitative reverse transcription polymerase chain reaction', *Journal of Gastroenterology and Hepatology*, vol. 20, no. 2, pp. 256-63.

Nunes-Correia, I, Eulálio, A, Nir, S, Düzgünes, N, Ramalho-Santos, J & Pedroso de Lima, MC 2002, 'Fluorescent probes for monitoring virus fusion kinetics: comparative evaluation of reliability', *Biochimica et Biophysica Acta (BBA) - Biomembranes*, vol. 1561, no. 1, pp. 65-75.

O'Halloran, TV, Ahn, R, Hankins, P, Swindell, E & Mazar, AP 2013, 'The many spaces of uPAR: delivery of theranostic agents and nanobins to multiple tumor compartments through a single target', *Theranostics*, vol. 3, no. 7, pp. 496-506.

Olivé, M, Cailleau, R, Young, R & Reeves, WJ 1974, 'Breast Tumor Cell Lines From Pleural Effusions2', *JNCI: Journal of the National Cancer Institute*, vol. 53, no. 3, pp. 661-74.

Oswald, M, Geissler, S & Goepferich, A 2016, 'Determination of the activity of maleimide-functionalized phospholipids during preparation of liposomes', *International Journal of Pharmaceutics*, vol. 514, no. 1, pp. 93-102.

Otterstrom, JJ, Brandenburg, B, Koldijk, MH, Juraszek, J, Tang, C, Mashaghi, S, Kwaks, T, Goudsmit, J, Vogels, R, Friesen, RH & van Oijen, AM 2014, 'Relating influenza virus membrane fusion kinetics to stoichiometry of neutralizing antibodies at the single-particle level', *Proceedings of the National Academy of Sciences of the United States of America*, vol. 111, no. 48, pp. E5143-8.

Oussoren, C & Storm, G 1999, 'Effect of Repeated Intravenous Administration on the Circulation Kinetics of Poly(Ethyleneglycol)-Liposomes in Rats', *Journal of Liposome Research*, vol. 9, no. 3, pp. 349-55.

Pan, H, Wu, N, Huang, Y, Li, Q, Liu, C, Liang, M, Zhou, W, Liu, X & Wang, S 2015, 'Aldehyde dehydrogenase 1 expression correlates with the invasion of breast cancer', *Diagnostic Pathology*, vol. 10, p. 66.

Park, JW, Kirpotin, DB, Hong, K, Shalaby, R, Shao, Y, Nielsen, UB, Marks, JD, Papahadjopoulos, D & Benz, CC 2001, 'Tumor targeting using anti-her2 immunoliposomes', *Journal of Controlled Release*, vol. 74, pp. 95-113.

Pattni, BS, Chupin, VV & Torchilin, VP 2015, 'New Developments in Liposomal Drug Delivery', *Chemical Reviews*, vol. 115, no. 19, pp. 10938-66.

Pearce, AK, Fuchs, AV, Fletcher, NL & Thurecht, KJ 2016, 'Targeting Nanomedicines to Prostate Cancer: Evaluation of Specificity of Ligands to Two Different Receptors In Vivo', *Pharmaceutical Research*, vol. 33, no. 10, pp. 2388-99.

Perche, F & Torchilin, VP 2013, 'Recent Trends in Multifunctional Liposomal Nanocarriers for Enhanced Tumor Targeting', *Journal of Drug Delivery*, pp. 1-32.

Perez, HL, Cardarelli, PM, Deshpande, S, Gangwar, S, Schroeder, GM, Vite, GD & Borzilleri, RM 2014, 'Antibody-drug conjugates: current status and future directions', *Drug Discov Today*, vol. 19, no. 7, pp. 869-81.

Pickl, M & Ries, CH 2009, 'Comparison of 3D and 2D tumor models reveals enhanced HER2 activation in 3D associated with an increased response to trastuzumab', *Oncogene*, vol. 28, no. 3, pp. 461-8.

Pierga, JY, Bonneton, C, Magdelenat, H, Vincent, A, Nos, C, Boudou, E, Pouillart, P, Thiery, JP & Cremoux, P 2005, 'Real-time quantitative PCR determination of urokinase-type plasminogen activator receptor (uPAR) expression of isolated micrometastatic cells from bone marrow of breast cancer patients', *International Journal of Cancer*, vol. 114, no. 2, pp. 291-8.

Pujals, S, Feiner-Gracia, N, Delcanale, P, Voets, I & Albertazzi, L 2019, 'Super-resolution microscopy as a powerful tool to study complex synthetic materials', *Nature Reviews Chemistry*, vol. 3, pp. 68-84.

Puttick, S, Boase, NRB, Blakey, I & Thurecht, KJ 2015, 'Imaging tumour distribution of a polymeric drug delivery platform in vivo by PET-MRI', *Journal of Chemical Technology and Biotechnology*, vol. 90, no. 7, pp. 1237-44.

Pyke, C, Ralfkiaer, E, Ronne, E, Hoyer-Hansen, G, Kirkeby, L & Dano, K 1994, 'Immunohistochemical detection of the receptor for urokinase plasminogen activator in human colon cancer', *Histopathology*, vol. 24, no. 2, pp. 131-8.

Rabenhold, M, Steiniger, F, Fahr, A, Kontermann, RE & Rüger, R 2015, 'Bispecific single-chain diabody-immunoliposomes targeting endoglin (CD105) and fibroblast activation protein (FAP) simultaneously', *Journal of Controlled Release*, vol. 201, pp. 56-67.

Rosenblum, D, Joshi, N, Tao, W, Karp, JM & Dan, P 2018, 'Progress and challenges towards targeted delivery of cancer therapeutics', *Nature Communications*, vol. 9, no. 1, p. 1410.

Ross, JS, Slodkowska, EA, Symmans, WF, Pusztai, L, Ravdin, PM & Hortobagyi, GN 2009, 'The HER-2 receptor and breast cancer: ten years of targeted anti-HER-2 therapy and personalized medicine', *Oncologist*, vol. 14, no. 4, pp. 320-68.

Rossi, M, Carioli, G, Bonifazi, M, Zambelli, A, Franchi, M, Moja, L, Zambon, A, Corrao, G, La Vecchia, C, Zocchetti, C & Negri, E 2016, 'Trastuzumab for HER2+ metastatic breast cancer in clinical practice: Cardiotoxicity and overall survival', *European Journal of Cancer*, vol. 52, pp. 41-9.

Ruysschaert, T, Marque, A, Duteyrat, J-L, Lesieur, S, Winterhalter, M & Fournier, D 2005, 'Liposome retention in size exclusion chromatography', *BMC Biotechnology*, vol. 5, no. 1, p. 11.

Safhi, MM, Sivakumar, SM, Jabeen, A, Zakir, F, Islam, F, Anwer, T, Bagul, US, Elmobark, ME, Khan, G, Siddiqui, R, Hussien, A & Alam, MF 2017, 'Chapter 8 - Nanoparticle System for Anticancer Drug Delivery: Targeting to Overcome Multidrug Resistance', in AM Grumezescu (ed.), *Multifunctional Systems for Combined Delivery, Biosensing and Diagnostics*, Elsevier, pp. 159-69.

Sagiv, E, Starr, A, Rozovski, U, Khosravi, R, Altevogt, P, Wang, T & Arber, N 2008, 'Targeting CD24 for treatment of colorectal and pancreatic cancer by monoclonal antibodies or small interfering RNA', *Cancer Research*, vol. 68, no. 8, pp. 2803-12.

Sapra, P & Allen, TM 2004, 'Improved outcome when B-cell lymphoma is treated with combinations of immunoliposomal anticancer drugs targeted to both the CD19 and CD20 epitopes', *Clinical Cancer Research*, vol. 10, no. 7, pp. 2530-7.

Saul, JM, Annapragada, AV & Bellamkonda, RV 2006, 'A dual-ligand approach for enhancing targeting selectivity of therapeutic nanocarriers', *Journal of Controlled Release*, vol. 114, pp. 277-87.

Sávia Caldeira de Araújo Lopes, CdSG, Talita Guieiro Ribeiro Rocha, Diêgo dos Santos Ferreira, Elaine Amaral Leite, Mônica Cristina Oliveira 2013, *Liposomes as Carriers of Anticancer Drugs*, 10.5772/55290.

Scaltriti, M, Rojo, F, Ocana, A, Anido, J, Guzman, M, Cortes, J, Di Cosimo, S, Matias-Guiu, X, Ramon y Cajal, S, Arribas, J & Baselga, J 2007, 'Expression of p95HER2, a truncated form of the HER2 receptor, and response to anti-HER2 therapies in breast cancer', *Journal of the National Cancer Institute*, vol. 99, no. 8, pp. 628-38.

Schnitt, SJ 2010, 'Classification and prognosis of invasive breast cancer: from morphology to molecular taxonomy', *Modern Pathology*, vol. 23, no. S2, pp. S60-4.

Sebolt-Leopold, JS & English, JM 2006, 'Mechanisms of drug inhibition of signalling molecules', *Nature*, vol. 441, no. 7092, pp. 457-62.

Senavirathna, LK, Fernando, R, Maples, D, Zheng, Y, Polf, JC & Ranjan, A 2013, 'Tumor Spheroids as an In Vitro Model for Determining the Therapeutic Response to Proton Beam Radiotherapy and Thermally Sensitive Nanocarriers', *Theranostics*, vol. 3, no. 9, pp. 687-91.

Serro, AP, Carapeto, A, Paiva, G, Farinha, JPS, Colaço, R & Saramago, B 2012, 'Formation of an intact liposome layer adsorbed on oxidized gold confirmed by three complementary techniques: QCM-D, AFM and confocal fluorescence microscopy', *Surface and Interface Analysis*, vol. 44, no. 4, pp. 426-33.

Shafaee, MN & Ellis, MJ 2017, 'Breast Cancer Patient-Derived Xenografts: Pros, Cons, and Next Steps', *JNCI: Journal of the National Cancer Institute*, vol. 109, no. 7, p. 307.

Shaheen, RM, Davis, DW, Liu, W, Zebrowski, BK, Wilson, MR, Bucana, CD, McConkey, DJ, McMahon, G & Ellis, LM 1999, 'Antiangiogenic therapy targeting the tyrosine kinase receptor for vascular endothelial growth factor receptor inhibits the growth of colon cancer liver metastasis and induces tumor and endothelial cell apoptosis', *Cancer Research*, vol. 59, no. 21, pp. 5412-6.

Shak, S, Bales, R, Baughman, SA, Curd, JG, Fuchs, HJ, Perry, C, Teeter, G & Leber, L 1998, 'Genentech and Breast Cancer Advocacy', *Breast Disease*, vol. 10, no. 5/6, pp. 61-4.

Sharma, G, Modgil, A, Zhong, T, Sun, C & Singh, J 2014, 'Influence of short-chain cell-penetrating peptides on transport of doxorubicin encapsulating receptor-targeted liposomes across brain endothelial barrier', *Pharmaceutical Research*, vol. 31, no. 5, pp. 1194-209.

Shashkova, S & Leake, MC 2017, 'Single-molecule fluorescence microscopy review: shedding new light on old problems', *Bioscience Reports*, vol. 37, no. 4, p. BSR20170031.

Shi, J, Kantoff, PW, Wooster, R & Farokhzad, OC 2017, 'Cancer nanomedicine: progress, challenges and opportunities', *Nature Reviews: Cancer*, vol. 17, no. 1, pp. 20-37.

Si, Y, Kim, S, Zhang, E, Tang, Y, Jaskula-Sztul, R, Markert, JM, Chen, H, Zhou, L & Liu, X 2019, 'Targeted Exosomes for Drug Delivery: Biomanufacturing, Surface Tagging, and Validation', *Biotechnology Journal*, vol. n/a, no. n/a, p. 1900163.

Siegler, EL, Kim, YJ & Wang, P 2016, 'Nanomedicine targeting the tumor microenvironment: Therapeutic strategies to inhibit angiogenesis, remodel matrix, and modulate immune responses', *Journal of Cellular Immunotherapy*, vol. 2, no. 2, pp. 69-78.

Sievers, EL & Senter, PD 2013, 'Antibody-drug conjugates in cancer therapy', *Annual Review of Medicine*, vol. 64, pp. 15-29.

Slamon, DJ, Clark, GM, Wong, SG, Levin, WJ, Ullrich, A & McGuire, WL 1987, 'Human breast cancer: correlation of relapse and survival with amplification of the HER-2/neu oncogene', *Science*, vol. 235, no. 4785, pp. 177-82.

Sledge, GW 2016, 'Curing Metastatic Breast Cancer', *Journal of Oncology Practice*, vol. 12, no. 1, pp. 6-10.

Smith, MC, Crist, RM, Clogston, JD & McNeil, SE 2017, 'Zeta potential: a case study of cationic, anionic, and neutral liposomes', *Analytical and Bioanalytical Chemistry*, vol. 409, no. 24, pp. 5779-87.

Solomayer, EF, Becker, S, Pergola-Becker, G, Bachmann, R, Kramer, B, Vogel, U, Neubauer, H, Wallwiener, D, Huober, J & Fehm, TN 2006, 'Comparison of HER2 status between primary tumor and disseminated tumor cells in primary breast cancer patients', *Breast Cancer Research and Treatment*, vol. 98, no. 2, pp. 179-84.

Soule, HD, Vazquez, J, Long, A, Albert, S & Brennan, M 1973, 'A Human Cell Line From a Pleural Effusion Derived From a Breast Carcinoma2', *JNCI: Journal of the National Cancer Institute*, vol. 51, no. 5, pp. 1409-16.

Soundararajan, A, Bao, A, Phillips, WT, Perez, R, 3rd & Goins, BA 2009, '[(186)Re]Liposomal doxorubicin (Doxil): in vitro stability, pharmacokinetics, imaging and biodistribution in a head and neck squamous cell carcinoma xenograft model', *Nuclear Medicine and Biology*, vol. 36, no. 5, pp. 515-24.

Sporikova, Z, Koudelakova, V, Trojanec, R & Hajduch, M 2018, 'Genetic Markers in Triple-Negative Breast Cancer', *Clinical Breast Cancer*, vol. 18, no. 5, pp. e841-e50.

Stutchbury, TK, Al-Ejeh, F, Stillfried, GE, Croucher, DR, Andrews, J, Irving, D, Links, M & Ranson, M 2007, 'Preclinical evaluation of 213Bi-labeled plasminogen activator inhibitor type 2 in an orthotopic murine xenogenic model of human breast carcinoma', *Molecular Cancer Therapeutics*, vol. 6, no. 1, pp. 203-12.

Subik, K, Lee, J-F, Baxter, L, Strzepek, T, Costello, D, Crowley, P, Xing, L, Hung, M-C, Bonfiglio, T, Hicks, DG & Tang, P 2010, 'The Expression Patterns of ER, PR, HER2, CK5/6, EGFR, Ki-67 and AR by Immunohistochemical Analysis in Breast Cancer Cell Lines', *Breast Cancer : Basic and Clinical Research*, vol. 4, pp. 35-41.

Sugiyama, T, Asai, T, Nedachi, YM, Katanasaka, Y, Shimizu, K, Maeda, N & Oku, N 2013, 'Enhanced active targeting via cooperative binding of ligands on liposomes to target receptors', *PloS One*, vol. 8, no. 6, p. e67550.

Swaminathan, S, Ngo, O, Basehore, S & Clyne, AM 2017, 'Vascular Endothelial–Breast Epithelial Cell Coculture Model Created from 3D Cell Structures', *ACS Biomaterials Science & Engineering*, vol. 3, no. 11, pp. 2999-3006.

Swenson, CE, Perkins, WR, Roberts, P & Janoff, AS 2001, 'Liposome technology and the development of Myocet™ (liposomal doxorubicin citrate)', *The Breast*, vol. 10, Supplement 2, pp. 1-7.

Szebeni, J 2014, 'Complement activation-related pseudoallergy: a stress reaction in blood triggered by nanomedicines and biologicals', *Molecular Immunology*, vol. 61, no. 2, pp. 163-73.

Szebeni, J, Muggia, F & Barenholz, Y 2016, 'Case Study: Complement Activation Related Hypersensitivity Reactions to PEGylated Liposomal Doxorubicin ? Experimental and Clinical Evidence, Mechanisms and Approaches to Inhibition', in *Handbook of Immunological Properties of Engineered Nanomaterials*, World Scientific, vol. 6, pp. 331-61.

Szebeni, J & Storm, G 2015, 'Complement activation as a bioequivalence issue relevant to the development of generic liposomes and other nanoparticulate drugs', *Biochemical and Biophysical Research Communications*, vol. 468, no. 3, pp. 490-7.

Tang, Y, Soroush, F, Sheffield, JB, Wang, B, Prabhakarpandian, B & Kiani, MF 2017, 'A Biomimetic Microfluidic Tumor Microenvironment Platform Mimicking the EPR Effect for Rapid Screening of Drug Delivery Systems', *Scientific Reports*, vol. 7, no. 1, p. 9359.

Tanner, NA & van Oijen, AM 2010, 'Visualizing DNA replication at the single-molecule level', *Methods in Enzymology*, vol. 475, pp. 259-78.

Tario, JD, Conway, AN, Muirhead, KA & Wallace, PK 2018, 'Monitoring Cell Proliferation by Dye Dilution: Considerations for Probe Selection', *Methods in Molecular Biology*, vol. 1678, pp. 249-99.

Tessler, LA & Mitra, RD 2011, 'Sensitive single-molecule protein quantification and protein complex detection in a microarray format', *Proteomics*, vol. 11, no. 24, pp. 4731-5.

Thoma, CR, Zimmermann, M, Agarkova, I, Kelm, JM & Krek, W 2014, '3D cell culture systems modeling tumor growth determinants in cancer target discovery', *Advanced Drug Delivery Reviews*, vol. 69-70, pp. 29-41.

Ticau, S, Friedman, LJ, Champasa, K, Correa, IR, Jr., Gelles, J & Bell, SP 2017, 'Mechanism and timing of Mcm2-7 ring closure during DNA replication origin licensing', *Nature Structural & Molecular Biology*, vol. 24, no. 3, pp. 309-15.

Troiani, T, Martinelli, E, Capasso, A, Morgillo, F, Orditura, M, De Vita, F & Ciardiello, F 2012, 'Targeting EGFR in pancreatic cancer treatment', *Current Drug Targets*, vol. 13, no. 6, pp. 802-10.

Tung, JK, Berglund, K, Gutekunst, C-A, Hochgeschwender, U & Gross, RE 2016, 'Bioluminescence imaging in live cells and animals', *Neurophotonics*, vol. 3, no. 2, p. 025001.

Turner, PV, Brabb, T, Pekow, C & Vasbinder, MA 2011, 'Administration of substances to laboratory animals: routes of administration and factors to consider', *Journal of the American Association for Laboratory Animal Science : JAALAS*, vol. 50, no. 5, pp. 600-13.

Un, K, Sakai-Kato, K, Oshima, Y, Kawanishi, T & Okuda, H 2012, 'Intracellular trafficking mechanism, from intracellular uptake to extracellular efflux, for phospholipid/cholesterol liposomes', *Biomaterials*, vol. 33, no. 32, pp. 8131-41.

Urban, P, Vuaroqueaux, V, Labuhn, M, Delorenzi, M, Wirapati, P, Wight, E, Senn, HJ, Benz, C, Eppenberger, U & Eppenberger-Castori, S 2006, 'Increased expression of urokinase-type plasminogen activator mRNA determines adverse prognosis in ErbB2-positive primary breast cancer', *Journal of Clinical Oncology*, vol. 24, no. 26, pp. 4245-53.

Uster, PS, Allen, TM, Daniel, BE, Mendez, CJ, Newman, MS & Zhu, GZ 1996, 'Insertion of poly(ethylene glycol) derivatized phospholipid into pre-formed liposomes results in prolonged in vivo circulation time', *FEBS Letters*, vol. 386, no. 2-3, pp. 243-6.

van der Geest, T, Laverman, P, Metselaar, JM, Storm, G & Boerman, OC 2016, 'Radionuclide imaging of liposomal drug delivery', *Expert Opinion on Drug Delivery*, vol. 13, no. 9, pp. 1231-42.

van der Meel, R, Vehmeijer, LJC, Kok, RJ, Storm, G & Van Gaal, EVB 2013, 'Ligand-targeted particulate nanomedicines undergoing clinical evaluation: Current status', *Advanced Drug Delivery Reviews*, vol. 65, no. 10, pp. 1284-98.

Velasco-Velazquez, MA, Popov, VM, Lisanti, MP & Pestell, RG 2011, 'The role of breast cancer stem cells in metastasis and therapeutic implications', *American Journal of Pathology*, vol. 179, no. 1, pp. 2-11.

Venkatesan, S & Swanton, C 2016, 'Tumor Evolutionary Principles: How Intratumor Heterogeneity Influences Cancer Treatment and Outcome', *Am Soc Clin Oncol Educ Book*, vol. 35, pp. e141-9.

Verschraegen, C 2012, 'The monoclonal antibody to cytotoxic T lymphocyte antigen 4, ipilimumab, in the treatment of melanoma', *Cancer Management and Research*, vol. 4, pp. 1-8.

Vijayakumar, MR, Kosuru, R, Vuddanda, PR, Singh, SK & Singh, S 2016, 'Trans resveratrol loaded DSPE PEG 2000 coated liposomes: An evidence for prolonged systemic circulation and passive brain targeting', *Journal of Drug Delivery Science and Technology*, vol. 33, pp. 125-35.

Vikas, P, Borcherding, N & Zhang, W 2018, 'The clinical promise of immunotherapy in triple-negative breast cancer', *Cancer Management and Research*, vol. 10, pp. 6823-33.

Vine, KL, Belfiore, L, Jones, L, Locke, JM, Wade, S, Minaei, E & Ranson, M 2016, 'N-alkylated isatins evade P-gp mediated efflux and retain potency in MDR cancer cell lines', *Heliyon*, vol. 2, no. 1, p. Article e00060.

Vine, KL, Chandran, VI, Locke, JM, Matesic, L, Lee, J, Skropeta, D, Bremner, JB & Ranson, M 2012, 'Targeting Urokinase and the Transferrin Receptor with Novel, Anti-Mitotic N-Alkylisatin Cytotoxin Conjugates Causes Selective Cancer Cell Death and Reduces Tumor Growth', *Current Cancer Drug Targets*, vol. 12, no. 1, pp. 64-73.

Vine, KL, Lobov, S, Chandran, VI, Harris, NLE & Ranson, M 2014, 'Improved Pharmacokinetic and Biodistribution Properties of the Selective Urokinase Inhibitor PAI-2 (SerpinB2) by Site-Specific PEGylation: Implications for Drug Delivery', *Pharmaceutical Research*, vol. 32, no. 3, pp. 1045-54.

Vine, KL, Locke, JM, Ranson, M, Pyne, SG & Bremner, JB 2007, 'An Investigation into the Cytotoxicity and Mode of Action of Some Novel N-Alkyl-Substituted Isatins', *Journal of Medicinal Chemistry*, vol. 50, no. 21, pp. 5109-17.

Wagner, A & Vorauer-Uhl, K 2011, 'Liposome Technology for Industrial Purposes', *Journal of Drug Delivery*, p. 591325.

Waks, AG & Winer, EP 2019, 'Breast Cancer Treatment: A ReviewBreast Cancer Treatment in 2019Breast Cancer Treatment in 2019', *JAMA*, vol. 321, no. 3, pp. 288-300.

Walker, JM 1996, 'The Bicinchoninic Acid (BCA) Assay for Protein Quantitation', in JM Walker (ed.), *The Protein Protocols Handbook*, Humana Press, Totowa, NJ, pp. 11-4.

Walkey, CD & Chan, WCW 2012, 'Understanding and controlling the interaction of nanomaterials with proteins in a physiological environment', *Chemical Society Reviews*, vol. 41, no. 7, pp. 2780-99.

Wang, AZ 2015, 'EPR or no EPR? The billion-dollar question', *Science Translational Medicine*, vol. 7, no. 294, p. 294ec112.

Wang, RH, Cao, HM, Tian, ZJ, Jin, B, Wang, Q, Ma, H & Wu, J 2015, 'Efficacy of dual-functional liposomes containing paclitaxel for treatment of lung cancer', *Oncology Reports*, vol. 33, no. 2, pp. 783-91.

Ward, EM, DeSantis, CE, Lin, CC, Kramer, JL, Jemal, A, Kohler, B, Brawley, OW & Gansler, T 2015, 'Cancer statistics: Breast cancer in situ', *CA: A Cancer Journal for Clinicians*, vol. 65, no. 6, pp. 481-95.

Watkins, LP & Yang, H 2005, 'Detection of intensity change points in time-resolved single-molecule measurements', *Journal of Physical Chemistry. B*, vol. 109, no. 1, pp. 617-28.

Weidner, N, Semple, JP, Welch, WR & Folkman, J 1991, 'Tumor angiogenesis and metastasis--correlation in invasive breast carcinoma', *New England Journal of Medicine*, vol. 324, no. 1, pp. 1-8.

Weigelt, B, Lo, AT, Park, CC, Gray, JW & Bissell, MJ 2010, 'HER2 signaling pathway activation and response of breast cancer cells to HER2-targeting agents is dependent strongly on the 3D microenvironment', *Breast Cancer Research and Treatment*, vol. 122, no. 1, pp. 35-43.

Weigelt, B, Peterse, JL & van 't Veer, LJ 2005, 'Breast cancer metastasis: markers and models', *Nature Reviews: Cancer*, vol. 5, no. 8, pp. 591-602.

Wilczynska, M, Lobov, S, Ohlsson, P-I & Ny, T 2003, 'A redox-sensitive loop regulates plasminogen activator inhibitor type 2 (PAI-2) polymerization', *The EMBO journal*, vol. 22, no. 8, pp. 1753-61.

Wilhelm, S, Tavares, AJ, Dai, Q, Ohta, S, Audet, J, Dvorak, HF & Chan, WCW 2016, 'Analysis of nanoparticle delivery to tumours', *Nat. Rev. Mater.*, vol. 1, p. 16014.

Willis, M & Forssen, E 1998, 'Ligand-targeted liposomes', *Adv Drug Deliv Rev*, vol. 29, no. 3, pp. 249-71.

Wood, KC 2015, 'Mapping the Pathways of Resistance to Targeted Therapies', *Cancer Research*, vol. 75, no. 20, pp. 4247-51.

Xiao, K, Li, Y, Luo, J, Lee, JS, Xiao, W, Gonik, AM, Agarwal, RG & Lam, KS 2011, 'The effect of surface charge on in vivo biodistribution of PEG-oligocholic acid based micellar nanoparticles', *Biomaterials*, vol. 32, no. 13, pp. 3435-46.

Yalcin, TE, Ilbasmis-Tamer, S, Ibisoglu, B, Özdemir, A, Ark, M & Takka, S 2018, 'Gemcitabine hydrochloride-loaded liposomes and nanoparticles: comparison of encapsulation efficiency, drug release, particle size, and cytotoxicity', *Pharmaceutical Development and Technology*, vol. 23, no. 1, pp. 76-86.

Yarden, Y 2001, 'Biology of HER2 and Its Importance in Breast Cancer', *Oncology*, vol. 61, pp. 1-13.

Ying, X, Wen, H, Lu, W-L, Du, J, Guo, J, Tian, W, Men, Y, Zhang, Y, Li, R-J, Yang, T-Y, Shang, D-W, Lou, J-N, Zhang, L-R & Zhang, Q 2010, 'Dual-targeting daunorubicin liposomes improve the therapeutic efficacy of brain glioma in animals', *Journal of Controlled Release*, vol. 141, no. 2, pp. 183-92.

Young, AIJ, Law, AMK, Castillo, L, Chong, S, Cullen, HD, Koehler, M, Herzog, S, Brummer, T, Lee, EF, Fairlie, WD, Lucas, MC, Herrmann, D, Allam, A, Timpson, P, Watkins, DN, Millar, EKA, O'Toole, SA, Gallego-Ortega, D, Ormandy, CJ & Oakes, SR 2016, 'MCL-1 inhibition provides a new way to suppress breast cancer metastasis and increase sensitivity to dasatinib', *Breast Cancer Research : BCR*, vol. 18, p. 125.

Younghoon, K, Sung Hoon, K, Tanyeri, M, Katzenellenbogen, JA & Schroeder, CM 2013, 'Dendrimer Probes for Enhanced Photostability and Localization in Fluorescence Imaging', *Biophysical Journal*, vol. 104, no. 7, pp. 1566-75.

Yumoto, K, Berry, JE, Taichman, RS & Shiozawa, Y 2014, 'A novel method for monitoring tumor proliferation in vivo using fluorescent dye DiD', *Cytometry A*, vol. 85, no. 6, pp. 548-55.

Zardavas, D, Irrthum, A, Swanton, C & Piccart, M 2015, 'Clinical management of breast cancer heterogeneity', *Nature Reviews: Clinical Oncology*, vol. 12, no. 7, pp. 381-94.

Zhang, B, Zhang, Y & Yu, D 2017, 'Lung cancer gene therapy: Transferrin and hyaluronic acid dual ligand-decorated novel lipid carriers for targeted gene delivery', *Oncology Reports*, vol. 37, no. 2, pp. 937-44.

Zhang, Q, Lu, L, Zhang, L, Shi, K, Cun, X, Yang, Y, Liu, Y, Gao, H & He, Q 2016, 'Dual-functionalized liposomal delivery system for solid tumors based on RGD and a pH-responsive antimicrobial peptide', *Scientific Reports*, vol. 6, p. 19800.

Zhao, M, Ding, XF, Shen, JY, Zhang, XP, Ding, XW & Xu, B 2017, 'Use of liposomal doxorubicin for adjuvant chemotherapy of breast cancer in clinical practice', *J Zhejiang Univ Sci B*, vol. 18, no. 1, pp. 15-26.

Zhao, Y, Houston, ZH, Simpson, JD, Chen, L, Fletcher, NL, Fuchs, AV, Blakey, I & Thurecht, KJ 2017, 'Using Peptide Aptamer Targeted Polymers as a Model Nanomedicine for Investigating Drug Distribution in Cancer Nanotheranostics', *Molecular Pharmaceutics*, vol. 14, no. 10, pp. 3539-49.

Zheng, C, Ma, G & Su, Z 2007, 'Native PAGE eliminates the problem of PEG-SDS interaction in SDS-PAGE and provides an alternative to HPLC in characterization of protein PEGylation', *Electrophoresis*, vol. 28, no. 16, pp. 2801-7.

Zhigaltsev, IV, Winters, G, Srinivasulu, M, Crawford, J, Wong, M, Amankwa, L, Waterhouse, D, Masin, D, Webb, M, Harasym, N, Heller, L, Bally, MB, Ciufolini, MA, Cullis, PR & Maurer, N 2010, 'Development of a weak-base docetaxel derivative that can be loaded into lipid nanoparticles', *Journal of Controlled Release*, vol. 144, no. 3, pp. 332-40.

Zoubari, G, Staufenbiel, S, Volz, P, Alexiev, U & Bodmeier, R 2017, 'Effect of drug solubility and lipid carrier on drug release from lipid nanoparticles for dermal delivery', *European Journal of Pharmaceutics and Biopharmaceutics*, vol. 110, pp. 39-46.

Appendices

Appendix A: Absorption spectra of *N*-AI and liposome phospholipid

The concentration of *N*-alkylisatin (*N*-AI) encapsulated in liposomes could not be determined by UV-vis spectrophotometry and interpolation from a *N*-AI standard curve as the liposome phospholipid interfered with the peak absorbance of *N*-AI at 310 nm and 435 nm (Fig. A1).

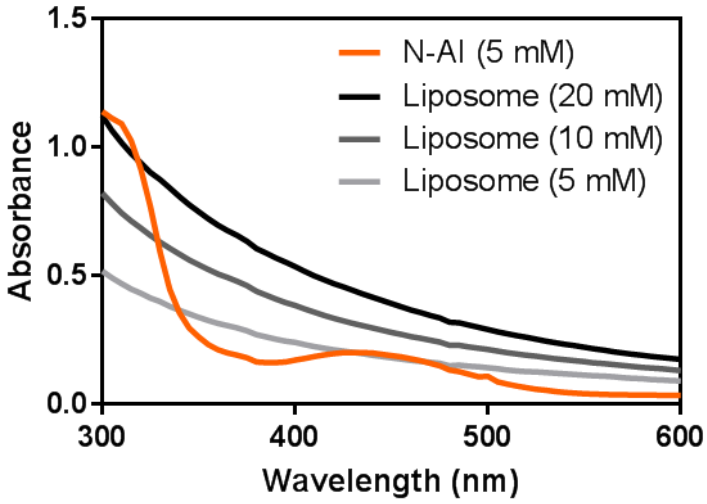

Figure A1: Liposome phospholipid interference with *N*-AI absorption spectrum. The phospholipid of empty liposomes interferes at 310 nm and 435 nm, the two peak absorption wavelengths for *N*-AI.

Appendix B: HPLC standard curve for *N*-AI quantification

The concentration of *N*-alkylisatin (*N*-AI) loaded into liposomes was determined by high performance liquid chromatography (HPLC), which showed an *N*-AI concentration of 2.2 mM, equating to 43.1% drug loading (% w/w) based on the starting amount of *N*-AI used in the liposome preparation. Concentration was determined by interpolation from an *N*-AI standard curve (Fig. B1).

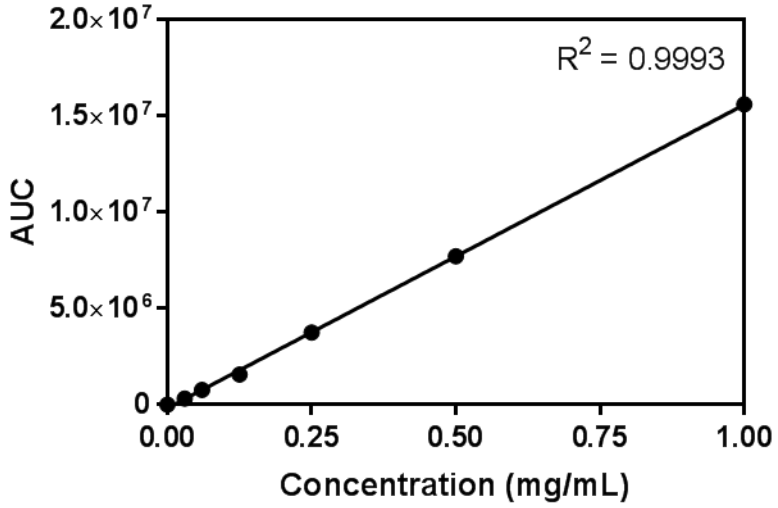

Figure B1: HPLC standard curve for quantifying *N*-AI encapsulated in liposomes.

Appendix C: Quantification of PAI-2 by Western blotting

A plasminogen activator inhibitor-2 (PAI-2) standard curve was successfully constructed using Western blotting and densitometry, which showed a linear relationship (Fig. C1).

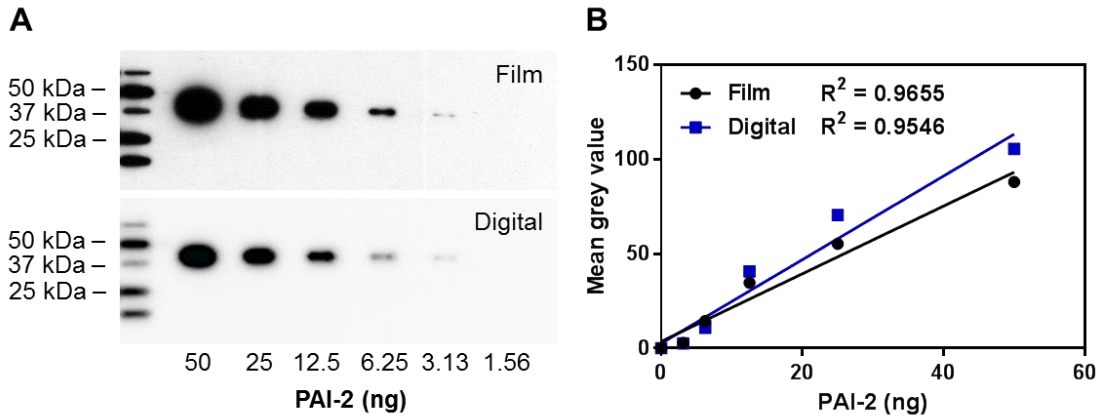

Figure C1: Western blot standard curve for quantification of PAI-2. (**A**) Various amounts of PAI-2 were run on a SDS-PAGE gel and then transferred to a nitrocellulose membrane for detection by Western blotting. (**B**) Quantification of PAI-2 bands using densitometry shows a linear relationship.

Appendix D: Toxicology of *N*-AI-loaded liposomes in mice

Toxicology studies performed by the Targeted Cancer Therapeutics Laboratory (University of Wollongong) have shown that *N*-alkylisatin (*N*-AI)-loaded liposomes are non-toxic in mice, with up to 100 mg/kg total dose of liposomal *N*-AI showing no adverse effects (Fig. D1).

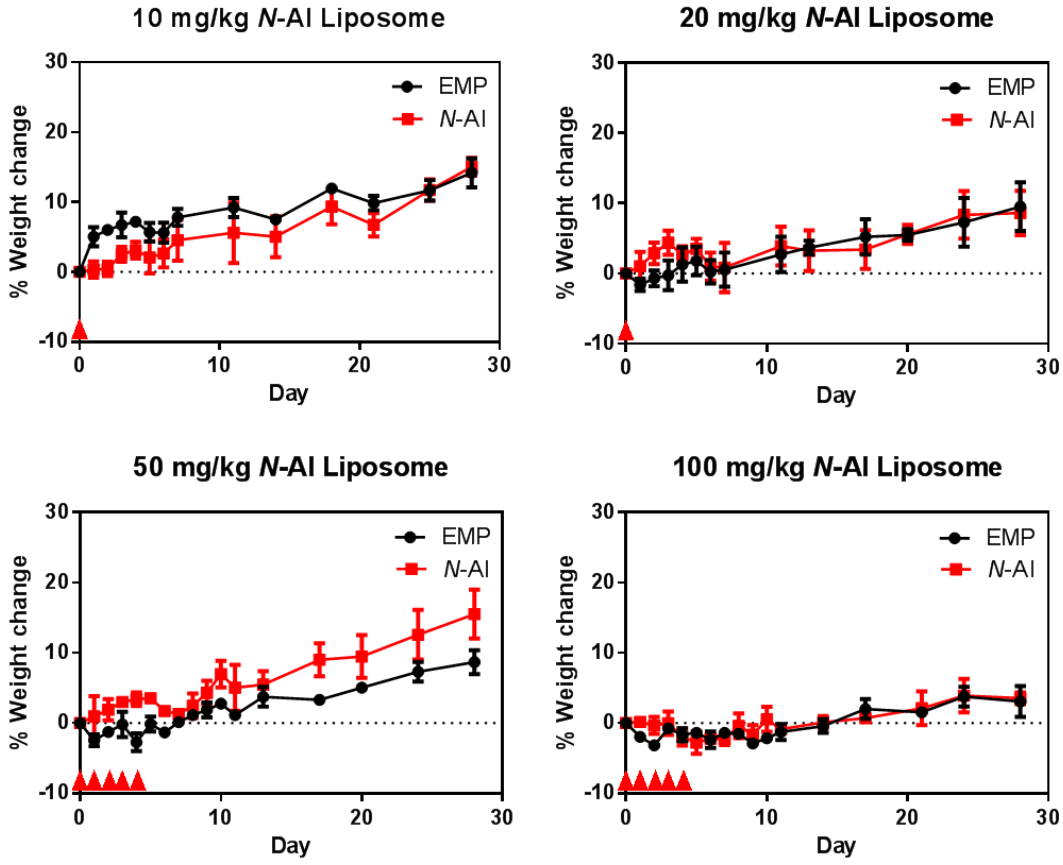

Figure D1: Toxicology testing of empty and *N*-AI-loaded liposomes in mice. Mice were treated with either a single bolus dose or multiple doses (indicated by arrows) of *N*-AI-loaded liposomes or empty (EMP) liposomes at an equivalent phospholipid concentration and weight change was monitored over time.

Appendix E: Final cohort organ weights in PK/BD study

To determine the pharmacokinetic and biodistribution (PK/BD) profiles of *N*-AI-loaded non-functionalised liposomes (*N*-AI) and *N*-AI-loaded PAI-2-functionalised liposomes (*N*-AI PAI-2) in tumour-bearing mice, liposomes were labelled with tritiated cholesteryl hexadecyl ether (^{3}H-CHE) to enable the detection of liposomes in plasma and tissues by liquid scintillation counting. Mice treated with *N*-AI and *N*-AI PAI-2 liposomes showed no significant differences in the average final weight of the kidneys, liver, spleen and lungs (Fig. E1).

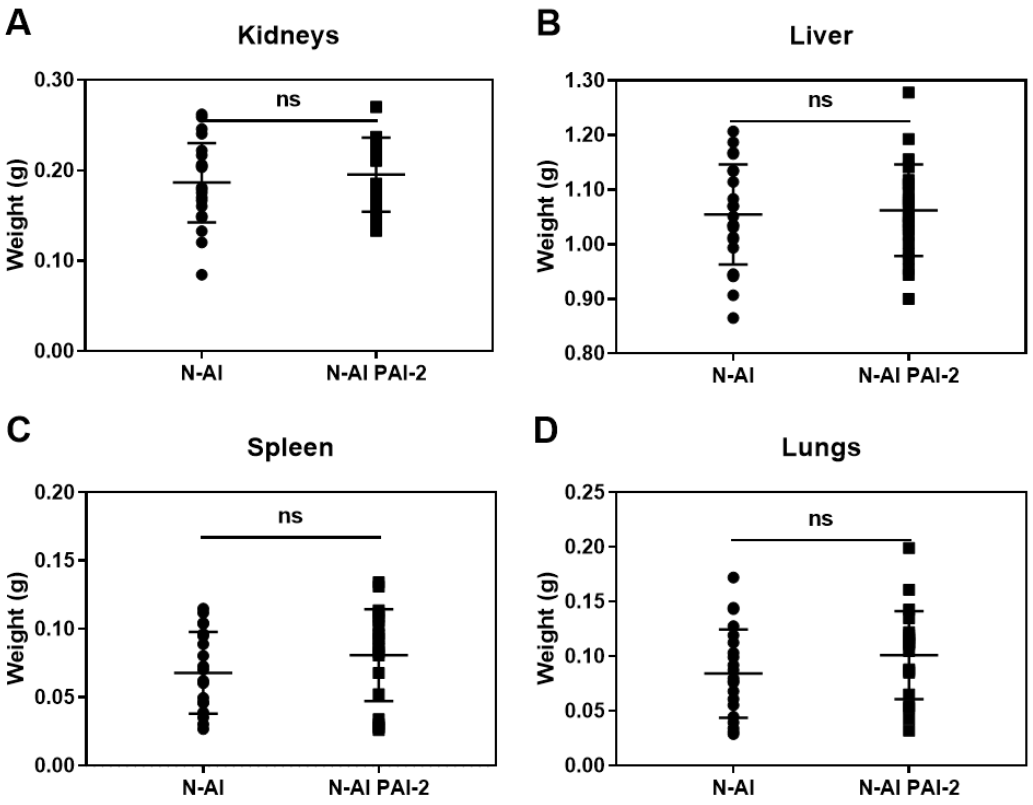

Figure E1: Final organ weights at experimental endpoint. At the end of each experimental time point, mice were euthanised by CO_2 inhalation, and the (**A**) kidneys, (**B**) liver, (**C**) spleen and (**D**) lungs were removed in whole and weighed. Values are the mean ± s.d. (n = 24). n.s., not significant ($P > 0.05$).

Appendix F: ESI-MS of CF647-labelled PAI-2

To visualise PAI-2 using single-molecule fluorescence microscopy, PAI-2 was labelled with a small red fluorophore (CF647, ~836 g/mol). Electrospray ionisation-mass spectrometry (ESI-MS) revealed up to 6 fluorophores per protein (average of 3) for CF647-labelled PAI-2 (Fig. F1).

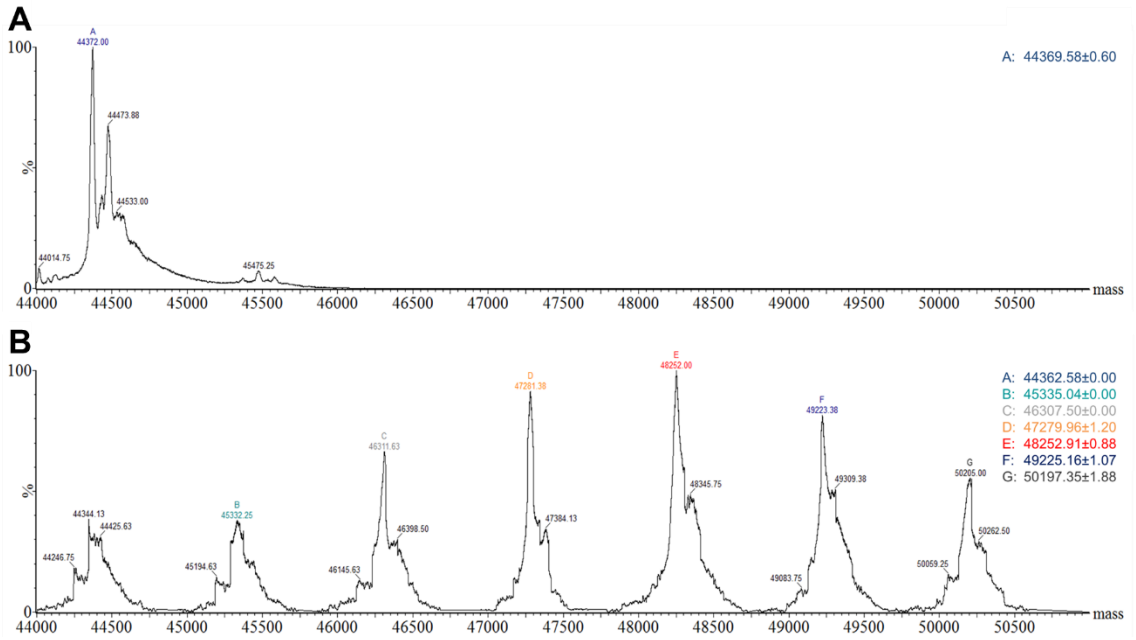

Figure F1: ESI-MS of CF647-labelled PAI-2. (**A**) Unlabelled PAI-2 and (**B**) CF647-labelled PAI-2. Masses refer to the molecular weight of unlabelled PAI-2 (~45 kDa) with varying numbers of attached CF647 (~0.836 kDa) molecules. Masses were generated using MassLynx V4.1 (Waters, MA, USA).

Appendix G: Diameter of CO and PI dual-functionalised liposomes

Liposomes functionalised with CF647-labelled PAI-2 and CF488-labelled trastuzumab (TZ) were prepared via the conventional (CO) or post-insertion (PI) method. Liposomes were analysed by dynamic light scattering before and after the functionalisation step to determine average liposome diameter. When the PI method was used, a significant increase in diameter ($P < 0.05$) was observed following functionalisation (Fig. G1). There was no significant increase in liposome diameter following functionalisation via the CO method.

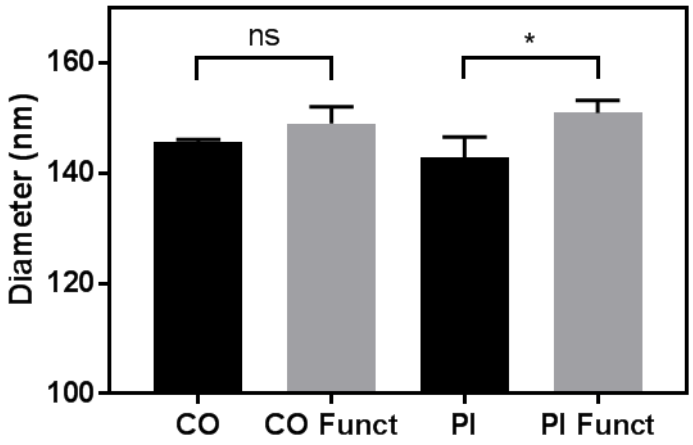

Figure G1: Diameter of liposomes before and after dual-functionalisation. A diameter increase was observed for liposomes prepared via the post-insertion (PI) method, but not for the conventional (CO) method, after functionalisation (funct). * = $P < 0.05$, n.s. = not significant ($P > 0.05$).